



UNIL | Université de Lausanne

Unicentre

CH-1015 Lausanne

<http://serval.unil.ch>

---

Year : 2017

## IMAGING AND BIOLOGICAL MARKERS IN RETINAL DISORDERS TO ASSESS GENE THERAPY SAFETY AND INVESTIGATE VASCULAR DISEASE MECHANISMS

Matet Alexandre

Matet Alexandre, 2017, IMAGING AND BIOLOGICAL MARKERS IN RETINAL DISORDERS  
TO ASSESS GENE THERAPY SAFETY AND INVESTIGATE VASCULAR DISEASE  
MECHANISMS

Originally published at : Thesis, University of Lausanne

Posted at the University of Lausanne Open Archive <http://serval.unil.ch>

Document URN : urn:nbn:ch:serval-BIB\_CF374B4068C01

### **Droits d'auteur**

L'Université de Lausanne attire expressément l'attention des utilisateurs sur le fait que tous les documents publiés dans l'Archive SERVAL sont protégés par le droit d'auteur, conformément à la loi fédérale sur le droit d'auteur et les droits voisins (LDA). A ce titre, il est indispensable d'obtenir le consentement préalable de l'auteur et/ou de l'éditeur avant toute utilisation d'une oeuvre ou d'une partie d'une oeuvre ne relevant pas d'une utilisation à des fins personnelles au sens de la LDA (art. 19, al. 1 lettre a). A défaut, tout contrevenant s'expose aux sanctions prévues par cette loi. Nous déclinons toute responsabilité en la matière.

### **Copyright**

The University of Lausanne expressly draws the attention of users to the fact that all documents published in the SERVAL Archive are protected by copyright in accordance with federal law on copyright and similar rights (LDA). Accordingly it is indispensable to obtain prior consent from the author and/or publisher before any use of a work or part of a work for purposes other than personal use within the meaning of LDA (art. 19, para. 1 letter a). Failure to do so will expose offenders to the sanctions laid down by this law. We accept no liability in this respect.



**UNIL** | Université de Lausanne

Faculté de biologie  
et de médecine

**Département : Ophtalmologie**

**IMAGING AND BIOLOGICAL MARKERS IN RETINAL DISORDERS TO  
ASSESS GENE THERAPY SAFETY AND INVESTIGATE VASCULAR  
DISEASE MECHANISMS**

**Thèse de doctorat ès sciences de la vie (PhD)**

présentée à la

Faculté de biologie et de médecine  
de l'Université de Lausanne

par

**Alexandre MATET**

Master de l'Université Pierre-et-Marie-Curie (Paris, France)

**Jury**

Prof. Nicolas Senn, Président  
Prof. Yvan Arsenijevic, Directeur de thèse  
Prof. Francine Behar-Cohen, Co-directrice  
Prof. Micah Murray, expert  
PD Dr. Pascal Escher, expert

Lausanne 2017

# Imprimatur

Vu le rapport présenté par le jury d'examen, composé de

<b>Président·e</b>	Monsieur Prof. Nicolas <b>Senn</b>
<b>Directeur·trice de thèse</b>	Monsieur Prof. Yvan <b>Arsenijevic</b>
<b>Co-directeur·trice</b>	Madame Prof. Francine <b>Behar-Cohen</b>
<b>Expert·e·s</b>	Madame Prof. Micah <b>Murray</b> Monsieur Dr Pascal <b>Escher</b>

le Conseil de Faculté autorise l'impression de la thèse de

**Monsieur Alexandre Matet**

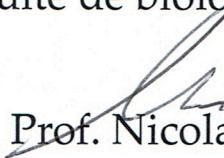
Master de l' Université Pierre et Marie Curie / Paris VI

intitulée

**IMAGING AND BIOLOGICAL MARKERS IN RETINAL  
DISORDERS TO ASSESS GENE THERAPY SAFETY  
AND INVESTIGATE VASCULAR DISEASE MECHANISMS**

Lausanne, le 30 octobre 2017

pour le Doyen  
de la Faculté de biologie et de médecine



Prof. Nicolas Senn

## ACKNOWLEDGEMENTS

I wish to express my absolute gratitude for their unlimited support to Professor Yvan Arsenijevic and Francine Behar-Cohen, thesis Director and Co-Director, and to Corinne Kostic, thesis supervisor, all outstanding scientists, exemplary mentors and noble persons. They provided an environment of knowledge, curiosity and freedom favoring research and initiative.

I warmly thank Professor Micah Murray and Pascal Escher, who accepted to participate to the Jury as Experts, and Professor Nicolas Senn, who presides the Jury.

I am grateful to the University of Lausanne, the Faculty of Biology and Medicine and the Doctoral School, as well as to the Research and Medical retina units at Hôpital ophtalmique Jules-Gonin, where most of the work was performed.

My deepest gratitude goes to all the colleagues and friends involved in the research projects, and those who provided useful advice, including Alexis Bemelmans, Laura Kowalczuk, Natacha Turck, Aurélien Thomas, Alexandre Moulin, Leonidas Zografos, Alejandra Daruich, Richard F. Spaide, Knut Stieger, Brigit Lorentz, Marianne Dor, Nasim Bararpour, Elena Brazhnikova, Céline Jaillard, Claire-Maëlle Fovet, Joanna Demilly, Lev Stimmer, Serge Rosolen, José-Alain Sahel, Samia Martin, Fulvio Mavilio, Vazrik Amirjanians, Michaël Nicolas, Francis Munier, Jérémie Canonica, Martial Mbefo, Sarah Decembrini, Florian Udry, Lilly Khamsy, Dana Wanner, Catherine Martin, Tatiana Favez, Charlène Joséphine, Solenne Metrailler, Damien Grize, Marc Curchod, and many more.

I acknowledge the financial support of Swiss Transmed and the Research Commission, Faculty of Biology and Medicine, University of Lausanne.

Finally, I would like to acknowledge the generous participation of the patients of the medical retina unit, Hôpital ophtalmique Jules-Gonin, who kindly contributed to many research projects with interest and good will, and whom I hope will benefit from the progresses achieved in current and upcoming projects.

This thesis is dedicated to Alejandra and Amalia.



## ABSTRACT

The retina is the neurosensory tissue responsible for the acquisition of visual stimuli. It is biologically separated from the systemic circulation by blood-retinal barriers, limiting the possibility for circulating markers to reflect retinal changes due to disease or therapeutic intervention. However, due to the transparency of ocular media, the retina is highly accessible to high-resolution imaging, and image processing provides access to physiological parameters quantitatively. In addition, the analysis of ocular media sampled during surgical procedures provides access to biological data regarding disease processes. In this work, imaging and biological markers were developed for several experimental and clinical situations: a gene therapy preclinical safety study (Project 1); the analysis of disease mechanisms in the choroical choroidal vascular disorder central serous chorioretinopathy (CSCR) (Project 2), and a similar translational approach in retinal vascular telangiectatic disorders (Project 3). Specific image processing algorithms were designed.

In Project 1, the preclinical safety of a lentiviral subretinal gene therapy for RPE65 replacement in Leber congenital amaurosis, LV-RPE65, was assessed on healthy non-human primates by conventional methods (*in vivo* electrophysiology, *ex vivo* immunohistochemistry, systemic biodistribution study) combined to *in vivo* analysis of the retinal structure by optical coherence tomography (OCT) at different timepoints, including early follow-up within 7 days. Imaging techniques revealed a transient and pronounced inflammatory process linked to LV-RPE65 injection that delayed retinal reattachment. Partial and transient photoreceptor loss was observed in the macular region, that was to a lesser extent also observed in control eyes injected with the vehicle. This work highlights the need to improve the surgical procedure for subretinal gene therapy delivery, and to consider using anti-inflammatory agents to prevent damaging processes occurring rapidly after subretinal injection.

In Project 2, mechanisms of CSCR, a retinal disease caused by choroidal vessel dilation leading to subretinal fluid accumulation, were explored. We analyzed predictive multimodal imaging factors of episode duration (2a) and recurrence (2b), evidencing in particular choroidal thickness as prognosis factor. Non-invasive OCT angiography images of the choriocapillaris, the innermost layer of the choroid beneath the retinal pigment epithelium, were processed to detect flow voids and investigate their distribution (2c). Finally, the molecular composition of subretinal fluid from a unique case of CSCR requiring subretinal surgery, was explored using a multi-omics approach (2d).

In Project 3, mechanisms of retinal vasculopathy were investigated in two pure phenotypes represented by telangiectatic disorders: type 1 macular telangiectasia (Mactel 1) (3a and 3b), and radiation maculopathy (3c). For the investigation of Mactel 1, image processing tools were used to compute global and local capillary density on OCT angiography images, showing that non-perfusion is a critical feature in Mactel 1, related to visual outcome and telangiectasia formation. This approach was combined to the biological investigation of aqueous humor from Mactel 1 cases. Intraocular levels of angiogenic factors demonstrated the involvement of placental growth factor in the pathophysiology of MacTel 1, that was correlated with multimodal imaging findings (3b). Finally, an image processing algorithm was designed and applied to radiation maculopathy, to compute automatically the fractal dimension of OCT angiography images. This parameter was relevant in assessing capillary network disruption, and demonstrated that alterations of the deep plexus influence independently visual function.

The strategies developed throughout these three projects demonstrate the interest of quantitative image analysis for the investigation of retinal disorders, and the possibility of coupling imaging and biological data. This approach contributed to identify potential imaging or biological markers for diagnosis, prognosis, therapeutic response and toxicity in several biomedical situations.



## RÉSUMÉ

La rétine est un tissu neurosensoriel responsable de l'acquisition des signaux visuels. Elle se trouve biologiquement séparée de la circulation systémique par les barrières hémato-rétiniennes, limitant la possibilité pour des marqueurs circulants de refléter des altérations du tissu rétinien, dus à des maladies ou secondaires à des interventions thérapeutiques. Cependant, en raison de la transparence des milieux oculaires, la rétine est accessible à l'imagerie haute résolution, et l'analyse d'images permet d'extraire des paramètres physiologiques quantitatifs. En outre, l'analyse des milieux oculaires prélevés au cours d'interventions chirurgicales permet d'accéder à des données biologiques concernant les processus physiopathologiques. Dans ce travail, des marqueurs biologiques et d'imagerie ont été développés pour plusieurs situations expérimentales et cliniques : une étude de sécurité préclinique en thérapie génique (Projet 1), l'analyse de mécanismes pathologiques dans la chorioretinopathie séreuse centrale (CRSC) (Projet 2), et dans les pathologies télangiectatiques vasculaires rétinienne (Projet 3). Des algorithmes de traitement d'image spécifiques ont été conçus.

Dans le Projet 1, la tolérance préclinique d'une thérapie génique sous-rétinienne lentivirale pour remplacement du gène RPE65 dans l'amaurose congénitale de Leber, LV-RPE65, a été évaluée sur des primates non humains sains par des méthodes conventionnelles (électrophysiologie *in vivo*, immunohistochimie *ex vivo*, étude de biodistribution systémique), et par analyse *in vivo* de la structure rétinienne par tomographie par cohérence optique (OCT) à différents points, y compris un suivi précoce dans les 7 jours. Les techniques d'imagerie ont révélé un processus inflammatoire transitoire lié à l'injection de LV-RPE65 qui a retardé le réattachement rétinien. Une perte partielle et transitoire des photorécepteurs a été observée dans la région maculaire, détecté également, et dans une moindre mesure dans les yeux témoins, injectés avec la solution véhicule. Ce travail souligne la nécessité d'améliorer la procédure chirurgicale pour l'administration de thérapies géniques sous-rétiniennes, et d'envisager l'usage d'agents anti-inflammatoires pour limiter ces altérations.

Dans le projet 2, les mécanismes de la CRSC, une maladie rétinienne causée par la dilatation des vaisseaux choroïdiens menant à l'accumulation de liquide sous-rétinien, ont été explorés. Nous avons analysé les facteurs d'imagerie multimodaux prédictifs de la durée des épisodes (2a) et de récurrence (2b), mettant en évidence notamment l'épaisseur choroïdienne comme facteur pronostic. Des images en OCT angiographie, non invasive, de la choriocapillaire, la couche la plus interne de la choroïde sous l'épithélium pigmentaire rétinien, ont été traitées pour détecter des lacunes dans le flux sanguin, et étudier leur distribution (2c). Enfin, la composition moléculaire du liquide sous-rétinien d'un cas rare de CRSC nécessitant une chirurgie sous-rétinienne, a été explorée en utilisant une approche multi-omique collaborative (2d).

Dans le projet 3, les mécanismes de vasculopathie rétinienne ont été étudiés dans deux phénotypes purs représentés par les troubles télangiectasiques : télangiectasie maculaire de type 1 (Mactel 1) (3a et 3b), et maculopathie radique (3c). Pour l'étude de Mactel 1, des outils de traitement d'images ont été utilisés pour calculer la densité capillaire globale et locale sur des images d'OCT angiographie, montrant que la non-perfusion est un paramètre critique dans les Mactel 1, corrélé à la fonction visuelle et à la formation des télangiectasies. Cette approche a été combinée à l'étude biologique de l'humeur aqueuse dans des cas de Mactel 1. Des niveaux intraoculaires de facteurs angiogéniques ont démontré l'implication du facteur de croissance placentaire dans la physiopathologie de MacTel1. De plus, ce facteur était corrélé avec la densité capillaire en OCT angiographie (3b). Enfin, un algorithme de traitement d'images a été conçu et appliqué à la maculopathie radique pour calculer automatiquement la dimension fractale des images d'OCT angiographie. Ce paramètre était pertinent dans l'évaluation de la perturbation du réseau capillaire, et a démontré que les altérations du plexus profond influencent indépendamment la fonction visuelle.

Les stratégies développées dans ce travail démontrent l'intérêt de l'analyse d'image quantitative pour l'étude des pathologies rétinienne, et la possibilité de coupler l'imagerie et les données biologiques. Cette approche a permis d'identifier des marqueurs biologiques ou d'imagerie potentiels pour le diagnostic, le pronostic, la réponse thérapeutique et la toxicité dans les différentes situations étudiées.



# TABLE OF CONTENTS

<b>INTRODUCTION.....</b>	<b>1</b>
<i>Overview of the structure and vasculature of the retina and choroid .....</i>	<i>1</i>
<i>Multimodal retinal imaging .....</i>	<i>3</i>
<i>Biomarkers in retinal diseases: an emerging field .....</i>	<i>5</i>
<i>Strategy to identify candidate biological and imaging markers .....</i>	<i>7</i>
<i>Image processing and analysis: general methodology.....</i>	<i>8</i>
<i>Biological markers in ocular media .....</i>	<i>10</i>
[Project 1] <i>Evaluation of tolerance to lentiviral LV-RPE65 gene therapy vector after subretinal delivery in non-human primates .....</i>	<i>12</i>
<i>Leber congenital amaurosis and the RPE65 gene .....</i>	<i>12</i>
<i>RPE65 gene therapy based on adeno-associated vectors .....</i>	<i>15</i>
<i>RPE65 lentiviral gene therapy .....</i>	<i>17</i>
[Project 2] <i>Translational approaches in the vascular disease central serous chorioretinopathy.....</i>	<i>19</i>
<i>CSCR: Clinical presentation .....</i>	<i>19</i>
<i>Clinical subtypes of CSCR.....</i>	<i>20</i>
<i>CSCR: a mysterious pathophysiology .....</i>	<i>23</i>
[Project 3] <i>Translational approaches in telangiectatic retinal vascular disorders: example of macular telangiectasia type 1 and radiation maculopathy.....</i>	<i>26</i>
<i>Angiogenic factors: the controversial role of the VEGFR-1 and -2 pathways in retinal vascular permeability.....</i>	<i>28</i>
<i>MacTel 1: a “pure” disease of retinal capillaries .....</i>	<i>28</i>
<i>Radiation maculopathy: a vision-threatening complication in eyes salvaged from an intraocular malignancy .....</i>	<i>30</i>
Aims of the thesis .....	31
<b>RESULTS .....</b>	<b>33</b>
[Project 1] <i>LV-RPE65 .....</i>	<i>33</i>
[Project 2] <i>CSCR .....</i>	<i>35</i>
<i>[2a] Acute CSCR: multimodal imaging and clinical prognosis markers influencing episode duration.....</i>	<i>35</i>
<i>[2b] Risk factors for recurrent CSCR: a multimodal imaging study .....</i>	<i>39</i>
<i>[2c] OCT and OCT angiography imaging of the choroidal vasculature in CSCR .....</i>	<i>41</i>
<i>[2d] Proteomics/metabolomics of subretinal fluid in CSCR .....</i>	<i>43</i>
[Project 3] <i>Telangiectatic retinal disorders .....</i>	<i>47</i>
<i>[3a] Capillary density and microvascular abnormalities assessed by OCT angiography in MacTel1 ..</i>	<i>47</i>
<i>[3b] Analysis of aqueous humor angiogenic profile in MacTel 1 and relationship to the efficacy of intravitreal aflibercept.....</i>	<i>49</i>
<i>[3c] Application of fractal analysis to the imaging of radiation maculopathy.....</i>	<i>51</i>
<b>DISCUSSION .....</b>	<b>53</b>
<i>Image processing: the critical issue of repeatability.....</i>	<i>54</i>
[Project 1] <i>LV-RPE65 .....</i>	<i>56</i>
<i>Hurdles for gene therapy delivery to the RPE via the subretinal route .....</i>	<i>56</i>
<i>Safety markers in retinal gene therapy trials: the role of retinal imaging .....</i>	<i>58</i>

<i>Perspectives</i> .....	58
[Project 2] CSCR.....	59
<i>From the observation of subretinal fluid kinetics to its molecular characterization</i> .....	59
<i>Perspectives: future imaging and biological markers in CSCR</i> .....	61
[Project 3] Telangiectatic retinal disorders.....	62
<i>The emergence of OCT angiography as non-invasive imaging marker of retinal diseases</i> .....	62
<i>PIGF, VEGF and their inhibition in retinal telangiectatic disorders</i> .....	63
<b>Conclusions</b> .....	<b>65</b>
<b>REFERENCES</b> .....	<b>67</b>
<b>ARTICLES</b> .....	<b>79</b>
[1] Preclinical safety evaluation of lentiviral LV-RPE65 gene therapy after subretinal delivery in non-human primates. <i>Transl Res</i> , 2017.....	79
[2a] Acute central serous chorioretinopathy: Factors influencing episode duration. <i>Retina</i> 2017.....	103
[2b] Risk factors for recurrent central serous chorioretinopathy. <i>Retina</i> 2017.....	117
[2c] Choriocapillaris flow voids in central serous chorioretinopathy: an optical coherence tomography angiography study (submitted).....	135
[2d] Proteome and metabolome of subretinal fluid in central serous chorioretinopathy and rhegmatogenous retinal detachment: a pilot case study (submitted).....	163
[3a] Macular telangiectasia type 1: capillary density and microvascular abnormalities assessed by optical coherence tomography angiography. <i>Am J Ophthalmol</i> 2016.....	195
[3b] Efficacy of intravitreal aflibercept in macular telangiectasia type 1 is linked to the ocular angiogenic profile. <i>Retina</i> 2016.....	215
[3c] Radiation maculopathy after proton beam therapy for uveal melanoma: optical coherence tomography angiography alterations influencing visual acuity. <i>Investigative Ophthalmology and Vision Science</i> 2017.....	233
<b>APPENDICES</b> .....	<b>I</b>
Appendix 1: MatLab code for perifoveal intercapillary areas on OCT angiography.....	I
Appendix 2: MatLab code for file moving and renaming.....	III
Appendix 3: MatLab code for extracting OCT angiography images from Angiovue screen captures.....	IV
Appendix 4: MatLab code for extracting OCT layer thickness quantitative values in injected and non-injected areas from Spectralis.....	V
Appendix 5: MatLab code for computing fluorescein expansion ratios on fluorescein angiography.....	XI
Appendix 6: MatLab code for segmenting subretinal fluid volume in OCT stacks.....	XII
Appendix 7: MatLab code for segmenting choriocapillaris flow voids on OCT angiography.....	XV
Appendix 8: MatLab code for global capillary density after subtraction of large vessels and cystoid spaces on OCT angiography.....	XVI
Appendix 9: MatLab code for local capillary density on OCT angiography.....	XVIII
Appendix 10: MatLab code for generation of randomly distributed circles over OCT angiography images.....	XX
Appendix 11: MatLab code for perifoveal intercapillary areas on fluorescein angiography.....	XXII
Appendix 12: MatLab code for cystoid cavities area and outlining.....	XXIII
Appendix 13: MatLab code for local fractal dimension on OCT angiography.....	XXIV

## ABBREVIATIONS

11 $\beta$ HSD2: 11- $\beta$  hydroxysteroid dehydrogenase type 2  
AAV: adeno-associated virus  
AH: aqueous humor  
AMD: age-related macular degeneration  
BEST: Biomarkers, EndpointS, and other Tools  
CMV: cytomegalovirus  
CRALBP: cellular retinoic acid binding-protein  
DCP: deep capillary plexus  
EDI-OCT: enhanced-depth imaging optical coherence tomography  
FA: fluorescein angiography  
FA: fundus albipunctatus  
FDA: Food and Drug Administration  
G: Gauge  
GCL: Ganglion Cell Layer  
GMP: good manufacturing practice  
ICG: indocyanine green  
ILM: Inner Limiting Membrane  
INL: Inner Nuclear Layer  
IPL: Inner Plexiform Layer  
IRBP: interphotoreceptor retinoid-binding protein  
IS: Inner Segment  
LCA: Leber congenital amaurosis  
LRAT: lecithin retinol acyltransferase  
MacTel: macular telangiectasia  
MR: mineralocorticoid receptor  
NFL: nerve fiber layer  
NHP: non-human primate  
NIH: National Health Institutes  
OCT: optical coherence tomography  
OCTA: optical coherence tomography angiography  
OLM: outer limiting membrane  
ONL: Outer Nuclear Layer  
OPL: Outer Plexiform Layer  
OS: Outer Segment  
RBP: retinol binding protein  
RGB: red, green, blue  
ROI: region of interest  
RP: retinitis pigmentosa  
RPE: retinal pigment epithelium  
RPE: Retinal Pigment Epithelium  
RRD: rhegmatogenous retinal detachment  
SCP: superficial capillary plexus  
SF: subretinal fluid  
SFCT: subfoveal choroidal thickness  
SS-OCT: swept-source optical coherence tomography  
STGD: Stargardt disease  
VSV-G: vesicular stomatitis virus glycoprotein  
WPRE: woodchuck hepatitis virus post-transcriptional regulatory element



# INTRODUCTION

## Overview of the structure and vasculature of the retina and choroid

The retina is a remarkable neurosensory organ ensuring the perception of light stimuli, the preliminary coding of visual signal and its transmission to the brain via the optic pathways. The highly demanding metabolic activity of the retina is supported by the retinal pigment epithelium (RPE), recycling essential compounds for the phototransduction cycle and maintaining photoreceptor homeostasis; by the choroid, an intermeshed vascular network located between the retina and the sclera, ensuring the blood supply of outer retinal layers; and by the retinal vasculature itself, divided into three parallel plexuses supplying the inner retina.<sup>1</sup> Other retinal cell types have critically supportive metabolic functions, such as glial cells consisting in astrocytes and Müller cells, that modulate the inner blood-retinal barrier and the retinal hydro-electrolytic homeostasis, deliver neuroactive substances and retinoids to cone photoreceptors, and degrade metabolic byproducts.

The neuroretina is a multi-layer specialized tissue (**Figure 1**), composed from the innermost to the outermost layer by the inner limiting membrane (ILM), basal membrane of the retinal Müller glial (RMG) cells, the nerve fiber layer, the ganglion cell layer, the inner plexiform layer (IPL) that contains synapses between ganglion cells and interneurons (or bipolar cells), the inner nuclear layer (INL), formed by nuclei of bipolar, amacrine, horizontal and RMG cells, the outer plexiform layer (OPL), composed by synaptic connections between visual neurons (or photoreceptors) and interneurons, the outer nuclear layer (ONL) formed by nuclei of cone and rod photoreceptors, and the inner and outer segments of the photoreceptors.<sup>2</sup> The outer limiting membrane (OLM) is formed by the cellular contacts between RMG cells and photoreceptor inner segments. Photoreceptor outer segments are in close contact with RPE microvilli, but no molecular adhesion or junction system maintains the neuroretina attached to the RPE. The RPE lies on the Bruch membrane, which outermost part forms the basal membrane of the choriocapillaris, the innermost vascular layer of the choroid.

The retina is vascularized by two independent vascular beds, the retinal and choroidal vasculatures. The larger retinal vessels, branches of the central retinal artery and vein, lay below

the ILM, and are surrounded by astrocytes, pericytes and RMG cells. Between pre-capillary arterioles and post-capillary venules, the retinal capillary network is arranged in three layers, the superficial, intermediate and deep plexuses located in the nerve fiber and ganglion cell layers, at the inner border of the IPL, and at the inner and outer border of the INL, respectively,<sup>3</sup> although current clinically available imaging techniques only allow to discriminate the superficial and deep plexuses.<sup>4</sup> Around the optic nerve head, a radial capillary network lays within the nerve fiber layer, along the temporal superior and inferior retinal vessels.<sup>5</sup>

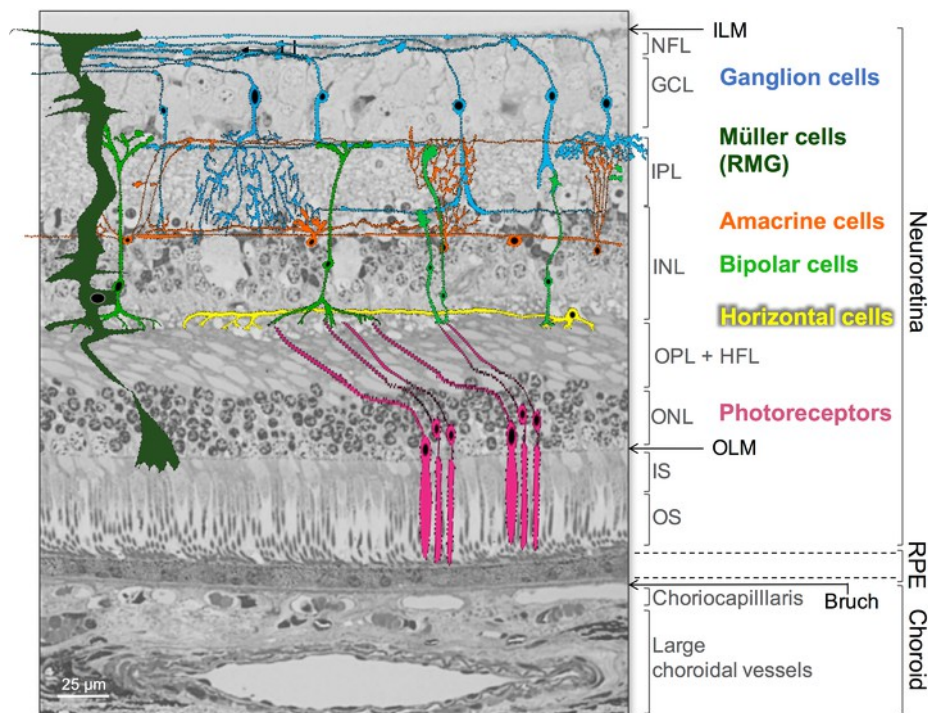


**Figure 1. Schematic representation of retinal layers and main retinal cell types.**

Histology section of a human retina at the mid-periphery, stained with hematoxylin-eosin. Color drawings of the different neuronal cell types and the retinal glial Müller cells (RMG) are superimposed on the histologic picture.

ILM= Inner Limiting Membrane; GCL= Ganglion Cell Layer; NFL= nerve fiber layer; IPL= Inner Plexiform Layer; INL= Inner Nuclear Layer; OPL= Outer Plexiform Layer; ONL= Outer Nuclear Layer; OLM= outer limiting membrane; IS= Inner Segment; OS= Outer Segment; RPE= Retinal Pigment Epithelium.

(Adapted with permission from Daruich *et al.*, *Prog Ret Eye Res* 2017. In press)<sup>6</sup>

Since the outer retinal layers are avascular, the choroidal vessels supply nutrients and oxygen to the high energy-demanding photoreceptors. Sympathetic regulation is present in the choroidal vasculature but not in retinal vessels. Most of the choroidal space is occupied by vessels organized in three vascular layers: the choriocapillaris, a thin interconnected capillary network is the innermost layer, the medium- and small-sized vessels form the intermediate Sattler's layer,

and large arteries derived from the short posterior ciliary arteries and large lumen veins form the outermost Haller's layer. The supra-choroid is the virtual space separating Haller's layer from the sclera. Numerous non-vascular cell types, such as melanocytes, macrophages/microglia and mast cells lay around choroidal vessels. Lymphatic-like vessels have been described in the human choroid, located in the innermost vascular layers external to the fenestrated vessels of the choriocapillaris.<sup>7</sup> In the normal retina, no lymphatic vessel has been identified.

Three types of glial cells are present in the neuroretina: astrocytes, located in the inner retina, at the vitreal interface and around vessels, microglial cells, which in physiologic conditions are ramified cells, located only in the inner retina and around retinal vessels, and RMG cells. RMG cells are the only cells spanning the entire thickness of the neuroretina, ensuring contact between all neuronal cell types, retinal vessels and the vitreous cavity.

The macula is a highly specialized region of the retina responsible for fine visual acuity. It is located temporal to the optic nerve head and can be recognized on fundus visualization by its yellow color, due to the accumulation of the xanthophyll pigments lutein and zeaxanthin. The center of the macula, the fovea, where inner retinal layers are displaced laterally, is exclusively composed of cone photoreceptors and specific foveal RMG cells. In the fovea, cones are densely packed, thinner, and have elongated outer segments, as compared to cones of the peripheral retina. The center of the macula is generally avascular, surrounded by circularly arranged capillaries delimitating the foveal avascular zone, a central 400-500- $\mu\text{m}$ -diameter area. There are important variations in the shape of the avascular zone among healthy subjects, with a small proportion of subjects harboring a vascularized fovea, with limited functional consequences.<sup>8</sup>

### Multimodal retinal imaging

The retina and choroid are the only internal vascular organs belonging to the central nervous system and directly accessible to visual examination by optical means, due to the transparency of ocular media. The multimodal imaging of intraocular structures, that started with the revolutionary invention of indirect ophthalmoscopy allowing fundus examination by Helmholtz in 1851,<sup>9,10</sup> has experienced a dramatic acceleration over the past decades, since the introduction and

progressive clinical developments of fluorescein angiography in the 1960's,<sup>11,12</sup> of indocyanine green angiography in the 1980's,<sup>13-16</sup> and of autofluorescence imaging in the 1990-2000's.<sup>17-20</sup>

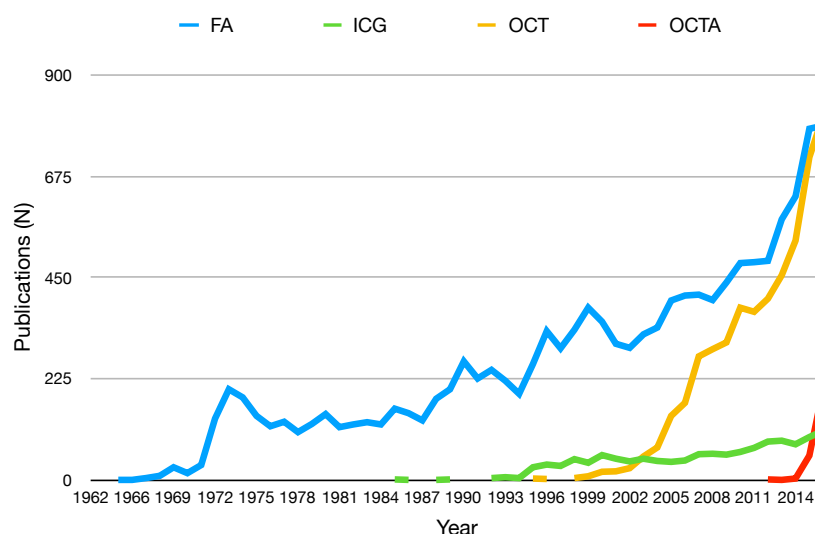


**Figure 2. History of retinal multimodal imaging since the advent of fluorescein angiography in 1962**, based on the number of publications per year registered on PubMed (<https://www.ncbi.nlm.nih.gov/pubmed/>). Note the steep rise of OCTA since its advent in 2012.

FA= fluorescein angiography; ICG= indocyanine green angiography; OCT= optical coherence tomography; OCTA= optical coherence tomography angiography

Search terms in PubMed (on August 16<sup>th</sup>, 2017):

"fluorescein angiography" AND retina WITHOUT "indocyanine"  
 "indocyanine angiography" or "indocyanine green angiography" AND eye  
 "optical coherence tomography" AND eye WITHOUT "angiography"  
 "optical coherence tomography angiography" AND eye

A major breakthrough was achieved with the advent of optical coherence tomography (OCT) in 1995,<sup>21</sup> that provides histology-like sections based on the infrared reflectivity of retinal and choroidal layers. It was then followed by improvements in data acquisition and processing, that led from time-domain to spectral-domain OCT, and its integration into multimodal devices, combining confocal fundus autofluorescence, angiography with fluorescein (FA) and indocyanine green (ICG), and OCT.<sup>22</sup> Enhanced-depth imaging (EDI-OCT)<sup>23</sup> and swept-source OCT (SS-OCT)<sup>24,25</sup> improved the visualization of choroidal layers. Further improvements consisted in volume reconstruction of OCT scans, allowing "en face" OCT representation.<sup>26</sup> Finally, these advancements in tridimensional viewing, combined to decorrelation algorithms, opened a new avenue with the emergence of OCT angiography in the 2010's,<sup>27</sup> imaging non-invasively (without intravenous dye injection) the vasculature of the retina and to a lesser extent, of the choroid.

A timeline of these innovations and their impact on clinical research is provided in **Figure 2.** according to the number of publications per year. It shows especially the sharp rise in publications based on OCT, and more recently on OCT angiography. The possibility to record disease processes manifesting on one or several imaging modalities (for instance, exudation/staining/non-perfusion on fluorescein angiography, hypercyanescence, hyperpermeability on ICG, alteration of retinal layers on OCT, capillary network disruption on OCTA) coupled to digital acquisition techniques opening the way to computerized processing, have allowed to extract qualitative or quantitative parameters from these images, that may serve as imaging biomarkers. Some of these markers are available via built-in tools and may be validated as endpoints in clinical ocular research on certified devices (such as retinal, choroidal or intraretinal layer thickness on OCT) or not (such as vascular density on OCTA), are qualitative and require the grading of a masked observer (such as presence of hyper/hypo-fluorescence, area of non-perfusion outlined manually on FA/ICG), or are quantitative and may be extracted by custom image processing techniques (such as fluorescein expansion ratio on FA,<sup>28</sup> subretinal fluid volume<sup>28</sup> or of cystoid cavity area on OCT,<sup>29</sup> local capillary density<sup>30</sup> or fractal dimension on OCTA,<sup>31</sup> developed in this thesis).

#### Biomarkers in retinal diseases: an emerging field

The fine balance of complex molecular and cellular communications between the retina, RPE and choroid that maintains the retinal homeostasis is deregulated in pathological conditions. Biological modifications detected in ocular and body fluids or morphological alterations detected by multimodal imaging of the retina, RPE or choroid may correlate with these deregulated processes, providing useful “biomarkers”. Biomarkers were recently classified according to their significance for disease diagnosis, monitoring, assessment of treatment safety, prognosis, etc, in the BEST glossary (Biomarkers, EndpointS, and other Tools) by the FDA-NIH Joint Leadership Council.<sup>32</sup> Biomarkers can also be extremely useful to expand our understanding of retinal disease pathophysiology. Since the blood-ocular barriers ensure a strict control of molecular exchanges between intraocular media and the systemic circulation, specific markers can be

detected in intraocular fluids (for instance in retinal exudative disorders) or in the systemic circulation (for instance in diseases affecting the choroidal vasculature, located upstream of the blood-retinal barrier).

The extensive classification by the BEST glossary includes diagnostic, monitoring, pharmacodynamics/treatment response, predictive, prognostic, safety or susceptibility/risk biomarkers. In order to be qualified as valid biomarkers, candidate parameters should ideally be recognized as surrogate endpoints. The concept of surrogacy implies that a parameter is intimately connected (for instance, statistically correlated) to a clinical outcome, or “hard endpoint” (for instance, visual acuity or retinal thickness, two frequent outcomes in retinal disease studies), and in the meantime, that this parameter has a mechanistic connection to the underlying disease process or therapeutic intervention, as illustrated in **Figure 3**.

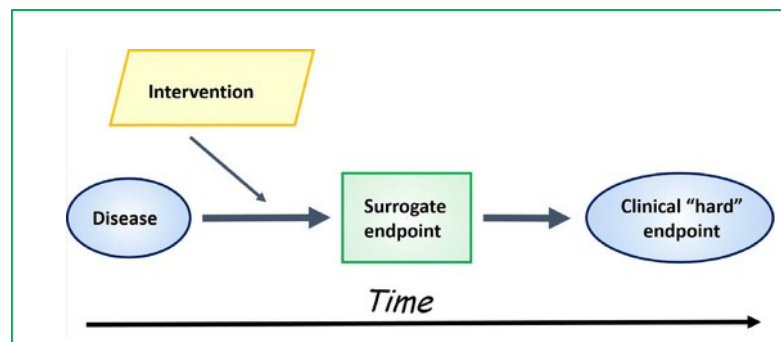


**Figure 3. Schematic representation of biomarkers validated as surrogate endpoints in ocular clinical research:** a direct causative and mechanistic link between the disease process/therapeutic intervention and clinical manifestations.

(reproduced from Vujosevic and Villani, *IOVS* 2017, under the CC BY-NC-ND 4.0 license)<sup>32</sup>

Exploration and validation of biomarkers are essential in the search of valid surrogate endpoints in pre-clinical and clinical ophthalmological research. In this thesis, we have explored imaging and biological markers to address several biomedical questions in three categories of retinal disorders: Project 1, to assess the ocular and systemic tolerance of a gene therapy strategy for Leber congenital amaurosis, an inherited retinal conditions of genetic origin; Project 2, to investigate candidate diagnosis and prognosis biomarkers related to different forms of central serous chorioretinopathy (CSCR), a condition that originates in the choroid and manifests with serous retinal detachments; Project 3, to investigate telangiectatic retinal disorders by

assessing intraocular levels of angiogenic factors, and extracting quantitative markers from cutting-edge OCT angiography imaging of retinal capillaries, coupled to custom image processing algorithms.

#### Strategy to identify candidate biological and imaging markers

In each project, several parameters relevant to a biological or clinical situation were assessed. The evaluation of each candidate marker, either extracted from image processing, or from biological experiments, followed a rationalized methodology: identification, testing, validation and attempted application (**Figure 4**).

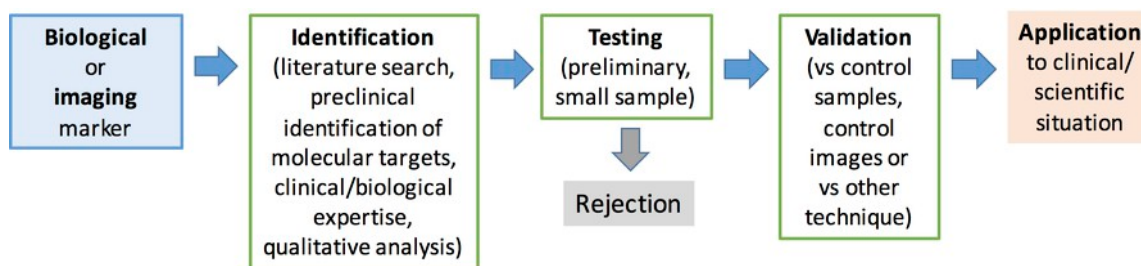


**Figure 4.** General methodology employed for the identification, testing, validation and application of ocular biological or imaging markers

This methodology can be exemplified by two representative markers explored in this thesis. First, PIGF, biological ocular marker elevated in the vascular disease MacTel 1 (Project 3b), was:

- 1) *identified* from a preclinical experiment (rat model overexpressing PIGF<sup>33</sup>)
- 2) then *tested* among other candidate angiogenic factors in aqueous humor from patients with a retinal vascular condition (MacTel 1). Its intraocular levels were higher in patients compared to age-matched control samples.
- 3) Several of these markers did not show different levels and were then *rejected* as potential disease markers
- 4) Finally, PIGF was further *validated* by showing correlations between its intraocular levels and morphological parameters using multimodal imaging.
- 5) This finding has an important clinical application since it supports the treatment of MacTel1, and possibly other retinal vascular disorders, by PIGF-neutralizing agents such as intravitreal aflibercept.

A second example is provided by the local fractal dimension in OCT angiography of radiation maculopathy (Project 3c). This parameter was:

- 1) *identified* from the scientific literature.<sup>34–36</sup>
- 2) *tested* on a subset of images, among other candidate imaging markers potentially reflecting the degree of capillary disorganization, such as perifoveal intercapillary areas (also identified from the literature<sup>37</sup>; code provided in the Appendix 1), that was *rejected* because not providing convincing results.
- 3) *validated* by showing a significant difference with healthy control eyes, and a significant correlation with numerous structural and functional parameters in affected eyes, especially visual acuity.
- 4) Potential applications are numerous, if such imaging tools were incorporated in daily practice. For instance, fractal dimension could serve as prognosis marker and help identify eyes without visual potential that should not undergo intense treatment.

Other approaches have been followed to fulfill each step of this process. For instance, the identification of a biological marker can be performed via unbiased molecular target identification using multi-omics screening (as on subretinal fluid samples in Project 2d). Imaging markers can also be derived from presumed pathological mechanisms, for instance choroidal thickening in CSCR,<sup>38,39</sup> and then tested and validated in cohorts of increasing sizes, as was performed in the literature to validate choroidal thickness as relevant marker of CSCR, although it is not a strict criteria to diagnose CSCR (see Introduction to Project 2).

#### Image processing and analysis: general methodology

Different image processing programs were developed in the works composing this thesis, each adapted to the specific features of the retinal disorder studied, and are provided in the Appendices section. This individualized approach allowed to extract the most relevant quantitative parameters adapted for each retinal disorder, in an exploratory pilot approach,

optimized on relatively small samples of images, and validated by the comparison to healthy control cases (for instance, fellow eyes in unilateral disorders). The different findings will require additional validation on larger cohorts, and some of the techniques developed may be more largely diffused by dedicated methodology publications.

MatLab (MathWorks, Natick, MA, USA)<sup>40</sup> is a high-level numerical computing environment and programming language, particularly adapted for the treatment of matrix data, and hence for image processing since the code source of digitalized images is composed of 2-dimension (grayscale image) or 3-dimension matrices (color image in RGB space). Its first release was issued in 1984 and its name is derived from “matrix laboratory”. It is widely used in fields like applied mathematics, engineering, and for academic purposes. Among other functions, MatLab allows matrix manipulations, plotting of functions and data, implementation of algorithms, creation of user interfaces.

Additional commercially available packages, or “Toolboxes” carry several preprogrammed function groups tailored for specific applications. The “Image processing toolbox” is an essential adjunct to MatLab for the manipulation of digital images.<sup>41</sup> It provides a comprehensive set of standard algorithms for image processing, analysis, visualization, and algorithm development. The main applications of these algorithms include image segmentation, particularly based on binarization techniques, image enhancement, noise reduction, geometric transformations, image registration, creation and manipulation of regions of interest (ROI).

The combination of the “Image processing toolbox” to basic MatLab file managing tools allows the programming of repeated automated functions for batch-processing of large datasets. This automation of image processing workflows is critical, since it warrants the intra- and inter-image reproducibility and repeatability when the image processing algorithm is 100% automated, or minimizes the variability in semi-automated processes. In contrast, a large proportion of publications based on retinal image processing are based on manual single file manipulation, using, for instance, the publicly available ImageJ (<https://imagej.nih.gov/ij/>) or Fiji (<https://fiji.sc>), an expanded version of ImageJ, which may raise concerns regarding the repeatability of operator-dependent processes, except when batch processing is performed via macro programming. An example of MatLab code for mass file processing is provided in the Appendix 2

(file moving and renaming) and 3 (extraction of OCT angiography images from exported screen captures on the Angiovue RTx100 device).

### Biological markers in ocular media

In recent years, many medical fields have been characterized by the discovery of multiple clinical, genetic, biological or imaging markers that provide diagnostic or prognostic information on diseases. In the near future, these markers, grouped under the term "biomarkers", could become common practice and revolutionize diagnostic and therapeutic strategies with a precise, individualized approach to medicine. This approach is exemplified by the research effort launched worldwide, such as the Precision Medicine Initiative<sup>42</sup> of the National Institutes of Health (USA), the Swiss Personalized Health Network,<sup>43</sup> the Joint Nordic Biobank Research Infrastructure<sup>44</sup> or the European Alliance for Personalized Medicine.<sup>45</sup>

The eye, by its accessibility, the diversity of the conditions this organ may present, and the need to detect early ocular affections that can leave irreversible visual sequelae, offers a target of choice for the search for biomarkers. In addition, intraocular tissues lay into aqueous media allowing sampling without any tissue lesions. The superficial localization of the eye and its transparency make it possible to retrieve ocular media, most often during a surgical procedure, with ethical approval from regulatory authorities and patient consent. In addition, blood-brain barriers and the immune privilege of the eye make it a "sanctuary" where local biochemical alterations, potentially causal or secondary to the disease process and/or to its progression, can be reflected in ocular fluids.

These local ocular fluids are, from the most superficial to the less accessible: tears, aqueous humor (which bathes the anterior chamber between the cornea and the lens), vitreous (aqueous gel filling the eyeball behind the lens), and subretinal fluid (when present in case of retinal detachment of various causes). Interestingly, in the blood, numerous alterations associated to retinal disorders have also been recognized.<sup>46,47</sup>

The different samples and their sampling routes are exposed on **Figure 5**. The retrieval of these samples is submitted to strict ethical regulations. A specific ethical authorization requiring

the informed consent of each patient was established at Jules-Gonin Eye Hospital, where the samples presented in this thesis were obtained. This authorization, delivered by the local ethics committee of the Swiss Federal Department of Health (CER-VD n°340/15) required each patient to agree to the research use of his/her samples, after anonymization.

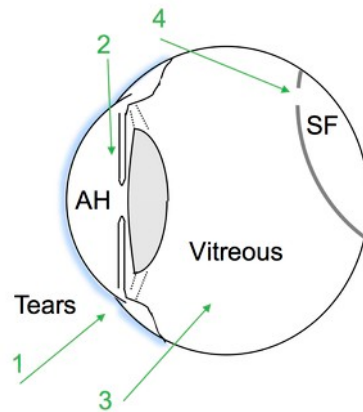


**Figure 5. Ocular samples and sampling routes.**

1. Tear sampling by Schirmer blotting paper in the inferior conjunctival fornix.
2. Aqueous humor sampling by a corneal puncture with a 30G needle (during intravitreal treatment administration) or 20-23G incision (during cataract surgery) at the temporal or nasal limbus.
3. Vitreous sampling by pars-plana vitrectomy, at the beginning of a surgical posterior segment procedure, without turning the infusion line on in order to obtain an undiluted sample.
4. Subretinal fluid sampling during surgical procedures for rhegmatogenous retinal detachment, with the vitrectomy probe, through the peripheral retinal tear, with the same precautions as vitreous sampling to avoid sample dilution.

G= Gauge; AH= aqueous humor; SF= subretinal fluid

Powerful analytical methods, such as proteomics, metabolomics, and increasingly fine biochemical assays (immuno-assays, spectroscopy) allow either a targeted, detailed analysis of these media, but also large-scale screening for instance through omics techniques.<sup>48</sup> In addition, advances in high-throughput sequencing have also allowed genomics to explore a large number of ocular pathologies.<sup>49</sup>

There is a recent surge in literature focusing on ophthalmic biomarkers, subject to a special issue of *Investigative Ophthalmology and Vision Sciences*,<sup>32,50–52</sup> and summarized in a recent review.<sup>53</sup>

The clinical and biological background of the 3 projects composing this thesis are detailed below, and the specific aims guiding these works are exposed at the end of the Introduction.

## [Project 1] Evaluation of tolerance to lentiviral LV-RPE65 gene therapy vector after subretinal delivery in non-human primates

### Leber congenital amaurosis and the RPE65 gene

Leber congenital amaurosis (LCA) is a juvenile, aggressive form of inherited retinal dystrophy, a wide group of Mendelian neurodegenerative conditions that also includes retinitis pigmentosa (rod or rod-cone dystrophies), macular dystrophies (Stargardt disease, pattern dystrophy, cone and cone-rod dystrophies), choroideremia, and other entities such as cone dysfunction syndromes, congenital stationary night blindness, syndromic presentations (Usher syndrome, Bardet-Biedl), etc.<sup>54-56</sup> According to reported rates, 6-15% of affected individuals present mutations in the RPE65 gene,<sup>57-59</sup> coding for a 65-kDa isomerase mainly expressed in the RPE, which plays a key role in the visual cycle by recycling the retinoids necessary for the phototransduction.<sup>60-63</sup> More specifically, RPE65 isomerizes within RPE cells all-*trans*-retinyl esters, either recycled from the light-triggered isomerization of 11-*cis*-retinal (bound to rhodopsin/opsins) to all-*trans*-retinal in photoreceptors, or originating from the circulation, to 11-*cis*-retinol (**Figure 6**).

Numerous other genes causing Leber congenital amaurosis have been identified, the most notable of which are involved in phototransduction (*AIPL1*, *GUCY2D*), the retinoid cycle (*RDH12*, *LRAT*), photoreceptor development and structure (*CRX*, *CRB1*), transport across the photoreceptor connecting cilium (*TULP1*, *RPGRIP1*, *CEP290*, Lebercilin) and other miscellaneous cellular functions (*IMPDH1*, *MERTK*, *RD3*). The most frequently mutated genes are *CEP290* (15%), *GUCY2D* (12%) and *CRB1* (10%). Yet, approximately one third of LCA cases still lack a specific genetic diagnosis, suggesting that unknown causing genes, or more complex molecular mechanisms are involved, for instance relying on multiple genes, on gene copy number variations, or on splice site/intronic mutations.<sup>57</sup>

Mutations in *RPE65* or other genes that cause LCA lead to heterogeneous clinical manifestations, with alteration of retinal function, manifesting in early childhood by reduced visual acuity, reduced night vision and dark adaptation, and progressive reduction in visual field

amplitude. Fundus shows progressive pigmented deposits ('osteoclasts'), and OCT shows outer retinal atrophy, that tend to aggravate over time in most patients (**Figure 7**).

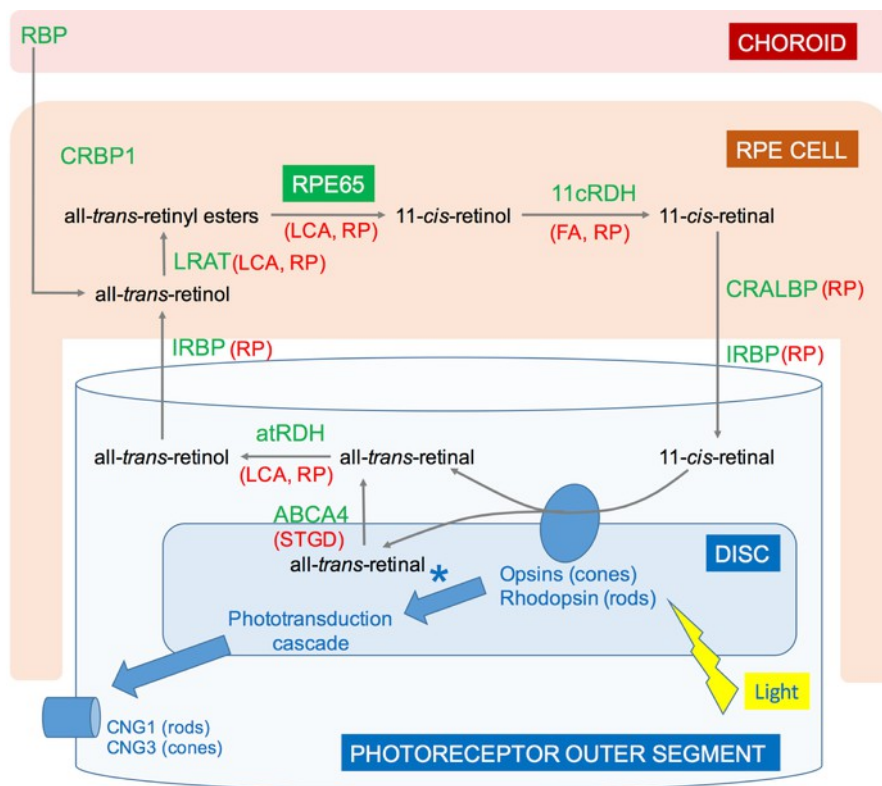


**Figure 6. Retinoid cycle showing the critical role of RPE65 that isomerizes all-trans retinyl esters into 11-cis-retinol, further recycled into 11-cis-retinal and transported to photoreceptor outer segments via CRALBP and IRBP.**

Upon light stimulation, 11-cis-retinal bound to opsins is converted to all-trans-retinal, triggering a complex phototransduction cascade that ultimately leads to opening of the cyclic nucleotide-gated cation channels (CNG1 in rods and CNG3 in cones) in the plasma membrane, and depolarization of the photoreceptor cell membrane. A fraction of all-trans-retinal is localized within discs, and is transported to the cytoplasmic space by the ABCA4 transporter. All-trans-retinal is converted to all-trans-retinol in the photoreceptors by a specific all-trans retinal dehydrogenase (atRDH), and then transported to the RPE by the interphotoreceptor retinoid-binding protein (IRBP). LRAT (lecithin retinol acyltransferase) converts all-trans-retinol (either recycled from the above-mentioned steps or originating from the circulation where it is bound to the retinol binding protein, RBP) to all-trans-retinyl esters, that serve as substrate for the isomerization reaction catalyzed by RPE65 to produce 11-cis-retinol. Finally, 11-cis-retinol is converted to 11-cis-retinal by other 11-cis specialized members of the RDH family (11cRDH), including RDH5 and RDH10, and is transported to the photoreceptor outer segments by several intra- and extracellular retinol-binding proteins such as CRALBP and IRBP.

Mutations in any of these enzymes or transporters involved in retinoid recycling may lead to inherited retinal dystrophies, indicated in red characters on the figure: LCA, RP, STGD, FA, and others.

LCA= Leber congenital amaurosis; STGD= Stargardt disease; RP= retinitis pigmentosa; FA= fundus albipunctatus; CRALBP=cellular retinoic acid binding-protein; IRBP= interphotoreceptor retinoid-binding protein; LRAT= lecithin retinol acyltransferase; RBP= retinol binding protein  
(Adapted from Palcewski *et al.*, *IOVS*, 2014)<sup>62</sup>

Nystagmus can be present, possibly developing as a result of the poor fixation in these patients, further aggravating their impaired visual ability.<sup>64</sup> Optic nerve hypoplasia, and various degrees of ocular colobomas may be associated to LCA. Other ocular manifestations, such as keratoconus and cataract, may develop. Regarding the extra-ocular manifestations, these young patients may also present mental retardation, autism, olfactory dysfunction, and a range of syndromic disorders.<sup>57</sup>

The diagnosis of LCA relies on a compatible clinical presentation, alteration in the function of rods, cones, or both on full-field electroretinography, and genetic confirmation.<sup>59,65,66</sup> The inheritance pattern of most genetic abnormalities causing the LCA phenotype is autosomal recessive, explaining the high rate of cases in rural areas of developing countries with high rates of consanguinity,<sup>67</sup> although a few families with autosomal dominant inheritance have also been reported.<sup>68</sup>

The RPE65 protein was first isolated from the RPE and characterized by Hamel *et al.* in 1993,<sup>63</sup> followed by successful cloning<sup>60</sup> and identification of its encoding gene.<sup>61</sup> A few years later, Hamel *et al.* demonstrated that mutations in *RPE65* cause the LCA phenotype.<sup>58</sup>

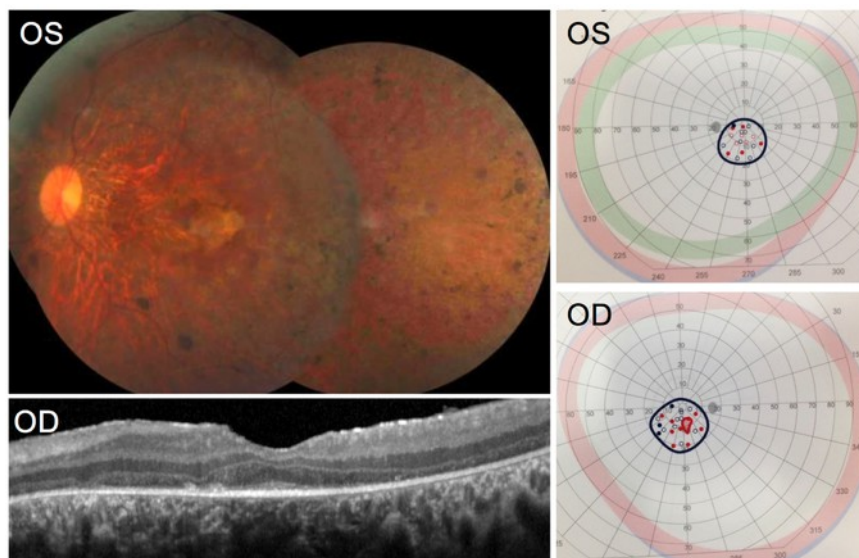


**Figure 7. Clinical presentation of RPE65 Leber congenital amaurosis in a 18-year old patient.**

Pigment clumping and diffuse retinal atrophy are shown on fundus examination (top left), while complete disappearance of photoreceptor outer segments and inner segment ellipsoid line is visible on OCT (bottom left), and advanced peripheral visual field loss leaving a tubular field (right).

(Courtesy Prof. Munier, Dr Tran, Dr Vaclavik)

Rapidly, *RPE65* was identified as an outstanding candidate for gene replacement therapy, given that 1) it is mainly expressed in RPE cells, and thus accessible to gene transfer after subretinal delivery; 2) the size of the *RPE65* gene is compatible with the cargo capability of existing viral vectors; 3) the *RPE65* protein exerts a unique enzymatic activity that, once replaced at sufficient level, may restore the retinoid cycle for ensuring a proper phototransduction, and hence potentially restore visual function; 4) there is prolonged photoreceptor survival despite the functional impairment, allowing for an extended treatment window and the possible rescue of more photoreceptors, as compared to other inherited retinal disorders originating from photoreceptor-specific protein deficiency.<sup>69</sup>

#### RPE65 gene therapy based on adeno-associated vectors

Shortly thereafter, models of *RPE65*-deficient animals were identified showing retinal structure abnormalities and altered visual function, that recapitulated the LCA phenotype. Several studies evaluated the subretinal treatment by adeno-associated virus (AAV)-mediated gene therapy and reported a restoration of visual function, both in dogs<sup>70</sup> and mice,<sup>71</sup> confirming the potential of this approach and the interest of the *RPE65* gene as candidate for gene augmentation therapy in humans. Studies in dogs have been of particular interest. First, because they were performed on a naturally occurring model of canine blindness in Briard dogs<sup>72</sup> that was shown to be due to *RPE65* mutations,<sup>73</sup> then, because it demonstrated the possibility of sustained long-term effect (up to a decade in the animal with the longest follow-up);<sup>74</sup> and finally, because it showed that optimal results were found in juvenile animals.<sup>75,76</sup>

Several groups have translated this gene therapy approach to human patients with *RPE65* Leber congenital amaurosis in Phase 1, 2, and 3 clinical trials (**Table 1**). To date, strategies that reached the clinical stages rely on adeno-associated viral vectors.<sup>77-79</sup> None of these studies has raised major safety concerns. One group (Consortium led by the Children Hospital of Philadelphia) has recently completed a Phase 3,<sup>80</sup> with promising short-term results. However, two other groups (University College London, University of Pennsylvania) had initially documented favorable short-term results in Phase 1 trials, with visual improvement peak at 6-12 months,<sup>77,81</sup> but limited long-term effect with subsequent visual loss in the following 3-6 years.<sup>78,79</sup>

Trial ID (Clinical-Trials.gov)	Vector	Phase	Start date	Sponsor	Center	References
NCT-00516477	AAV2-hRPE65v2	1/2	2007	Spark therapeutics	CHOP, UPENN, Ulowa (USA)	Phase 1/2: Maguire <i>et al.</i> , 2008 <sup>82</sup> Maguire <i>et al.</i> , 2009 <sup>83</sup> Simonelli <i>et al.</i> , 2010 <sup>84</sup> Testa <i>et al.</i> , 2013 <sup>85</sup>
NCT-01208389		1 follow-on	2010			Phase 1 follow-on: Bennett <i>et al.</i> , 2012 <sup>86</sup> Bennett <i>et al.</i> , 2016 <sup>87</sup>
NCT-00999609		3	2014			Phase 3 : Russel <i>et al.</i> , 2017
NCT-00481546	AAV2-CBSB-hRPE65	1	2007	UPENN	UPENN, UFL (USA)	Cideciyan <i>et al.</i> , 2008 <sup>69</sup> Hauswirth <i>et al.</i> , 2008 <sup>88</sup> Cideciyan <i>et al.</i> , 2009 <sup>77</sup> Cideciyan <i>et al.</i> , 2013 <sup>74</sup> Jacobson <i>et al.</i> , 2012 <sup>89</sup> Jacobson <i>et al.</i> , 2015 <sup>79</sup>
NCT-00643747	rAAV2/2.hRPE65 p.hRPE65	1-2	2007	UCL	Moorefields, UCL (UK)	Bainbridge <i>et al.</i> , 2008 <sup>90</sup> Bainbridge <i>et al.</i> , 2015 <sup>78</sup>
NCT-00749957	AAV2-CB-hRPE65	1	2008	Applied Gen. Tech. Corp.	OHSU, UMass (USA)	-
NCT-00821340	AAV2-CB-hRPE65	1	2010	Hadassah	Hadassah Hospital (Jerusalem, Israël)	-
NCT-01496040	rAAV2/4.hRPE65	1-2	2011	Nantes Univ.	Nantes Univ Hospital (France)	-

**Table 1. Human clinical trials for RPE65 Leber congenital amaurosis** registered on [www.clinicaltrials.gov](http://www.clinicaltrials.gov) (accessed July 7<sup>th</sup>, 2017). All trials use the subretinal route.

CHOP= Children Hospital of Philadelphia (USA); UPENN= University of Pennsylvania (USA), UFL= University of Florida (USA); Ulowa= University of Iowa (USA); OHSU= Oregon Health Sciences University; UMass= University of Massachusetts (USA); UCL= University College London (UK)

Importantly, these pioneering studies have demonstrated the feasibility of human ocular gene therapy via the subretinal route, showed some degree of visual cortex reactivation in areas corresponding to the topography of treated retinal areas,<sup>91</sup> and established the tolerance of re-injection in the contralateral untreated eye in human subjects, without elicited immune reaction either in the first or second injected eye.<sup>86,87</sup> As a result, the only Phase 3 trial to date was designed with bilateral treatment.<sup>80</sup>

These trials have also investigated novel endpoints and developed specific tools to assess retinal function impairment and recovery, that conventional methods such as visual acuity, visual field testing or microperimetry were unable to detect at sufficient sensitivity. For instance, the groups from the Children Hospital of Philadelphia (Bennett, Maguire) and from University College London (Bainbridge, Ali) used vision-guide ambulatory navigation tests, a widely employed

method to test animal mobility in vision research, adapted and optimized for visually impaired patients, including young infants. In addition to conventional visual field testing (Goldman kinetic testing and Humphrey/Octopus automated testing), these groups also used dark-adapted perimetry and full-field light sensitivity threshold testing.<sup>78,80,87</sup> Furthermore, the London group reported their perimetry explorations in a novel manner by plotting the number of retinal loci with significant improvement in sensitivity.<sup>78</sup> Finally, the group from the University of Pennsylvania (Hauswirth, Cideciyan, Jacobson) also relied mostly on dark-adapted perimetry testing, but reported their results differently by displaying serial time-dependent maps of retinal sensitivity, and plotting the areas of retinal sensitivity at different sensitivity levels extracted from these maps, and their evolution over time. Although these innovative methods raise concerns as to their comparability, both groups from London and the University of Pennsylvania reported a similar initial increase in retinal sensitivity after treatment, followed by a secondary decrease, probably due to the continuing degenerative process and to the transient, partial restoration of retinal function after gene therapy administration.<sup>78,89</sup>

Characterization of retinal structure was also critical, and these trials relied on different custom retinal layer segmentation techniques. It showed a continuing degenerative process manifesting by retinal thinning.<sup>78,79</sup> Moreover, this retinal thinning and foveal morphological changes may result also from the subretinal injection under the macula (see paragraph below). To note, the sole phase 3 study to date did not include retinal structural parameters (such as total retinal or specific layer thicknesses) among study endpoints.<sup>80</sup>

In addition, despite improvements in visual sensitivity, these clinical trials reported that the degenerative rate of the treated eye remained similar to the non-treated eye,<sup>78,79</sup> indicating either an unstoppable disease progression, inappropriate treatment delivery (timing of treatment, surgical techniques), or an insufficient vector efficacy. Moreover, combinatorial strategies relying on gene transfer and neural growth factor administration may be of interest.

#### RPE65 lentiviral gene therapy

The available amount of chromophore is determinant for photoreceptor function and survival, and consequently RPE65 protein expression levels are correlated to retinal function and to the

rate of retinal degeneration in animal models. For instance, in the *Rpe65*<sup>R91W/R91W</sup> mouse model, where the amount of the RPE65 protein is decreased by around 90%, electroretinography showed a 3-log reduction in retinal sensitivity at 1-month of age, as compared to wild-type mice, which is correlated to the levels of the RPE65 protein.<sup>92</sup> In human, no ERG responses were observed after AAV-mediated *RPE65* gene transfer, whereas similar doses in dogs deficient for the same gene led to clinical responses, such as recovery of retinal activity on ERG and vision-guided mobility.<sup>93</sup> To note, dogs injected with suboptimal doses also showed improvement of visual behavior without ERG amelioration.<sup>78</sup> These discrepancies between clinical observations and animal studies raised concerns over required therapeutic protein levels in humans.

Over the last decade, Corinne Kostic and Yvan Arsenijevic at the Unit of gene therapy and stem cell biology (currently, the Unit of retinal degeneration and regeneration) at Jules-Gonin Eye Hospital have developed an alternative, lentiviral-based strategy for *RPE65* gene transfer. This strategy relies on a lentiviral vector encoding a wild type RPE65 cDNA under the control of a fragment of the RPE65 human gene promoter (0.8 kb), followed by the woodchuck hepatitis virus post-transcriptional regulatory element (WPRE), and pseudotyped with the Vesicular Stomatitis Virus Glycoprotein (VSVG) envelop protein conferring broad-range specificity.

Previous studies in *Rpe65*-knockout mice confirmed that this approach was efficient to protect cone photoreceptors from degeneration and to preserve the function of these surviving cones until at least four months (after treatment at postnatal day 5), an age at which almost all cones have degenerated in untreated *Rpe65*-deficient mice, and to preserve the function of these surviving cones.<sup>94,95</sup> In addition, this lentiviral strategy also slowed down the cone degeneration process, and restored the expression of the RPE65 protein in cones of *Rpe65*<sup>R91W/R91W</sup> mouse model,<sup>92</sup> harboring the frequent R91W mutation among LCA patients.<sup>96</sup> Treatment of young adult mice (postnatal day 30) was more efficient in presence of this mutation than in knockout mice suggesting that patients harboring missense mutations may benefit from an extended treatment window.<sup>92</sup>

To further progress towards the clinical application of lentiviral vectors for RPE65 deficiency, we have evaluated the safety of a Good Manufacturing Practice (GMP)-like production of lentiviral vector expressing human RPE65 cDNA under this human RPE65 partial promoter,

injected subretinally in healthy non-human primates (NHPs), reported in Project 1.<sup>97</sup> The LV-RPE65 lentiviral vector solution used in this study is a GMP-like production of a vector containing a transgene cassette similar to the one evaluated previously in *Rpe65*-deficient mice but with a human cDNA and a mutated WPRE sequence devoid of promoter activities or open-reading frames.<sup>92,94,95,98</sup> LV-RPE65 is an integrative, third-generation, replication-defective, self-inactivating lentiviral vector, produced at the Genethon facility (Evry, France).

## [Project 2] Translational approaches in the vascular disease central serous chorioretinopathy

### CSCR: Clinical presentation

Our group, including the PhD candidate as co-first author, has published in mid-2015 a comprehensive review on CSCR in *Progress in Retinal and Eye Research*.<sup>99\*</sup> We will summarize below the major features of the clinical presentations and current pathophysiological understanding of CSCR. For more details, the reader is invited to refer to this review, that is accessible open access.

Central serous chorioretinopathy (CSCR) is a retinal disorder consisting in spontaneous serous detachments of the neuroretina from the retinal pigment epithelium (RPE).

The term “central” refers to the form of the disease causing visual symptoms due to the presence of serous detachments in the macular area. But asymptomatic subjects may have presented one or multiple episodes of extramacular serous detachments, as often observed in the contralateral eye of an active CSCR patient or when systematically examining relatives of CSCR patients.<sup>100,101</sup> The prevalence of CSCR is therefore likely to have been underestimated, and CSCR is considered the fifth most frequent retinal disorder, ranking after age-related macular degeneration (AMD), diabetic retinopathy, retinal vein occlusion and rhegmatogenous retinal detachment.<sup>102</sup>

It most frequently occurs in middle-aged men,<sup>99</sup> and the acute, predominant form is self-resolving within 6 months in 80% of cases.<sup>28</sup> However, the clinical diagnosis of chronic forms of

---

\* where it ranks as the most downloaded article, as of August 2017

the disease may be more challenging, as chronic CSCR may resemble AMD, complicated or not by choroidal neovascularization (CNV).<sup>103–105</sup>

CSCR is the only retinal disease (besides bacterial or viral infectious posterior uveitis) that can be provoked or exacerbated after systemic corticosteroid intake. Moreover, psychological stress,<sup>106,107</sup> and a range of personality profiles<sup>108</sup> and psychological traits<sup>109,110</sup> are considered risk factors for CSCR, the most frequent of which being ‘type-A’ personality.<sup>111</sup>

Advances in multimodal imaging and the advent of enhanced-depth imaging (EDI) of the choroid with SD-OCT<sup>23,112</sup> has improved the investigation of choroidal changes in CSCR, and has clearly identified increased choroidal thickness, or ‘pachychoroid’,<sup>113</sup> as the hallmark of CSCR.<sup>114</sup> Although clinically relevant, the ‘pachychoroid’ concept has to be used with caution, since there is no definitive threshold separating ‘normal’ from ‘thick’ choroids, and since ‘pachychoroid’ is not a definitive criteria to diagnose CSCR, that can occur in subjects not presenting increased choroidal thickness. In a review of published studies reporting choroidal thickness in healthy subjects, Lehman *et al.* have proposed that 395 µm be considered a reasonable minimal threshold to define ‘pachychoroid’.<sup>100</sup>

Based on these observations, it was recently proposed that CSCR belongs to the “pachychoroid spectrum” of diseases, ranging from “pachychoroid pigment epitheliopathy”,<sup>113</sup> an often asymptomatic, dormant form of RPE alteration with increased choroidal thickness, to polypoidal choroidal vasculopathy,<sup>115</sup> a neovascular condition arising in the choroid.

### Clinical subtypes of CSCR

There is no consensual definition of the various clinical subtypes of CSCR, although determining their exact limits is critical in the prospect of therapeutic clinical trial design. In particular, the term ‘chronic’ is employed in the literature to designate both non-resolving acute CSCR episodes after 3-6 months, and long-standing cases with specific signs of chronic retinal disease. The following definitions have been proposed in a review by our group as an attempt to solve these inconsistencies,<sup>99</sup> although some of the proposed subtype raised some issues recapitulated here:

- *Acute CSCR*: subretinal detachment lasting for less than 6 months (**Figure 8**).
- *Persistent CSCR (also termed non-resolving)*: acute CSCR with duration of subretinal detachment longer than 6 months after onset of symptoms. This form is often associated with elongated photoreceptor outer segments on SD-OCT, indicating potential visual recovery.
- *Recurrent CSCR*: episode of acute CSCR with history of previous episode(s) followed by complete resolution of subretinal detachment. Recurrent CSCR may originate from the same or from a new leakage point on fluorescein angiography. If lasting more than 6 months, a recurrent CSCR episode would be considered as a persistent episode. The term *recurrent persistent CSCR* could be added to the classification but complicates the terminology.
- *Chronic CSCR*: persistent CSCR associated with chronic signs of RPE decompensation, such as confluent hyper-/hypoautofluorescent areas on fundus autofluorescence, and RPE alterations on OCT. Chronic CSCR cases may have fluctuating subretinal fluid, and whether cases without active subretinal detachment should be classified as chronic CSCR is subject of debate. Indeed, the chronic epitheliopathy affecting the RPE, and other frequent signs such as flat irregular pigment epithelial detachments, that may be caused by type 1 choroidal neovascularization<sup>116</sup> and intraretinal cystoid degenerative edema<sup>117–119</sup> are manifestations of *chronic CSCR* potentially decreasing vision (**Figure 9**).
- *Diffuse retinal pigment epitheliopathy*: this term characterizes advanced *chronic CSCR* where confluent hyper-/hypo-autofluorescent areas adopt a gravitational topography, probably due to chronic subretinal fluid movement, and are termed ‘descending tracks’.<sup>120,121</sup>
- *Inactive CSCR*: patients with history of CSCR but without SRD at the time of evaluation. The recently introduced ‘pachychoroid pigment epitheliopathy’ entity could be included among the *inactive CSCR*, yet there is no certainty that patients with ‘pachychoroid pigment epitheliopathy’ have experienced previous CSCR episode(s). Fundus autofluorescence may harbor sequellae of previous episodes (often,

hyperautofluorescent areas). In addition, patients with alterations suggestive of chronic CSCR may rather be classified as *chronic* than *inactive*.

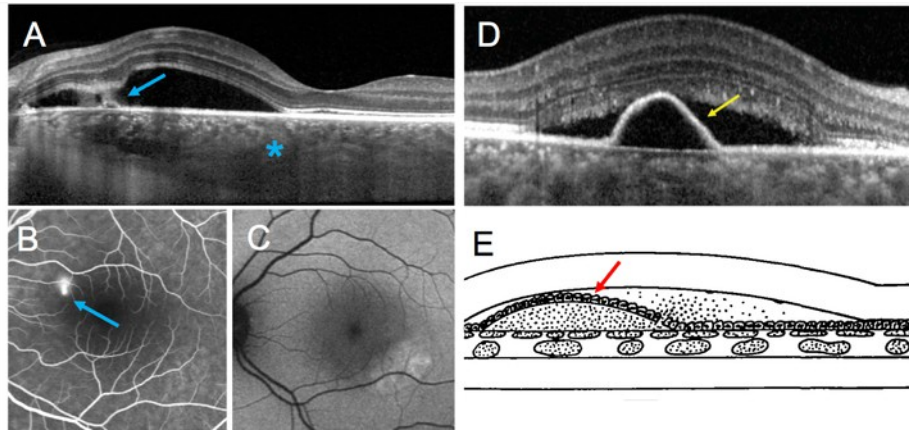


**Figure 8. Clinical illustration of acute CSCR** with small pigment epithelial detachment and hyperreflective leakage (blue arrow) on OCT (A), fluorescein angiography showing a clear leakage site (B) and subnormal fundus autofluorescence (C). Increased choroidal thickness is visible on OCT (A, star). An OCT from a different case of acute CSCR harboring an elevated pigment epithelial detachment (yellow arrow) demonstrates a striking similitude with a sketch drawn by Gass in 1967 (E, red arrow).

(E: adapted from Gass, *Am J Oph* 1967)<sup>122</sup>

An illustration of these clinical subtypes is provided in **Figures 8 and 9**. This classification, as any proposed attempt to categorize CSCR subtypes,<sup>102,123</sup> has several limitations. In particular, the strict determination of the time of onset of a CSCR episode is challenging, since serous detachments probably start before macular involvement when the leakage point is not strictly macular. Neither considering the time of symptom onset, nor the time of diagnosis, is therefore fully satisfactory. In addition, patients may have bilateral CSCR but different stages in each eye, or unilateral CSCR with RPE alterations on fundus autofluorescence in the contralateral eye, as often observed, which could modulate this classification and its clinical significance. Finally, it is unclear whether there is a strict continuum between *acute CSCR* and the long-standing variants of the disease (*chronic CSCR* and *diffuse retinal pigment epitheliopathy*), or whether they should be considered as distinct clinical entities, with only sporadic reports of cases progressing from the acute to the severe chronic form.<sup>124–126</sup>

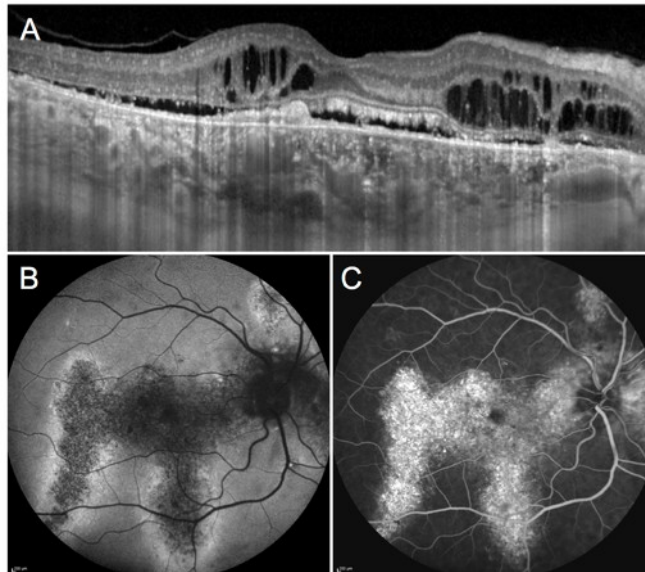


**Figure 9. Clinical illustration of diffuse retinal pigment epitheliopathy, the most severe form of chronic CSCR.** OCT shows an increased choroidal thickness with deep choroidal vasodilation, a flat irregular pigment epithelial detachment, subretinal fluid and intraretinal cystoid degeneration, a frequent finding in chronic CSCR (A). Fundus autofluorescence shows extended descending gravitational tracks (B), and fluorescein angiography show an extended window defect indicating diffuse epitheliopathy and multiple pin points suggestive of multifocal chronic leakage sites (C).

#### CSCR: a mysterious pathophysiology

Combining fundus observations and nascent fluorescein angiography, Gass described in 1967 the canonical hallmarks of CSCR: fluorescein leakage in the subretinal space, combined to neurosensory and pigment epithelial detachments,<sup>122</sup> that would be detected on OCT three decades later (**Figure 8**).

Several theories have been proposed to explain fluid entry from the choroid towards the subretinal space: dilated and hyper-permeable choroidal vessels, choriocapillaris non-perfusion, all favoring trans- or intercellular entry flow through the retinal pigment epithelium (RPE). This flow can result from changes in RPE cell polarity altering hydro-ionic pumping direction, uni- or multifocal rupture of the RPE barrier, or active reverse flow by unknown triggering mechanisms. Although serous macular detachments form rapidly and may last 3 to 6 months in most acute CSCR cases (see Article 2a),<sup>28</sup> visual acuity is usually preserved, suggesting a good maintenance of photoreceptors.<sup>8</sup> This differs strikingly from macula-off rhegmatogenous retinal detachment (RRD), in which detachment lasting more than 3-5 days leads to irreversible visual impairment.<sup>127</sup>

Recently, Zhao *et al.* and Bousquet *et al.* (group of Francine Behar-Cohen) showed that mineralocorticoid-receptor (MR) over-activation, especially in the choroidal vasculature, induced a CSCR-like phenotype in rats,<sup>128</sup> and that treatment of patients presenting long-standing CSCR with the commercially available oral MR antagonists eplerenone or spironolactone had a beneficial effect in reducing the amount of subretinal fluid.<sup>129,130</sup> A schematic representation of the putative MR-mediated mechanisms leading to choroidal vasodilation is provided in **Figure 10**.

Moreover, the MR over-activation hypothesis accounts for the exceptional pro-CSCR effect of systemic corticosteroids, regardless of the route of administration, and may explain a range of systemic conditions often associated with CSCR, that may also result from abnormal MR stimulation.<sup>99</sup> The relationship between CSCR and corticosteroids is probably one of the most intriguing aspects of the disease. Glucocorticoids efficiently reduce macular edema of many origins, even when associated with subretinal fluid,<sup>131,132</sup> but glucocorticoids can aggravate subretinal fluid accumulation in CSCR patients. Even exposure to low-dose non-ocular corticosteroids has been associated with the occurrence of CSCR.<sup>133,134</sup> Yet, high-dose intraocular injection of glucocorticoids, routinely administered for the treatment of macular edema, has not been associated with increased incidence of CSCR. Such discrepancies reflect the still non-elucidated complexity of steroid regulation on ocular physiopathology.

Since glucocorticoids aggravate rather than improve CSCR, inflammation was disregarded among potential disease mechanisms, but this notion should be revisited, from the perspective of other “non-inflammatory” vascular retinal disorders, in which inflammation and para-inflammation<sup>135</sup> are recognized as key mechanistic players, such as diabetic retinopathy<sup>47,136</sup> or neovascular age-related macular degeneration.<sup>137,138</sup>

Specific psychological profiles have been associated with CSCR (see above) but the exact link between anxiety-sensitive personalities and steroid biology has not been elucidated. Similarly, CSCR patient tend to present cardiovascular risk factors, and recent evidence suggest a possible link between cardiovascular risk and steroid biology. Interestingly, the systemic steroid hormonal profile of CSCR patients has been partially explored, and showed for instance that ~50% of patients with active acute CSCR have elevated 24-hour urine cortisol or tetrahydroaldosterone levels.<sup>139–141</sup>

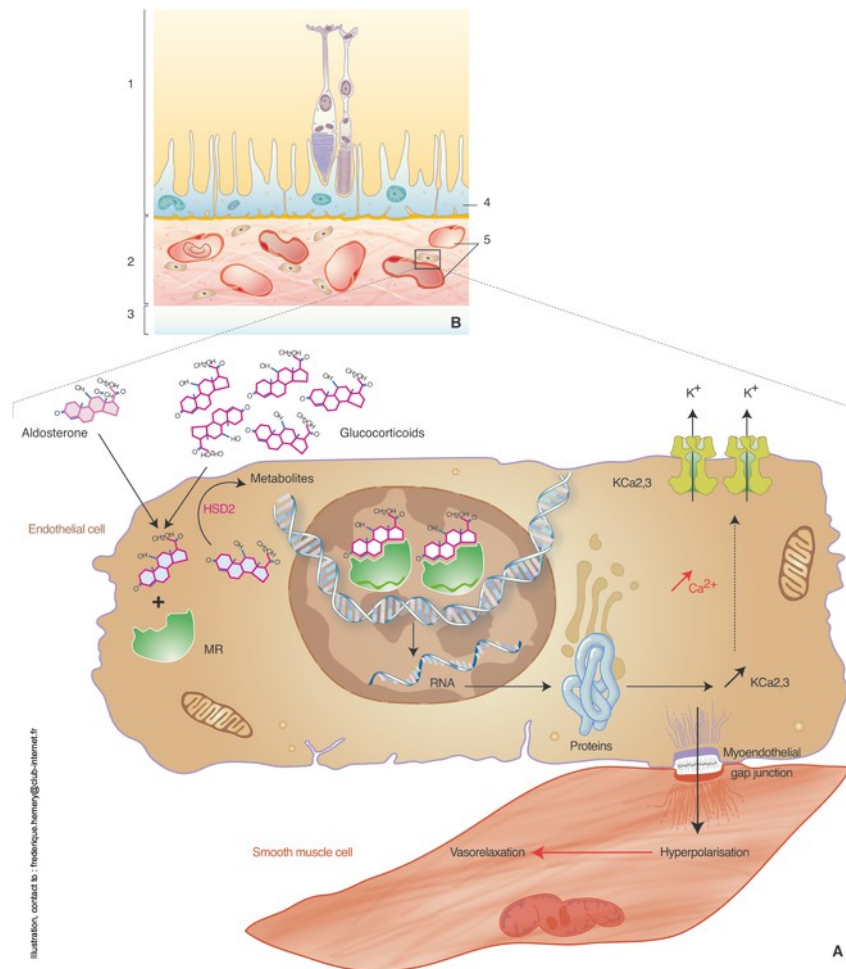


**Figure 10. Putative pathophysiology of CSCR based on the mineralocorticoid-receptor over-activation hypothesis.**

A. Permanent MR occupancy by glucocorticoids is prevented by the metabolizing enzyme 11- $\beta$  hydroxysteroid dehydrogenase type 2 (11 $\beta$ HSD2), which transforms the glucocorticoids into metabolites that have a weak affinity for MR. Activation of the MR pathway by either aldosterone or glucocorticoids induces up-regulation of the endothelial vasodilatory potassium channel KCa2.3 (calcium-dependent channel) that leads to the hyperpolarization of endothelial cells and underlying smooth muscle cells (electric coupling through myo-endothelial gap junctions) resulting in choroid vasodilation.

B. Vasodilation of large choroidal vessels exerts vascular or mechanical effects on the choriocapillaris and retinal pigment epithelium (RPE), leading to fluid leakage through the RPE and accumulation in the subretinal space.

K<sup>+</sup> = potassium; Ca<sup>2+</sup> = calcium.

(reproduced from Daruich *et al.*, *Prog Ret Eye Res* 2015, under the CC BY-NC-ND 4.0 license)<sup>99</sup>

In this context, the MR over-activation hypothesis in CSCR pathogenesis is relevant in that it could account for the observed systemic associations of CSCR. The MR pathway is indeed involved in psycho-neurological biology<sup>142,143</sup> and in cardiovascular remodeling.<sup>144,145</sup> More recently, circadian deregulation in shift workers has also been linked to CSCR,<sup>146</sup> and is related to steroid biology through the morning cortisol peak.<sup>147</sup>

Four articles addressing different clinical and pathophysiological aspects of CSCR are presented in this thesis. First, we investigated the clinical and imaging risk factors related to episode duration in acute CSCR [Article 2a], and to recurrence of CSCR after an acute episode [Article 2b], using clinical data and custom image processing techniques. Then, we explored the structural changes affecting the choriocapillaris using OCT angiography. This layer is of particular interest (**Figure 1**), since it is located at the interface between large choroidal vessels, where the disease is thought to originate (**Figure 10**), and the RPE, whose disruption leads to subretinal fluid accumulation and clinical expression [Article 2c]. Finally, we contributed to investigate the molecular composition of subretinal fluid, retrieved from a unique case requiring intraocular surgery, by a multi-omics approach [Article 2d].

### [Project 3] Translational approaches in telangiectatic retinal vascular disorders: example of macular telangiectasia type 1 and radiation maculopathy

Macular telangiectasia type 1 (MacTel 1) and radiation maculopathy are two vascular retinal diseases of distinct origins, that share very similar clinical manifestations. Both present a “pure” phenotype associating macular telangiectasia, capillary depletion, and macular edema secondary to increased capillary permeability leading to rupture of the inner blood-retinal barrier. Therefore, they provide an interesting model to develop biological and imaging tools that could be expanded to other multifactorial vascular disorders, such as diabetic retinopathy, or retinal vascular occlusive disease. In addition, history of radiation has been recognized as risk factor for retinal telangiectasia,<sup>148</sup> and both conditions respond poorly to intravitreal bevacizumab/ranibizumab, monoclonal antibodies designed to neutralize vascular endothelial growth factor (VEGF)-A, but favorably to intravitreal aflibercept,<sup>29,149</sup> a monoclonal antibody neutralizing both VEGF-A and Placental Growth Factor (PlGF), suggesting possible common mechanisms.

The majority of existing experimental work on retinal vascular disorders has focused on diseases that have well-established animal models, such as retinopathy of prematurity or diabetic retinopathy.<sup>150</sup> These two disorders are characterized by wide areas of retinal non-perfusion and

develop subsequently retinal neovascularization, due to the release of pro-angiogenic factors, predominantly VEGF, that stimulates angiogenesis.

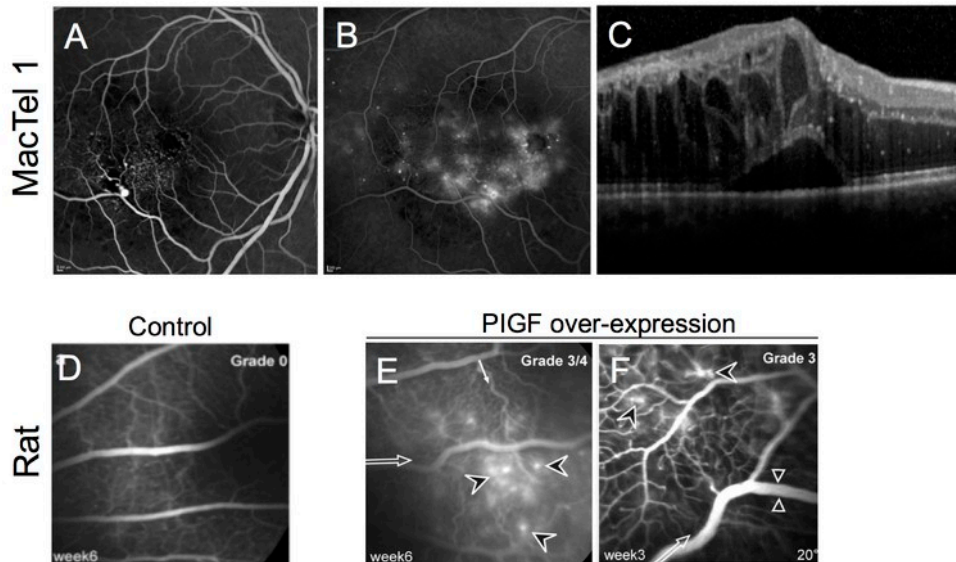


**Figure 11. MacTel 1: clinical presentation and animal model of PIGF overexpression.**

MacTel 1 associates exudative telangiectasia on early (A) and midphase fluorescein angiography (B), and subsequent macular edema on OCT (C). A rat model of intraocular PIGF overexpression in otherwise healthy rats (D) led to the formation of multiple diffuse telangiectasia resembling MacTel 1 (E, F).

(D-F: reproduced from Kowalczyk *et al.*, 2011, under the Creative Commons Attribution License)

However, several vascular diseases, including pre-proliferative stages of diabetic retinopathy (before the development of neovascularization), manifest with increased microvascular permeability. In humans, the macular region is particularly susceptible to alterations of the inner blood-retinal barrier, which, among numerous other factors, leads to macular edema.<sup>6</sup> A model of altered retinal microvasculopathy was created by Kowalczyk *et al.* (Behar-Cohen group) in healthy rats, secondary to long-term continuous intraocular PIGF overexpressing by ciliary muscle electrotransfer of a PIGF-coding plasmid.<sup>33</sup> This model developed focal exudative capillary dilations (**Figure 11**), resembling diffusing telangiectasia observed in patients with MacTel 1 (see clinical description below). Therefore, we wished to validate clinically the role of the different angiogenic factors, and particularly PIGF, in this disorder.

## Angiogenic factors: the controversial role of the VEGFR-1 and -2 pathways in retinal vascular permeability

VEGF receptors are tyrosine kinase receptors localized at the cell surface. Upon binding to one of their ligands, they dimerize and trigger intracellular signaling. Both VEGFR-1 and -2 have critical roles in retinal vessel development and in the maintenance of retinal vessel integrity. From the perspective of retinal vascular disease, VEGFR-2, is mainly involved in angiogenesis.<sup>151</sup> On the contrary, the exact functions of VEGFR-1 (also termed Flt-1) are less clear. VEGFR-1 is thought to regulate VEGFR-2 signaling and may possibly act as decoy receptor, sequestering VEGF-A from VEGFR-2 (**Figure 12**).<sup>152</sup> These effects result in the modulation of capillary vessel permeability, essential to maintain the inner blood-retinal barrier integrity, whose disruption leads to macular edema. While VEGF-A is considered the main ligand of VEGFR-2 (also bound by VEGF-C, -D and -E), both VEGF-A and PlGF bind to VEGFR-1 (also bound by VEGF-B). Historically, VEGF was first designated as “vascular permeability factor”,<sup>153,154</sup> highlighting its multiple roles in angiogenesis and vascular permeability. VEGF-C, via the VEGFR-3 receptor, is mainly an inducer of lymphangiogenesis.<sup>155</sup>

These different actions of VEGF receptor pathways have clinical implications. For instance, bevacizumab and ranibizumab are specific anti-VEGF-A monoclonal antibodies, whereas aflibercept functions as a soluble decoy receptor with a chimeric structure built from binding domains of both VEGFR-1 and VEGFR-2, thus binding both VEGF-A and PlGF.<sup>156</sup> Therefore, the involvement of PlGF in the pathophysiology of certain retinal diseases, may open therapeutic perspectives, and PlGF may be considered as a prognosis marker related to treatment response.

## MacTel 1: a “pure” disease of retinal capillaries

MacTel 1 is a rare congenital or developmental vascular disorder affecting mostly male subjects and consisting in focal, exudative dilations of perifoveal retinal capillaries.<sup>157</sup> These telangiectasia have altered blood-retinal barrier properties, inducing focal intraretinal leakage and macular edema, responsible for vision loss. To date, little is known on the pathophysiology of this “orphan” disease and treatment options are limited. MacTel 1 is usually unilateral and may extend beyond the macula. Therefore, it may be part of the larger spectrum of Coats disease, an

aggressive congenital disorder manifesting in early childhood with peripheral retinal telangiectasia and exudation, but that may also develop in young adults with milder presentations.<sup>158</sup>

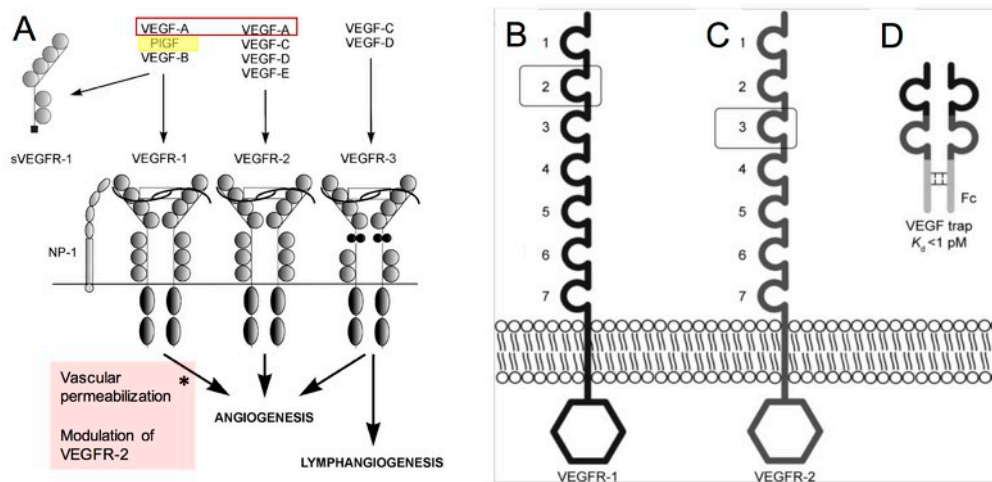


**Figure 12. Schematic structure and ligands of VEGF receptors, and structure of aflibercept**

A. VEGF-A binds to both VEGFR-1 and -2, while PIGF binds specifically to VEGFR-1. VEGFR-2 stimulates angiogenesis, while VEGFR-1 is involved in vascular permeability and modulates the effect of VEGFR-2 signaling. VEGFR-3 is involved in lymphangiogenesis.

B-D. Schematic representation of VEGFR-1 (B) and 2 (C), and structure of aflibercept, fusion of the 2<sup>nd</sup> and 3<sup>rd</sup> binding domains of VEGFR-1 and 2, respectively, over the Fc region of a human immunoglobulin G. This structure explains why aflibercept neutralizes both VEGF and PIGF.

VEGF= vascular endothelial growth factor; VEGF-R= VEGF receptor; PIGF= placental growth factor; sVEGFR-1= soluble VEGF receptor 1

(A: adapted with permission from Witmer *et al.*, *Prog Ret Eye Res* 2003)<sup>159</sup>

(B: adapted with permission from Balaratnasingam *et al.*, *Clin Oph* 2015)<sup>156</sup>

Historically, several classifications have been proposed and the condition has been termed “miliary aneurysms” by Leber, “idiopathic juxtafoveal telangiectasia” (group 1A-1B) by Gass and Blodi,<sup>160</sup> “Type 1 aneurysmal telangiectasia” by Yannuzzi *et al.*<sup>161</sup> and finally MacTel 1 in the recent classification by the MacTel Study Group.<sup>162</sup>

In contrast with type 2 idiopathic macular telangiectasia or “MacTel2”, where telangiectasia develop along with pathognomonic degenerative alterations of the retinal architecture linked to RMG cell depletion,<sup>163</sup> MacTel 1 is primarily a vascular disease, complicated by macular edema originating from the exudative telangiectasias.<sup>161</sup> FA allows the visualization of telangiectasias but its ability to image the fine perifoveal capillaries at high resolution and to discriminate between the superficial and deep capillary plexuses is limited. Therefore, OCT angiography may provide a useful tool in imaging details of the perifoveal capillary network and its alterations in MacTel 1,

and to gain insight into the disease manifestations at the capillary level, as developed in Project 3a.

Radiation maculopathy: a vision-threatening complication in eyes salvaged from an intraocular malignancy

Radiation maculopathy is a devastating cause of visual loss occurring in eyes receiving radiotherapy for ocular or orbital malignancies. It develops in approximately 50-60% of eyes treated by plaque brachytherapy or proton beam therapy for intraocular tumors,<sup>164</sup> the most frequent indication being uveal melanoma, and results in variable degrees of visual alteration. Tumors located inside or close to the macular area are at higher risk to develop this complication.<sup>165</sup> The tumoricidal effect of radiation relies on two mechanisms: the 'direct' action produces DNA damages that impair endothelial cell division, and the 'indirect' action generates free radicals from water and other molecules, which in turn induce DNA alterations.<sup>166</sup> Radiation of the retinal vasculature generates endothelial cell loss and capillary closure, leading to microangiopathy. In the macular area, this microangiopathy also leads to cystoid macular edema.<sup>167</sup> The diagnostic of radiation maculopathy relies on multimodal imaging, with the presence of possible lipid exudates and hemorrhages on fundus examination, cystoid macular edema on OCT, and exudative telangiectasia in the macular area on FA. FA also reveals the morphology of the perifoveal capillary network during early phases and the presence of increased vascular permeability with progressive dye diffusion.

Since OCT angiography provides a representation of the macular microvasculature via flow detection, it may overcome limitations of FA due to dye diffusion. It also images the parafoveal capillary network and its alterations at higher resolution than FA.<sup>168,169</sup> Moreover, by segmenting OCT angiography volumes allows to analyze separately the superficial and the deep retinal capillary plexuses, where specific lesions may be identified. OCT angiography was applied to radiation maculopathy in the Article 3c,<sup>170</sup> in order to identify prognosis markers related to the visual function of irradiated eyes.

## Aims of the thesis

The investigations of biological and imaging markers applied performed in this thesis aim at:

- 1) Identify novel parameters relevant for non-standard clinical situations lacking established endpoints (gene therapy preclinical safety study): **toxicity markers**
- 2) Improve our understanding of manifestations and **mechanisms** of retinal and choroidal vascular disorders and identify **diagnosis markers**
- 3) Improve our understanding of treatments effect and guide therapeutic decision in these disorders: **therapeutic response markers**
- 4) Identify new potential molecular therapeutic targets in these disorders
- 5) Identify **prognostic markers** in these disorders.



## RESULTS

### [Project 1] LV-RPE65

#### *Aim*

The aim of this project was to evaluate the ocular and systemic tolerance of this lentiviral-based therapy (LV-RPE65) in five healthy non-human primates following subretinal administration, in terms of retinal structure, retinal function, and systemic biodistribution. Contrary to previous safety studies in large animals (Briard dogs, non-human primates),<sup>75,76,93,171</sup> no systemic adjuvant corticosteroids were administered, as in the rodent experiments, to avoid masking potential side effects in primates not observed in rodents. The detailed study is found in the Article 1 below.<sup>97</sup>

#### *Methods*

Two doses of LV-RPE65 were employed: low (2 eyes), and high (2 eyes), corresponding to a 1:1 and 10:1 ratio of lentiviral particle per RPE cell in the treated area, respectively. To assess retinal structure changes, we used multimodal imaging with extraction of segmented retinal layers, and *ex vivo* immunohistochemical analysis. Retinal function was assessed with electroretinography. To analyze vector systemic biodistribution, regularly sampled tears, urine and serum, were analyzed for lentiviral particle presence, and critical organs were tested post-sacrifice for lentiviral genomic DNA integration (quantitative PCR and RT-PCR were performed by A. Bemelmans, INSERM).

#### *Image processing*

OCT images graphically segmented on the Spectralis device (Heidelberg Engineering, Germany) were processed with a custom MatLab algorithm (Mathworks, Natick, MA) to extract quantitative thicknesses along retinal sections (Appendix 4). This program processed the layer thickness profile segmented by the OCT device, and extracted from the image the thickness values at each pixel location in the detached area, resulting in a mean thickness in the detached part of the retinal section. This analysis was confirmed by a second method in collaboration with

K. Stieger and B. Lorenz (Giessen University, Germany), who analyzed with another custom, device-independent OCT segmentation software,<sup>172</sup> the retinal layer thicknesses within a fixed area, that was included in the detached zone in all eyes, allowing for a better inter-animal comparability.

### *Results*

- Multimodal imaging: the early kinetics of retinal detachment at 2, 4, and 7 days post-subretinal injection revealed prolonged reattachment times in LV-RPE65-injected eyes compared to vehicle-injected eyes. All LV-RPE65-injected eyes showed an initial perivascular inflammatory reaction that resolved spontaneously within 14 days but raised concerns regarding the immune response to LV-RPE65.

- OCT segmentation: Low- (n=2) and high-dose (n=2) LV-RPE65-injected eyes presented a reduction of the outer nuclear and photoreceptor outer segment layer thickness in the detached part of the macula, that was more pronounced than in vehicle-injected eyes (n=4). Inner layer thinning was not observed, which indicates that the transient perivascular inflammatory reaction, mostly localized around retinal venules in the inner layers, had absent or limited long-term structural consequences.

- Electroretinography: despite foveal structural changes, full-field electroretinography indicated that the overall retinal function was preserved over time.

- Immunohistochemistry: we identified no difference in glial (GFAP staining), microglial (Iba-1 staining) or leukocyte (CD45 staining) ocular activation between low-dose, high-dose and vehicle-injected eyes (1 or 3 months after injection).

- Systemic vector distribution: LV-RPE65-injected animals did not show any sign of vector shedding signs from Day 2 post-injection to the end of follow-up in tears, serum, urine, or extra-ocular genomic DNA integration at the time of animal sacrifice, confirming the safe ocular restriction of the vector.

## [Project 2] CSCR

[2a] Acute CSCR: multimodal imaging and clinical prognosis markers influencing episode duration

### *Aim*

This work<sup>28</sup> aimed at identifying prospectively the rate of self-resolution and the factors influencing episode duration in acute CSCR episodes. Despite their accessibility in routine medical retina clinical settings, these clinical characteristics had not been previously reported in the era of modern multimodal imaging.

### *Methods*

Thirty-one patients with a first episode of acute CSCR, followed for 6 months without therapeutic intervention, were included in the study. The mean time from the initial visit (corresponding to the first objective identification of serous retinal detachment) to CSCR resolution was  $83 \pm 46$  days. Twenty-six patients (84%) were self-resolved by 6 months.

The multimodal imaging parameters extracted as potential prognosis markers of resolution reflected the choroidal status (subfoveal choroidal thickness, SFCT on EDI-OCT; pattern of choroidal vascular hyperpermeability on ICG angiography), the RPE status (elevation of pigment epithelial detachments on OCT; intensity of fluorescein leakage on FA), and finally the time-dependent kinetic of subretinal fluid volume resorption (initial subretinal fluid volume on OCT; observation of a peak in subretinal fluid volume during follow-up, on OCT).

In addition, systemic markers reflecting the current understanding of CSCR pathophysiology were evaluated, that included age, corticosteroid intake, and hypertension.

### *Image processing*

Two custom algorithms were designed on MatLab for this study.

- First, an assessment of the leakage intensity was performed using fluorescein expansion ratio (Appendix 5), semi-automatically computing the area of the fluorescein leakage on FA, and comparing this area between mid-phase (2-2.5 min) and early (40-60 s) fluorescein angiograms. The area were detected via an intensity-based

algorithm, using image binarization, by adapting a method described by Pryds *et al.* (Figure 3 of Article 2a).<sup>173</sup> The grayscale intensity binarization threshold was determined as  $0.75 \times I_{\max}$ , where  $I_{\max}$  is the maximal fluorescence intensity at the leakage site (a threshold of 0.50 had been employed by Pryds *et al.*). This method was semi-automatic, and required the operator to detect grossly the localization of the leakage point, then the program identified the local maximal intensity pixel, and searched for the 0.75- mean intensity isopter centered on this point, yielding the fluorescein leakage area. Incorporating the fully automatic detection of this maximum intensity pixel in the program proved difficult given the variability of both pattern (smokestack, ink blot, pin points, faint or absent leakage) and intensity of leakage sites in acute CSCR, requiring a trained observer for appropriate detection.

- Second, a segmentation method was designed to measure subretinal fluid volume from stacks of OCT sections encompassing the macula (Appendix 6). This method was also semi-automatic, since the observer labeled an area comprised within the serous retinal detachment in one of the OCT sections, and the borders of the serous retinal detachment were then segmented on each scan using an intensity-based method and a variable binarization threshold depending on the subretinal fluid intensity. Briefly, a circular detection of the serous retinal detachment borders (RPE or elongated photoreceptor outer segments, both relatively hyper-reflective structures on OCT) was performed. After visual verification of the segmentation, the total volume of subretinal fluid was estimated across the 97 OCT sections by trapezoidal integration, and a heat map representing the subretinal detachment morphology was generated (Figures 5 and 6 of Article 2a). The kinetics of subretinal volume reabsorption was then analyzed in each patient by comparing volumes at each time-point, identifying the initial volume and the patients who presented a volume peak during follow-up.

### *Results*

In the univariate analysis, episode duration was longer in cases with SFCT  $\geq 500 \mu\text{m}$  ( $p=0.0002$ ), RPE elevation at leakage sites  $\geq 50 \mu\text{m}$  ( $p=0.033$ ), and a peak in subretinal volume

observed during follow-up ( $p=0.013$ ), and there was a near-significant association of intense fluorescein leakage ( $p=0.074$ ) with longer episodes.

Using multivariate analysis, SFCT  $\geq 500$   $\mu\text{m}$  ( $p=0.017$ ), RPE elevation at leakage sites  $\geq 50$   $\mu\text{m}$  ( $p=0.010$ ) and patient age  $\geq 40$  years ( $p=0.010$ ) were significantly and independently associated to longer episodes. ICG angiography pattern, corticosteroid intake and blood pressure did not influence episode duration.

These results highlighted the interest of customized imaging segmentation techniques adapted to a given clinical problematic. They identified an influence of choroidal dilation, RPE alteration, and patient age on acute CSCR episode duration, in agreement with current pathophysiology concepts.



## [2b] Risk factors for recurrent CSCR: a multimodal imaging study

### *Aim*

This retrospective study is a follow-on to study [2a], analyzing the course of acute CSCR after resolution of the initial episode. It aimed at describing recurrence patterns in CSCR patients, and investigating the influence of a panel of candidate systemic and imaging ocular markers on the risk of recurrence.

While acute episodes are usually self-resolving, ~20-50%<sup>174-176</sup> of affected eyes may later present one or several recurrences. Despite a remarkable resistance of photoreceptors to serous detachments during single CSCR episodes,<sup>177,178</sup> repeated episodes and prolonged serous detachment lead to irreversible photoreceptor/RPE damage, and vision loss.<sup>179</sup> Yet, little is known about the underlying mechanisms triggering recurrences and leading to chronic forms of the disease. Whether recognized risk factors for CSCR or anatomical changes in the choroid, RPE and retina do also influence the recurrence rate of the disease has not been comprehensively explored. Identifying factors predisposing for CSCR recurrences would help detect patients at higher risk of recurrence, potentially needing preventive and/or more aggressive therapeutic interventions.

### *Method*

In 46 patients with acute CSCR and follow-up >12 months after first episode resolution, parameters influencing recurrences were retrospectively evaluated using a frailty Cox proportional hazard survival model. Covariates included baseline systemic findings: age, gender, corticosteroid use, stress, shift work, sleep disorder, depression, allergy, cardiovascular risk; baseline optical coherence tomography findings: subfoveal choroidal thickness (SFCT), pigment epithelial detachment pattern (regular/bump/irregular), number of subretinal hyper-reflective foci at leakage site; baseline angiographic findings: fluorescein leakage intensity (intense/moderate/subtle/absent), hyper-permeability pattern on indocyanine-green angiography (focal/multifocal); and episode-related findings: duration and treatment of previous episode.

### *Image processing*

The previously developed algorithm extracting leakage intensity ratio from fluorescein angiograms (Appendix 5), was employed as a cross-validation of a subjective, multi-observer grading of fluorescein intensity as intense, moderate, subtle or absent. There was a significant correlation between fluorescein leakage intensity (graded as none, subtle, moderate, intense) and fluorescein leakage expansion ratios ( $P=0.0002$ ,  $r=0.54$ ) (Table, Supplemental Digital Content 4).

### *Results*

Twenty of 46 subjects (43%) presented  $\geq 1$  recurrences during a mean follow-up of  $29.9 \pm 9.5$  months [range, 15-54 months]. Follow-up duration did not differ between cases with or without recurrences ( $P=0.3$ ). Worse final visual acuity levels (logarithm of the minimal angle of resolution) were associated with a higher number of episodes during follow-up ( $P=0.032$ ,  $r=0.28$ ). In a univariate analysis, higher SFCT ( $P=0.021$ ), non-intense fluorescein leakage (=moderate/subtle/absent,  $P=0.033$ ), multiple subretinal hyper-reflective foci ( $P=0.026$ ), and shift work ( $P<0.0001$ ) were significantly associated with recurrences, with a near-significant influence of irregular pigment epithelial detachment ( $P=0.093$ ). In a multivariate analysis, higher SFCT ( $P=0.007$ ), non-intense fluorescein leakage ( $P=0.003$ ) and shift work ( $P<0.0001$ ) remained significant and independent risk factors for recurrences.

Multiple factors influence the risk of CSCR recurrence. These findings may contribute to identify patients at higher risk, who could benefit from earlier or more intensive treatment. Moreover, they highlight the contribution to disease recurrence of important mechanistic players in CSCR pathophysiology, such as choroidal vasodilation, circadian rhythm disruption and RPE integrity reflected by the leakage intensity. The identification of these markers is important because recurrence of CSCR indicates the conversion from a benign, self-resolving ocular disorder to a potentially vision-threatening, chronic disease.

## [2c] OCT and OCT angiography imaging of the choroidal vasculature in CSCR

Articles 2a<sup>28</sup> and 2b<sup>180</sup> have highlighted the paramount role of the choroid in several clinical forms of CSCR. Historically, the clinical observation by *in vivo* imaging of choroidal vascular dilation and hyperpermeability on indocyanine-green angiography,<sup>38,39</sup> and choroidal thickening on OCT,<sup>114</sup> have revealed the central role of the choroid in CSCR patients. Some authors have also proposed that the vasodilation of large choroidal vessels characterizing CSCR is locally associated with a thinning of inner choroidal layers and choriocapillaris, based on EDI-OCT<sup>181</sup> and choroidal maps after choroidal layer segmentation obtained by SS-OCT.<sup>182</sup>

The advent of OCT angiography has provided unprecedented access to the choriocapillaris blood flow *in vivo*. Current OCT angiography imaging technology does not allow to penetrate deeper than the choriocapillaris, but this layer lying just beneath the RPE (see **Figure 1** in the Introduction) is finely imaged by commercially available devices.

Two groups have described features of the choriocapillaris in CSCR eyes using OCT angiography, and showed the presence of “dark spots or “flow voids”.<sup>183,184</sup> However, no detailed analysis of factors influencing their extension or topography has been advanced.

Recently, Spaide has described small hyporeflective flow voids in normal eyes, and showed that they correlated with age, hypertension and presence of pseudodrusen in the fellow eye.<sup>185</sup> This author employed local thresholding and image binarization on the publicly available Fiji software to extract the areas of these flow voids.

We have adapted this strategy in an automated, batch-processing algorithm on MatLab (Appendix 7), applied to a set of normal healthy eyes for validation, and to CSCR eyes. Moreover, the two largest flow voids were selected and reported on the corresponding Spectralis EDI-OCT scans to assess choroidal morphology at these sites.

Fifty-three eyes from 48 subjects were included, and 34 control eyes. Twenty-two eyes were classified as acute, 15 eyes as recurrent and 13 eyes as chronic CSCR. CSCR eyes presented a higher total flow void area, and a higher number of flow void lesions as compared to normal subjects (P=.0004 and .003, respectively). In a univariate evaluation of CSCR eyes, age

( $P=.0002$ ), duration since CSCR diagnosis ( $P=.004$ ) and CSCR type (factorized as acute, recurrent, chronic) ( $P<.0001$ ) had a significant influence on the total flow void area. In a multivariate analysis, age ( $P=.023$ ) and CSCR type ( $P=.007$ ) remained the only independent contributors to the total area of flow voids ( $R^2=.35$ ).

Regarding the correlation of flow voids with choroidal morphology on EDI-OCT, deep choroidal vessel diameter was higher ( $P<.0001$ ), and choriocapillaris was thinner ( $P<.0001$ ) at flow void sites compared to “normal” sites, independently from eccentricity of sites from the fovea.

This study provides the first assessment of choriocapillaris morphology coupled to the kinetics of choriocapillaris blood flow in CSCR. Indeed, previous studies had employed flow laser Doppler velocimetry to assess choroidal blood flow, with variable results, but the contribution of the choriocapillaris to these measurements could not be discriminated.<sup>186-188</sup>

It confirms the pathophysiology notion that choriocapillaris thinning results from a possible compression by inwardly displaced large choroidal vessels, possibly impeding proper blood flow in this layer.<sup>182</sup>

Finally these results provide a possible explanation bridging choroidal changes observed in all forms of CSCR – explored in detail in this thesis in both acute<sup>28</sup> (Article 2a) and recurrent CSCR<sup>180</sup> (Article 2b), and possible causes for subretinal fluid accumulation, whose molecular composition will be assessed in detail in the next subproject (Article 2d). A focally decreased or absent blood flow in the choriocapillaris may result in focal RPE ischemia, possibly leading to abnormal hydro-ionic exchanges, or to the disruption of intercellular junctions, resulting in the leakage classically observed on fluorescein angiography.

## [2d] Proteomics/metabolomics of subretinal fluid in CSCR

In the previous works (Articles 2a and 2b), we identified imaging markers predictive of the time course of various CSCR subtypes, bridging clinical manifestations with microstructural choroidal and RPE morphological changes. Then (Article 2c), we imaged dynamically and analyzed the blood flow within the choriocapillaris layer using cutting-edge OCT angiography, demonstrating the high number of flow voids compared to normal eyes, and analyzed how choroidal vasodilation affects the choriocapillaris and induces focal RPE disturbances. This analysis provided a dynamic, high-resolution visualization of blood supply at an almost cellular scale. Pursuing the path towards assessing at finer level the pathophysiology events leading to CSCR, we have explored the molecular composition of subretinal fluid, that may reflect molecular processes potentially contributing to the disease, in the hope of identifying clinically relevant candidate biological markers of the disease.

### *Aim*

The aim of this pilot study, in collaboration with the proteomics laboratory, University of Geneva (N. Turck), and the metabolomics laboratory, University of Lausanne/CHUV (A. Thomas), was to assess the feasibility of subretinal fluid analysis using proteomics and metabolomics, and to investigate the molecular composition of subretinal fluid in CSCR and RRD using this approach. We compared the subretinal molecular profile from one case with severe CSCR and two pooled samples from cases with chronic RRD.

Severe CSCR can present as bullous exudative retinal detachment with persistence of subretinal material,<sup>189</sup> exceptionally requiring surgery. During the procedure, subretinal fluid can be collected. The composition of subretinal fluid from a CSCR patient has never been analyzed, and may provide a mechanistic insight into the complex processes leading to subretinal fluid accumulation.

As developed in the Introduction to CSCR (Project 2), the function and structure of photoreceptors in the detached retina is much better preserved in CSCR than in RRD, although serous macular detachments usually last for several months in CSCR, and for only a few days in RRD undergoing surgical repair. Mechanisms of photoreceptor cell death after RRD are multiple,

triggered by oxidative and metabolic stress, complement alternative pathway activation, immune response and inflammation.<sup>190,191</sup> In RRD, subretinal fluid originates mainly from liquefied vitreous, which diffuses under the neurosensory retina through a peripheral retinal tear. Whether the composition of subretinal fluid differs in CSCR and RRD, and influences the differential photoreceptor survival and visual prognosis is presumed, but, to date, has not been investigated.

### *Methods*

We compared the subretinal fluid profile from one case with severe CSCR and two cases with chronic RRD. Proteomics and metabolomics analysis were performed independently, and both experimental procedure and bio-informatics analyses were carried out by the two collaborative teams mentioned above.

Proteins were trypsin-digested, labeled with Tandem-Mass-Tag and fractionated according to their pI for identification and quantification by tandem mass spectrometry. Independently, metabolites were extracted on cold methanol/ethanol, and identified by untargeted ultra-high-performance liquid chromatography and high-resolution mass spectrometry. Bioinformatics analyses were conducted, including comparison to protein and metabolite databases, protein, metabolite and pathway over-representation analysis, and gene ontology.

### *Results*

In total, 291 proteins and 651 metabolites were identified in subretinal fluid samples. One-hundred twenty-eight proteins (77 down-regulated; 51 up-regulated) and 76 metabolites (43 down-regulated; 33 up-regulated) differed in the subretinal fluid from CSCR compared to RRD. In summary, protein and metabolites notably deregulated in CSCR were related to:

- glycolysis/gluconeogenesis
- inflammation (including serum amyloid P component, versican)
- alternative complement pathway (complement factor H and complement factor H-related protein)
- cellular adhesion
- biliary acid metabolism (farnesoid X receptor/retinoid X receptor)

- gluco- and mineralocorticoid systems (aldosterone, angiotensin and corticosteroid-binding globulin)

These results proved the feasibility of multi-omics techniques applied to subretinal fluid, a biological material rarely retrieved from RRD eyes during surgery, and exceptionally from CSCR eyes. In addition, they identified key pathways consistent with the current understanding of CSCR mechanisms, including cellular adhesion (potentially intervening in the disruption of RPE cell-cell adhesion at leakage sites), alternative complement (polymorphism in the complement factor H gene was identified in CSCR patients<sup>192,193</sup>), and gluco- and mineralocorticosteroid systems, whose roles in CSCR have been discussed in the Introduction of this thesis.



## [Project 3] Telangiectatic retinal disorders

### [3a] Capillary density and microvascular abnormalities assessed by OCT angiography in MacTel1

We developed a custom semi-automated image processing method on Matlab to extract global and local capillary density from OCT angiography images, based on binarization and skeletonization. This approach is adapted to MacTel 1, a disease characterized by focal areas of capillary non-perfusion on fluorescein angiography.<sup>157</sup> A simulation-based statistical strategy was used to generate  $N$  circular non-overlapping areas within an OCT angiography image and compare the local density within these areas to the density of peri-telangiectasia regions of interest. This method was applied to describe microvascular abnormalities and global/focal capillary density in an observational case series of MacTel 1 patients.

Seven OCTA acquisitions from patients with MT1 and 12 age-matched controls were included. Focal microvascular dilations were identified on  $3\times 3$ -mm OCT angiography and early-frame fluorescein angiography images. OCT angiography images were processed to determine the global capillary density after subtraction of larger vessels and cystoid edema cavities (code provided in Appendix 8). Local capillary densities were calculated inside  $100\text{-}\mu\text{m}$  circles around telangiectasias, projected over superficial (SCP) and deep capillary plexuses (DCP) (code in Appendix 9). They were compared to a random sample of  $100\text{-}\mu\text{m}$  circles generated in each OCT angiography image (code in Appendix 10). fluorescein angiograms were processed to measure mean perifoveal intercapillary areas, inversely reflecting capillary density (code in Appendix 11)

The global capillary density on OCT angiography was significantly lower in MacTel 1 eyes than in fellow and control eyes: SCP, 0.347 versus 0.513 ( $p=0.004$ ) and 0.560 ( $p=0.0005$ ); DCP, 0.357 versus 0.682 ( $p=0.016$ ) and 0.672 ( $p=0.0005$ ). Capillary density was significantly reduced around telangiectasia, in both SCP ( $p=0.021$ ) and DCP ( $p=0.042$ ). Capillary density of the SCP correlated inversely with the mean perifoveal intercapillary areas on fluorescein angiography ( $r= -0.94$ ,  $p=0.017$ ). LogMAR visual acuity was inversely correlated with SCP ( $r= -0.88$ ,  $p=0.012$ ) and DCP capillary densities ( $r= -0.79$ ,  $p=0.048$ ).

These results confirmed that MacTel 1 eyes present global and focal capillary depletion. The latter is either a local triggering factor for the development of telangiectasia, or results from higher intraretinal oxygen diffusion surrounding telangiectasia, focally inhibiting capillary angiogenesis.

### [3b] Analysis of aqueous humor angiogenic profile in MacTel 1 and relationship to the efficacy of intravitreal aflibercept

Based on the similarity of clinical manifestations of MacTel 1 with the retinal phenotype of a rat model overexpressing the angiogenic Placental growth factor (PIGF),<sup>33</sup> a co-ligand of the VEGF Receptor-1 (VEGFR-1), along with VEGF-A, we measured the ocular angiogenic profile in MacTel 1 patients and analyzed the effect of intravitreal aflibercept.

Eight subjects with MacTel 1 refractory to bevacizumab, ranibizumab, or laser therapy and switched to aflibercept were included. Best-corrected visual acuity, central macular thickness, and cystic areas quantified on OCT B-scans were assessed over 12 months. Perifoveal capillary densities were obtained using the built-in analysis software of the OCT angiography device. Aqueous humor was sampled from six patients and eight control subjects undergoing cataract extraction. Growth factors were quantified using a high-sensitive multiarray immunoassay.

Over 12 months, patients received  $6.6 \pm 1.4$  (range, 5–8) intravitreal aflibercept injections. Twelve months after switching to aflibercept, best-corrected visual acuity increased by >5 letters in 5 of 8 patients, compared with pre-aflibercept levels. Mean best-corrected visual acuity improved from 79.6 to 88.0 Early Treatment Diabetic Retinopathy Study letters ( $P=0.042$ ), and central macular thickness decreased from  $434 \pm 98$   $\mu\text{m}$  to  $293 \pm 59$   $\mu\text{m}$  ( $P=0.014$ ). Compared with control subjects, the profile of angiogenic factors in MacTel 1 eyes revealed no difference in VEGF-A levels but significantly higher levels of placental growth factor ( $P=0.029$ ), soluble vascular endothelial growth factor receptor-1 (sVEGFR-1 or sFlt1;  $P=0.013$ ), vascular endothelial growth factor-D ( $P=0.050$ ), and Tie-2 ( $P=0.019$ ). Possible correlations between angiogenic factors and the capillary density on OCT angiography parameters

Placental growth factor was the only biological factor whose levels were correlated with both superficial and deep capillary plexus densities on (Spearman  $r = -0.89$ ,  $P=0.03$ ). The correlation revealed that the higher PIGF, the lower the capillary density. Importantly, this correlation was fully automated and performed with the built-in algorithm of the AngioVue device, warranting the comparability of values across subjects.

In summary, the clinical response to aflibercept coupled to the angiogenic profile of MacTel 1 eyes supports the implication of the placental growth factor/VEGFR-1 pathway in MacTel 1. This

study showed that intraocular levels of angiogenic factors (here, PIGF) may be related to the efficacy of anti-angiogenic treatments and serve as prognosis markers. Moreover, it demonstrated a relationship between morphologic parameters derived from multimodal imaging, and levels of certain angiogenic factors.

A semi-automated algorithm calculating the areas of cystoid edema cavities on OCT sections was designed for this work, and the results showed a significant difference at 12 months after initiation of aflibercept therapy among the 8 study patients, compared to baseline. This analysis was finally removed from the final manuscript since it was considered redundant with the central macular thickness analysis by one of the Reviewers of Article 3b. Consequently, it was only employed to outline the contour of cystoid cavities in the Figures 1 and 2 of Article 3b. Its code sequence is provided in the Appendix 12.

### [3c] Application of fractal analysis to the imaging of radiation maculopathy

Radiation maculopathy presents similarities with MacTel 1 in that it manifests with retinal capillary telangiectasia in the macular area, leading to leakage and macular edema, as exposed in the Introduction to Project 3. However, due to the specific radiation-induced mechanisms causing radiation maculopathy, entire areas of capillary network are disrupted and the organization of this network is altered.

The consequences of proton-beam therapy have not been assessed to date using the non-invasive OCT angiography technique, allowing visualization of the different retinal plexuses forming the retinal vasculature. In this study, we investigated the spectrum of structural and microvascular alterations in radiation maculopathy after proton-beam therapy for uveal melanoma, and their respective influence on visual acuity, using OCT and OCT angiography, combined to an image processing tool. This tool was based on the fractal dimension (code in Appendix 13), a parameter that has been recently employed in several OCT angiography studies<sup>34-36</sup> and that seems to conveniently provide a unique quantitative measure reflecting the degree of capillary network disorganization.

Ninety-three consecutive patients with radiation maculopathy, 12 months or more after proton-beam irradiation for uveal melanoma, and imaged with fluorescein angiography, OCT and OCT angiography were included. Clinical parameters potentially affecting visual acuity were recorded, including OCT-angiography-derived metrics: foveal avascular zone area, vascular density and local fractal dimension of the superficial (SCP) and deep capillary plexuses (DCP). An automated tool extracting the local fractal dimension of skeletonized OCT angiography images was developed on MatLab, based on the counting box method and the estimation of the fractal dimension over a limited range of box sizes, reflecting the partial fractal behavior of the perifoveal vascular network. Fractal dimension is particularly suitable to analyze the morphology of vascular networks in radiation maculopathy, a disease that is characterized by a progressive disorganization of the capillary network and a loss of its branching pattern, with complete disappearance of the network in extreme cases.

Thirty-five non-irradiated fellow eyes served as controls. The foveal avascular zone was larger, SCP/DCP capillary density and local fractal dimension were lower in the 35 irradiated versus 35 fellow eyes ( $P < 0.0001$ ). In the 93 irradiated study eyes, microvascular alterations graded on fluorescein angiography (minimally damaged/disrupted/disorganized) were correlated to foveal avascular zone area and SCP/DCP density on OCT angiography ( $P < 0.01$ ).

By univariate analysis, worse visual acuity was associated to macular detachment at presentation ( $P = 0.024$ ), total macular irradiation ( $P = 0.0008$ ), higher CMT ( $P = 0.019$ ), higher absolute CMT variation ( $P < 0.0001$ ), cystoid edema ( $P = 0.030$ ), ellipsoid zone disruption ( $P = 0.002$ ), larger foveal avascular zone ( $P < 0.0001$ ), lower SCP ( $P = 0.001$ ) and DCP capillary density ( $P < 0.0001$ ), and lower SCP ( $P = 0.009$ ) and DCP local fractal dimension ( $P < 0.0001$ ).

Two multivariate models with either capillary density or fractal dimension as covariate showed that younger age ( $P = 0.014/0.017$ ), ellipsoid zone disruption ( $P = 0.034/0.019$ ), larger foveal avascular zone ( $P = 0.0006/0.002$ ), and lower DCP density ( $P = 0.008$ ) or DCP fractal dimension ( $P = 0.012$ ), respectively, were associated with worse visual acuity.

Visual acuity of eyes with radiation maculopathy is influenced by structural and microvascular factors identified with OCT angiography, including foveal avascular zone area and DCP integrity. Local fractal dimension is a useful quantitative imaging marker in radiation maculopathy assessing the level of disorganization of the perifoveal capillary network.

Further studies are needed to validate fractal dimension, either local or global, and its relation to visual function, for the analysis of OCT angiography in retinal vascular disorders.

## DISCUSSION

The projects presented in this thesis followed a scientific strategy aimed at identifying imaging and/or biological parameters that can serve as biomarkers for the diagnosis, prognosis, therapeutic response or safety in a range of retinal diseases. The markers identified (or under progress) are summarized in **Table 2**. Custom algorithms were developed using the MatLab program to extract relevant quantitative parameters from OCT and OCT angiography imaging, and were applied serially to image datasets by batch processing.

Encouraging results in different settings (tolerance to subretinal gene therapy in Project 1; translational exploration in CSCR and telangiectatic retinal disorders in Projects 2 and 3, respectively) suggest that the investigated biological and imaging parameters could provide potential biomarkers for the diagnosis, follow-up, prognosis, or safety assessment in retinal diseases.

Project	Imaging markers			Biological markers		
	Marker	Modality	Marker category	Marker	Fluid/organ	Marker category
<b>1 [LV-RPE65]</b>	Segmented retinal layer thickness in detached retina	OCT	Toxicity	Circulating lentiviral RNA	Serum	Toxicity
				Neutralizing antibodies against LV-RPE65 (in progress)	Serum	
				Integrated lentiviral DNA	Organs	
<b>2 [CSCR]</b>	Fluorescein expansion ratio	FA	Prognosis	Deregulated pathways: glycolysis/gluconeogenesis, inflammation, alternative complement, cellular adhesion, biliary acid metabolism and gluco/mineralocorticoid	Subretinal fluid	Diagnosis/mechanisms
	Subretinal fluid volume	OCT	Prognosis	Markers of mineralocorticoid activation (in progress)	Serum	Diagnosis/mechanisms
	Density of choriocapillaris flow voids	OCT-A	Diagnosis/mechanisms			
<b>3 [Telangiectatic disorders]</b>	Local and global capillary density	OCT-A	Diagnosis/mechanisms	PIGF, VEGF and other angiogenic factors	Aqueous humor	Diagnosis/mechanisms
	Local fractal dimension	OCT-A	Diagnosis/mechanisms/ Toxicity/ Prognosis	PIGF, VEGF and other angiogenic factors (in progress)	Aqueous humor	Diagnosis/mechanisms

**Table 2. Biological and imaging markers evaluated in Projects 1, 2 and 3**

Importantly, several parameters were assessed, but not all candidates passed the testing process, as detailed in the Introduction (**Figure 3**). The markers discussed through Projects 1 to 3, represent essentially markers that were successfully validated, reflecting a clear publication bias since the present thesis report is based on published articles.

#### Image processing: the critical issue of repeatability

The image processing tools developed for Projects 1, 2 and 3, their function and main characteristics are summarized in **Table 3**.

A proportion of the image processing tools developed throughout Projects 1, 2 and 3, relied on fully automated processes. In these instances, the repeatability of the process is 100% since the same code is applied to each image. A residual variability is still present, which is due to the variations in image acquisition, although they were performed by the same operator (AM, in Project 1), or trained optometrists (Projects 2 and 3). These variations may result from acquisition artifacts, due to poor image fixation of visually impaired eyes, to different pigmentation of ocular structures, especially the RPE, that may alter the absorption spectrum of infrared OCT radiations by the retina and choroid.

The nascent OCT angiography technology presents also several artifacts during acquisition (projection artifacts, eye movements), built-in image processing (segmentation defects, inappropriate binarization), image display (wrongful representation) and image analysis by the OCT angiography device (erroneous binarization yielding false density values).<sup>194</sup> Noticeably, artifacts of OCT angiography are exacerbated in low-vision eyes, such as those irradiated for intraocular tumors. Say *et al.* showed recently that the quality of images (as represented by the signal strength index provided by the device) was correlated to the degree of visual impairment in these eyes.<sup>195</sup> Therefore, in our study on irradiated eyes (Article 3c), we excluded all eyes with signal strength index < 40 in order to limit the influence of bad image quality, a potential confounder in the OCT angiography-derived metrics reflecting the integrity of capillary networks (capillary density and local fractal dimension). In the developed automated algorithms, a special care was taken to control for these artifacts, by assessing the test-retest reliability. For instance, repeated measures were performed by varying the binarization parameters (choriocapillaris flow

voids, Project 2c), or the obtained values were correlated to a subjective multi-observer clinical grading, after validation by Cohen's kappa for qualitative data, or intraclass correlation coefficient for quantitative data (fractal analysis of retinal capillary plexuses in radiation maculopathy, Project 3c).

Project	Function name	Action	Automated	Batch processing	Complete code
3c	intercapillary_area_iteration	Intercapillary areas on OCTA	Yes	Yes	Appendix 1
3c	MoveRename	File displacement and renaming	Yes	Yes	Appendix 2
2c	crop_octa	Extraction of OCTA image from screen capture	Yes	Yes	Appendix 3
1	layer_png	Extraction of thickness values from OCT thickness profile	Semi	Yes	Appendix 4
2a-2b	leak_area	Fluorescein leakage area	Semi	No	Appendix 5
2a	srf_segment	Subretinal fluid volume segmentation	Semi	Yes	Appendix 6
2c	octa_voids_analysis	Choriocapillaris flow void detection on OCTA	Yes	Yes	Appendix 7
3a	vesseldensity_square	Global capillary density on OCTA	Semi	No	Appendix 8
3a	local_density	Local capillary density on OCTA	Semi	No	Appendix 9
3a	random_local_density2	Random distribution of circles over OCTA	Yes	No	Appendix 10
3a	PIA_angiofluo_square	Intercapillary areas on FA	Semi	No	Appendix 11
3b	edema	Cystoid space areas on OCT	Semi	No	Appendix 12
3c	fractal_sector	Local fractal dimension on OCTA	Yes	Yes	Appendix 13

**Table 3. Main image processing tools developed on MatLab for Projects 1, 2, and 3.**

Complete code sequences are provided in the Appendices.

OCT= optical coherence tomography; OCTA= optical coherence tomography angiography; FA= fluorescein angiography

Another fraction of the processing tools developed here was based on semi-automated algorithms, which signifies that an observer intervention was necessary at one or several steps during the image processing. For instance, an observer was required to identify a specific region of interest (such as background intensity), or a pathologic feature (such as leakage point on

CSCR or telangiectasias in MacTel 1). These semi-automated processes allowed the program to adapt to inherently heterogeneous clinical material, but at the cost of decreased repeatability. Therefore, validations of the processes were carried out on healthy control eyes (Projects 3a and 3c), by comparing measurements with those obtained by built-in analytic softwares (estimates of subretinal fluid volumes derived from the Spectralis segmentation in Project 2a), or with an external validating procedure (segmentation by a different methodology, Project 1).

### [Project 1] LV-RPE65

In vivo imaging markers are essential to evaluate dynamically the retinal response to injected therapeutic agents. Indeed, most of existing preclinical studies of retinal gene therapy have analyzed the retinal structure at fixed, later time-points (usually 30 days). This follow-up schemes may have missed the transitory inflammatory response that may manifest an occult immune response with potential long-term consequences, such as elimination of the transgene and loss of efficacy. The second important aspect of this study as compared to previous tolerance studies was the similar assessment of the effects of the vehicle-treated eyes, allowing to characterize the effect of the subretinal injection per se. Using imaging and biological markers, we evidenced a partial ocular tolerance in term of retinal structure integrity, and a favorable systemic tolerance to LV-RPE65 subretinal administration without adjuvant anti-inflammatory prophylaxis in healthy non-human primates. Two types of local retinal complications were observed:

- 1) outer retinal structural alterations on OCT, especially ONL and photoreceptor layer thinning, probably linked to the subretinal route of administration.

- 2) a peri-vascular inflammatory reaction that may contribute to retinal alterations and may be controlled by co-administering an anti-inflammatory prophylaxis.

### Hurdles for gene therapy delivery to the RPE via the subretinal route

The subretinal route allows the specific delivery of therapeutic agents to the RPE, while limiting systemic distribution and potential side effects in other organs. However, performing iatrogenic retinal detachment, especially when involving the macula, is potentially harmful for

retinal cells, particularly photoreceptor, and even more in eyes with inherited retinal disorders eligible for future gene augmentation therapy.<sup>196</sup> Numerous studies have shown the deterioration of photoreceptors after macula-off rhegmatogenous retinal detachment.<sup>197</sup> Since one essential role of the RPE is to maintain photoreceptor outer segment metabolism, and that photoreceptor outer segments do reform in ~2 months in primates,<sup>198</sup> a normal or subnormal outer retinal morphology is expected to recover within 2-3 months, as observed in our study using serial OCT segmentation and layer thickness extraction. However, this assessment is limited by the poor sensitivity of SD-OCT for RPE analysis.

The exact effect of subretinal delivery on photoreceptors is controverted, with groups having identified and reported deleterious effects of foveal detachments,<sup>89</sup> while other reported no evident adverse reaction.<sup>199</sup> To note, the comparison of these discrepant results is difficult, since treatments were administered with different gene therapy products (AAV2.hRPE65 for LCA,<sup>89</sup> or AAV.REP1 to treat choroideremia by replacing the Rab Escort Protein 1<sup>199</sup>), different vehicles, and different ages (younger patients for the former study).<sup>89</sup> Moreover, the latter study was performed several years later,<sup>199</sup> possibly taking advantage of the experience gained and shared by other pioneer groups in injected a gene therapy vector solution subfoveally.

The subretinal route in our hands would require further optimization, as evidenced by the outer retinal alteration observed in Project 1. Several key parameters contributing to the injection procedure can be improved, including surgical technique (with or without vitrectomy), the injected volume and concentration of viral vector, the injection site (localization; single/multiple), detachment of the fovea or its prevention (for instance via the use of perfluorocarbonate tamponade<sup>200</sup>), subretinal cannula, automated syringe controlling infusion pressure, or adjuvant neuroprotective agents.

Finally, alternate approaches such as intravitreal delivery of viral vectors,<sup>196,201,202</sup> or non-viral suprachoroidal electrotransfer,<sup>203</sup> have been explored, that may allow to overcome the above-mentioned limitations of the subretinal route, but their ability to transduce photoreceptors or RPE cells and the safety of these approaches are not fully established.

## Safety markers in retinal gene therapy trials: the role of retinal imaging

In addition to functional efficacy markers, including visual acuity and various tools assessing retinal sensitivity (mentioned in the Introduction to Project 1), consensual markers of retinal safety after subretinal gene therapy are crucially needed to homogenize study results. Retinal layer segmentation based on a shared software would offer an objective tool to extract reproducible values, reflecting potential retinal damage or restoration. Indeed, in existing reports, different OCT treatment and custom segmentation techniques have been employed, limiting the comparability of results. For instance, Jacobson *et al.* (University of Pennsylvania) used a MatLab-based segmentation of retinal layers, with OCT scans acquired on the RTVue-100 OCT device (Optovue, Fremont, CA, USA), compared to a reference control group.<sup>79</sup> On the other hand, Testa *et al.* (Children Hospital of Philadelphia) used a Cirrus HD-OCT (Carl Zeiss, Dublin, CA, USA) and the built-in segmentation software to extract total retinal thickness value. Finally, Bainbridge *et al.* have assessed only the total retinal thickness at the macula, based on different devices, including both time-domain (at baseline in some patients) and spectral-domain OCT, and report qualitatively the integrity of the photoreceptor layer.

We have used a custom-built method, and an external validation by additional image segmentation by a group not involved in the development of LV-RPE65 (Giessen University, Germany). This group has developed a device-independent OCT segmentation tool<sup>172</sup> (using here the raw OCT data in .E2E file format from the Spectralis). Such tools, if adopted by groups involved in clinical and preclinical gene therapy evaluation, could prove relevant in increasing the comparability of results among different studies.

## Perspectives

Further pre-clinical investigations in primates or other large animals are needed to ascertain the ocular tolerance of LV-RPE65, especially with the use of systemic corticosteroid prophylaxis. The investigation of the early and transient inflammatory response observed is currently ongoing with the search of neutralizing antibodies against capsid proteins of the lentiviral LV-RPE65

vector, in serum sampled at different time points from the non-human primates of Project 1, after gene therapy administration.

The development and translation to human diseases of robust lentiviral vectors for gene therapy delivery to the retina will prove useful since there is an estimated 40-80% seroprevalence of AAV-specific antibodies in the general population,<sup>204</sup> which is an obstacle to the efficacy of AAV-based gene transfer, especially after systemic administration.<sup>205</sup> Clinical safety is a critical issue for novel therapies, especially when derived from pathogenic agents, and when administered in the central nervous system.

## [Project 2] CSCR

From the observation of subretinal fluid kinetics to its molecular characterization

In the Articles 2a and 2b, we characterized the course of subretinal detachments during CSCR, including the time to resolution of acute detachments, and the rate of ulterior recurrences. Moreover, we investigated the multimodal imaging parameters influencing the time-course of subretinal fluid resolution and recurrence, and identified imaging markers presumed to be involved in the complex pathophysiology of CSCR, such as choroidal thickness and RPE alterations.

In the Article 2c, we described a detailed patterns of blood flow alteration in the choriocapillaris of CSCR patients, and showed that it was related to the vasodilation of deeper choroidal vessels. This analysis provided a substrate for a putative mechanism linking choroidal vasodilation and RPE defects, the hallmarks of CSCR identified in studies 2a and 2b as key players in the course of the disease. This link could reside in the choriocapillaris, the thin innermost layer of the choroid where blood flow derives from large choroidal vessels (see **Figure 1**), that supplies the adjacent RPE. Local choriocapillaris non-perfusion could lay the ground for focal ischemic RPE damage, resulting in RPE leakage sites.

Moreover, we showed that the degree of this choriocapillaris flow disturbance was linked to patient age (which has also been observed in healthy subjects<sup>185</sup>) and to the severity of CSCR

(acute, recurrent or chronic). Consistently, in acute cases, limited focal damage is suffered by the RPE, that preserves an efficient healing capacity; therefore, episodes last a few months until the leak resolves and the leakage site is sealed (by new intercellular junctions, in the hypothesis of intercellular adhesion defects in the RPE). However, in recurrent or chronic cases, the more extended ischemic damage to the RPE, due to more numerous choriocapillaris non-perfusion sites, would result in a delayed healing process, long-standing subretinal fluid, and chronic epitheliopathy, characterized on fluorescein angiography by multiple pin-point leakage sites.

Finally, the scope of investigation progressed farther to reach the molecular level, with the exploration of the subretinal fluid composition from a CSCR patient in Article 2d. This analysis revealed pathways that were consistent with the above-mentioned hypothesis, especially the gluco- and mineralocorticoid system, and adhesion molecules. It also opens new insight in the pathophysiology of the disease. Particularly, decreased activation of the alternative complement pathway as compared to RRD, suggests that sublytic membrane attack complex may be defective in CSCR patients, resulting in decreased trans-RPE transport and subsequent inter-RPE cell breakdown. The identification of gluco/neoglycogenesis by both metabolomics and proteomics stresses the major importance of retinal metabolism in the survival and function of photoreceptors, a subject actively explored by many teams. Specific proteins have also been identified and are currently being validated using other biologic samples from CSCR patients.

Moreover, the results suggested potential molecular or cellular neuroprotective mechanisms activated in CSCR eyes, that prevent photoreceptor degeneration, and could be explored as neuroprotective adjuvant therapies in RRD, where photoreceptor degeneration occurs despite prompt surgical retinal reattachment.

These analyses recognized biological compounds deregulated in CSCR eyes, suggesting candidate markers of disease activity that will require further investigation. These markers could be present in more accessible body fluids, such as tears or serum, which would have broad translational applications in the clinical setting. For instance, these markers could facilitate the diagnosis of complex clinical presentations between chronic CSCR and polypoidal choroidal vasculopathy, AMD, or inflammatory retinal or tumoral entities that may mimic CSCR manifestations (choroidal hemangioma, tuberculous uveitis, etc). Two projects are currently

ongoing, to investigate markers of MR activation in the serum of CSCR patients (collaboration with Min Zhao, Emilie Picard and Francine Behar-Cohen, INSERM, Paris; and Jérémie Canonica, Lausanne) and to investigate the proteome in tears from CSCR patients (collaboration with Natacha Turck, Genève).

#### Perspectives: future imaging and biological markers in CSCR

The studies presented here were aimed at expanding the current understanding of CSCR pathophysiology.

Regarding imaging markers, these results indicate that choroidal thickness or height of RPE defects may be used to predict the duration of episodes and the risk of recurrence. Choroidal flow voids are a powerful tool in assessing choroidal perfusion of the RPE and to foster the understanding of the disease, but may not have direct clinical applications. Future investigations should focus on novel imaging markers, that require a simple computational process and may be soon embedded in OCT devices. For instance, another parameter reflecting choroidal changes in CSCR is the choroidal vascularity index,<sup>206,207</sup> that reflects the proportion of the choroidal tissue occupied by vessels. This ratio can be estimated by automated image segmentation and binarization processes. Choroidal vascularity index could become an imaging biomarker with diagnosis and prognosis value in CSCR and subtypes of the disease, that would better reflect choroidal thickening and vasodilation changes than choroidal thickness or choriocapillaris flow voids separately.

Regarding biological markers, candidate pathways contributing to CSCR pathophysiology have been identified in Article 2d. Relevant molecules derived from these pathways should be investigated in more accessible body fluids, such as tears or serum, in order to fulfill the requirements for potential diagnosis or prognosis biomarkers. In particular, molecules related to MR pathway were identified, which is consistent with the pathophysiology hypothesis of MR overactivation,<sup>208</sup> and with recent genetic evidence of haplotypes of the MR gene (*NR3C2*) associated with CSCR.<sup>209</sup> In serum of patients with essential hypertension or kidney disease, markers related to MR overactivation have been identified.<sup>210</sup> However, these markers have not been

explored in CSCR patients. Among candidate molecules, the circulating protein lipocalin-2 (also named NGAL, Neutrophil gelatinase-associated lipocalin), which binds matrix metalloproteinase 9 (MMP9) and modulates its stability, is a primary target of the aldosterone/MR pathway in the cardiovascular system, and plays a key role in MR-mediated cardiovascular fibrosis.<sup>211</sup> Serum levels of Lipocalin-2 and its complex with MMP9 are currently being investigated in the serum of patients with CSCR, and could further confirm the involvement of the MR pathway in CSCR pathophysiology, and provide clinically applicable markers of CSCR activity.

### [Project 3] Telangiectatic retinal disorders

The emergence of OCT angiography as non-invasive imaging marker of retinal diseases

The results obtained in Articles 3a, 3b and 3c based on OCT angiography illustrate the strength of this non-invasive technique to gain a detailed insight into *in vivo* pathological processes, and extract relevant information regarding disease pathophysiology.

Immediate after the first qualitative descriptions of retinal or choroidal features by OCT angiography in health and disease, quantitative tools emerged. These tools were particularly appropriate given the digitalized nature of the grayscale OCT angiography images. For instance, the first commercially available Angiovue RTx100 system (Optovue, Fremont, CA, USA), provides 304×304-pixel “en face” images extracted after layer-specific segmentation with maximal intensity projection of voxels from the raw volume scan. The first quantitative parameters derived from these scans and reported in the literature were vascular density, a ratio of 1 versus 0 pixels after image binarization at different grayscale intensity thresholds (arbitrary; mean[image intensity] - 1×SD; mean[image intensity] - 2×SD; etc). Soon (early 2016), this ‘vascular density’ function was embedded in the built-in Angiovue software (AngioAnalytics), increasing the repeatability of this outcome, with the drawback that the manufacturer did not make public its protected algorithm, resulting in a paradoxical situation where abundant literature reports, although gaining reproducibility, do rely on an unknown calculation method. Before the embedding of this vascular density within the device, we designed our own algorithm to compute

vascular density from OCT angiography acquisitions, and have added a local density function to assess the vascular density in regions of interests around remarkable features, as exemplified in Article 3a with retinal vascular telangiectasias.

Article 3c demonstrates how computerized image analysis can meet qualitative clinical observations by deriving complex parameters from OCT angiography reflecting the degree of disorganization of capillary networks, such as local fractal dimension. Interestingly, this dimension was correlated to a masked, qualitative grading by retina specialists, indicating the potential of this parameter. However, this correlation was not stronger than between the qualitative grading and capillary density, suggesting that local fractal dimension is a relevant endpoint that needs to be further optimized to outscore other quantitative parameters, and tested in many other retinal disorders, starting with the most frequent (retinal vein occlusions, diabetic retinopathy).

#### PIGF, VEGF and their inhibition in retinal telangiectatic disorders

Article 3b demonstrates how intraocular biological markers contribute to improve the mechanisms of retinal vascular disorders. Particularly, the ocular levels of angiogenic factors in MacTel 1 eyes, selected as phenotype of “pure” vascular disease of developmental origin, bridges preclinical findings in an animal model (that allowed the identification of the relevant marker, PIGF) with clinical evidence and therapeutic applications with the efficacy of aflibercept in treating this disorder. Moreover, an additional validation was brought by the correlation of PIGF levels with OCT angiography capillary density. This correlation is an illustration of the surrogate endpoint criteria exposed in the Introduction, since PIGF levels are connected both to a clinical “hard” endpoint (visual acuity recovery, macular thickness decrease) and to a putative mechanism (relationship with capillary network integrity, supported by OCT angiography findings and the preclinical evidence in PIGF-overexpressing rats<sup>33</sup>).

This study highlighted the role of PIGF and the VEGFR-1 pathway in retinal vascular pathogenesis, but it did not rule out the contribution of VEGF. First, both VEGF and PIGF bind to VEGFR-1. Second, the conventional anti-VEGF agents bevacizumab and ranibizumab, that were employed before aflibercept, had a partial effect on macular edema. Then, the study is limited by

the small cohort size, and outlier values may have an important effect on the statistical comparisons performed (although the superior outliers on the [PIGF] and [VEGF-A] aqueous humor plots of MacTel 1 did not correspond to the same subject).

The similarities between manifestations of MacTel 1 and radiation maculopathy suggested to carry out similar analysis in radiation maculopathy, where in addition we observed a favorable response to aflibercept. An enhanced analysis is currently ongoing with the exploration of angiogenic factors, coupled to inflammatory mediators (cytokines, etc) by multi-array immunoassay, in the low-volume aqueous humor samples retrieved from radiation maculopathy eyes. Moreover, possible correlations with imaging metrics will also be investigated in these eyes.

## Conclusions

The works performed in this thesis followed a “bench to bedside” strategy, investigating biological and imaging markers derived from preclinical, mechanistic or imaging observations, that were tested and validated on clinical situations with the perspective of applications as diagnosis, prognosis, monitoring or safety markers.

In particular, the interest of coupling multimodal ocular imaging and biological markers has been established in Article 3b (MacTel 1), and its application to other conditions will require additional development.

The aims stated in the Introduction have been at least partially met:

- 1) Novel parameters have been developed for non-standard clinical situations lacking established endpoints, such as retinal gene therapy testing (Project 1), choriocapillaris imaging in CSCR (Project 2c) or fractal analysis in radiation maculopathy (Project 3c).
- 2) Progresses were made in the understanding of retinal disorder mechanisms using imaging and molecular investigations (Projects 2 and 3)
- 3) Progresses were made in the understanding of treatment effects, and in parameters guiding therapeutic decision (Project 1, 2a, 2d and 3b).
- 4) New potential molecular therapeutic targets were identified (Projects 2d and 3b).
- 5) Prognosis markers were identified (all projects, particularly 2a, 2b, 3a and 3c).

Yet, several works remain under progress, as detailed in the specific Discussion of each Project, such as:

- Project 1:
  - characterization of the ocular and systemic immune response to the LV-RPE65 vector
  - tolerance assessment to LV-RPE65 with co-administration of systemic corticosteroids as adjuvant anti-inflammatory prophylaxis
- Project 2:
  - investigate candidate serum markers of CSCR

- investigate new imaging parameters such as choroidal vascular index (ratio of hyper-reflective tissue to intraluminal hypo-reflective area on choroidal OCT scans)
- investigate potential correlations between choroidal morphological parameters and biological parameters (especially serum markers), further elucidating disease mechanisms
- Project 3:
  - explore the ocular angiogenic factor profile of radiation maculopathy eyes, and possible correlations with imaging markers
  - further assess the test-retest reliability and inter-operator repeatability of fully automated and semi-automated image processing algorithms, respectively

This approach contributed to the development of dedicated clinical tools for orphan retinal diseases (MacTel 1, CSCR), or exceptional therapeutic situations (gene therapy for LCA, maculopathy post-irradiation for intraocular tumors). It also derives on larger, public-health scale perspectives, since these biological and imaging markers could also accelerate medical tests, especially in high workflow, low-medical staff clinical settings such as medical retina outpatient clinics, in remote areas or developing countries, via telemedicine.

Finally, further validation and consolidation of image processing algorithms employed here (and detailed in the Appendices) will be required, and the most relevant algorithms should be made available to the research community, via this thesis manuscript and via future submissions to journals specialized in imaging methodology.

## REFERENCES

1. Kolb E, Nelson R, Fernandez E, Jones B. Webvision - The organization of the retina and visual system. <http://webvision.med.utah.edu> (accessed July 16th, 2017).
2. Hogan MJ, Alvarado JA, Weddel JE. *Histology of the Human Eye*. Philadelphia: W.B. Saunders Company; 1971.
3. Zhang M, Hwang TS, Dongye C, Wilson DJ, Huang D, Jia Y. Automated Quantification of Nonperfusion in Three Retinal Plexuses Using Projection-Resolved Optical Coherence Tomography Angiography in Diabetic Retinopathy. *Investig Ophthalmology Vis Sci*. 2016;57(13):5101. doi:10.1167/iovs.16-19776.
4. Bonnín S, Mané V, Couturier A, et al. New Insight Into the Macular Deep Vascular Plexus Imaged By Optical Coherence Tomography. *Retina*. 2015;35(11):2347-2352. doi:10.1097/IAE.0000000000000839.
5. Henking P, De Oliveira LF. Development of retinal vessels in the rat. *Invest Ophthalmol*. 1967;6(5):520-530.
6. Daruich A, Matet A, Moulin A, et al. Mechanisms of macular edema: beyond the surface. *Prog Retin Eye Res*. 2017;In press.
7. Schrödl F, Kaser-Eichberger A, Trost A, et al. Lymphatic Markers in the Adult Human Choroid. *Investig Ophthalmology Vis Sci*. 2015;56(12):7406. doi:10.1167/iovs.15-17883.
8. Provis JM, Dubis AM, Maddess T, Carroll J. Adaptation of the central retina for high acuity vision: cones, the fovea and the avascular zone. *Prog Retin Eye Res*. 2013;35:63-81. doi:10.1016/j.preteyeres.2013.01.005.
9. von Helmholtz HLF. Beschreibung eines Augen-Spiegels. *Förstnerische Verlagsbuchhandlung Berlin*. 1851.
10. Keeler CR. The Ophthalmoscope in the Lifetime of Hermann von Helmholtz. *Arch Ophthalmol*. 2002;120(2):194-201. doi:10.1001/archophth.120.2.194.
11. Novotny HR, Alvis DL. A method of photographing fluorescence in circulating blood in the human retina. *Circulation*. 1961;24:82-86.
12. Marmor MF, Ravin JG. Fluorescein Angiography. *Arch Ophthalmol*. 2011;129(7):943. doi:10.1001/archophthalmol.2011.160.
13. Guyer DR, Puliafito CA, Monés JM, Friedman E, Chang W, Verdooner SR. Digital indocyanine-green angiography in chorioretinal disorders. *Ophthalmology*. 1992;99(2):287-291.
14. Hayashi K, de Laey JJ. Indocyanine green angiography of choroidal neovascular membranes. *Ophthalmologica*. 1985;190(1):30-39.
15. Hochheimer BF. Angiography of the retina with indocyanine green. *Arch Ophthalmol (Chicago, Ill 1960)*. 1971;86(5):564-565.
16. Yannuzzi LA, Slakter JS, Sorenson JA, Guyer DR, Orlock DA. Digital indocyanine green videoangiography and choroidal neovascularization. *Retina*. 1992;12(3):191-223.
17. von Rückmann A, Fitzke FW, Bird AC. Distribution of fundus autofluorescence with a scanning laser ophthalmoscope. *Br J Ophthalmol*. 1995;79(5):407-412.
18. Lois N, Halfyard a S, Bird a C, Fitzke FW. Quantitative evaluation of fundus autofluorescence imaged "in vivo" in eyes with retinal disease. *Br J Ophthalmol*. 2000;84(7):741-745. doi:10.1136/bjo.84.7.741.
19. Lois N, Halfyard AS, Bunce C, Bird AC, Fitzke FW. Reproducibility of fundus autofluorescence measurements obtained using a confocal scanning laser ophthalmoscope. *Br J Ophthalmol*. 1999;83(3):276-279.
20. Schmitz-Valckenberg S, Holz FG, Bird AC, Spaide RF. Fundus autofluorescence imaging: review and perspectives. *Retina*. 2008;28(3):385-409. doi:10.1097/IAE.0b013e318164a907.

21. Puliafito CA, Hee MR, Lin CP, et al. Imaging of macular diseases with optical coherence tomography. *Ophthalmology*. 1995;102(2):217-229.
22. Hassenstein A, Meyer CH. Clinical use and research applications of Heidelberg retinal angiography and spectral-domain optical coherence tomography - a review. *Clin Experiment Ophthalmol*. 2009;37(1):130-143. doi:10.1111/j.1442-9071.2009.02017.x.
23. Spaide RF, Koizumi H, Pozonni MC. Enhanced Depth Imaging Spectral-Domain Optical Coherence Tomography. 2008. doi:10.1016/j.ajo.2008.05.032.
24. Hirata M, Tsujikawa A, Matsumoto A, et al. Macular Choroidal Thickness and Volume in Normal Subjects Measured by Swept-Source Optical Coherence Tomography. *Investig Ophthalmology Vis Sci*. 2011;52(8):4971. doi:10.1167/iovs.11-7729.
25. Jirarattanasopa P, Ooto S, Tsujikawa A, et al. Assessment of macular choroidal thickness by optical coherence tomography and angiographic changes in central serous chorioretinopathy. *Ophthalmology*. 2012;119(8):1666-1678. doi:10.1016/j.ophtha.2012.02.021.
26. Rosen RB, Hathaway M, Rogers J, et al. Multidimensional en-face OCT imaging of the retina. *Opt Express*. 2009;17(5):4112-4133.
27. Jia Y, Tan O, Tokayer J, et al. Split-spectrum amplitude-decorrelation angiography with optical coherence tomography. *Opt Express*. 2012;20(4):4710-4725. doi:10.1364/oe.20.004710.
28. Daruich A, Matet A, Marchionno L, et al. Acute central serous chorioretinopathy: factors influencing episode duration. *Retina*. January 2017;1. doi:10.1097/IAE.0000000000001443.
29. Kowalczyk L, Matet A, Dirani A, et al. Efficacy of intravitreal aflibercept in macular telangiectasia type 1 is linked to the ocular angiogenic profile. *Retina*. 2016;pp: 1.
30. Matet A, Daruich A, Dirani A, Ambresin A, Behar-Cohen F. Macular Telangiectasia Type 1: Capillary Density and Microvascular Abnormalities Assessed by Optical Coherence Tomography Angiography. *Am J Ophthalmol*. 2016;167. doi:10.1016/j.ajo.2016.04.005.
31. Matet A, Daruich A, Zografos L. Radiation Maculopathy After Proton Beam Therapy for Uveal Melanoma: Optical Coherence Tomography Angiography Alterations Influencing Visual Acuity. *Investig Ophthalmology Vis Sci*. 2017;58(10):3851. doi:10.1167/iovs.17-22324.
32. Villani E, Vujosevic S, RM. C. Foreword: Biomarkers and Surrogate Endpoints in Ophthalmic Clinical Research. *Investig Ophthalmology Vis Sci*. 2017;58(6):BIOi. doi:10.1167/iovs.17-22128.
33. Kowalczyk L, Touchard E, Omri S, et al. Placental Growth Factor Contributes to Micro-Vascular Abnormalization and Blood-Retinal Barrier Breakdown in Diabetic Retinopathy. *PLoS One*. 2011;6(3). doi:10.1371/journal.pone.0017462.
34. Zahid S, Dolz-Marco R, Freund KB, et al. Fractal Dimensional Analysis of Optical Coherence Tomography Angiography in Eyes With Diabetic Retinopathy. *Investig Ophthalmology Vis Sci*. 2016;57(11):4940. doi:10.1167/iovs.16-19656.
35. Kim AY, Rodger DC, Shahidzadeh A, et al. Quantifying Retinal Microvascular Changes in Uveitis Using Spectral-Domain Optical Coherence Tomography Angiography. *Am J Ophthalmol*. 2016;171:101-112. doi:10.1016/j.ajo.2016.08.035.
36. Bhanushali D, Anegondi N, Gadde SGK, et al. Linking retinal microvasculature features with severity of diabetic retinopathy using optical coherence tomography angiography. *Investig Ophthalmol Vis Sci*. 2016;57(9):519-525. doi:10.1167/iovs.15-18901.
37. Arend O, Wolf S, Jung F, et al. Retinal microcirculation in patients with diabetes mellitus: dynamic and morphological analysis of perifoveal capillary network. *Br J Ophthalmol*. 1991;75(9):514-518.
38. Guyer DR, Yannuzzi LA, Slakter JS, Sorenson JA, Ho A, Orlock D. Digital indocyanine green videoangiography of central serous chorioretinopathy. *Arch Ophthalmol*. 1994;112(8):1057-1062.
39. Prünke C. Indocyanine green angiographic findings in central serous chorioretinopathy. *Int Ophthalmol*. 1995;19(2):77-82.
40. MATLAB Product Description - MATLAB - Simulink - MathWorks Suisse.

- [https://ch.mathworks.com/help/matlab/learn\\_matlab/product-description.html](https://ch.mathworks.com/help/matlab/learn_matlab/product-description.html). Accessed August 16, 2017.
41. Image Processing Toolbox Product Description - MATLAB & Simulink - MathWorks Suisse. <https://ch.mathworks.com/help/images/product-description.html>. Accessed August 16, 2017.
  42. National Institutes of Health (NIH) - Precision Medicine Initiative. <https://allofus.nih.gov/>. Accessed August 17, 2017.
  43. Swiss Personalized Health Network. <http://www.samw.ch/fr/Projets/Swiss-Personalized-Health-Network.html>. Accessed August 17, 2017.
  44. Joint Nordic Biobank Research Infrastructure — NordForsk. <https://www.nordforsk.org/en/programmes-and-projects/projects/joint-nordic-biobank-research-infrastructure>. Accessed August 17, 2017.
  45. European Alliance for Personalised Medicine. <http://euapm.eu/>. Accessed August 17, 2017.
  46. Kersten E, Paun CC, Schellevis RL, et al. Systemic and ocular fluid compounds as potential biomarkers in age-related macular degeneration. *Surv Ophthalmol*. May 2017. doi:10.1016/j.survophthal.2017.05.003.
  47. Vujosevic S, Simó R, Arrigg PG, Casciano M, Cavarzeran F, M. M. Local and Systemic Inflammatory Biomarkers of Diabetic Retinopathy: An Integrative Approach. *Investig Ophthalmology Vis Sci*. 2017;58(6):BIO68. doi:10.1167/iovs.17-21769.
  48. den Hollander AI. Omics in Ophthalmology: Advances in Genomics and Precision Medicine for Leber Congenital Amaurosis and Age-Related Macular Degeneration. *Investig Ophthalmology Vis Sci*. 2016;57(3):1378. doi:10.1167/iovs.15-18167.
  49. Sheffield VC, Stone EM. Genomics and the eye. *N Engl J Med*. 2011;364(20):1932-1942. doi:10.1056/NEJMra1012354.
  50. Villani E, Massaro D, Scaramuzzi M, Hamrah P, Medeiros FA, Nucci P. Decade-Long Profile of Imaging Biomarker Use in Ophthalmic Clinical Trials. *Investig Ophthalmology Vis Sci*. 2017;58(6):BIO76. doi:10.1167/iovs.17-21790.
  51. Lauwen S, de Jong EK, Lefebber DJ, den Hollander AI, S. Y, KG. C. Omics Biomarkers in Ophthalmology. *Investig Ophthalmology Vis Sci*. 2017;58(6):BIO88. doi:10.1167/iovs.17-21809.
  52. Denniston AK, Keane PA, Srivastava SK, et al. Biomarkers and Surrogate Endpoints in Uveitis: The Impact of Quantitative Imaging. *Investig Ophthalmology Vis Sci*. 2017;58(6):BIO131. doi:10.1167/iovs.17-21788.
  53. Matet A, Daruich A, Behar-Cohen F. [Ophthalmology in 2016 : the advent of ocular biomarkers]. *Rev Med Suisse*. 2017;13(544-545):84-87.
  54. Pagon RA, Adam MP, Ardinger HH, et al. *GeneReviews*®. University of Washington, Seattle; 1993.
  55. Hamel CP. Gene discovery and prevalence in inherited retinal dystrophies. *Comptes Rendus - Biol*. 2014;337(3):160-166. doi:10.1016/j.crv.2013.12.001.
  56. Hamel CP. Les dystrophies rétinienne héréditaires : apports de la génétique moléculaire. *Biol Aujourd'hui*. 2013;207(2):73-85. doi:10.1051/jbio/2013007.
  57. den Hollander AI, Roepman R, Koenekoop RK, Cremers FPM. Leber congenital amaurosis: genes, proteins and disease mechanisms. *Prog Retin Eye Res*. 2008;27(4):391-419. doi:10.1016/j.preteyeres.2008.05.003.
  58. Marlhens F, Bareil C, Griffoin JM, et al. Mutations in RPE65 cause Leber's congenital amaurosis. *Nat Genet*. 1997;17(2):139-141. doi:10.1038/ng1097-139.
  59. Hanein S, Perrault I, Gerber S, et al. [Leber congenital amaurosis: comprehensive survey of genetic heterogeneity. A clinical definition update]. *J Fr Ophthalmol*. 2005;28(1):98-105.
  60. Hamel CP, Tsilou E, Pfeffer BA, Hooks JJ, Detrick B, Redmond TM. Molecular cloning and expression of RPE65, a novel retinal pigment epithelium-specific microsomal protein that is post-transcriptionally regulated in vitro. *J Biol Chem*. 1993;268(21):15751-15757.

61. Hamel CP, Jenkins NA, Gilbert DJ, Copeland NG, Redmond TM. The Gene for the Retinal Pigment Epithelium-Specific Protein RPE65 Is Localized to Human 1p31 and Mouse 3. *Genomics*. 1994;20(3):509-512. doi:10.1006/geno.1994.1212.
62. Palczewski K. Chemistry and biology of the initial steps in vision: the Friedenwald lecture. *Invest Ophthalmol Vis Sci*. 2014. doi:10.1167/iovs.14-15502.
63. Hamel CP, Tsilou E, Harris E, et al. A developmentally regulated microsomal protein specific for the pigment epithelium of the vertebrate retina. *J Neurosci Res*. 1993;34(4):414-425. doi:10.1002/jnr.490340406.
64. Thompson DA, Gyürüs P, Fleischer LL, et al. Genetics and phenotypes of RPE65 mutations in inherited retinal degeneration. *Invest Ophthalmol Vis Sci*. 2000;41(13):4293-4299.
65. Chung DC, Traboulsi EI. Leber congenital amaurosis: Clinical correlations with genotypes, gene therapy trials update, and future directions. *J AAPOS*. 2009. doi:10.1016/j.jaapos.2009.10.004.
66. Cideciyan A V. Leber congenital amaurosis due to RPE65 mutations and its treatment with gene therapy. *Prog Retin Eye Res*. 2010. doi:10.1016/j.preteyeres.2010.04.002.
67. Chouchene I, Largueche L, Derouiche K, Mabrouk S, Abdelhak S, El Matri L. [Molecular exploration of the R91W (RPE65 gene) in Tunisian patients with early onset retinal dystrophy and early onset retinitis pigmentosa]. *Tunis Med*. 2015;93(7):445-448.
68. Lorenz B, Gyürüs P, Preising M, et al. Early-onset severe rod-cone dystrophy in young children with RPE65 mutations. *Invest Ophthalmol Vis Sci*. 2000;41(9):2735-2742.
69. Cideciyan A V., Aleman TS, Boye SL, et al. Human gene therapy for RPE65 isomerase deficiency activates the retinoid cycle of vision but with slow rod kinetics. *Proc Natl Acad Sci U S A*. 2008;105(39):15112-15117. doi:10.1073/pnas.0807027105.
70. Acland GM, Aguirre GD, Ray J, et al. Gene therapy restores vision in a canine model of childhood blindness. *Nat Genet*. 2001;28(1):92-95. doi:10.1038/88327.
71. Lai C-M, Yu MJ, Brankov M, et al. Recombinant adeno-associated virus type 2-mediated gene delivery into the Rpe65(-/-) knockout mouse eye results in limited rescue. *Genet Vaccines Ther*. 2004;2(1):3. doi:10.1186/1479-0556-2-3.
72. Narfström K, Wrigstad A, Nilsson SE. The Briard dog: a new animal model of congenital stationary night blindness. *Br J Ophthalmol*. 1989;73(9):750-756.
73. Veske A, Nilsson SE, Narfström K, Gal A. Retinal dystrophy of Swedish briard/briard-beagle dogs is due to a 4-bp deletion in RPE65. *Genomics*. 1999;57(1):57-61. doi:10.1006/geno.1999.5754.
74. Cideciyan A V., Jacobson SG, Beltran WA, et al. Human retinal gene therapy for Leber congenital amaurosis shows advancing retinal degeneration despite enduring visual improvement. *Proc Natl Acad Sci*. 2013;110(6):E517-E525. doi:10.1073/pnas.1218933110.
75. Acland GM, Aguirre GD, Bennett J, et al. Long-term restoration of rod and cone vision by single dose rAAV-mediated gene transfer to the retina in a canine model of childhood blindness. *Mol Ther J Am Soc Gene Ther*. 2005;12(6):1072-1082. doi:10.1016/j.ymthe.2005.08.008.
76. Bennicelli J, Wright JF, Komaromy A, et al. Reversal of blindness in animal models of leber congenital amaurosis using optimized AAV2-mediated gene transfer. *Mol Ther*. 2008;16(3):458-465. doi:10.1038/sj.mt.6300389.
77. Cideciyan A V., Hauswirth WW, Aleman TS, et al. Human RPE65 gene therapy for Leber congenital amaurosis: persistence of early visual improvements and safety at 1 year. *Hum Gene Ther*. 2009;20(9):999-1004. doi:10.1089/hum.2009.086.
78. Bainbridge JWB, Mehat MS, Sundaram V, et al. Long-term effect of gene therapy on Leber's congenital amaurosis. *N Engl J Med*. 2015;372(20):1887-1897. doi:10.1056/NEJMoa1414221.
79. Jacobson SG, Cideciyan A V., Roman AJ, et al. Improvement and decline in vision with gene therapy in childhood blindness. *N Engl J Med*. 2015;372(20):1920-1926. doi:10.1056/NEJMoa1412965.

80. Russell S, Bennett J, Wellman JA, et al. Efficacy and safety of voretigene neparvovec (AAV2-hRPE65v2) in patients with RPE65-mediated inherited retinal dystrophy: a randomised, controlled, open-label, phase 3 trial. *Lancet*. July 2017. doi:10.1016/S0140-6736(17)31868-8.
81. Bainbridge JWB, Smith AJ, Barker SS, et al. Effect of gene therapy on visual function in Leber's congenital amaurosis. *N Engl J Med*. 2008;358:2231-2239. doi:10.1056/NEJMoa0802268.
82. Maguire AM, Simonelli F, Pierce EA, et al. Safety and efficacy of gene transfer for Leber's congenital amaurosis. *N Engl J Med*. 2008;358(21):2240-2248. doi:10.1056/NEJMoa0802315.
83. Maguire AM, High KA, Auricchio A, et al. Age-dependent effects of RPE65 gene therapy for Leber's congenital amaurosis: a phase 1 dose-escalation trial. *Lancet (London, England)*. 2009;374(9701):1597-1605. doi:10.1016/S0140-6736(09)61836-5.
84. Simonelli F, Maguire AM, Testa F, et al. Gene therapy for Leber's congenital amaurosis is safe and effective through 1.5 years after vector administration. *Mol Ther J Am Soc Gene Ther*. 2010;18(3):643-650. doi:10.1038/mt.2009.277.
85. Testa F, Maguire AM, Rossi S, et al. Three-year follow-up after unilateral subretinal delivery of adeno-associated virus in patients with Leber congenital Amaurosis type 2. *Ophthalmology*. 2013;120(6):1283-1291. doi:10.1016/j.optha.2012.11.048.
86. Bennett J, Ashtari M, Wellman J, et al. AAV2 Gene Therapy Readministration in Three Adults with Congenital Blindness. *Sci Transl Med*. 2012;4(120):120ra15-120ra15. doi:10.1126/scitranslmed.3002865.
87. Bennett J, Wellman J, Marshall KA, et al. Safety and durability of effect of contralateral-eye administration of AAV2 gene therapy in patients with childhood-onset blindness caused by RPE65 mutations: a follow-on phase 1 trial. *Lancet (London, England)*. 2016;388(10045):661-672. doi:10.1016/S0140-6736(16)30371-3.
88. Hauswirth WW, Aleman TS, Kaushal S, et al. Treatment of Leber Congenital Amaurosis Due to RPE65 Mutations by Ocular Subretinal Injection of Adeno-Associated Virus Gene Vector: Short-Term Results of a Phase I Trial. *Hum Gene Ther*. 2008. doi:10.1089/hum.2008.107.
89. Jacobson SG, Cideciyan A V, Ratnakaram R, et al. Gene Therapy for Leber Congenital Amaurosis caused by RPE65 mutations: Safety and Efficacy in Fifteen Children and Adults Followed up to Three Years. *Arch Ophthalmol*. 2012;130(1). doi:10.1001/archophthalmol.2011.298.
90. Bainbridge JWB, Smith AJ, Barker SS, et al. Effect of Gene Therapy on Visual Function in Leber's Congenital Amaurosis. *N Engl J Med*. 2008. doi:10.1056/NEJMoa0802268.
91. Ashtari M, Cyckowski LL, Monroe JF, et al. The human visual cortex responds to gene therapy-mediated recovery of retinal function. *J Clin Invest*. 2011;121(6):2160-2168. doi:10.1172/JCI57377.
92. Kostic C, Crippa SV, Pignat V, et al. Gene therapy regenerates protein expression in cone photoreceptors in Rpe65(R91W/R91W) mice. *PLoS One*. 2011;6(2):e16588. doi:10.1371/journal.pone.0016588.
93. Le Meur G, Stieger K, Smith AJ, et al. Restoration of vision in RPE65-deficient Briard dogs using an AAV serotype 4 vector that specifically targets the retinal pigmented epithelium. *Gene Ther*. 2007;14(4):292-303. doi:10.1038/sj.gt.3302861.
94. Bemelmans A-P, Kostic C, Crippa S V., et al. Lentiviral gene transfer of RPE65 rescues survival and function of cones in a mouse model of Leber congenital amaurosis. *PLoS Med*. 2006;3(10):e347. doi:10.1371/journal.pmed.0030347.
95. Bemelmans A-P, Kostic C, Cachafeiro M, et al. Lentiviral gene transfer-mediated cone vision restoration in RPE65 knockout mice. *Adv Exp Med Biol*. 2008;613:89-95. doi:10.1007/978-0-387-74904-4\_9.
96. El Matri L, Ambresin A, Schorderet DF, et al. Phenotype of three consanguineous Tunisian families with early-onset retinal degeneration caused by an R91W homozygous mutation in the RPE65 gene. *Graefe's Arch Clin Exp Ophthalmol*. 2006;244(9):1104-1112. doi:10.1007/s00417-005-0096-2.

97. Matet A, Kostic C, Bemelmans A-P, et al. Evaluation of tolerance to lentiviral LV-RPE65 gene therapy vector after subretinal delivery in non-human primates. *Transl Res.* 2017;188:40-57.e4. doi:10.1016/j.trsl.2017.06.012.
98. Schambach A, Bohne J, Baum C, et al. Woodchuck hepatitis virus post-transcriptional regulatory element deleted from X protein and promoter sequences enhances retroviral vector titer and expression. *Gene Ther.* 2006;13(7):641-645. doi:10.1038/sj.gt.3302698.
99. Daruich A, Matet A, Dirani A, Bousquet E. Central serous chorioretinopathy : Recent findings and new physiopathology hypothesis. *Prog Retin Eye Res.* 2015;48. doi:10.1016/j.preteyeres.2015.05.003.
100. Lehmann M, Bousquet E, Beydoun T, Behar-cohen F. Pachychoroid: An Inherited condition? *Retina.* 2015;35:10-16.
101. Weenink AC, Borsje RA, Oosterhuis JA. Familial chronic central serous chorioretinopathy. *Ophthalmologica.* 2001;215(3):183-187. doi:50855.
102. Liew G, Quin G, Gillies M, et al. Central serous chorioretinopathy: a review of epidemiology and pathophysiology: Central serous chorioretinopathy. *Clin Experiment Ophthalmol.* 2013;41(2):201-214. doi:10.1111/j.1442-9071.2012.02848.x.
103. Schatz H, Madeira D, Johnson RN, McDonald HR. Central serous chorioretinopathy occurring in patients 60 years of age and older. *Ophthalmology.* 1992;99(1):63-67. doi:10.1016/S0161-6420(92)32010-X.
104. Fung AT, Yannuzzi L a., Freund K. Type 1 (Sub-Retinal Pigment Epithelial) Neovascularization in Central Serous Chorioretinopathy Masquerading As Neovascular Age-Related Macular Degeneration. *Retina.* 2012;1:1. doi:10.1097/IAE.0b013e3182680a66.
105. Pang CE, Freund KB. Pachychoroid Neovascularopathy. *Retina.* 2015;35(1):1-9. doi:10.1097/IAE.0000000000000331.
106. Tittl MK, Spaide RF, Wong D, et al. Systemic findings associated with central serous chorioretinopathy. *Am J Ophthalmol.* 1999;128(1):63-68.
107. Sahin A, Bez Y, Kaya MC, Türkcü FM, Sahin M, Yüksel H. Psychological distress and poor quality of life in patients with central serous chorioretinopathy. *Semin Ophthalmol.* 2014;29(2):73-76. doi:10.3109/08820538.2013.793728.
108. Piskunowicz M, Jaracz M, Lesiewska H, Malukiewicz G, Brozek-Pestka M, Borkowska A. Temperament profile in patients with central serous chorioretinopathy: a case-control study. *Eur J Ophthalmol.* 2014;24(3):392-395. doi:10.5301/ejo.5000377.
109. Conrad R, Weber NF, Lehnert M, et al. Alexithymia and emotional distress in patients with central serous chorioretinopathy. *Psychosomatics.* 2007;48(6):489-495. doi:10.1176/appi.psy.48.6.489.
110. Wynn PA. Idiopathic central serous chorioretinopathy--a physical complication of stress? *Occup Med (Lond).* 2001;51(2):139-140.
111. Yannuzzi LA. Type-A behavior and central serous chorioretinopathy. *Retina.* 1987;7(2):111-131.
112. Margolis R, Spaide RF. A pilot study of enhanced depth imaging optical coherence tomography of the choroid in normal eyes. *Am J Ophthalmol.* 2009;147(5):811-815. doi:10.1016/j.ajo.2008.12.008.
113. Warrow DJ, Hoang Q V., Freund KB. Pachychoroid Pigment Epitheliopathy. *Retina.* 2013;33(8):1659-1672. doi:10.1097/IAE.0b013e3182953df4.
114. Imamura Y, Fujiwara T, Margolis R, Spaide RF. Enhanced depth imaging optical coherence tomography of the choroid in central serous chorioretinopathy. *Retina.* 2009;29:1469-1473. doi:10.1097/IAE.0b013e3181be0a83.
115. Imamura Y, Engelbert M, Iida T, Freund KB, Yannuzzi LA. Polypoidal choroidal vasculopathy: a review. *Surv Ophthalmol.* 2010;55(6):501-515. doi:10.1016/j.survophthal.2010.03.004.
116. Hage R, Mrejen S, Krivosic V, Quentel G, Tadayoni R, Gaudric A. Flat irregular retinal pigment

- epithelium detachments in chronic central serous chorioretinopathy and choroidal neovascularization. *Am J Ophthalmol.* 2015;159(5):890-903.e3. doi:10.1016/j.ajo.2015.02.002.
117. Iida T, Yannuzzi LA, Spaide RF, Borodoker N, Carvalho CA, Negrao S. Cystoid macular degeneration in chronic central serous chorioretinopathy. *Retina.* 2003;23(1):1-7-138.
  118. Piccolino FC, De La Longrais RR, Manea M, Cicinelli S. Posterior cystoid retinal degeneration in central serous chorioretinopathy. *Retina.* 2008;28(7):1008-1012. doi:10.1097/IAE.0b013e31816b4b86r00006982-200807000-00014 [pii].
  119. Piccolino FC, De La Longrais RR, Manea M, Cicinelli S, Ravera G. Risk factors for posterior cystoid retinal degeneration in central serous chorioretinopathy. *Retina.* 2008;28(8):1146-1150. doi:10.1097/IAE.0b013e318175421f.
  120. Yannuzzi LA, Shakin JL, Fisher YL, Altomonte MA. Peripheral retinal detachments and retinal pigment epithelial atrophic tracts secondary to central serous pigment epitheliopathy. *Ophthalmology.* 1984;91(12):1554-1572.
  121. Yannuzzi LA, Slakter JS, Kaufman SR, Gupta K. Laser treatment of diffuse retinal pigment epitheliopathy. *Eur J Ophthalmol.* 1992;2(3):103-114.
  122. Gass JD. Pathogenesis of disciform detachment of the neuroepithelium. *Am J Ophthalmol.* 1967;63(3):Suppl:1-139.
  123. Quin G, Liew G, Ho I-VI-V, et al. Diagnosis and interventions for central serous chorioretinopathy: review and update. *Clin Experiment Ophthalmol.* 2013;41(2):187-200. doi:10.1111/j.1442-9071.2012.02847.x.
  124. Bujarborua D. Long-term follow-up of idiopathic central serous chorioretinopathy without laser. *Acta Ophthalmol Scand.* 2001;79(4):417-421.
  125. Katsimpris JM, Pournaras CJ, Sehgelmeble CW, Petropoulos IK. Severe bilateral central serous chorioretinopathy in a black patient: 16 years follow-up. *Graefe's Arch Clin Exp Ophthalmol.* 2007;245(3):460-463. doi:10.1007/s00417-006-0342-2.
  126. Castro-Correia J, Coutinho MF, Rosas V, Maia J. Long-term follow-up of central serous retinopathy in 150 patients. *Doc Ophthalmol.* 1992;81(4):379-386. doi:10.1007/BF00169099.
  127. van Bussel EM, van der Valk R, Bijlsma WR, La Heij EC. Impact of duration of macula-off retinal detachment on visual outcome. *Retina.* 2014;34(10):1917-1925. doi:10.1097/IAE.0000000000000296.
  128. Zhao M, Célérier I, Bousquet E, et al. Mineralocorticoid receptor is involved in rat and human ocular chorioretinopathy. 2012;122(7):1-8. doi:10.1172/JCI61427DS1.
  129. Bousquet E, Beydoun T, Zhao M, Hassan L, Offret O, Behar-Cohen F. Mineralocorticoid receptor antagonism in the treatment of chronic central serous chorioretinopathy: a pilot study. *Retina.* 2013;33(10):2096-2102. doi:10.1097/IAE.0b013e318297a07a.
  130. Bousquet E, Beydoun T, Rothschild P-R, et al. Spironolactone for nonresolving central serous chorioretinopathy: A Randomized Controlled Crossover Study. *Retina.* 2015;35(12):2505-2515. doi:10.1097/IAE.0000000000000614.
  131. Noma H, Funatsu H, Mimura T, Shimada K. Comparison of the efficacy of intravitreal triamcinolone acetonide for cystoid macular edema with versus without serous retinal detachment in branch retinal vein occlusion: influence on macular sensitivity and morphology. *BMC Ophthalmol.* 2012;12:39. doi:10.1186/1471-2415-12-39.
  132. Ossewaarde-van Norel J, Berg EM, Sijssens KM, Rothova A. Subfoveal serous retinal detachment in patients with uveitic macular edema. *Arch Ophthalmol.* 2011;129(2):158-162. doi:10.1001/archophthalmol.2010.337.
  133. Bouzas EA, Karadimas P, Pournaras CJ, et al. Central serous chorioretinopathy and glucocorticoids. *Surv Ophthalmol.* 2002;47(5):431-448.
  134. Thinda S, Lam K, Park SS. Unintentional secondary exogenous corticosteroid exposure and central serous chorioretinopathy. *Eye (Lond).* January 2015. doi:10.1038/eye.2014.328.
  135. Xu H, Chen M, Forrester J V. Para-inflammation in the aging retina. *Prog Retin Eye Res.*

- 2009;28(5):348-368. doi:10.1016/j.preteyeres.2009.06.001.
136. Klaassen I, Van Noorden CJF, Schlingemann RO. Molecular basis of the inner blood-retinal barrier and its breakdown in diabetic macular edema and other pathological conditions. *Prog Retin Eye Res.* 2013;34:19-48. doi:10.1016/j.preteyeres.2013.02.001.
  137. Zarbin M a. Current concepts in the pathogenesis of age-related macular degeneration. *Arch Ophthalmol.* 2004;122(4):598-614. doi:10.1001/archoph.122.4.598.
  138. Ardeljan D, Chan C-C. Aging is not a disease: distinguishing age-related macular degeneration from aging. *Prog Retin Eye Res.* 2013;37:68-89. doi:10.1016/j.preteyeres.2013.07.003.
  139. Zakir SM, Shukla M, Simi Z-U-R, Ahmad J, Sajid M. Serum cortisol and testosterone levels in idiopathic central serous chorioretinopathy. *Indian J Ophthalmol.* 2009;57(6):419-422. doi:10.4103/0301-4738.57143.
  140. Haimovici R, Rumelt S, Melby J. Endocrine Abnormalities in Patients with Central Serous Chorioretinopathy. 2003;6420(2):698-703. doi:10.1016/S0161-6420(02)01975-9.
  141. Garg SP, Dada T, Talwar D, Biswas NR. Endogenous cortisol profile in patients with central serous chorioretinopathy. *Br J Ophthalmol.* 1997;81(11):962-964.
  142. Ter Heegde F, De Rijk RH, Vinkers CH. The brain mineralocorticoid receptor and stress resilience. *Psychoneuroendocrinology.* 2015;52C:92-110. doi:10.1016/j.psyneuen.2014.10.022.
  143. Hawkins UA, Gomez-Sanchez EP, Gomez-Sanchez CM, Gomez-Sanchez CE. The ubiquitous mineralocorticoid receptor: clinical implications. *Curr Hypertens Rep.* 2012;14(6):573-580. doi:10.1007/s11906-012-0297-0.
  144. Brown NJ. Contribution of aldosterone to cardiovascular and renal inflammation and fibrosis. *Nat Rev Nephrol.* 2013;9(8):459-469. doi:10.1038/nrneph.2013.110.
  145. Young MJ, Rickard AJ. Mineralocorticoid receptors in the heart: lessons from cell-selective transgenic animals. *J Endocrinol.* 2015;224(1):R1-13. doi:10.1530/JOE-14-0471.
  146. Bousquet E, Dhundass M, Lehmann M, et al. Shift work: a risk factor for central serous chorioretinopathy. *Am J Ophthalmol.* 2016. doi:10.1016/j.ajo.2016.02.012.
  147. Goodwin JE, Zhang J, Geller DS. A critical role for vascular smooth muscle in acute glucocorticoid-induced hypertension. *J Am Soc Nephrol JASN.* 2008;19(7):1291-1299. doi:10.1681/ASN.2007080911.
  148. Maberley DA, Yannuzzi LA, Gitter K, et al. Radiation exposure: a new risk factor for idiopathic perifoveal telangiectasis. *Ophthalmology.* 1999;106(12):2248-52-3. doi:10.1016/S0161-6420(99)90523-7.
  149. Loukianou E, Loukianou G. Intravitreal Aflibercept in Recalcitrant Radiation Maculopathy due to External Beam Radiotherapy for Nasopharyngeal Cancer: A First Case Report. *Case Rep Ophthalmol.* 8(1):87-90. doi:10.1159/000456535.
  150. Grossniklaus HE, Kang SJ, Berglin L. Animal models of choroidal and retinal neovascularization. *Prog Retin Eye Res.* 2010;29(6):500-519. doi:10.1016/j.preteyeres.2010.05.003.
  151. Holmes K, Roberts OL, Thomas AM, Cross MJ. Vascular endothelial growth factor receptor-2: structure, function, intracellular signalling and therapeutic inhibition. *Cell Signal.* 2007;19(10):2003-2012. doi:10.1016/j.celsig.2007.05.013.
  152. Karkkainen MJ, Petrova T V. Vascular endothelial growth factor receptors in the regulation of angiogenesis and lymphangiogenesis. *Oncogene.* 2000;19(49):5598-5605. doi:10.1038/sj.onc.1203855.
  153. Senger DR, Galli SJ, Dvorak AM, Perruzzi CA, Harvey VS, Dvorak HF. Tumor cells secrete a vascular permeability factor that promotes accumulation of ascites fluid. *Science.* 1983;219(4587):983-985.
  154. Ribatti D. The crucial role of vascular permeability factor/vascular endothelial growth factor in angiogenesis: a historical review. *Br J Haematol.* 2005;128(3):303-309. doi:10.1111/j.1365-

2141.2004.05291.x.

155. Veikkola T, Jussila L, Makinen T, et al. Signalling via vascular endothelial growth factor receptor-3 is sufficient for lymphangiogenesis in transgenic mice. *EMBO J*. 2001;20(6):1223-1231. doi:10.1093/emboj/20.6.1223.
156. Balaratnasingam C, Dhrami-Gavazi E, McCann J, Ghadiali Q, Freund KB. Aflibercept: a review of its use in the treatment of choroidal neovascularization due to age-related macular degeneration. *Clin Ophthalmol*. 2015;9:2355. doi:10.2147/OPHT.S80040.
157. Yannuzzi LA, Bardal AMC, Freund KB, Chen K-J, Eandi CM, Blodi B. Idiopathic macular telangiectasia. *Arch Ophthalmol*. 2006;124(4):450-460. doi:10.1001/archophth.124.4.450.
158. Cahill M, O'Keefe M, Acheson R, et al. Classification of the spectrum of Coats' disease as subtypes of idiopathic retinal telangiectasis with exudation. *Acta Ophthalmol Scand*. 2001;79(6):596-602.
159. Witmer A. Vascular endothelial growth factors and angiogenesis in eye disease. *Prog Retin Eye Res*. 2003;22(1):1-29. doi:10.1016/S1350-9462(02)00043-5.
160. Gass DM, Blodi BA. Idiopathic Juxtafoveolar Retinal Telangiectasis: Update of Classification and Follow-up Study. *Ophthalmology*. 1993;100(10):1536-1546. doi:10.1016/S0161-6420(93)31447-8.
161. Yannuzzi LA, Bardal AMC, Freund KB, Chen K-J, Eandi CM, Blodi B. Idiopathic Macular Telangiectasia. *Arch Ophthalmol*. 2006;124:450-460.
162. Engelbert M, Chew EY, Yannuzzi LA. Macular Telangiectasia.
163. Charbel Issa P, Gillies MC, Chew EY, et al. Macular telangiectasia type 2. *Prog Retin Eye Res*. 2013;34:49-77. doi:10.1016/j.preteyeres.2012.11.002.
164. Giuliari GP, Sadaka A, Hinkle DM, Simpson ER. Current treatments for radiation retinopathy. *Acta Oncol*. 2011;50(1):6-13. doi:10.3109/0284186X.2010.500299.
165. Patel A V., Lane AM, Morrison MA, et al. Visual Outcomes after Proton Beam Irradiation for Choroidal Melanomas Involving the Fovea. *Ophthalmology*. November 2015. doi:10.1016/j.ophtha.2015.09.031.
166. Horgan N, Shields CL, Mashayekhi A, Shields JA. Classification and treatment of radiation maculopathy. *Curr Opin Ophthalmol*. 2010;21(3):233-238. doi:10.1097/ICU.0b013e3283386687.
167. Reichstein D. Current treatments and preventive strategies for radiation retinopathy. *Curr Opin Ophthalmol*. 2015;26(3):157-166. doi:10.1097/ICU.0000000000000141.
168. Nagiel A, Disorders R, Eye S, Geffen D. A Promising Future for Optical Coherence Tomography Angiography. 2015;133(6):1-2. doi:10.1001/jamaophthalmol.2015.0668.Conflict.
169. Jia Y, Bailey ST, Hwang TS, et al. Quantitative optical coherence tomography angiography of vascular abnormalities in the living human eye. *Proc Natl Acad Sci U S A*. 2015;112(18):E2395-2402. doi:10.1073/pnas.1500185112.
170. Matet A, Daruich A, Zografos L. Radiation Maculopathy After Proton Beam Therapy for Uveal Melanoma: Optical Coherence Tomography Angiography Alterations Influencing Visual Acuity. *Investig Ophthalmology Vis Sci*. 2017;58(10):3851. doi:10.1167/iovs.17-22324.
171. Annear MJ, Bartoe JT, Barker SE, et al. Gene therapy in the second eye of RPE65-deficient dogs improves retinal function. *Gene Ther*. 2011;18(1):53-61. doi:10.1038/gt.2010.111.
172. Ehnes A, Wenner Y, Friedburg C, et al. Optical Coherence Tomography (OCT) Device Independent Intraretinal Layer Segmentation. *Transl Vis Sci Technol*. 2014;3(1):1. doi:10.1167/tvst.3.1.1.
173. Pryds A, Sander B, Larsen M. Characterization of subretinal fluid leakage in central serous chorioretinopathy. *Investig Ophthalmol Vis Sci*. 2010;51(11):5853-5857. doi:10.1167/iovs.09-4830.
174. Gilbert CM, Owens SL, Smith PD, et al. Long-term follow-up of central serous chorioretinopathy. *Br J Ophthalmol*. 1984;68(11):815-820. doi:10.1136/bjo.68.11.815.

175. Ozkaya A, Alkin Z, Ozveren M, Yazici AT, Taskapili M. The time of resolution and the rate of recurrence in acute central serous chorioretinopathy following spontaneous resolution and low-fluence photodynamic therapy: a case-control study. *Eye (Lond)*. 2016;30(7):1005-1010. doi:10.1038/eye.2016.79.
176. Kitzmann AS, Pulido JS, Diehl NN, Hodge DO, Burke JP. The incidence of central serous chorioretinopathy in Olmsted County, Minnesota, 1980-2002. *Ophthalmology*. 2008;115(1):169-173. doi:10.1016/j.ophtha.2007.02.032.
177. Yu J, Jiang C, Shi G, Li L, Xu G. Variable photoreceptor inner and outer segment junction appearance in central serous chorioretinopathy. *Retina*. 2014;34(7):1492-1493. doi:10.1097/IAE.000000000000103.
178. Iacono P, Battaglia PM, Papayannis A, La Spina C, Varano M, Bandello F. Acute central serous chorioretinopathy: a correlation study between fundus autofluorescence and spectral-domain OCT. *Graefes Arch Clin Exp Ophthalmol*. 2015. doi:10.1007/s00417-014-2899-5.
179. Loo R, Scott IU, Flynn HW, et al. Factors associated with reduced visual acuity during long-term follow-up of patients with idiopathic central serous chorioretinopathy. *Retina*.6-11.
180. Matet A, Daruich A, Zola M, Behar-Cohen F. Risk factors for recurrences of central serous chorioretinopathy. *Retina*. May 2017;1. doi:10.1097/IAE.0000000000001729.
181. Yang L, Jonas JB, Wei W. Optical coherence tomography-assisted enhanced depth imaging of central serous chorioretinopathy. *Investig Ophthalmol Vis Sci*. 2013;54(7):4659-4665. doi:10.1167/iovs.12-10991.
182. Dansingani KK, Balaratnasingam C, Naysan J, Freund KB. En face imaging of pachychoroid spectrum disorders with swept-source optical coherence tomography. *Retina*. August 2015. doi:10.1097/IAE.0000000000000742.
183. Costanzo E, Cohen SY, Miere A, et al. Optical Coherence Tomography Angiography in Central Serous Chorioretinopathy. *J Ophthalmol*. 2015;2015:1-10. doi:10.1155/2015/134783.
184. Teussink MM, Breukink MB, van Grinsven MJJP, et al. OCT Angiography Compared to Fluorescein and Indocyanine Green Angiography in Chronic Central Serous Chorioretinopathy. *Investig Ophthalmology Vis Sci*. 2015;56(9):5229. doi:10.1167/iovs.15-17140.
185. Spaide RF. Choriocapillaris Flow Features Follow a Power Law Distribution: Implications for Characterization and Mechanisms of Disease Progression. *Am J Ophthalmol*. 2016. doi:10.1016/j.ajo.2016.07.023.
186. Tittl M, Maar N, Polska E, Weigert G, Stur M, Schmetterer L. Choroidal hemodynamic changes during isometric exercise in patients with inactive central serous chorioretinopathy. *Invest Ophthalmol Vis Sci*. 2005;46(12):4717-4721. doi:10.1167/iovs.05-0268.
187. Saito M, Saito W, Hashimoto Y, et al. Macular choroidal blood flow velocity decreases with regression of acute central serous chorioretinopathy. *Br J Ophthalmol*. 2013;97(6):775-780. doi:10.1136/bjophthalmol-2012-302349.
188. Kitaya N, Nagaoka T, Hikichi T, et al. Features of abnormal choroidal circulation in central serous chorioretinopathy. *Br J Ophthalmol*. 2003;87(6):709-712. doi:10.1136/bjo.87.6.709.
189. Balaratnasingam C, Freund KB, Tan AM, et al. Bullous Variant of Central Serous Chorioretinopathy. *Ophthalmology*. 2016;123(7):1541-1552. doi:10.1016/j.ophtha.2016.03.017.
190. Murakami Y, Notomi S, Hisatomi T, et al. Photoreceptor cell death and rescue in retinal detachment and degenerations. *Prog Retin Eye Res*. 2013. doi:10.1016/j.preteyeres.2013.08.001.
191. Sweigard JH, Matsumoto H, Smith KE, et al. Inhibition of the alternative complement pathway preserves photoreceptors after retinal injury. *Sci Transl Med*. 2015;7(297):297ra116. doi:10.1126/scitranslmed.aab1482.
192. Miki A, Kondo N, Yanagisawa S, Bessho H, Honda S, Negi A. Common variants in the complement factor H gene confer genetic susceptibility to central serous chorioretinopathy. *Ophthalmology*. 2014;121(5):1067-1072. doi:10.1016/j.ophtha.2013.11.020.
193. de Jong EK, Breukink MB, Schellevis RL, et al. Chronic Central Serous Chorioretinopathy Is

- Associated with Genetic Variants Implicated in Age-Related Macular Degeneration. *Ophthalmology*. November 2014. doi:10.1016/j.ophtha.2014.09.026.
194. Spaide RF, Fujimoto JG, Waheed NK. Image artifacts in optical coherence tomography angiography. *Retina*. 2015;35(11):2163-2180. doi:10.1097/IAE.0000000000000765.
  195. Say EAT, Ferenczy S, Magrath GN, Samara WA, Khoo CTL, Shields CL. Image quality and artifacts on optical coherence tomography angiography. *Retina*. November 2016:1. doi:10.1097/IAE.0000000000001414.
  196. Duncan JL. Visual Consequences of Delivering Therapies to the Subretinal Space.
  197. dell'Omo R, Viggiano D, Giorgio D, et al. Restoration of Foveal Thickness and Architecture After Macula-Off Retinal Detachment Repair. *Invest Ophthalmol Vis Sci*. 2015;56(2):1040-1050. doi:10.1167/iovs.14-15633.
  198. Guérin CJ, Lewis GP, Fisher SK, Anderson DH. Recovery of photoreceptor outer segment length and analysis of membrane assembly rates in regenerating primate photoreceptor outer segments. *Invest Ophthalmol Vis Sci*. 1993;34(1):175-183.
  199. Simunovic MP, BChir M, Xue K, Jolly JK, MacLaren RE. Structural and Functional Recovery Following Limited Iatrogenic Macular Detachment for Retinal Gene Therapy. doi:10.1001/jamaophthalmol.2016.5630.
  200. Pierce EA, Bennett J. The Status of RPE65 Gene Therapy Trials: Safety and Efficacy. *Cold Spring Harb Perspect Med*. January 2015. doi:10.1101/cshperspect.a017285.
  201. MacLachlan TK, Lukason M, Collins M, et al. Preclinical Safety Evaluation of AAV2-sFLT01—A Gene Therapy for Age-related Macular Degeneration. *Mol Ther*. 2011. doi:10.1038/mt.2010.258.
  202. van Adel BA, Kostic C, Déglon N, Ball AK, Arsenijevic Y. Delivery of ciliary neurotrophic factor via lentiviral-mediated transfer protects axotomized retinal ganglion cells for an extended period of time. *Hum Gene Ther*. 2003;14(2):103-115. doi:10.1089/104303403321070801.
  203. Touchard E, Berdugo M, Bigey P, et al. Suprachoroidal Electrotransfer: A Nonviral Gene Delivery Method to Transfect the Choroid and the Retina Without Detaching the Retina. 2012. doi:10.1038/mt.2011.304.
  204. Ku CA, Pennesi ME. Retinal Gene Therapy: Current Progress and Future Prospects. *Expert Rev Ophthalmol*. 2015;10(3):281-299. doi:10.1586/17469899.2015.1035711.
  205. Willett K, Bennett J. Immunology of AAV-Mediated Gene Transfer in the Eye. *Front Immunol*. 2013;4:261. doi:10.3389/fimmu.2013.00261.
  206. Agrawal R, Chhablani J, Tan K-A, Shah S, Sarvaiya C, Banker A. Choroidal Vascularity Index in Central Serous Chorioretinopathy. *Retina*. 2016:1-6. doi:10.1097/IAE.0000000000001040.
  207. Agrawal R, Salman M, Tan K-A, et al. Choroidal Vascularity Index (CVI)—A Novel Optical Coherence Tomography Parameter for Monitoring Patients with Panuveitis? *PLoS One*. 2016;11(1):e0146344. doi:10.1371/journal.pone.0146344.
  208. Zhao M, Célérier I, Bousquet E, et al. Mineralocorticoid receptor is involved in rat and human ocular chorioretinopathy. *J Clin Invest*. 2012;122(7):2672-2679. doi:10.1172/JCI61427.
  209. van Dijk EHC, Schellevis RL, van Bergen MGJM, et al. Association of a Haplotype in the NR3C2 Gene, Encoding the Mineralocorticoid Receptor, With Chronic Central Serous Chorioretinopathy. *JAMA Ophthalmol*. 2017;135(5):446-451. doi:10.1001/jamaophthalmol.2017.0245.
  210. Latouche C, El Moghrabi S, Messaoudi S, et al. Neutrophil gelatinase-associated lipocalin is a novel mineralocorticoid target in the cardiovascular system. *Hypertension*. 2012. doi:10.1161/HYPERTENSIONAHA.111.187872.
  211. Tarjus A, Martinez-Martinez E, Amador C, et al. Neutrophil Gelatinase-Associated Lipocalin, a Novel Mineralocorticoid Biotarget, Mediates Vascular Profibrotic Effects of Mineralocorticoids Novelty and Significance. *Hypertension*. 2015;66(1):158-166. doi:10.1161/HYPERTENSIONAHA.115.05431.

212. Matet A, Daruich A, Dirani A, Ambresin A, Behar-Cohen F. Macular telangiectasia type 1: capillary density and microvascular abnormalities assessed by optical coherence tomography angiography. *Am J Ophthalmol*. April 2016. doi:10.1016/j.ajo.2016.04.005.

## ARTICLES

[1] Preclinical safety evaluation of lentiviral LV-RPE65 gene therapy after subretinal delivery in non-human primates. *Transl Res*, 2017

Matet A, Kostic C, Bemelmans AP, Moulin AP, Rosolen S, Martin S, Mavilio F, Amirjanians V, Stieger K, Lorenz B, Behar-Cohen F, Arsenijevic Y<sup>97</sup>

doi: 10.1016/j.trsl.2017.06.012.

Contribution of PhD candidate:

- Animal experiments: treatment procedure, animal follow-up, ocular examination and imaging, animal sacrifice
- Ocular tissue preparation and immunohistochemistry
- Analysis of multimodal imaging
- Processing and analysis of OCT data
- Drafting the manuscript



# ORIGINAL ARTICLES

## Evaluation of tolerance to lentiviral LV-RPE65 gene therapy vector after subretinal delivery in non-human primates



**ALEXANDRE MATET, CORINNE KOSTIC, ALEXIS-PIERRE BEMELMANS, ALEXANDRE MOULIN, SERGE G. ROSOLEN, SAMIA MARTIN, FULVIO MAVILIO, VAZRIK AMIRJANIANS, KNUT STIEGER, BIRGIT LORENZ, FRANCINE BEHAR-COHEN, and YVAN ARSENIJEVIC**

LAUSANNE, SWITZERLAND; FONTENAY-AUX-ROSES, ASNIÈRES, PARIS, EVRY, FRANCE; AND GIESSEN, GERMANY

Several approaches have been developed for gene therapy in RPE65-related Leber congenital amaurosis. To date, strategies that have reached the clinical stages rely on adeno-associated viral vectors and two of them documented limited long-term effect. We have developed a lentiviral-based strategy of RPE65 gene transfer that efficiently restored protein expression and cone function in RPE65-deficient mice. In this study, we evaluated the ocular and systemic tolerances of this lentiviral-based therapy (LV-RPE65) on healthy nonhuman primates (NHPs), without adjuvant systemic anti-inflammatory prophylaxis. For the first time, we describe the early kinetics of retinal detachment at 2, 4, and 7 days after subretinal injection using multimodal imaging in 5 NHPs. We revealed prolonged reattachment times in LV-RPE65-injected eyes compared to vehicle-injected eyes. Low- (n = 2) and high-dose (n = 2) LV-RPE65-injected eyes presented a reduction of the outer nuclear and photoreceptor outer segment layer thickness in the macula, that was more pronounced than in vehicle-injected eyes (n = 4). All LV-RPE65-injected eyes showed an initial perivascular reaction that resolved spontaneously within 14 days. Despite foveal structural changes, full-field electroretinography indicated that the overall retinal function was preserved over time and immunohistochemistry identified no difference in glial, microglial, or leucocyte ocular activation between

From the Unit of Retinal Degeneration and Regeneration, Department of Ophthalmology, University of Lausanne, Jules-Gonin Eye Hospital, Fondation Asile des Aveugles, Lausanne, Switzerland; Commissariat à l’Energie Atomique et aux Energies Alternatives (CEA), Direction de la Recherche Fondamentale (DRF), Institut d’Imagerie Biomédicale (I2BM), Molecular Imaging Research Center (MIRCen), Fontenay-aux-Roses, France; Centre National de la Recherche Scientifique (CNRS), Université Paris-Sud, Université Paris-Saclay, UMR 9199, Neurodegenerative Diseases Laboratory, Fontenay-aux-Roses, France; Pathology Unit, Department of Ophthalmology, University of Lausanne, Jules-Gonin Eye Hospital, Fondation Asile des Aveugles, Lausanne, Switzerland; Clinique Vétérinaire Voltaire, Asnières, France; UPMC Univ Paris 06, UMR\_S 968, Centre de Recherche Institut de la Vision, Paris, France; Genethon, Evry, France; Department of Ophthalmology, Justus-Liebig-University Giessen, Giessen, Germany; Inserm U1138, Team 17, From Physiopathology of Ocular Diseases to

Clinical Development, Université Paris Descartes Sorbonne Paris Cité, Centre de Recherche des Cordeliers, Paris, France.

Submitted for publication January 19, 2017; revision submitted April 30, 2017; accepted for publication June 30, 2017.

Reprint requests: Yvan Arsenijevic, Unit of Retinal Degeneration and Regeneration, Hôpital Ophtalmique Jules-Gonin, University of Lausanne, Avenue de France 15, Case Postale 5143, 1002 Lausanne, Switzerland; e-mail: [yvan.arsenijevic@fa2.ch](mailto:yvan.arsenijevic@fa2.ch) or Corinne Kostic, Group of Retinal Disorder Research, Hôpital Ophtalmique Jules-Gonin, University of Lausanne, Avenue de France 15, Case Postale 5143, 1002 Lausanne, Switzerland; e-mail: [corinne.kostic@fa2.ch](mailto:corinne.kostic@fa2.ch).

1931-5244/\$ - see front matter

© 2017 The Authors. Published by Elsevier Inc. This is an open access article under the CC BY-NC-ND license (<http://creativecommons.org/licenses/by-nc-nd/4.0/>).

<http://dx.doi.org/10.1016/j.trsl.2017.06.012>

**low-dose, high-dose, and vehicle-injected eyes. Moreover, LV-RPE65-injected animals did not show signs of vector shedding or extraocular targeting, confirming the safe ocular restriction of the vector. Our results evidence a limited ocular tolerance to LV-RPE65 after subretinal injection without adjuvant anti-inflammatory prophylaxis, with complications linked to this route of administration necessitating to block this transient inflammatory event. (Translational Research 2017;188:40–57)**

**Abbreviations:** NHP = nonhuman primates; LE = left eye; RE = right eye; IOP = intraocular pressure; EZ = ellipsoid zone; ONL = outer nuclear layer; ERG = electroretinogram

## AT A GLANCE COMMENTARY

Matet A, et al.

### Background

Leber congenital amaurosis, a severe and early-onset form of retinitis pigmentosa is historically the first eye disease to benefit from gene therapy, with several groups worldwide developing AAV-based gene replacement approaches for *RPE65*, one of the causative genes. However, some clinical trials showed limited safety and only partial recovery which could be linked to the subretinal surgical route, or to subtherapeutic protein levels. Simultaneously, our group has developed a HIV-1–derived lentivirus-based strategy (LV-RPE65), using the high transduction capability of this vector to target epithelia such as the retinal pigment epithelium, which expresses the RPE65 enzyme. LV-RPE65 can restore photoreceptor integrity and function, as previously demonstrated by our group in 2 rodent models of RPE65 deficiency. In this study, we have pursued the translational development of LV-RPE65, to evaluate the ocular and systemic tolerance to LV-RPE65 after subretinal injection in 5 nonhuman primates without antiinflammatory prophylaxis.

### Translational Significance

In the present study, the absence of systemic LV-RPE65 vector particle shedding after subretinal injection in body fluids, or of vector genome integration in various organs is promising for the ocular use of lentiviral vector. Nevertheless, a transient perivascular retinal reaction occurred at very early stages (2 days) following vector administration, and a thinning of the photoreceptor layer at the macula level was observed in all groups, including vehicle-treated animals. No other major ocular adverse event was recorded, except in one eye that inadvertently received intraocular doses due to a leak into the vitreous cavity. Importantly, we

were not able to find any other preclinical study in the literature reporting ocular and retinal monitoring at early time points after subretinal gene therapy administration. Our report is thus the first to give insight into these early events and may contribute to elucidate several limitations of the subretinal route approach. These observations contribute to optimizing the translational process of retinal gene therapy, from both the surgical and the gene transfer perspectives, and highlight the necessity to improve lentiviral vector tolerance by antiinflammatory pretreatment.

## INTRODUCTION

Retinal dystrophies, especially those with childhood onset, are a lifetime burden for affected individuals, with no available treatments. Recently, retinal gene therapy based on subtypes of adeno-associated virus (AAV)<sup>1–6</sup> or lentivirus-derived vectors<sup>7–10</sup> has made tremendous advances to correct several monogenic diseases in rodent and large animal models providing the ground to design first clinical trials and translate this technology in humans.<sup>11</sup> The first gene augmentation strategy in an inherited retinal disorder was developed clinically for patients with Leber congenital amaurosis due to RPE65 deficiency.<sup>12</sup> RPE65 is a retinal pigment epithelium (RPE)–expressed enzyme with isomerase activity, which plays a key role in the visual cycle by recycling chromophores necessary for the phototransduction.<sup>13–15</sup> Three main clinical trials initiated in the US<sup>16,17</sup> and UK<sup>18</sup> based on the AAV2/2-vector approach demonstrated a limited safety with partial, and in 2 trials transitory, visual function restoration. In one trial, inflammation induced by AAV2/2 vector at the highest dose required redesigning of the vector using an AAV5 capsid.<sup>19</sup> In addition, ongoing trials are conducted in Israel with the AAV2/2 vector developed by the group of Hauswirth,<sup>20</sup> and in France with the AAV2/4 vector.<sup>21</sup> The major visual improvements were attested using

dark-adapted perimetry,<sup>22,23</sup> that identified an increased retinal sensitivity in the treated area of certain patients. Functional magnetic resonance imaging of the visual cortex showed contrast discrimination enhancement, for a subset of patients<sup>24</sup> and mobility testing demonstrated the ability to better navigate after treatment in certain patients.<sup>22,25</sup> Differences in the effect of gene therapy between these different trials, or between treated patients, results probably from multiple factors, including the timing of intervention during disease course, surgical delivery techniques (administered volume, flow rate, procedure), vector designs, and patient genetic backgrounds. Moreover, subjective parameters used to reveal the effect of gene therapy such as visual acuity or retinal sensitivity testing might be biased, despite efficient viral transduction, because of cortical amblyopia following long-standing visual loss in early childhood.

The major hurdle experienced in these trials was that subretinal injection under the macula induced, in several patients, retinal thinning and/or foveal morphologic changes, which were not foreseeable and may have contributed to the lack of central vision restoration.<sup>22,26</sup> Because inclusion of control subjects receiving the buffer solution subretinally was not planned in these studies for obvious ethical reasons, it is not clear whether the surgery by itself is deleterious or whether the vector contributes to these unexpected retinal alterations.

In addition, despite improvements in visual sensitivity, the degenerative rate of the treated eye remained similar to the nontreated eye,<sup>22,23</sup> indicating either an unstoppable disease progression, inappropriate treatment delivery (timing of treatment, surgical techniques), or an insufficient vector efficacy.<sup>19</sup> The available amount of chromophore is determinant for photoreceptor function and survival, and consequently RPE65 expression levels are correlated to retinal function and to the rate of retinal degeneration in animal models. For instance, in the *Rpe65*<sup>R91W/R91W</sup> mouse model, where the amount of RPE65 is decreased by around 90%, electroretinography showed a 3-log reduction in retinal sensitivity at 1-month of age, as compared with wild-type mice, which is correlated to the level of RPE65 protein.<sup>27</sup> In human, no electroretinogram (ERG) responses were observed after *RPE65* gene transfer, whereas similar doses in dogs deficient for the same gene led to clinical responses, such as recovery of retinal activity and vision-guided mobility.<sup>21,28</sup> To note, dogs injected with suboptimal doses also showed improvement of visual behavior without ERG amelioration.<sup>22,29</sup> These discrepancies between clinical observations and animal studies raised concerns over viral vector efficacy in humans. Taking into account the data generated by

Bainbridge et al. (2015), a 200-fold increase in gene expression could be necessary in humans to reach similar therapeutic effects as in canine models.<sup>19,22</sup>

In this context, the development of optimized vectors is a necessary step to improve gene expression after gene transfer. We previously investigated the efficacy of lentiviral vectors (LVs) for RPE65 gene transfer in rodent models, and showed the rescue of 100% of cones in the treated area of *Rpe65* knock-out mice<sup>30</sup> and the reactivation of cone cellular function during the course of degeneration in *Rpe65*<sup>R91W/R91W</sup> mice,<sup>31</sup> an effect not reported so far. To further progress toward the clinical application of LVs for RPE65 deficiency, we have evaluated a GMP (Good Manufacturing Practice)-like production of an LV expressing the hRPE65 gene under the hRPE65 promoter,<sup>30</sup> injected subretinally into the eyes of nonhuman primates (NHPs). No systemic adjuvant anti-inflammatory prophylaxis was administered, contrary to other safety studies performed in large animals,<sup>21,28,32-34</sup> to detect potential side effects not observed in rodents that may occur when translating this gene therapy to primates.

The aim of this study was to evaluate the ocular and systemic safety of this LV following subretinal administration, in terms of retinal structure, retinal function, and systemic biodistribution.

## METHODS

**Animals and study design.** This safety study on 5 naïve female *Macaca fascicularis* (3–6 years old), adhered to the ARVO Statement for the Use of Animals in Ophthalmic and Vision Research and obtained an institutional permission from the French Ministry of Agriculture after evaluation by the local ethical committee (2015062915001228v1). All procedures were performed in an approved user establishment (agreement number 92-032-02), in compliance with the European directive 2010/63/UE and French regulations. Animals were socially housed, had access to standard certified commercial primate food (Altromin, Genestil, Royaucourt, France) and processed municipal tap water, with food supplements such as fresh fruits. Room temperature was maintained at 20°C–24°C, with 55 ± 10% humidity and 12/12 light-dark cycle. Psychological and environmental enrichment was provided. Animals were regularly checked for clinical signs or other changes by caretakers and examined by the veterinary staff when needed.

To reduce the number of animals used in the study, and according to existing reports indicating an absence of systemic inflammatory reaction following

**Table I.** Description of eyes receiving the LV-RPE65 lentiviral vector or the vehicle (TSSM), in 5 female *Macaca fascicularis*

Monkey ID	Eye	Group	Time of sacrifice	Comments
1A	RE	TSSM	30 d after RE/LE injection	Injected same day as RE
	LE	LV-RPE65 dose 1		
1B	RE	LV-RPE65 dose 1	30 d after RE injection	
	LE	-		
2A	RE	TSSM	90 d after LE injection	Injected 30 d after RE
	LE	LV-RPE65 dose 2		
2B	RE	TSSM	90 d after LE injection	Injected 30 d after RE (1 accidental intravitreal dose + 1 subretinal dose)
	LE	LV-RPE65 dose 2		
C	RE	TSSM	90 d after RE injection	
	LE	-		

Abbreviations: LE, left eye; RE, right eye.

subretinal injection of TSSM, 3 NHPs received the LV solution (LV-RPE65) in one eye and the vehicle (TSSM) in the other eye. The fourth NHP received LV-RPE65 only in one eye and the fifth NHP received the vehicle only in one eye, this latter serving as negative control for the systemic biodistribution study (Table I). Two NHPs received a dose 1 of LV-RPE65 solution ( $2.8 \times 10^5$  IU in 100  $\mu$ L; animals 1A and 1B), estimated to yield approximately one infectious particle per RPE cell in the detached retinal area and 2 other NHPs received LV-RPE65 at dose 2 =  $10 \times$  dose 1 ( $2.8 \times 10^6$  IU in 100  $\mu$ L; animals 2A and 2B). After the last clinical evaluation time point corresponding to the date of scheduled death, animals were sacrificed by intravenous injection of sodium pentobarbital and eyes and other organs were sampled.

**Lentiviral vector production.** The LV-RPE65 LV solution used in this study is a GMP-like production of a vector whose recombinant genome is similar to the one evaluated previously in RPE65-deficient mice.<sup>30,31,35</sup> Briefly, the LV-RPE65 is an integrative, third-generation, replication-defective, self-inactivating human immunodeficiency virus (HIV)-1-derived LV, with a mutated Woodchuck hepatitis virus Posttranscriptional Regulatory Element (WPRE) sequence devoid of promoter activities or open-reading frames.<sup>36</sup> It contains the R0.8 promoter (800 bp of the human RPE65 promoter)<sup>28,37</sup> which drives directly the expression of the RPE65 cDNA (without introns). For this study, we used the human RPE65 cDNA, while the mouse RPE65 cDNA was used previously to demonstrate vector efficacy in RPE65 mouse models.<sup>30,31,35</sup>

The RPE65 LV (LV-RPE65) was produced by transient transfection of suspended HEK293 T cells in a serum-free media (customized F17 medium, Invitrogen, Carlsbad, Calif), in a 10-L glass bioreactor

(Biostat B-DCU, Sartorius, Göttingen, Germany). Briefly, LV-RPE65 was produced by transient 4-plasmid transfection with polyethylenimine (PEIpro, Polyplus-transfection, Illkirch-Graffenstaden, France) as transfection reagent. To enhance viral production, sodium butyrate was added 24 hours after transfection at a final concentration of 10 mM. To remove contaminating DNA a benzonase/Dnase solution (50 U/mL) was added 24 hours after transfection in the culture media. The cell supernatant was harvested 48-hour after transfection and filtered through 20/3/0.45- $\mu$ m filters to discard cell debris and purified by following pre-GMP guidelines. The downstream purification process included an ion exchange chromatography, a concentration using a tangential flow filtration in a hollow fiber with 750-kDa cutoff (GE Healthcare, Little Chalfont, UK) and a final formulation in TSSM buffer (tromethamine 20 mM, NaCl 100 mM, sucrose 10 mg/mL, and mannitol 10 mg/mL).

**Subretinal administration of LV or vehicle.** Surgical procedures were performed after an overnight fasting period under general anesthesia with tracheal intubation and maintenance of spontaneous breathing. Anesthesia was induced by intramuscular ketamine chlorhydrate (100 mg/ml; 0.4-0.8 ml) and xylazine (20 mg/ml; 0.1-0.15 ml), followed by continuous intravenous propofol infusion (10 mg/ml; 1 ml then 3-5 ml/h).

All surgeries were performed by an experienced vitreoretinal surgeon (FBC) using a 3-port, sutureless pars plana vitreoretinal surgery system with valved 25-gauge trocars (Constellation, Alcon Laboratories, Inc, Fort Worth, Tex), after pupil dilation with tropicamide 1% and double povidone iodine disinfection of periocular skin, eyelids, and conjunctiva. The infusion line was placed inferotemporally, the left superior port was used for the light fiber and the right superior port for the injection cannula. A 41-gauge 'De Juan'

Cannula (Synergetics, Inc, O'Fallon, Mo) was used for subretinal injections. To minimize dead volume, it was connected via a custom low-caliber line to a 100- $\mu$ L Hamilton Syringe (Sigma-Aldrich, St. Louis, Mo). Subretinal injections were performed at a site superior to the macula and adjacent to the superior arcade to obtain a macular detachment. No prophylactic systemic anti-inflammatory treatment was administered before or at the time of the procedure. After injections, eyes received a single application of dexamethasone/oxytetracycline ointment. In one case of intense intraocular inflammation during the first postoperative week, anti-inflammatory treatment by intravenous or intramuscular methylprednisolone 1 mg/kg was administered daily during 3 days.

**Clinical evaluation and multimodal retinal imaging.** At each clinical evaluation time-point, anesthesia was performed similarly as for surgical procedures. Urine ( $\sim$ 150  $\mu$ L), venous blood ( $\sim$ 150  $\mu$ L), and tears ( $\sim$ 20–50  $\mu$ L) were sampled for viral particle shedding assays at days 0, 2, 4, 7, 14, and 28 in all animals, and additionally at day 90 for animals 2A, 2B, and C. Intraocular pressure (IOP) was measured using the iCare rebound tonometer (Icare Finland Oy, Vantaa, Finland). After pupil dilation with tropicamide 1%, the degree of intraocular inflammation was assessed by a trained ophthalmologist by grading the density of cells in the anterior chamber and vitreous in a  $1 \times 1$ -mm focused slit-lamp beam with  $25 \times$  magnification: 0 (no cells), 1+ (5–10 cells), 2+ (10–25 cells), 3+ (25–50 cells), and 4+ (>50 cells).

The fundus was assessed by indirect fundoscopy and fundus color photograph with the Smartscope camera (Optomed, Oy, Oulu, Finland). Optical coherence tomography (OCT), infrared reflectance, short-wavelength autofluorescence, and blue reflectance imaging were performed on Spectralis (Heidelberg Engineering, Heidelberg, Germany). If needed, fluorescein and indocyanine green angiography were additionally performed using Spectralis.

**Optical coherence tomography analysis.** Serial horizontal and vertical 30-degree OCT sections acquired at the level of the fovea were processed using the automated layer segmentation tool of the Spectralis software (Heidelberg Eye Explorer, version 1.9.10.0) to obtain the layer thickness profiles for the total neurosensory retina (from internal limiting membrane to RPE), the outer nuclear layer (ONL, from its interface with the outer plexiform layer to the outer limiting membrane, OLM), and the photoreceptor outer segments–RPE complex (POS + RPE, from OLM to RPE). In each scan, the mean thickness corresponding to the detached area of the retina was extracted and calculated using a custom algorithm on MATLAB

(version 2015b, MathWorks, Natick, Mass). At each time point, the mean layer thickness was estimated within the detached area by averaging the thickness obtained from the horizontal and vertical OCT scans.

An additional segmentation of retinal layers was performed using the custom-made DiOCTA software for OCT raw data analysis as described previously,<sup>38</sup> over an identical area within the detached retina in all eyes. This 1-mm-diameter circular area was located 1.1 mm superior and 2.2 mm nasal to the fovea, using as horizontal reference a straight line from the optic disc center to the fovea (Supplementary Fig 1). The distance between the injection site and this area was at least 3 disc diameters.

**Electrophysiology.** The ERG recordings were performed in all animals 1 week before the surgical procedures (baseline), 16 days and 30 days after the procedure, and additionally 90 days after the procedure in animals 2A, 2B, and C. Anesthesia with tracheal intubation and spontaneous breathing was obtained by intramuscular ketamine chlorhydrate and intravenous medetomidine hydrochloride administrations. Animals were prepared and recorded in a dim light room as previously described.<sup>39,40</sup> A 10.2.55 version Visiosystem (Siem Bio-Médicale, Nîmes, France) was used to generate the flash stimuli, as well as to record and analyze the ERG responses. Binocular full-field ERGs were elicited with 2 photostimulators (source: achromatic LEDs) for background conditions and flash stimulations (maximum intensity: 1.9 log cds/m<sup>2</sup>). First, the cone system was tested in photopic conditions against a bright background (25 cd.m<sup>-2</sup>) aimed at desensitizing the rod system during 10 minutes. Photopic responses were obtained with 9 decreasing intensities of a series of 15 white LED bright flashes stimuli (from 1.90 log cd.s.m<sup>-2</sup> to  $-0.80$  log cd.s.m<sup>-2</sup>) delivered at 1.3 Hz (interstimuli interval of 769 ms) to determine the “ $I_{\max}$ ” intensity corresponding to the maximum b-wave amplitude ( $V_{\max}$ ) observed at the saturation point of the luminance curve (maximum cone system response).<sup>41,42</sup> Following determination of the  $I_{\max}$  at each time point, the flicker ERG responses were obtained with white flash stimuli of  $I_{\max}$  intensity delivered at 30 Hz during at least 15 seconds. Then the light was switched off and the rod system tested in scotopic conditions. After 20 minutes of dark adaptation, scotopic responses were obtained in dark conditions with an average of 5 dim light flashes (intensity:  $-1.1$  log cd.s.m<sup>-2</sup>) delivered at 0.1 Hz temporal frequency, corresponding to 10-second interstimuli intervals. Two minutes after the last scotopic flash, in the same scotopic conditions, the combined rod-cone response was elicited with a unique  $I_{\max}$  white flash.

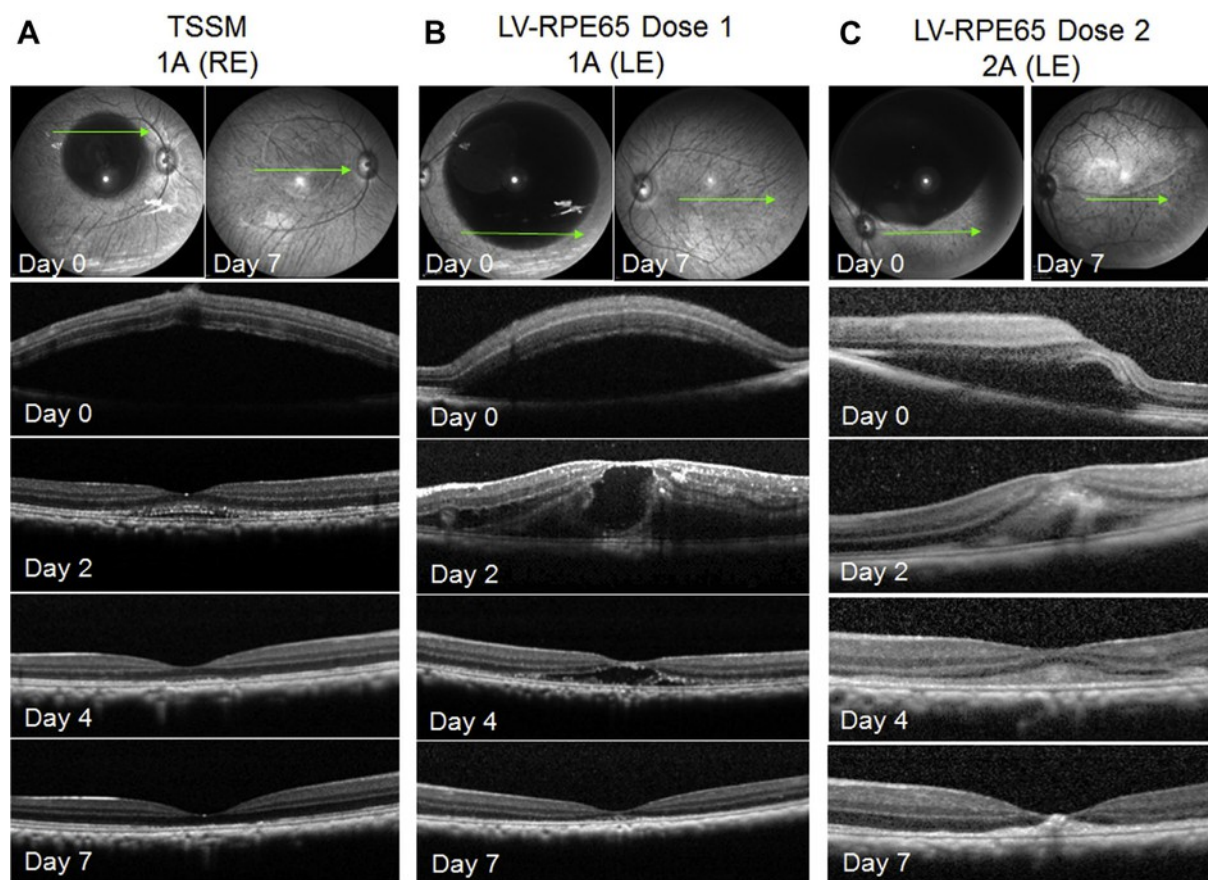


**Fig 1.** Course of progressive retinal reattachment after subretinal administration of vehicle or lentiviral vector preparation. In 3 representative eyes receiving the vehicle (TSSM, **A**), the LV-RPE65 lentiviral vector at dose 1 (**B**) or dose 2 (**C**), the upper panel shows infrared reflectance images immediately (left) and 7 days (right) after injection. Serial optical coherence tomography of the macula (green arrows) performed immediately and at days 2, 4, and 7 after administration show a progressive retinal reattachment. From the vehicle-injected eye to dose 1– and dose 2–injected eyes, there was an increasing reattachment delay and an increasing degree of early outer retinal alterations. LE, left eye; RE, right eye.

**Assessment of shedding and distribution of LV particles.** Shedding of lentiviral particles in body fluids (urine, blood, and tears) after injection was evaluated after RNA extraction of each fluid sample (NucleoSpin RNA Virus Kit, Macherey-Nagel, Düren, Germany) and storage at  $-80^{\circ}\text{C}$ . Lentiviral particles were quantified by quantitative reverse transcriptase-polymerase chain reaction (qRT-PCR) targeting specific sequences of the lentiviral genome. Briefly, for each sample, 400 ng RNA were subjected to DNase digestion and reverse transcribed using SuperScript VILO cDNA synthesis kit (Life Technologies, Carlsbad, Calif) according to the manufacturer's instructions. The targeted transgene sequence was then amplified using iTaq universal SYBR Green Supermix on a CFX384 wells thermocycler (Biorad, Marnes-la-Coquette, France) with the following primers: forward primer, 5'-ATCCCTGTACCTTTCATGG-3'; reverse primer,

5'-TGGGAATAAATGGCGGTAAG-3' designed with Primer3 version 2.3.7 (<http://sourceforge.net/projects/primer3>). Samples and standard points were tested in duplicate.

The possible integration of lentiviral genome was assessed on genomic DNA extracted from flash frozen organ biopsies using the DNeasy blood and tissue kit (Qiagen, Hilden, Germany). DNA samples were stored at  $-20^{\circ}\text{C}$  and processed for quantitative PCR targeting the human RPE65 mRNA sequence using the primer pair described above.

**Ocular immunohistochemistry study.** Enucleated eyes were fixed in 4% paraformaldehyde immediately after scheduled death procedures for 1 hour, then preserved in 1% paraformaldehyde, until they were equilibrated overnight in sucrose 30% and embedded in albumin from hen egg white (Fluka, Buchs, Switzerland). Sixteen- $\mu\text{m}$  cryosections were obtained

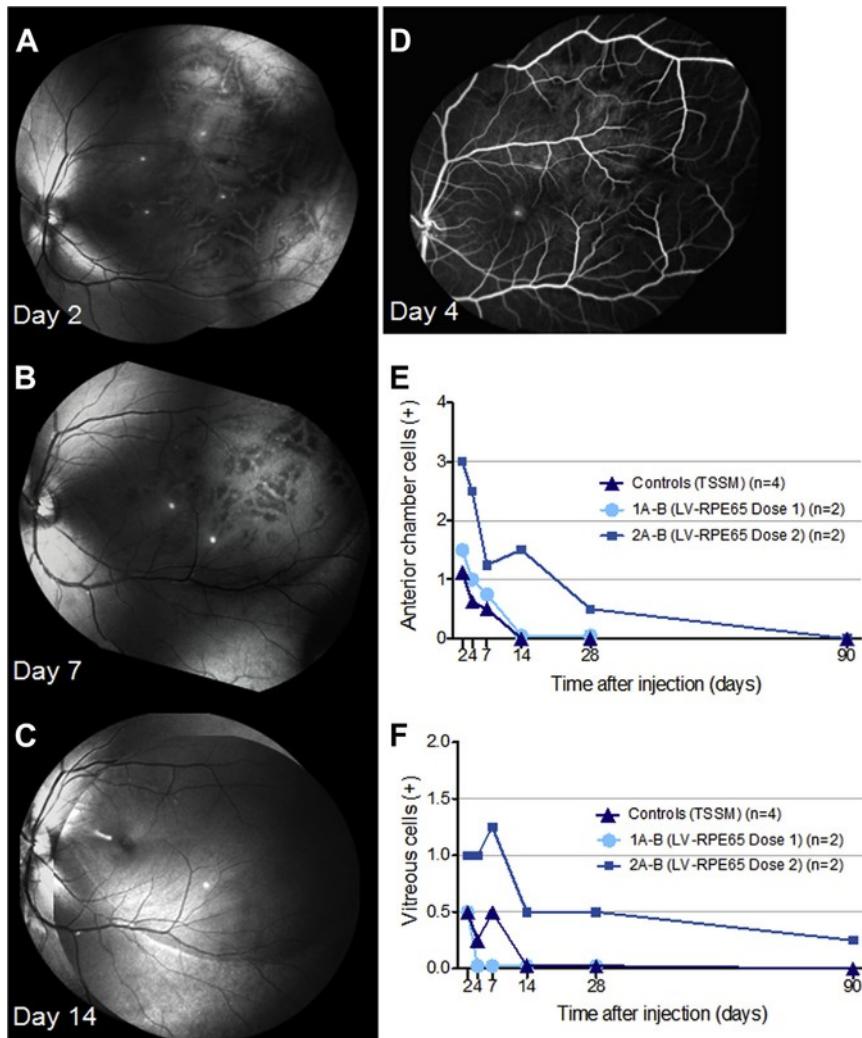


**Fig 2.** Assessment of ocular and retinal inflammation after LV-RPE65 subretinal injection. In (A) to (C) is displayed the Fundus blue reflectance imaging from the left eye of animal 1A, 2 days after the subretinal delivery of dose 1 LV-RPE65. (A) shows an early vasculitis-like perivenular reaction with progressive fading by day 7 (B) and resolution by day 14 (C). Fluorescein angiography in (D) performed at day 4 after administration did not reveal any active vasculitis. Anterior chamber cell count (E) showed a transient mild inflammation in TSSM- and dose 1-injected eyes and a more intense reaction in dose 2-injected eyes that resolved progressively over the course of follow-up. Similarly, vitreous cell count (F) showed a transient mild inflammation in TSSM- and dose 1-injected eyes and a moderately intense inflammation in dose 2-injected eyes that also resolved progressively over the course of follow-up. LE, left eye; RE, right eye.

from the temporal periphery to the optic nerve head. Immunohistochemistry was performed on macular and extramacular sections containing the injected area with antibodies directed against CD45 (#M0701, Dako, Zug, Switzerland), glial fibrillary acid protein (GFAP, #G3893, Sigma, Buchs, Switzerland), vimentin (#MA5-11883, Thermofischer Rockford, Ill), Iba-1 (#019-19741, Wako, Neuss, Germany), and M-Op sin (#AB5405, Chemicon, Temecula, Calif) which were revealed with the appropriate secondary antibodies coupled with

Alexa Fluor488 (Molecular Probes, Eugene, Ore). Cryosections were also processed for hematoxylin-eosin stain.

**Organ histology.** Organ biopsies from inferior eyelids, right/left optic nerves, right/left geniculate bodies, right/left visual cortex, heart, liver, right/left lung, right/left ovary, right/left kidney, and right/left mandibular lymph nodes were obtained after sacrifice and transferred into formalin. After conventional tissue processing, evaluation for macroscopic/microscopic morphologic alterations and signs of inflammation

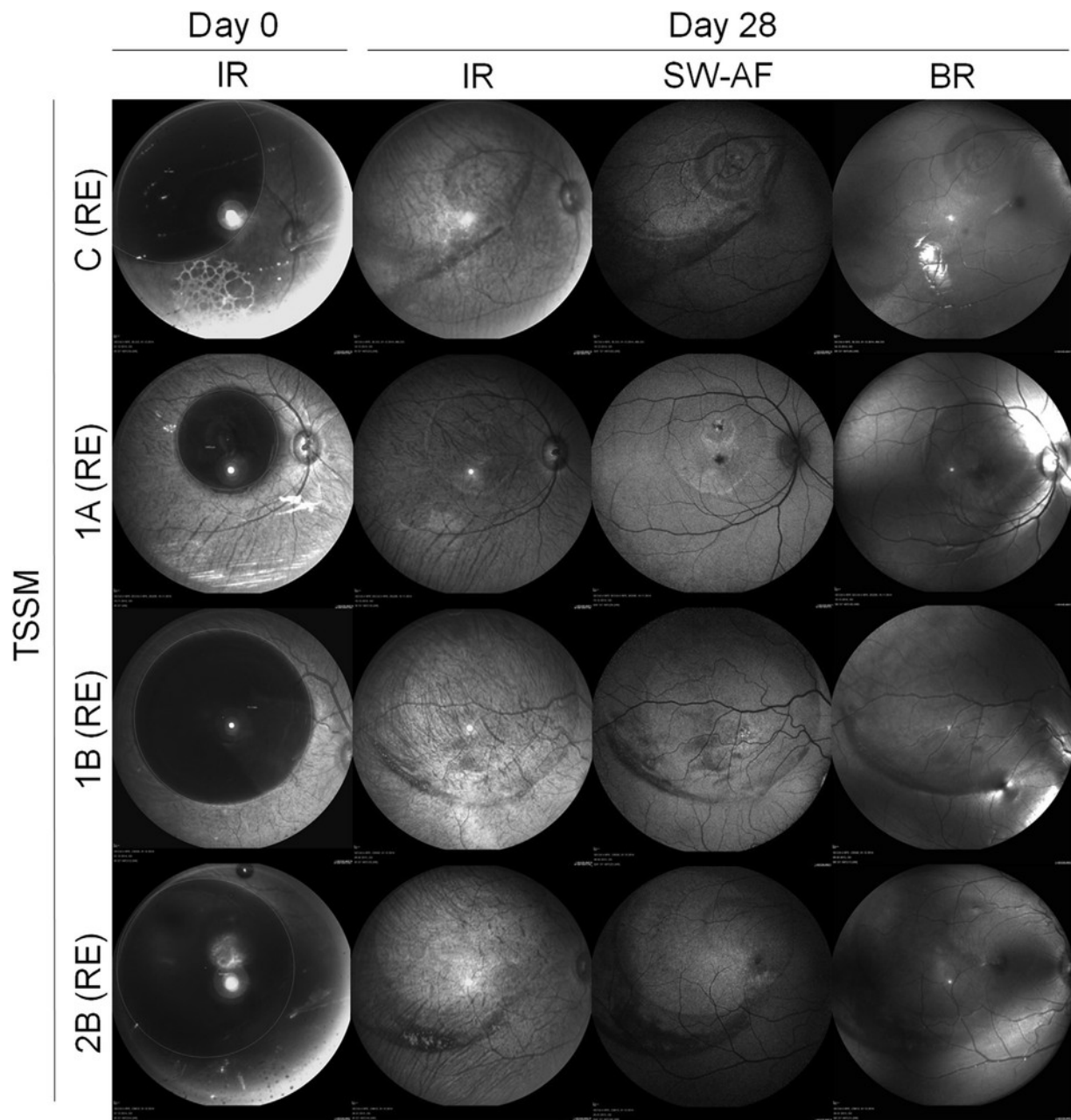


**Fig 3.** Multimodal imaging following subretinal administration of TSSM in 4 control *Macaca fascicularis* eyes. Infrared reflectance (IR) performed immediately after subretinal injection (day 0) showed the topography of the subretinal bleb, and revealed variable degrees of fundus pigmentary changes at day 28 after injection. Similarly, short-wavelength autofluorescence (SW-AF) and blue reflectance (BR) showed retinal pigment epithelium changes related to the detached retinal area or the injection site. Noticeably, the eye C (RE) exhibited a perifoveal concentric circular pattern in the 3 modalities, and the eyes C (RE), 1B (RE), and 2B (RE) showed a concentric hyporeflective and hypoautofluorescent ring at the periphery of the detached retinal area. LE, left eye; RE, right eye.

was performed by an experienced pathologist who was masked to group assignment.

## RESULTS

**Subretinal administration of LV-RPE65 vector and vehicle.** A subretinal detachment of the macular area

was obtained in all the 8 injected eyes (TSSM: 4 eyes; LV-RPE65 dose 1: 2 eyes; and LV-RPE65 dose 2: 2 eyes). The mean detached surface was  $119 \pm 4.2 \text{ mm}^2$  among the 4 eyes injected with LV-RPE65, showing good reproducibility for the delivery process. In the left eye (LE) of animal 2B

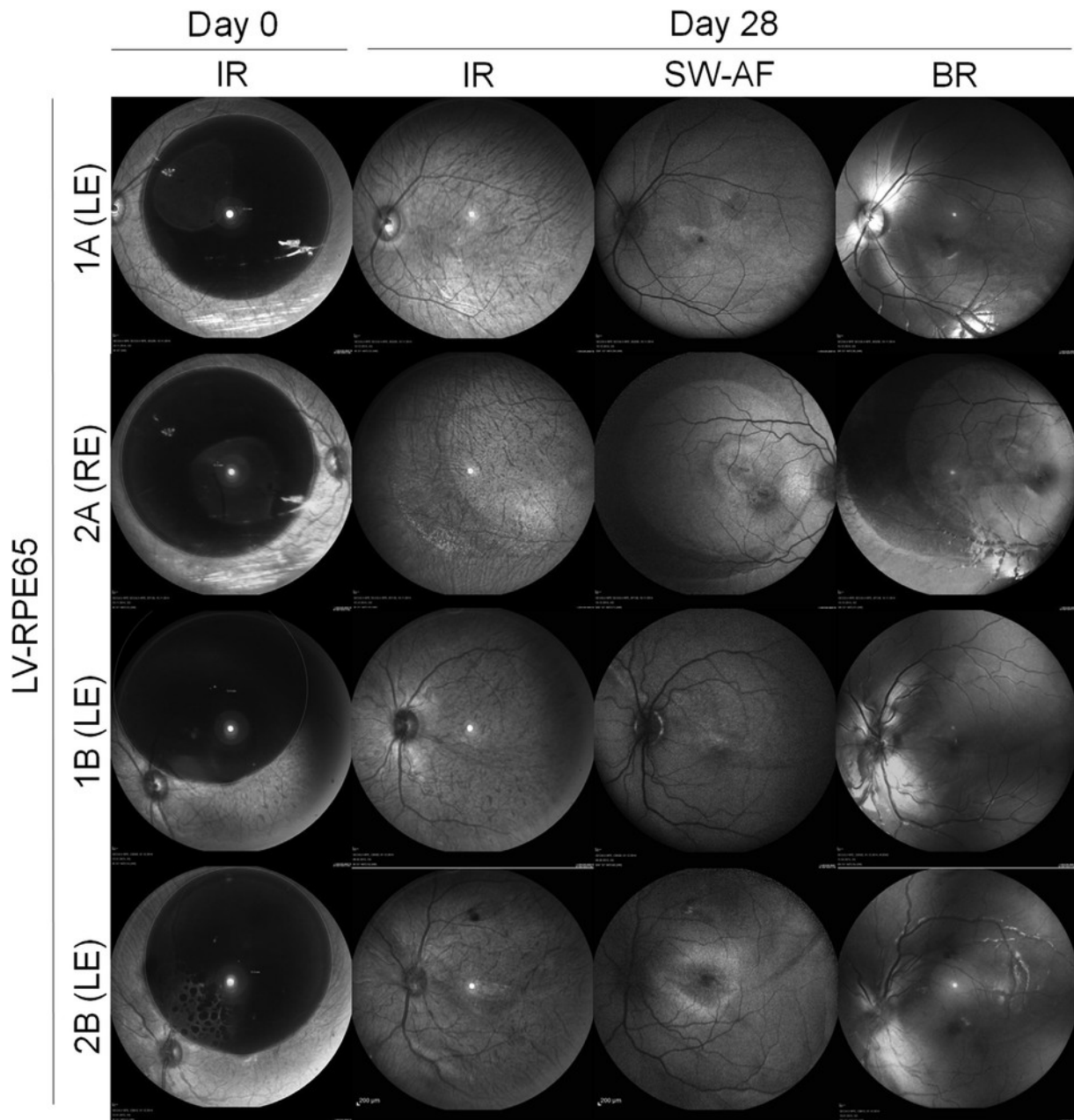


**Fig 4.** Multimodal imaging following subretinal administration of LV-RPE65 in 4 control *Macaca fascicularis* eyes. Infrared reflectance (IR) performed immediately after subretinal injection (day 0) showed the topography of the subretinal bleb and revealed mild fundus pigmentary changes at day 28 after injection. Similarly, short-wavelength autofluorescence (SW-AF) and blue reflectance (BR) showed moderate retinal pigment epithelium changes related to the detached retinal area or the injection site. Particularly, the 2A (RE) eye showed a concentric peripheral ring similar to those observed in TSSM-injected animals (Fig 3). The 2B (LE) eye that received an additional intravitreal dose of LV-RPE65 presented a macular hyperautofluorescence suggestive of more advanced alterations of the outer retina and retinal pigment epithelium. By day 28, BR imaging showed no residual signs of the early, vasculitis-like reaction displayed in Fig 2. LE, left eye; RE, right eye.

(LV-RPE65 dose 2), the first attempt resulted in a retrohyaloidal injection with dispersion of the lentiviral solution within the vitreous cavity, and was followed by a second successful subretinal

injection resulting in a 121-mm<sup>2</sup> bleb. OCT and fundus infrared reflectance images showing blebs immediately after injection are displayed in Figs 1–3, respectively.

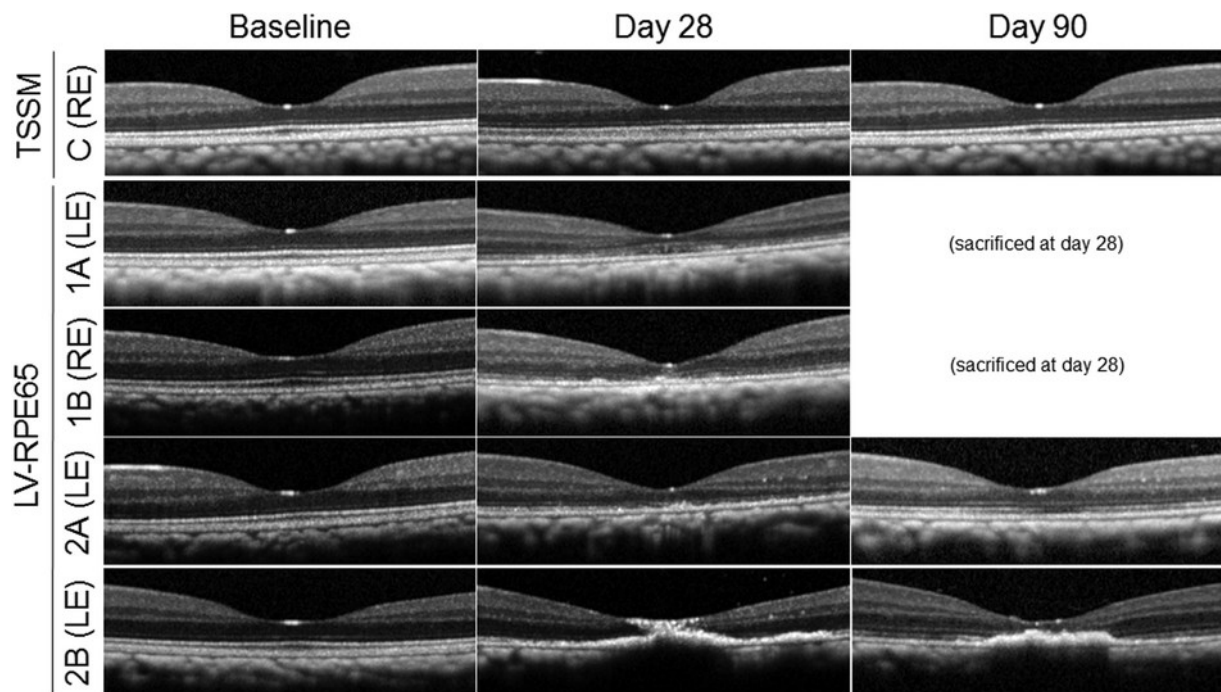


**Fig 5.** Optical coherence tomography of the fovea after subretinal administration of the LV-RPE65 lentiviral vector or the vehicle (TSSM). Horizontal optical coherence tomography scans at baseline (before subretinal administration), day 28, and day 90 (when available) showed minimal, reversible outer retinal changes with ellipsoid zone hyporeflectivity in one TSSM-injected eye (C [RE]). There was mild outer retinal alterations by day 28 in eyes receiving dose 1 LV-RPE65 (1A [LE], 1B [RE]), for which no imaging was available by day 90 due to earlier sacrifice in the study design. Similarly, there were moderate changes with a granular appearance of the ellipsoid zone in one dose 2 LV-RPE65-injected eye (2A [LE]), with recovery of ellipsoid zone integrity by day 90, but there was more pronounced outer retinal alterations with the presence of an hyperreflective material in the other LV-RPE65-injected eye (2B [LE]), that also received an accidental intravitreal dose of lentiviral vector. LE, left eye; RE, right eye.

**Systemic assessment.** A moderate weight loss was observed in 2 LV-RPE65-injected NHPs at the 30-day time point (animal 1A:  $-0.34$  kg, animal 2A:  $-0.52$  kg) that had resolved by 90 days for the animal that reached this time point (2A). Animal C who was dosed subretinally with TSSM only also presented a transitory weight loss ( $-0.41$  kg) at 30 days that had resolved by 90 days. There were no unscheduled deaths during the study period.

**Clinical and imaging ocular observations.** The evaluation of subretinal blebs by serial OCTs during the first postoperative week showed a progressive reattachment that was completed at the fovea by day 4 in TSSM-injected eyes, and by day 7, at the latest, in LV-RPE65 dose 1-injected eyes. LV-RPE65 dose 2-injected eyes showed persistence of subretinal material at day 7, as illustrated in Fig 1, B and C.

Two days after subretinal injection, biomicroscopy revealed a moderate-to-intense anterior chamber and vitreous cellular reaction, which slowly resolved over the follow-up period. This reaction was more intense in dose 2-injected eyes than in dose 1- and vehicle-injected eyes (Fig 2, E and F). In

particular, the LE of animal 2B which had received an extra intravitreal dose of LV-RPE65 presented initially an intense anterior chamber reaction (4+), requiring an intravenous dose of methylprednisolone, followed by progressive resolution of the intraocular reaction.

Surprisingly, all 4 eyes receiving LV-RPE65 presented an early vasculitis-like reaction with perivenular whitening and blood extravasation, suggestive of frost-branch angiitis. There was no sign suggestive of retinal necrosis, and the retinal signs subsided progressively over 14 days (Fig 2). This reaction was best recorded on fundus blue reflectance, indicating its localization to the inner retina around middle-sized retinal venules. Fluorescein and indocyanine green angiography performed at day 2 (animals 2A and 2B) or day 4 (animals 1A and 1B) did not show signs of active vasculitis, pointing to the early and transitory timing of this phenomenon.

There were variable fundus pigmentary changes in TSSM- and LV-RPE65-injected eyes, as illustrated in Figs 3 and 4. A circular hyperpigmentation was frequently visible at the periphery of the detached

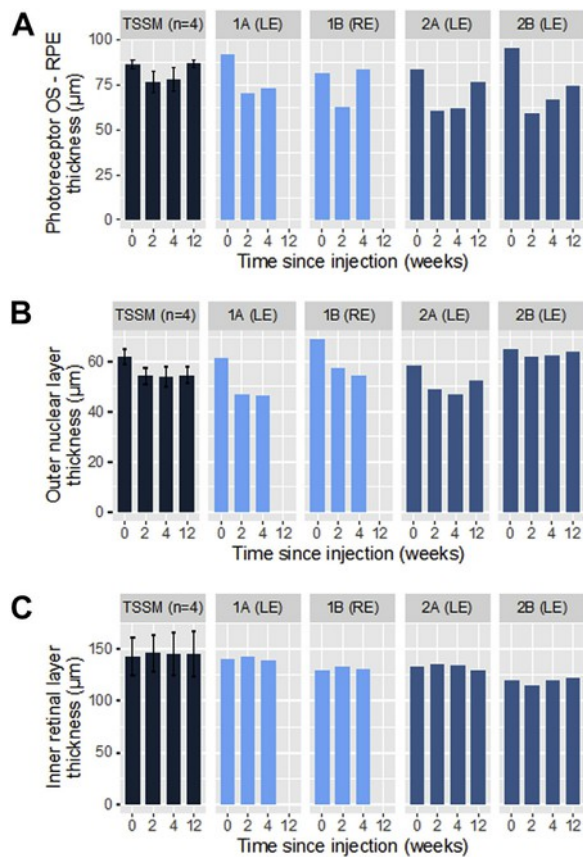


**Fig 6.** Changes in retinal layer thickness following subretinal administration of LV-RPE65 or the vehicle (TSSM). Retinal layer thicknesses were computed as the mean thickness within the detached area, along one vertical and one horizontal axis through the fovea. They are reported for 4 TSSM-injected control eyes (values pooled as mean  $\pm$  SD, dark blue), and 4 LV-RPE65-injected eyes receiving dose 1 (animals 1A left eye, and 1B right eye, pale blue) or dose 2 (animals 2A left eye, and 2B left eye, mid-blue). (A) represents photoreceptor outer segment-retinal pigment epithelium thickness. An initial thinning was observed in control eyes dosed with TSSM, and in eyes receiving LV-RPE65 where it was more pronounced, with progressive recovery of photoreceptor outer segment-retinal pigment epithelium thickness over the follow-up. In the eye 2B (LE) that inadvertently received an extra intravitreal high dose of LV-RPE65 during administration procedure, a significant residual thinning persisted at day 90. (B) Quantification of the outer nuclear layer thickness shows an initial thinning effect and partial resolution in LV-RPE65-injected eyes evaluated at day 90. Control eyes receiving TSSM showed a milder outer nuclear layer thinning, which remained stable until day 90. (C) Inner retinal layers thickness, from the internal limiting membrane to the interface of the inner nuclear/outer plexiform layers, did not show major significant variation. Thickness of inner retinal layers was very close to baseline values by days 28 and 90 in TSSM-injected and LV-RPE65 injected eyes. LE, left eye; RE, right eye.

area, with a clear hyperpigmented ring in 3 TSSM-injected and 1 LV-RPE65-injected eye, visible on infrared and blue reflectance, and short-wavelength autofluorescence. There was also hypo/hyperautofluor-

escent changes related to the injection site, and a pattern formed by multiple concentric rings variably observed around the fovea.

A transient decrease in IOP was observed in all eyes after surgery, and was more pronounced in LV-RPE65-injected eyes than TSSM-injected eyes, probably related to the degree of postoperative intraocular inflammation. However, it was self-resolving with mean IOP measurements of 10-mm Hg, 8-mm Hg, and 11-mm Hg at day 28 in eyes dosed with LV-RPE65 dose 1, dose 2, and TSSM, respectively.

**Assessment of retinal layers on OCT.** The qualitative evaluation of retinal layers at the macula with serial OCT showed outer retinal changes at day 28 in LV-RPE65-injected eyes (Fig 5). The ellipsoid zone (EZ) demonstrated an irregular aspect in eyes 1A (LE), 1B (right eye [RE]), and 2A (LE), while the hyperreflective material observed after bleb formation (Fig 1) persisted in the LE of animal 2B, impairing the visualization of outer retinal layers at the macula. The ONL also showed a relative thinning in eyes dosed with LV-RPE65. At the 90-day time point, eye 2A (LE) showed a partial restoration of EZ, and eye 2B (LE) showed a partial regression of the dense hyperreflective material, and persistence of outer retinal layer alterations. EZ disruption and ONL thinning were also observed, but to a milder degree, in eyes dosed with TSSM (Fig 5 shows OCTs from animal C [RE]). For all groups but not for all animals, accumulation of subretinal hyperreflective material was observed at the bleb edge (not shown).

A quantitative assessment of retinal layer thickness changes on OCT scans positioned at the fovea in detached retinal areas is displayed in Fig 6. It showed in LV-RPE65-injected eyes a transient, partially reversible POS-RPE layer thinning. The ONL thickness was also moderately affected. To a lesser degree, outer retinal layer thicknesses in control TSSM-injected eyes were also altered by the subretinal detachment, and demonstrated similar trends with reversible outer segment thinning and a moderate, persistent ONL thinning in the detached area. A similar assessment was performed for the inner retinal layers (from the internal limiting membrane to the outer plexiform/inner nuclear layer interface), that showed no relevant thickness changes in TSSM-injected and LV-RPE65-injected eyes.

An analysis of retinal layer thickness change was also conducted over an identical location close to the macula in all eyes,<sup>38</sup> allowing a better intereyes comparability of the results in terms of relative change. This analysis showed a reversible decline in ONL thickness and a relative, partial decrease in POS/RPE thickness in all

LV-RPE65–injected eyes (Supplementary Fig 2). It also confirmed that the inner retinal layer thickness was not modified after LV-RPE65 injection.

**Electroretinography.** To evaluate the effects of subretinal administration of either LV-RPE65 or TSSM on retinal activity, we compared full-field ERG recordings performed 14, 28, and 90 days after injection with baseline measures acquired before treatment, in each animal (Table II). Baseline responses showed evident interindividual quantitative variations of the a- and b-wave amplitudes. For example, min-max values ranged from 40 to 108  $\mu$ V for the b-wave amplitude of the rod response or from 22 to 49  $\mu$ V for the a-wave amplitude of the cone response. We thus decided to evaluate intraindividual variations at the different time points. Of the 4 TSSM-injected eyes, 3 eyes maintained equivalent retinal activity (Fig 7B). In the fourth TSSM-injected eye C (RE), we observed over 40% decrease in response amplitudes to all illumination conditions after injection as compared to baseline, but no differences in peak times. Absent or minor modifications of ERG responses were noticed for the 2 LV-RPE65–injected eyes 1B (RE; dose 1) and 2A (LE; dose 2; Fig 7, C and D and Table II), whereas the 1A (LE) dose 1 showed significantly reduced amplitudes at the latest time point by 40% or more, but without peak time increase. The fourth eye injected with LV-RPE65 dose 2 (2B [LE]) showed 90 days post-injection both reduced amplitude and increase in peak time in scotopic conditions, which could be the manifestation of retinal cellular suffering (Table I). We were not able to identify exclusive inner retinal dysfunction in LV-RPE65– or TSSM-injected eye following ERG analysis of a- and b-wave amplitudes and peak times.

**Biodistribution and organ toxicology.** To optimize quantitative PCR sensitivity for detecting circulating lentiviral particles or integrated lentiviral genomes, we designed a primer pair targeting specifically the lentiviral transgene cassette. The forward primer is located on RPE65 cDNA and the reverse primer on the Woodchuck hepatitis virus Posttranscriptional Regulatory Element sequence added in the vector, thereby avoiding putative amplification of the endogenous *RPE65* macaque gene. This primer pair allowed to detect unequivocally 10 copies of target matrix DNA in the reaction mixture (Supplementary Fig 3).

**Circulating particles.** To evaluate the extraocular shedding of lentiviral particles after subretinal delivery, qRT-PCR was performed on lachrymal fluid, serum, and urine collected at regular intervals (days 2, 4, 7, 14, 30, and 90). Based on the sensitivity of the qPCR and the amount of RNA extracted from the different fluids, we calculated a detection threshold of 250 particles/ml

for serum, 60 particles/ml for lachrymal fluid, and 10 particles/ml for urine. No viral particle was detected in any body fluid regardless the time points or the animal being studied all quantification cycles (Cq) being equivalent or above negative control (Supplementary Fig 3).

**Integrated lentiviral sequences in genomic DNA.** Despite the very limited shedding of the vector, we prospected for extraocular genomic integration of the LV. Biopsies from inferior eyelids, right/left optic nerves, right/left geniculate bodies, right/left visual cortex, heart, liver, right/left lung, right/left ovary, right/left kidney, and right/left mandibular lymph nodes were collected at the end of the experiment and genomic DNA was extracted for quantitative PCR of the integrated therapeutic cassette. The threshold sensitivity of our procedure was 10 copies in 50 ng of genomic DNA, the lowest detected point of the standard curve being 10 copies. This limit of detection was estimated to be at  $0.8 \times 10^6$  copies/organ for heart (containing around  $4.9 \times 10^{14}$  diploid genomes),  $1 \times 10^6$  copies/organ for lung (containing around  $6.8 \times 10^{14}$  diploid genomes),  $2 \times 10^6$  copies/organ for kidney (containing around  $15.8 \times 10^{14}$  diploid genomes),  $12 \times 10^6$  copies/organ for liver (containing around  $76.5 \times 10^{14}$  diploid genomes), and brain (containing around  $75.8 \times 10^{14}$  diploid genomes). We did not detect any integration of the recombinant lentiviral genome in any samples tested showing the systemic safety of lentiviral administration into the subretinal space.

**Organ histology.** No macroscopic or microscopic morphologic alterations nor signs of unexpected inflammation could be detected in biopsies sampled from inferior eyelid, optic nerve, geniculate bodies, visual cortex, mandibular lymph node, heart, lung, liver, kidney, and ovary tissues in animals sacrificed at day 28 (1A-B) or day 90 (2A-B) after LV-RPE65 subretinal administration nor in the animal sacrificed 90 days after receiving TSSM only (C).

**Ocular histology and immunohistochemistry.** After sacrifice at day 28 for dose 1 LV-RPE65–injected animals and at day 90 for dose 2 LV-RPE65–injected animals, eyes were processed for histologic and immunohistochemical analysis. Conventional hematoxylin-eosin stain showed normal ocular structures in all eyes and revealed a mild choroidal lymphocytic infiltrate in animal 1A (RE; TSSM), and a similar finding associated to focal outer blood-retinal barrier breakdown and mild vitritis in animal 2B (LE; LV-RPE65 dose 2). To evidence remnants of inflammatory cell migration, a retinal section containing the region of subretinal injection (bleb) was labeled for the CD45 leukocyte marker. No differences in CD45-positive labeling were observed between noninjected, TSSM-injected, or LV-RPE65–

**Table II.** Retinal activity characterization using full field electroretinogram (ERG) recordings following subretinal injection

ID	Eye	Group	Time	Photopic (cone responses) at i-max 0.4 log cds/m <sup>2</sup>					Scotopic (rod responses) at -0.8 log cds/m <sup>2</sup>		Scotopic (mixed rod-cone responses) at i-max 0.4 log cds/m <sup>2</sup>					
				a-wave		b-wave		FI-wave	b-wave		a-wave		b-wave		Ratio b/a	
				Amp (μV)	Peak time (ms)	Amp (μV)	Peak time (ms)		Ratio b/a	Amp (μV)	Peak time (ms)	Amp (μV)	Peak time (ms)	Amp (μV)		Peak time (ms)
C	LE	-	Baseline	47	14	205	31	4.36	190	92	60	145	16	367	38	2.53
			D15	34	14	137	30	4.03	123	54	62	100	17	243	39	2.43
			D30	33	14	136	30	4.12	129	55	61	98	16	254	38	2.59
			D90	22	14	134	29	6.09	128	61	61	105	17	285	38	2.71
1B	LE	-	Baseline	29	14	126	27	4.34	105	51	56	104	16	251	36	2.41
			D15	38	14	119	32	3.13	111	64	62	130	14	270	36	2.08
			D30	30	13	127	30	4.23	140	57	59	132	14	298	34	2.26
C	RE	TSSM	Baseline	49	14	213	30	4.35	186	93	60	147	16	382	38	2.60
			D15	30	15	125*	30	4.17	94*	46*	64	97	17	214*	41	2.21
			D30	22*	14	105*	30	4.77	96*	34*	60	79*	16	194*	39	2.46
			D90	23*	15	107*	29	4.65	96*	42*	61	86*	17	224*	38	2.60
1A	RE	TSSM	Baseline	32	14	153	29	4.78	109	54	60	119	17	287	40	2.41
			D15	41	13	158	28	3.85	130	75	60	144	16	346	38	2.40
			D30	22	15	122	29	5.55	69	44	58	109	17	240	41	2.20
2A	RE	TSSM	Baseline	25	13	149	27	5.96	144	88	55	110	16	360	39	3.27
			D15	35	14	150	29	4.29	120	84	57	107	16	332	39	3.10
			D30	32	13	168	27	5.25	172	118	53	134	15	454	40	3.39
			D133	29	13	137	27	4.72	131	79	53	97	15	299	40	3.08
2B	RE	TSSM	Baseline	25	13	109	27	4.36	107	65	57	107	15	305	35	2.85
			D15	38	12	116	32	3.05	148	64	60	138	13	320	35	2.32
			D30	43	11	140	32	3.26	181	89	57	152	14	387	34	2.55
			D133	29	13	112	28	3.86	101	60	61	104	16	266	38	2.56
1A	LE	Dose 1	Baseline	32	12	160	29	5.00	129	61	61	130	17	302	40	2.32
			D15	28	14	112	28	4.00	166	53	62	102	16	230	39	2.25
			D30	19*	15	91*	29	4.79	53*	27*	59	83	17	194	42	2.34
1B	RE	Dose 1	Baseline	22	14	97	27	4.41	84	40	56	91	16	212	35	2.33
			D15	41	14	109	32	2.66	120	50	64	129	15	246	37	1.91
			D30	39	13	110	31	2.82	140	50	59	138	15	288	35	2.09
2A	LE	Dose 2	Baseline	27	13	163	27	6.04	163	108	54	113	15	400	40	3.54
			D22	22	13	111	28	5.05	105	73	55	91	16	305	40	3.35
			D30	20	14	120	28	6.00	105	82	57	93	16	293	42	3.15
			D90	16*	14	96*	28	6.00	93*	71	54	88	16	294	41	3.34
2B	LE	Dose 2	Baseline	36	13	139	27	3.86	151	83	57	129	15	365	35	2.83
			D22	29	13	140	29	4.83	97	67	64	115	17	286	41	2.49
			D30	38	14	123	32	3.24	120	54 <sup>†</sup>	62 <sup>†</sup>	131	16	318	38	2.43
			D90	19*	14	93	29	4.89	68*	51 <sup>†</sup>	63 <sup>†</sup>	79 <sup>†</sup>	17 <sup>†</sup>	213 <sup>†</sup>	40 <sup>†</sup>	2.70

\* &gt; 40% decrease compare to baseline.

<sup>†</sup> decrease of amplitude coupled to mild increase of peak time.

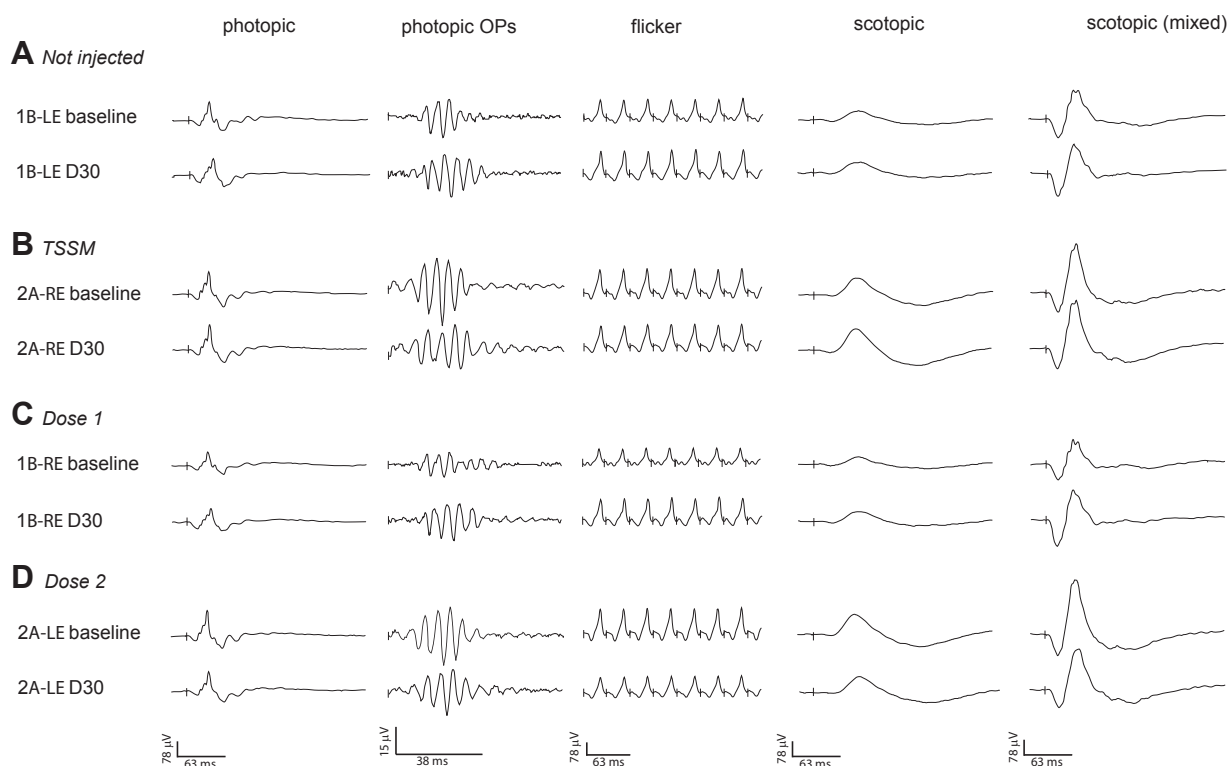


**Fig 7.** Retinal activity evaluation 30 days after subretinal injection. ERG tracings obtained at baseline and 30 days after injection in photopic and scotopic conditions. In photopic conditions, the  $I_{\max}$  flash response was obtained by 15 stimuli delivered at 1.3 Hz against a  $25 \text{ cd/m}^2$  background (first column). The oscillatory potentials were extracted from the  $I_{\max}$  photopic response (second column). A final 30-Hz flicker at  $I_{\max}$  stimuli was recorded (third column). After 20 minutes of dark adaptation, scotopic responses to  $0.4 \text{ cd.s/m}^2$  stimuli (average of 5 flashes) were recorded in dark (fourth column). Finally, in similar scotopic conditions, a unique flash at  $I_{\max}$  intensity was applied to record the mixed rod-cone response (fifth column). The displayed tracings were obtained in (A) an un-injected eye (1B [LE]), (B) a TSSM- injected eye (2A [RE]), (C) a dose 1 LV-injected eye (1B [RE]), and (D) a dose 2 LV-injected eye (2A [LE]). All eyes maintained photopic and scotopic retinal activity 30 days after injection. LE, left eye; RE, right eye.

injected eyes (Supplementary Fig 4). The GFAP and Vimentin glial markers labeling Müller cells and astrocytes did not show any difference between these eyes (Supplementary Fig 4). Finally, the microglia Iba-1 staining did not either demonstrate differences in microglial activation or migration between these groups 30 or 90 after injection (Supplementary Fig 4).

## DISCUSSION

In this preclinical study, we assessed the ocular and systemic safety after subretinal administration of an LV for RPE65 gene replacement in healthy NHPs. Considering that no systemic or periocular anti-inflammatory agents were preventively administered to the subretinally injected animals, subretinal injection of an LV was well tolerated in low-dose injected animals, but not in the high-dose injected animals who developed a strong retinal and ocular inflammatory

reaction, that did not persist but induced seemingly irreversible structural alterations. This observation suggests that the alterations observed at the fovea level could be markedly reduced if the injection procedure and the retina environment are well controlled. This moderate tolerance has to be compared with previous preclinical and clinical studies with AAV vectors, in which large animals or patients all received periocular<sup>16,28,43</sup> or systemic<sup>18,33</sup> anti-inflammatory therapy. An exception was made for animal 2B which endured an accidental intravitreal extra-injection and developed a marked, but transient intraocular inflammation and who received an intravenous anti-inflammatory treatment. This animal developed a mild transient weight loss, but this phenomenon was also observed in one TSSM-injected animal and might be caused by repetitive anesthesia imposed by the study design. Remarkably, no vector shedding or inaccurate extraocular targeting was demonstrated, showing the safe restriction of the vector

in the eye. This observation is consistent with previous reports suggesting a high systemic safety of nonhuman LVs administered subretinally.<sup>44-47</sup>

In the present study, in contrast with previous reports that did not focus on early events, animals were followed at short intervals with multimodal imaging to assess *in vivo* the acute effects of subretinal LV administration on retinal structures. Interestingly, the kinetics of subretinal bleb detachment showed prolonged reattachment times (by 3–4 days) for LV-RPE65–injected eyes as compared with vehicle-injected eyes. This phenomenon may be caused by a transient impairment of the RPE pumping capacity during an acute phase corresponding to the vector entry and integration into RPE cells, the latter process starting within 4 hours and reaching a plateau at 24–48 hours.<sup>48</sup> Alternatively, the transient presence of viral particles in the subretinal fluid could provoke an osmolality imbalance that maintains the detachment of the neurosensory retina from the RPE longer than in control-injected eyes. Whether this prolonged detachment results from the alteration of RPE cell functions in reaction to vector entry, from an inflammatory process, or from an osmolality effect remains to be determined.

Noticeably, we observed an early perivascular reaction, evidenced at day 2 and self-resolving within 14 days, consisting perivenular whitening at the level of retinal venules within the detached area. There was no angiographic vasculitis at day 2, suggesting that severe blood-retinal barrier rupture did not occur or occurred before this time point. Although a similar reaction has not been reported by other groups, we did not find previous reports of fundus examination or blue-reflectance imaging, which best evidenced the phenomenon, as early as day 2 after subretinal delivery of viral vectors. To investigate its cause, we searched for several inflammatory and glial markers by immunohistochemistry but did not find overexpression of CD45 (lymphocytes), Iba-1 (microglia), GFAP or vimentin (astrocytes and Müller cells) in LV-RPE65–injected as compared with vehicle-injected eyes. This may result in part from the delayed *ex vivo* evaluation at 1 and 3 months after administration. Nonetheless, these histologic data assess that this transient reaction did not provoke a chronic modification of the glial cells often observed after retinal injuries.<sup>49,50</sup>

Importantly, the *in vivo* evaluation of retinal layer thickness by serial OCT scans did not show any significant thinning of inner retinal layers, where the perivascular reaction was detected.

While the perivascular phenomenon occurred in all eyes receiving LV-RPE65, no significant ERG alterations were observed in all the 4 animals, indicating limited consequences on retinal function. Similarly,

ERG alterations observed in LV-RPE65–injected eyes did not preferentially involve b-wave responses, suggesting that the immediate post-injection vasculitis-like process did not result in specific inner retinal cellular defects detectable by this analysis. Moreover, no isolated b-wave modifications were observed, suggesting they were rather caused by a-wave changes originating from outer retinal variations rather than from inner retinal damages.

Outer retinal alterations were also manifested on multimodal imaging as hyper/hypopigmentation, and hyper/hypoautofluorescence mostly at the borders of the detached areas. OCT also showed a partially reversible thinning of outer retinal layers. Similarly to ERG a-wave variations, these changes were more frequent and more severe in LV-RPE65–injected eyes, but were also observed to a variable and milder degree in vehicle-injected eyes. Despite the limited number of injected eyes (4 with TSSM, 2 with low-dose LV-RPE65, and 2 with high-dose LV-RPE65), these observations emphasize the limits of the subretinal route with current injection methods and devices that do not prevent retinal suffering, particularly at the POS/RPE interface, and that lack reproducibility. The crescent-shaped pigmentary and autofluorescent modifications visible on [Figs 3 and 4](#) variably affected both vehicle- and lentivirus-injected eyes. This imaging pattern points to a biological effect of the retinal detachment rather than to an infectious manifestation. Moreover, although restoring a retinal function in the macular area should bring major benefits to the patients, this area appears to be especially vulnerable to the damaging effects of acute detachment, as was already highlighted in one clinical study evaluating AAV-based RPE65 gene therapy.<sup>26</sup> In the present study, 3 out of 4 animals presented at 1 or 3 months a partial improvement of early macular changes visible on OCT after LV-RPE65 administration. In contrast, animal 2B which received an extra intravitreal dose followed by an intense intraocular inflammation presented a subfoveal hyperreflective deposit that had not resolved at the 3-month time point, showing the higher susceptibility of the fovea for focal damage in case of an adverse event. Among patients included in AAV-RPE65 gene therapy clinical trials, structural damage of the fovea has been reported, such as macular hole formation<sup>17</sup> and foveal thinning.<sup>22,23,26</sup> To prevent these drawbacks, alternate strategies have been advanced, such as minimizing hydrodynamic stress during injection<sup>51,52</sup> or performing multiple perimacular detachments.<sup>26</sup>

Animal models of retinal detachment have shown that detachment of the neurosensory retina from the RPE leads to a glial reaction mediated by Müller cells<sup>53,54</sup> and microglia,<sup>55</sup> and to photoreceptor damage with outer segment shortening.<sup>56</sup> Photoreceptor damage results from

the activation of multiple pathways, including the alternative complement<sup>57</sup> and RhoA pathways.<sup>58</sup> Interestingly, there is a decrease in glial markers overexpression<sup>59</sup> and progressive restoration of POSs<sup>56</sup> after lengthy periods of reattachment (~5 months), which is consistent with our findings. Recently, imaging studies using OCT segmentation on patients with rhegmatogenous retinal detachment also showed a re-increase in POS volume after retinal reattachment.<sup>60</sup> In LV-RPE65–injected eyes, damages related to the induced retinal detachment may be potentiated by the inflammation reaction to the viral vector, explaining the less-pronounced photoreceptor restoration as compared with control eyes. However, multimodal imaging findings in the present study showed a variability in retinal alterations after subretinal administration of TSSM or the lentiviral solution, as reported in patients who received subretinal gene therapy.<sup>22,26</sup> Additional studies with increased number of vector-injected eyes will be necessary to demonstrate in greater detail the functional and structural effects of subfoveal injections.

The blood-retinal barrier, by contributing to the intraocular immune privilege, favors the systemic tolerance of subretinally injected vectors. However, mechanical alterations of the RPE induced by the detachment, and the transient perivascular reaction observed in this study may compromise the integrity of the outer and inner blood-retinal barriers, respectively. Although the analysis of body fluids and organs did not indicate shedding of viral particles, it may have elicited a subclinical, low-grade immune reaction, which raises concerns regarding possible vector reinjection.<sup>43,61</sup> The evaluation of the immune response against the LV-RPE65 vector will be addressed in a future report.

Limitations of this study include the limited number of NHPs due to ethical restrictions, and the fact that one animal was treated after surgery with systemic corticosteroids due to an intense intraocular inflammation. Additional experiments are needed to evaluate the dose safety, to determine whether vitrectomy should be performed systematically before subretinal injection, whether the injection site should be located in a specific area or sealed to reduce vitreal leakage of the vector, and whether local or systemic corticosteroids should be administered.

The current RPE65 clinical trials are proposing an AAV-based gene transfer for gene replacement in RPE cells. Despite positive effects in the first years following vector administration, several long-term reports show continuation of retinal degeneration, and loss of early visual benefits several years after treatment<sup>22,23,62</sup> One hypothesis explaining this major drawback is the low level of therapeutic gene expression obtained in these

trials, which is incompatible with the level required in the human retina.<sup>22</sup> Thus, the development of alternate gene transfer tools could open new therapeutic perspectives.<sup>19</sup> Given the previously established high efficiency of LVs to target RPE cells,<sup>30,31,63,64</sup> this vector may be a potential candidate for inherited retinal disorders due to RPE65 deficiency, but also for other RPE-specific diseases such as Best vitelliform macular dystrophy, provided that its local tolerance is improved. This improvement may be achieved by the co-administration of a systemic adjuvant anti-inflammatory prophylaxis and/or optimization of the vector delivery. The study herein further supports the limited systemic dispersion of LVs following subretinal administration. It also demonstrates that further optimization of the retinal tolerance to the LV-RPE65 LV and to its subretinal delivery technique are crucial to render the vector eligible for gene transfer in the human retina.

#### ACKNOWLEDGMENTS

Conflicts of Interest: All authors have read the journal's policy on disclosure of potential conflicts of interest and have none to declare. This work was supported by SwissTransmed and the Fondation l'Occitane. The authors thank Solenne Métrailler and Damien Grize for technical assistance. The authors are also particularly grateful to José-Alain Sahel, Céline Jaillard, Elena Brazhnikova, Claire-Maëlle Fovet, Joanna Demilly, and Lev Stimmer for granting access to the animal facility and their assistance in animal experiments and to Charlène Joséphine for performing quantitative PCR experiments.

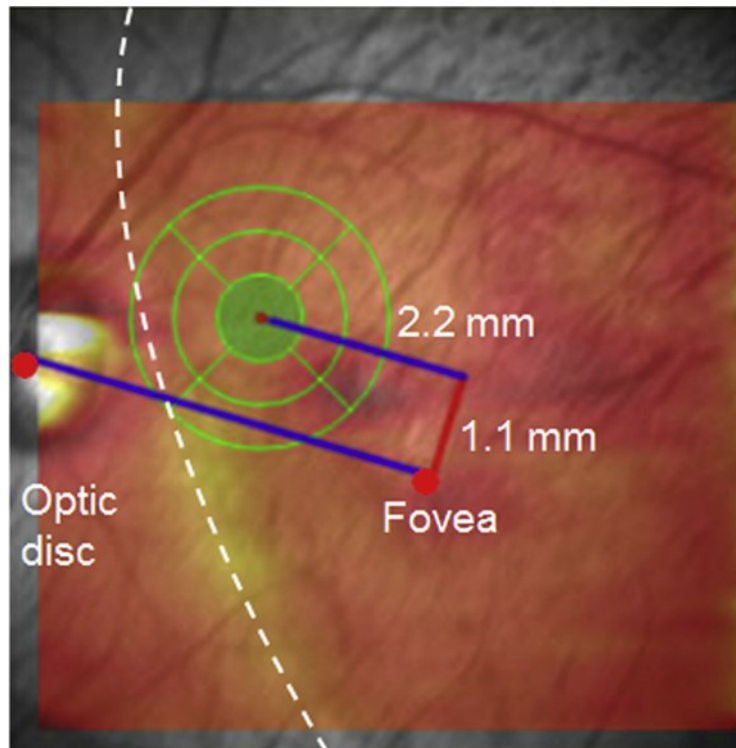
#### REFERENCES

1. Ali RR, Reichel MB, Thrasher AJ, et al. Gene transfer into the mouse retina mediated by an adeno-associated viral vector. *Hum Mol Genet* 1996;5:591–4.
2. Flannery JG, Zolotukhin S, Vaquero MI, LaVail MM, Muzyczka N, Hauswirth WW. Efficient photoreceptor-targeted gene expression in vivo by recombinant adeno-associated virus. *Proc Natl Acad Sci U S A* 1997;94:6916–21.
3. Bennett J, Maguire AM, Cideciyan AV, et al. Stable transgene expression in rod photoreceptors after recombinant adeno-associated virus-mediated gene transfer to monkey retina. *Proc Natl Acad Sci U S A* 1999;96:9920–5.
4. Bennett J, Tanabe T, Sun D, et al. Photoreceptor cell rescue in retinal degeneration (rd) mice by in vivo gene therapy. *Nat Med* 1996;2:649–54.
5. Smith AJ, Bainbridge JWB, Ali RR. Gene supplementation therapy for recessive forms of inherited retinal dystrophies. *Gene Ther* 2012;19:154–61.
6. Boye SE, Boye SL, Lewin AS, Hauswirth WW. A comprehensive review of retinal gene therapy. *Mol Ther* 2013;21:509–19.

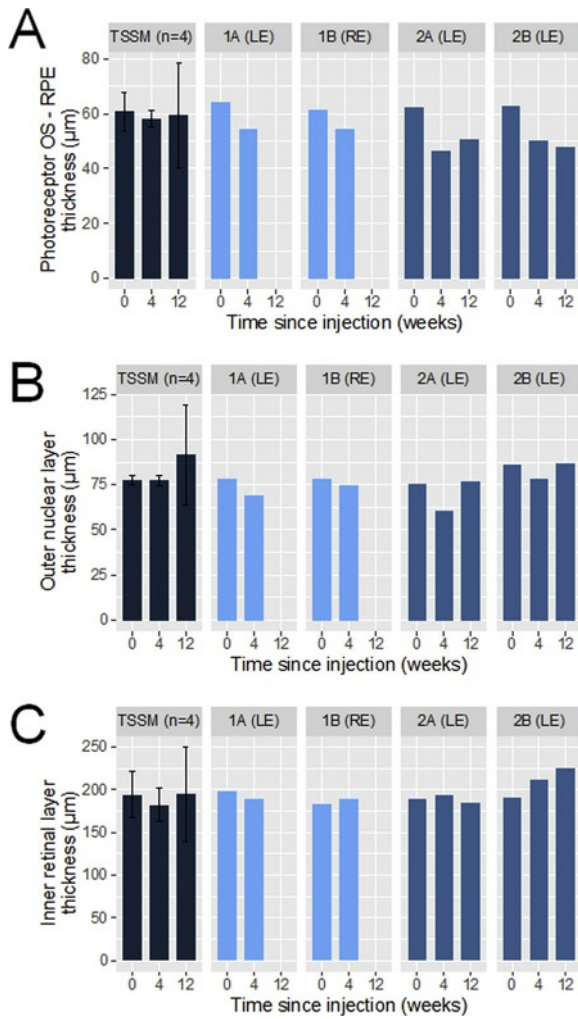
7. Miyoshi H, Takahashi M, Gage FH, Verma IM. Stable and efficient gene transfer into the retina using an HIV-based lentiviral vector. *Proc Natl Acad Sci U S A* 1997;94:10319–23.
8. Bainbridge JW, Stephens C, Parsley K, et al. In vivo gene transfer to the mouse eye using an HIV-based lentiviral vector; efficient long-term transduction of corneal endothelium and retinal pigment epithelium. *Gene Ther* 2001;8:1665–8.
9. van Adel BA, Kostic C, Déglon N, Ball AK, Arsenijevic Y. Delivery of ciliary neurotrophic factor via lentiviral-mediated transfer protects axotomized retinal ganglion cells for an extended period of time. *Hum Gene Ther* 2003;14:103–15.
10. Balaggan KS, Binley K, Esapa M, et al. Stable and efficient intraocular gene transfer using pseudotyped EIAV lentiviral vectors. *J Gene Med* 2006;8:275–85.
11. Colella P, Auricchio A. Gene therapy of inherited retinopathies: a long and successful road from viral vectors to patients. *Hum Gene Ther* 2012;23:796–807.
12. Cideciyan AV. Leber congenital amaurosis due to RPE65 mutations and its treatment with gene therapy. *Prog Retin Eye Res* 2010;29:398–427.
13. Redmond TM, Yu S, Lee E, et al. Rpe65 is necessary for production of 11-cis-vitamin A in the retinal visual cycle. *Nat Genet* 1998;20:344–51.
14. Marlhens F, Bareil C, Griffoin JM, et al. Mutations in RPE65 cause Leber's congenital amaurosis. *Nat Genet* 1997;17:139–41.
15. den Hollander AI, Roepman R, Koenekoop RK, Cremers FPM. Leber congenital amaurosis: genes, proteins and disease mechanisms. *Prog Retin Eye Res* 2008;27:391–419.
16. Hauswirth WW, Aleman TS, Kaushal S, et al. Treatment of leber congenital amaurosis due to RPE65 mutations by ocular subretinal injection of adeno-associated virus gene vector: short-term results of a phase I trial. *Hum Gene Ther* 2008;19:979–90.
17. Maguire AM, Simonelli F, Pierce EA, et al. Safety and efficacy of gene transfer for Leber's congenital amaurosis. *N Engl J Med* 2008;358:2240–8.
18. Bainbridge JWB, Smith AJ, Barker SS, et al. Effect of gene therapy on visual function in Leber's congenital amaurosis. *N Engl J Med* 2008;358:2231–9.
19. Georgiadis A, Duran Y, Ribeiro J, et al. Development of an optimized AAV2/5 gene therapy vector for Leber congenital amaurosis owing to defects in RPE65. *Gene Ther* 2016;23:857–62.
20. Banin E, Obolensky A, Hemo Y, et al. Phase I gene therapy trial in Israeli patients with leber congenital amaurosis caused by a founder RPE65 mutation: safety and efficacy update with up to two years of follow-up. *Invest Ophthalmol Vis Sci* 2013;54:2709.
21. Le Meur G, Stieger K, Smith AJ, et al. Restoration of vision in RPE65-deficient Briard dogs using an AAV serotype 4 vector that specifically targets the retinal pigmented epithelium. *Gene Ther* 2007;14:292–303.
22. Bainbridge JWB, Mehat MS, Sundaram V, et al. Long-term effect of gene therapy on Leber's congenital amaurosis. *N Engl J Med* 2015;372:1887–97.
23. Jacobson SG, Cideciyan AV, Roman AJ, et al. Improvement and decline in vision with gene therapy in childhood blindness. *N Engl J Med* 2015;372:1920–6.
24. Ashtari M, Cyckowski LL, Monroe JF, et al. The human visual cortex responds to gene therapy-mediated recovery of retinal function. *J Clin Invest* 2011;121:2160–8.
25. Maguire AM, High KA, Auricchio A, et al. Age-dependent effects of RPE65 gene therapy for Leber's congenital amaurosis: a phase 1 dose-escalation trial. *Lancet* 2009;374:1597–605.
26. Jacobson SG, Cideciyan AV, Ratnakaram R, et al. Gene therapy for leber congenital amaurosis caused by RPE65 mutations: safety and efficacy in 15 children and adults followed up to 3 years. *Arch Ophthalmol* 2012;130:9–24.
27. Samardzija M, von Lintig J, Tanimoto N, et al. R91W mutation in Rpe65 leads to milder early-onset retinal dystrophy due to the generation of low levels of 11-cis-retinal. *Hum Mol Genet* 2008;17:281–92.
28. Acland GM, Aguirre GD, Bennett J, et al. Long-term restoration of rod and cone vision by single dose rAAV-mediated gene transfer to the retina in a canine model of childhood blindness. *Mol Ther* 2005;12:1072–82.
29. Annear MJ, Mowat FM, Bartoe JT, et al. Successful gene therapy in older Rpe65-deficient dogs following subretinal injection of an adeno-associated vector expressing RPE65. *Hum Gene Ther* 2013;24:883–93.
30. Bemelmans A-P, Kostic C, Crippa SV, et al. Lentiviral gene transfer of RPE65 rescues survival and function of cones in a mouse model of Leber congenital amaurosis. *PLoS Med* 2006;3:e347.
31. Kostic C, Crippa SV, Pignat V, et al. Gene therapy regenerates protein expression in cone photoreceptors in Rpe65(R91W/R91W) mice. *PLoS One* 2011;6:e16588.
32. Bencicelli J, Wright JF, Komaromy A, et al. Reversal of blindness in animal models of leber congenital amaurosis using optimized AAV2-mediated gene transfer. *Mol Ther* 2008;16:458–65.
33. Annear MJ, Bartoe JT, Barker SE, et al. Gene therapy in the second eye of RPE65-deficient dogs improves retinal function. *Gene Ther* 2011;18:53–61.
34. Narfström K, Vaegan, Katz M, Bragadottir R, Rakoczy EP, Seeliger M. Assessment of structure and function over a 3-year period after gene transfer in RPE65<sup>-/-</sup> dogs. *Doc Ophthalmol* 2005;111:39–48.
35. Bemelmans A-P, Kostic C, Cachafeiro M, et al. Lentiviral gene transfer-mediated cone vision restoration in RPE65 knockout mice. *Adv Exp Med Biol* 2008;613:89–95.
36. Schambach A, Bohne J, Baum C, et al. Woodchuck hepatitis virus post-transcriptional regulatory element deleted from X protein and promoter sequences enhances retroviral vector titer and expression. *Gene Ther* 2006;13:641–5.
37. Dinculescu A, Glushakova L, Min S-H, Hauswirth WW. Adeno-associated virus-vectored gene therapy for retinal disease. *Hum Gene Ther* 2005;16:649–63.
38. Ehnes A, Wenner Y, Friedburg C, et al. Optical coherence tomography (OCT) device independent intraretinal layer segmentation. *Transl Vis Sci Technol* 2014;3:1.
39. Rosolen SG, Rigaudière F, Le Gargasson J-F, Brigell MG. Recommendations for a toxicological screening ERG procedure in laboratory animals. *Doc Ophthalmol* 2005;110:57–66.
40. Rosolen SG, Kolomiets B, Varela O, Picaud S. Retinal electrophysiology for toxicology studies: applications and limits of ERG in animals and ex vivo recordings. *Exp Toxicol Pathol* 2008;60:17–32.
41. Lachapelle P, Rufiange M, Dembinska O. A physiological basis for definition of the ISCEV ERG standard flash (SF) based on the photopic hill. *Doc Ophthalmol* 2001;102:157–62.
42. Rufiange M, Dassa J, Dembinska O, et al. The photopic ERG luminance-response function (photopic hill): method of analysis and clinical application. *Vision Res* 2003;43:1405–12.
43. Amado D, Mingozzi F, Hui D, et al. Safety and efficacy of subretinal readministration of a viral vector in large animals to treat congenital blindness. *Sci Transl Med* 2010;2:21ra16.
44. Binley K, Widdowson P, Loader J, et al. Transduction of photoreceptors with equine infectious anemia virus lentiviral vectors: safety and biodistribution of StarGen for Stargardt disease. *Invest Ophthalmol Vis Sci* 2013;54:4061–71.
45. Binley K, Widdowson PS, Kelleher M, et al. Safety and biodistribution of an equine infectious anemia virus-based gene

- therapy, RetinoStat(®), for age-related macular degeneration. *Hum Gene Ther* 2012;23:980–91.
46. Zallocchi M, Binley K, Lad Y, et al. EIAV-based retinal gene therapy in the shaker1 mouse model for usher syndrome type 1B: development of UshStat. *PLoS One* 2014;9:e94272.
  47. Ikeda Y, Yonemitsu Y, Miyazaki M, et al. Acute toxicity study of a simian immunodeficiency virus-based lentiviral vector for retinal gene transfer in nonhuman primates. *Hum Gene Ther* 2009;20:943–54.
  48. Thomas JA, Gagliardi TD, Alvord WG, Lubomirski M, Bosche WJ, Gorelick RJ. Human immunodeficiency virus type 1 nucleocapsid zinc-finger mutations cause defects in reverse transcription and integration. *Virology* 2006;353:41–51.
  49. Luna G, Kjellstrom S, Verardo MR, et al. The effects of transient retinal detachment on cavity size and glial and neural remodeling in a mouse model of X-linked retinoschisis. *Invest Ophthalmol Vis Sci* 2009;50:3977–84.
  50. Sakai T, Calderone JB, Lewis GP, Linberg KA, Fisher SK, Jacobs GH. Cone photoreceptor recovery after experimental detachment and reattachment: an immunocytochemical, morphological, and electrophysiological study. *Invest Ophthalmol Vis Sci* 2003;44:416–25.
  51. Testa F, Maguire AM, Rossi S, et al. Three-year follow-up after unilateral subretinal delivery of adeno-associated virus in patients with Leber congenital amaurosis type 2. *Ophthalmology* 2013;120:1283–91.
  52. Fischer MD, Hickey DG, Singh MS, MacLaren RE. Evaluation of an optimized injection system for retinal gene therapy in human patients. *Hum Gene Ther Methods* 2016;27:150–8.
  53. Verardo MR, Lewis GP, Takeda M, et al. Abnormal reactivity of muller cells after retinal detachment in mice deficient in GFAP and vimentin. *Invest Ophthalmol Vis Sci* 2008;49:3659–65.
  54. Lewis GP, Chapin EA, Luna G, Linberg KA, Fisher SK. The fate of Müller's glia following experimental retinal detachment: nuclear migration, cell division, and subretinal glial scar formation. *Mol Vis* 2010;16:1361–72.
  55. Lewis GP, Sethi CS, Carter KM, Charteris DG, Fisher SK. Microglial cell activation following retinal detachment: a comparison between species. *Mol Vis* 2005;11:491–500.
  56. Guérin CJ, Lewis GP, Fisher SK, Anderson DH. Recovery of photoreceptor outer segment length and analysis of membrane assembly rates in regenerating primate photoreceptor outer segments. *Invest Ophthalmol Vis Sci* 1993;34:175–83.
  57. Sweigard JH, Matsumoto H, Smith KE, et al. Inhibition of the alternative complement pathway preserves photoreceptors after retinal injury. *Sci Transl Med* 2015;7:297ra116.
  58. Wang J, Zarbin M, Sugino I, Whitehead I, Townes-Anderson E. RhoA signaling and synaptic damage occur within hours in a live pig model of CNS injury, retinal detachment. *Invest Ophthalmol Vis Sci* 2016;57:3892–906.
  59. Guérin CJ, Anderson DH, Fisher SK. Changes in intermediate filament immunolabeling occur in response to retinal detachment and reattachment in primates. *Invest Ophthalmol Vis Sci* 1990;31:1474–82.
  60. Narala R, Scarinci F, Shaarawy A, Simonett JM, Flaxel CJ, Fawzi AA. Longitudinal quantitative evaluation of photoreceptor volume following repair of macula-off retinal detachment. *Retina* 2016;36:1432–8.
  61. Anand V, Chirmule N, Fersh M, Maguire AM, Bennett J. Additional transduction events after subretinal readministration of recombinant adeno-associated virus. *Hum Gene Ther* 2000;11:449–57.
  62. Cideciyan AV, Jacobson SG, Beltran WA, et al. Human retinal gene therapy for Leber congenital amaurosis shows advancing retinal degeneration despite enduring visual improvement. *Proc Natl Acad Sci U S A* 2013;110:E517–25.
  63. Kostic C, Chiodini F, Salmon P, et al. Activity analysis of housekeeping promoters using self-inactivating lentiviral vector delivery into the mouse retina. *Gene Ther* 2003;10:818–21.
  64. Yáñez-Muñoz RJ, Balagán KS, MacNeil A, et al. Effective gene therapy with nonintegrating lentiviral vectors. *Nat Med* 2006;12:348–53.

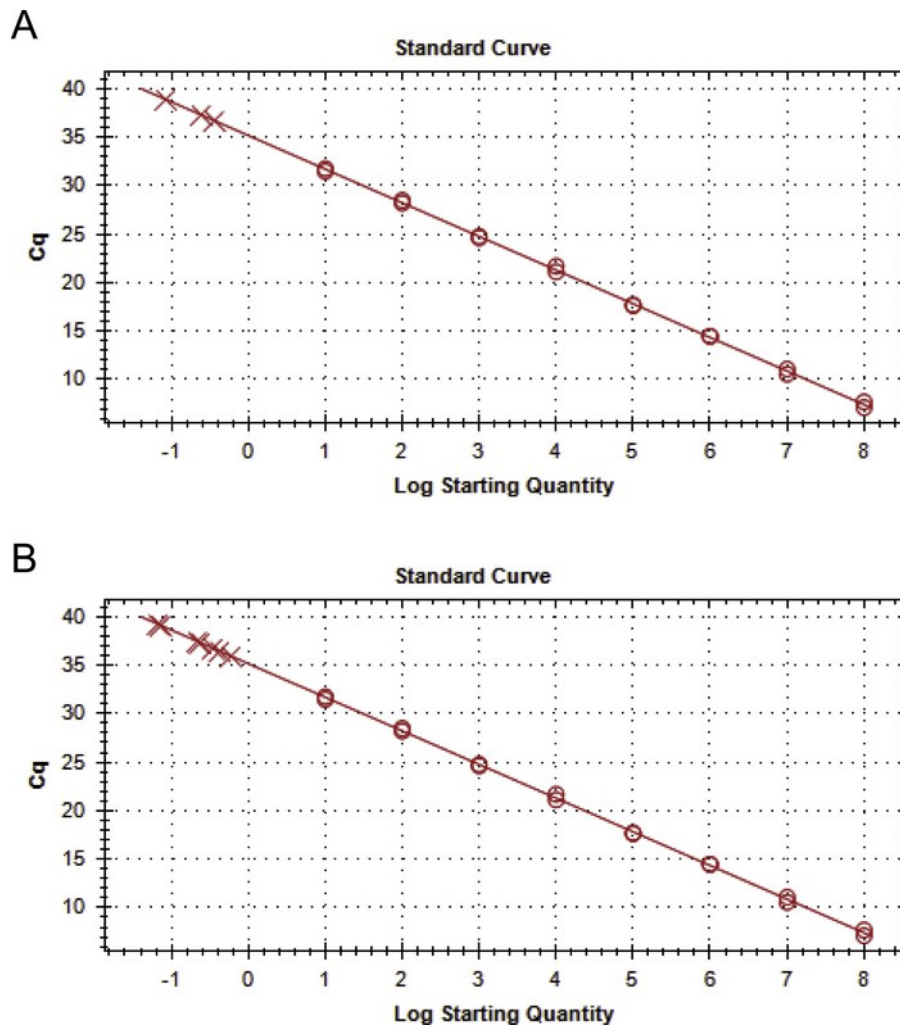
## APPENDIX



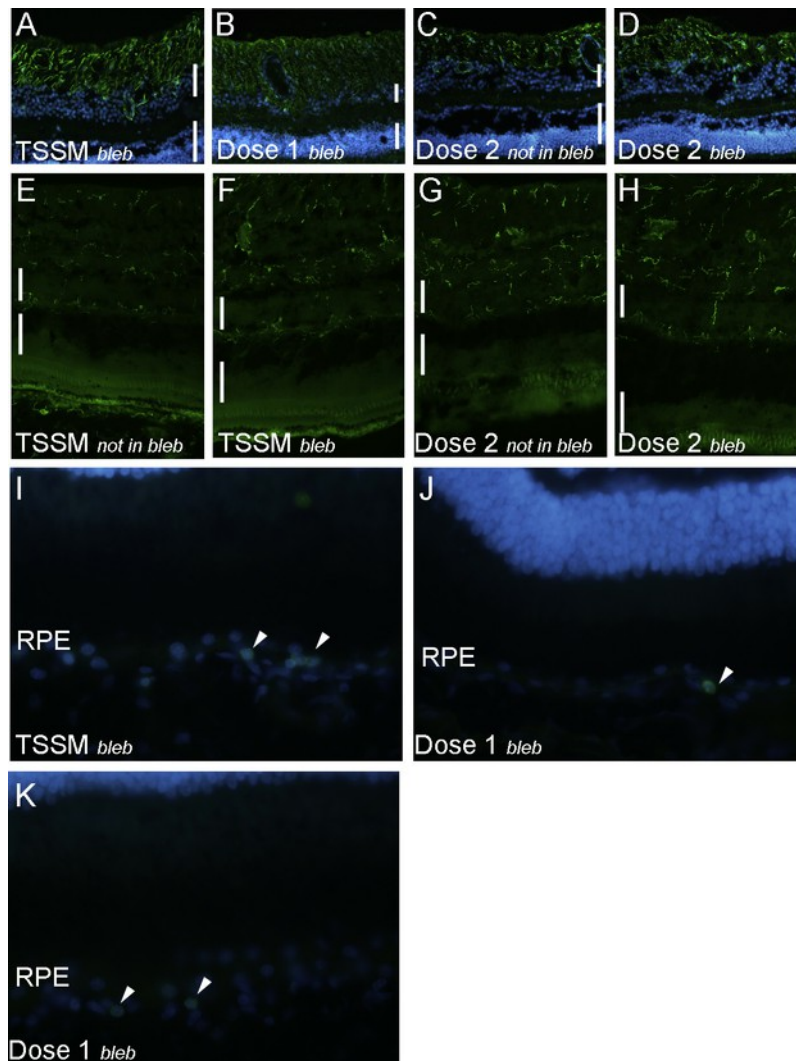
**Supplementary Fig 1.** Localization of the region of interest for segmentation of retinal layers over an identical area within the detached retina in all injected eyes, using a custom algorithm. Heat map of the total retinal thickness superimposed over the infrared reflectance image of the left eye of animal 1A, at day 30 after injection. The green disc at the center of the circular grid represents the 1-mm diameter region of interest, located 1.1 mm superior and 2.2 mm nasal to the fovea with the axis between optic disc center and fovea used as horizontal reference. A custom algorithm on the DiOCTA software was used to segment the retinal layers of this disc.



**Supplementary Fig 2.** Segmentation of retinal layers at the level of a 1-mm diameter circular region of interest localized within the detached area of all subretinally injected eyes. The region of interest is described in [Supplementary Fig 1](#). **(A)** The thickness of the photoreceptor outer segments/retinal pigment epithelium showed a moderate decrease in TSSM-injected eyes and a more pronounced decrease in LV-RPE65-injected eyes. In one eye (2A [LE]), there was a late re-increase of outer segment thickness. **(B)** The thickness of the outer nuclear layer was stable in TSSM-injected eyes, with an increase in variation at the 12-week time point and showed a moderate decrease in all LV-RPE65-injected eyes, followed by a late return to baseline thickness in eyes followed up until 12-weeks. **(C)** The thickness of inner retinal layers from the inner limiting membrane to the outer limit of the outer plexiform layer was globally stable after injection of TSSM, LV-RPE65 dose 1, or dose 2. OS, outer segment; RPE, retinal pigment epithelium; RE, right eye; LE, left eye.



**Supplementary Fig 3.** Quantitative PCR standard curve and serum samples from macaque 2A. **(A)** Standard curve was established with the shuttle plasmid containing the RPE65 recombinant lentiviral genome. Open circles represent 10-fold serial dilutions of plasmid DNA ranging from  $10^8$  to 10 copies (duplicates). Crosses represent the negative control without DNA showing the absence of amplification (triplicate). Linear regression:  $r^2 = 0.999$ . **(B)** The same standard curve as in A (open circles, duplicates) and serum samples of macaque 2A (each cross represents one sample in duplicate,  $n = 6$  postinjection samples + 1 baseline sample) were processed in the same experiment. For all the samples tested ( $n = 91$ ), either amplification did not reach the detection threshold or the Cq value did not fall below 35.



**Supplementary Fig 4.** Long-term evaluation of retinal reattachment using immunohistochemistry. (A–D) GFAP labeling (green) of the region of retinal detachment (detached) after injection of TSSM (A, animal C-RE), LV-RPE65 dose 1 (B, animal 1A-LE), or LV-RPE65 dose 2 (D, animal 2B-LE) is not different from labeling of retinal region not targeted by injection (undetached; C, animal 2B-LE). (E–H) Iba-1 labeling (green) of microglial cells is also similar between detached retina after injection of TSSM (F, animal C-RE) or after injection of LV-RPE65 dose 2 (H, animal 2A-LE) and undetached region of the same eye (respectively, E and G). (I–K) CD45 labeling (green) of leukocytes (arrowheads) revealed few leukocytes localized close to the RPE layer in both TSSM (I, animal 1A-RE) or LV-RPE65-injected eyes (J, animal 1B-RE, K, 1A-LE). A–D, I–K: DAPI counterstaining in blue; A–H: upper vertical white bars localize the inner nuclear layer and lower vertical white bars localize the outer nuclear layer; RPE, retinal pigment epithelium; GFAP, glial fibrillary acid protein.

[2a] Acute central serous chorioretinopathy: Factors influencing episode duration. *Retina* 2017

Daruich A, Matet A, Marchionno L, De Azavedo JD, Ambresin A, Mantel I, Behar-Cohen F<sup>28</sup>

doi: 10.1097/IAE.0000000000001443.

Contribution of PhD candidate:

- Processing and analysis of multimodal imaging data
- Survival statistical analysis
- Co-drafting the manuscript



# ACUTE CENTRAL SEROUS CHORIORETINOPATHY

## Factors Influencing Episode Duration

ALEJANDRA DARUICH, MD,\* ALEXANDRE MATET, MD,\* LAETITIA MARCHIONNO, OD,\* JEAN-DOMINIQUE DE AZEVEDO, OD,\* AUDE AMBRESIN, MD,\* IRMELA MANTEL, MD,\* FRANCINE BEHAR-COHEN, MD, PhD\*†‡§

**Purpose:** To evaluate the influence of clinical and multimodal imaging parameters on the duration of acute central serous chorioretinopathy (CSCR) episodes.

**Methods:** Consecutive patients with first, treatment-naïve central serous chorioretinopathy episodes presenting within 20 days of symptoms onset were prospectively included. They were reevaluated 15 days to 20 days later, followed by monthly evaluation for 6 months. Subfoveal choroidal thickness (SFCT), fluorescein leakage intensity on fluorescein angiography, elevation of retinal pigment epithelium (RPE) lesions at leakage sites, focal/multifocal pattern of indocyanine green angiography (ICGA) at baseline, time-dependent pattern of subretinal fluid (SRF) resorption on OCT using volume segmentation, history of corticosteroid intake and mean blood pressure were evaluated using univariate (Log rank test) and multivariate (Cox proportional hazard regression) survival analysis.

**Results:** Thirty-one patients were included (26 men, 5 women, mean age:  $40.0 \pm 8.9$  years, range: 24–58), of which 26 (84%) had episode resolution by 6 months. Using univariate analysis, episode duration was longer in cases with subfoveal choroidal thickness  $\geq 500 \mu\text{m}$  ( $P = 0.0002$ ), retinal pigment epithelium elevation at leakage sites  $\geq 50 \mu\text{m}$  ( $P = 0.033$ ), and a peak in subretinal fluid observed during follow-up ( $P = 0.013$ ), and there was a near-significant association of intense fluorescein leakage ( $P = 0.074$ ) with longer episodes. Using multivariate analysis, subfoveal choroidal thickness  $\geq 500 \mu\text{m}$  ( $P = 0.017$ ), retinal pigment epithelium elevation at leakage sites  $\geq 50 \mu\text{m}$  ( $P = 0.010$ ) and patient age  $\geq 40$  years ( $P = 0.010$ ) were significantly and independently associated to longer episodes. Indocyanine green angiography pattern, corticosteroid intake, and blood pressure did not influence episode duration.

**Conclusion:** Older age, higher subfoveal choroidal thickness, and higher degree of retinal pigment epithelium alteration at leakage sites are independent factors of longer acute central serous chorioretinopathy episodes.

RETINA 0:1–11, 2016

Central serous chorioretinopathy (CSCR) is a chorioretinal disorder characterized by serous retinal detachments frequently involving the macula and usually associated with focal pigment epithelial detachments (PED), choroidal hyperpermeability, and increased choroidal thickness. Acute CSCR classically affects middle-aged working male individuals, whose working ability may be compromised by the associated visual burden. Because serous retinal detachments resolve spontaneously within six months in most acute CSCR episodes,<sup>1–3</sup> observation without treatment is generally recommended as initial management.<sup>4</sup> For cases with persistent serous retinal detachment or

severe vision loss, several treatment options are available. Photocoagulation of extramacular leaking points by direct argon<sup>2,3</sup> or micropulse laser<sup>5,6</sup> can reduce the duration of single episodes. Half-dose or half-fluence verteporfin photodynamic therapy (PDT) may contribute to shorten episode duration.<sup>7–12</sup> Oral treatment by mineralocorticoid-receptor (MR) antagonists has also shown beneficial effects.<sup>4,13–18</sup> However, the ideal timing for these different interventions still remains to be determined. A better understanding of factors influencing episode duration would help to detect and treat earlier cases at risk for persistence, before the development of photoreceptor and RPE damage

because of long-lasting subretinal detachment. Because choroidal vasodilation and leakage through the RPE are key mechanisms leading to CSCR<sup>4</sup> and because most of subretinal fluid resorption depends on the pumping capacity of RPE cells, several features involved in choroid/RPE physiology may influence acute episode duration, among which subfoveal choroidal thickness, elevation of PED, intensity of RPE leakage and choroidal hyperpermeability, initial subretinal fluid volume, time-dependent fluid resorption pattern, patient age, history of steroid intake, and arterial blood pressure. Although these factors can be accessed on routine clinical examination and retinal imaging, their influence on episode duration has not been previously investigated.

The aim of this study was to evaluate the influence of these ocular and systemic factors on the duration and resolution of first, treatment-naïve, acute CSCR episodes.

## Methods

### Subjects

This observational, single-center, prospective study was designed in accordance with the tenets of the Declaration of Helsinki. Data collection and analysis was approved by the Ethics Committee of the Swiss Federal Department of Health (CER-VD no. 19/15). All patients signed an informed consent. Consecutive patients presenting at Jules-Gonin Eye Hospital (Lausanne, Switzerland) with a first episode of acute, unilateral, and treatment-naïve CSCR from January 1, 2014 to October 31, 2015 were included. A CSCR episode was defined as the association of visual symptoms (vision impairment, metamorphopsia, micropsia, dyschromatopsia or central scotoma) in the presence of subretinal fluid on spectral-domain optical coherence tomography (SD-OCT) with a leaking site on

fluorescein angiography (FA) and choroidal vascular hyperpermeability on indocyanine green angiography (ICGA). Exclusion criteria were: initial presentation later than 20 days after symptoms onset, follow-up shorter than 6 months without resolution, spherical error superior to 2 D, and presence of pigmentary changes on funduscopy or fundus autofluorescence modifications suggestive of previous CSCR episodes. The follow-up scheme for this observational study included a second visit within 10 days to 20 days of the baseline visit, followed by repeated monthly clinical evaluation for 6 months. Ocular and medical history, including history of corticosteroid intake, ocular examination, arterial blood pressure measured at the initial visit, and the time from symptoms onset (vision loss, metamorphopsia, micropsia, dyschromatopsia, or central scotoma) to the first visit, were recorded. Central serous chorioretinopathy episode resolution was defined as the complete reabsorption of subretinal fluid (SRF) on SD-OCT images acquired as described below. In case of nonresolution of SRF at six months, a rescue therapy was proposed. Laser photocoagulation was performed if the leaking site was located more than 1,000  $\mu\text{m}$  from the foveal center. If laser was not possible, mineralocorticoid-receptor antagonist therapy by oral eplerenone (25 mg daily) or spironolactone (25 mg daily) was administered in the absence of contraindications, and otherwise photodynamic therapy was used.

### Retinal Imaging

Imaging was performed after standard pupillary dilation using tropicamide 0.5% drops with the Spectralis (Heidelberg Engineering, Heidelberg, Germany). At all visits, a  $20^\circ \times 20^\circ$  97-sections SD-OCT macular volume, a  $30^\circ$  enhanced-depth imaging (EDI) SD-OCT horizontal scan through the fovea the “automatic real time” averaging set at the maximal value of 100 images, a  $30^\circ \times 30^\circ$  fundus infrared reflectance, and a  $30^\circ \times 30^\circ$  fundus autofluorescence were acquired. Fluorescein angiography and green indocyanine-green angiography were performed at the baseline visit.

For each case, the site of maximum fluorescein leakage on FA was identified by one observer (FBC). The height of pigment epithelial defects at these sites, consisting in PED or RPE bumps, was measured by a single observer (AD) using the built-in Spectralis software (Heidelberg Eye Explorer, version 1.9.10.0). Elevation was defined as 0  $\mu\text{m}$  when no RPE lesion associated with the leakage site was observed.

The subfoveal choroidal thickness (SFCT) was measured by the same observer on baseline enhanced-depth imaging scans as the axial distance from the RPE to the outer choroid/sclera interface. In

From the \*Department of Ophthalmology, University of Lausanne, Jules-Gonin Eye Hospital, Fondation Asile des Aveugles, Lausanne, Switzerland; †Sorbonne Universités, UPMC Université Paris 06, UMR 1138, Centre de Recherche des Cordeliers, Team 1 and 17, Paris, France; ‡INSERM, UMR 1138, Centre de Recherche des Cordeliers, Paris, France; and §Université Paris Descartes, Sorbonne Paris Cité, UMR 1138, Centre de Recherche des Cordeliers, Paris, France.

None of the authors has any financial/conflicting interests to disclose.

This is an open-access article distributed under the terms of the Creative Commons Attribution-Non Commercial-No Derivatives License 4.0 (CCBY-NC-ND), where it is permissible to download and share the work provided it is properly cited. The work cannot be changed in any way or used commercially without permission from the journal.

Reprint requests: Francine Behar-Cohen, MD, PhD, Department of Ophthalmology, University of Lausanne, Jules-Gonin Eye Hospital, Fondation Asile des Aveugles Avenue de France 15, 1004 Lausanne, Switzerland; e-mail: francine.behar@gmail.com

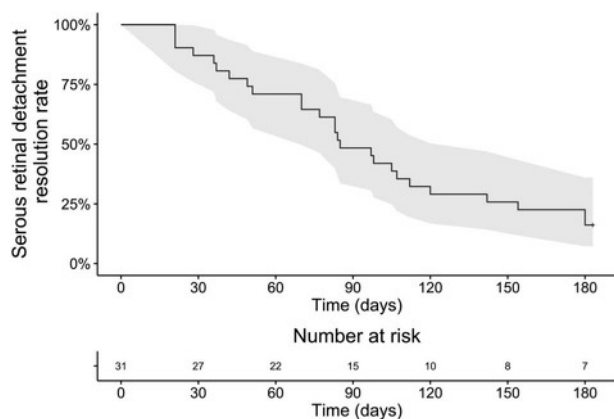


**Fig. 1.** Survival curve showing the time-dependent resolution rate of 31 acute episodes of central serous chorioretinopathy from the time of the initial visit. All patients presented within 20 days after onset of symptoms. By 6 months, resolution was observed in 26 patients. The 95% confidence interval is colored in gray.

cases where the interface was ambiguous, the senior author (FBC) determined the SFCT. The maximal height of subretinal detachment was measured similarly as the axial distance between the RPE and the outer aspect of photoreceptor outer segments.

The macular volume was automatically measured by the software over an Early Treatment Diabetic Retinopathy Study (ETDRS) grid centered on the macula.

Multifocal choroidal hyperpermeability was defined as the presence of several hypercyanescent areas on midphase indocyanine-green angiography (10–12 minutes after dye injection).

#### Fluorescein Expansion Ratio

The intensity of leakage at the previously identified leakage sites on FA was estimated by quantifying the relative expansion of hyperfluorescence from early phase (40–60 seconds) to midphase (2–2.5 minutes). Angiograms were exported as TIFF files and were processed on Matlab using a semiautomated custom algorithm adapted from the method described by Prydz et al.<sup>19</sup> The leakage site was indicated manually, and the borders of the hyperfluorescent area were automatically detected using the grayscale intensity threshold of  $0.75 \times I_{max}$ , where  $I_{max}$  is the maximal fluorescence intensity at the leakage site. The ratio between hyperfluorescent areas at midphase and early phase was calculated to provide the fluorescein leakage ratio.

#### Subretinal Fluid Volume

The volume of subretinal fluid was calculated at each timepoint using a custom-built algorithm on Matlab (version 2015b; Mathworks, Natick, MA). Briefly, the 97 SD-OCT scans corresponding to the macular volume

**Table 1.** Clinical and Imaging Characteristics of 31 Patients With a First Episode of Acute, Treatment-Naive Central Serous Chorioretinopathy

Subjects (male/female), N	31 (26/5)
Age, years	40.0 ± 8.9 (24.3–58.3)
Cases with CSCR episode resolution by 6 months, N (%)	26 (83.9)
Time to CSCR episode resolution, days	83 ± 46 (21–180)
Time from symptoms onset to first visit, days	9.0 ± 6.2 (0–20)
Type of RPE lesion at leakage sites, N (%)	
PED	13 (41.9)
REP bump	14 (45.2)
No lesion	4 (12.9)
RPE elevation at leakage sites, $\mu\text{m}$	58.1 ± 53.3 (0–279)
Subfoveal choroidal thickness, $\mu\text{m}$	479.9 ± 82.2 (302–619)
Fluorescein expansion ratio on FA	2.8 ± 2.1 (1.0–9.4)
Multifocal choroidal hyperpermeability on ICGA, N (%)	13 (41.9)
Initial SRF volume, mL	0.92 ± 0.95 (0.03–4.27)
Observation of a peak in SRF volume, N (%)	13 (41.9)
Time from first visit to SRF peak observation, days	42.6 ± 18.2 (15–64)
Baseline visual acuity logMAR (Snellen equivalent)	0.10 ± 0.13 (0–0.53) (~20/25 [20/66–20/20])
Final visual acuity logMAR (Snellen equivalent)	0.03 ± 0.08 (0–0.30) (~20/21 [20/40–20/20])
Mean blood pressure, mmHg	110.9 ± 9.4 (92.5–136.5)
History of corticosteroid intake, N (%)	11 (35.4)

Continuous values are reported as mean ± SD (range), where appropriate.

CSCR, central serous chorioretinopathy; FA, fluorescein angiography; ICGA, indocyanine green angiography; logMAR, logarithm of the minimal angle of resolution; RPE, retinal pigment epithelium; SRF, subretinal fluid.

were exported as PNG files, and the borders of the serous retinal detachment were segmented on each scan using an intensity-based method. After visual verification of the segmentation, the volume was obtained by trapezoidal integration, and a heat map of the subretinal detachment was generated. The kinetics of SRF resorption was then analyzed in each patient by comparing SRF volumes at each timepoint.

#### Statistical Analyses

Survival analyses were performed using the R software (version 3.1.3; R Foundation for Statistical Computing, R Core Team, 2015, Vienna, Austria).

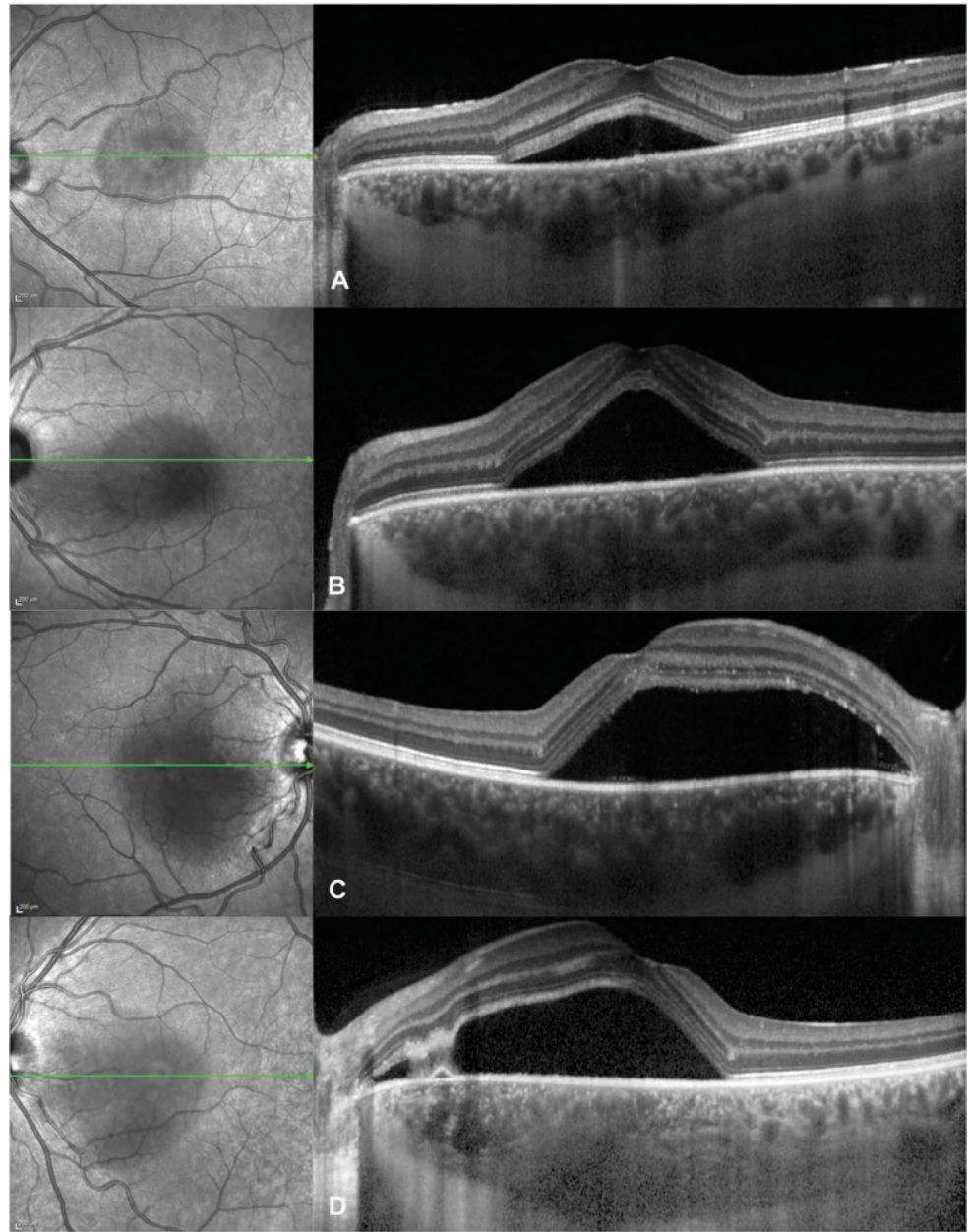


**Fig. 2.** Spectrum of subfoveal choroidal thickness in acute central serous chorioretinopathy, visible on optical coherence tomography scans (right) passing through the fovea as indicated by the green arrows on infrared images (left): (A) 403  $\mu$ m in a 37-year-old man, (B) 469  $\mu$ m in a 28-year-old man, (C) 519  $\mu$ m in a 38-year-old man, and (D) 617  $\mu$ m in a 34-year-old man.

<http://www.R-project.org/>). The Kaplan–Meier method with log-rank tests was used for univariate analyses, and the Cox proportional hazard method for the multivariate analysis, with the “survival”<sup>20</sup> package. Results were expressed in terms of hazard ratio and adjusted hazard ratio, respectively. Parameters resulting in a  $P$  value  $\leq 0.2$  in the univariate analysis were entered in the multivariate model, followed by stepwise regression with the “MASS”<sup>21</sup> package. Survival curves were generated with the “ggplot”<sup>22</sup> and “survminer” packages. For each investigated parameter, a dichotomizing value was searched that defined 2 groups with a significant difference in

episode resolution rate, under the condition that the smallest group was formed by  $\geq 11$  patients (one-third of the study population).

Agreement between segmentation of subretinal fluid volume, maximal subretinal fluid height on SD-OCT, and macular volume was estimated using Cohen’s Kappa on R, with the “irr” package.<sup>23</sup>

Spearman correlation coefficients were used to investigate association between variables on GraphPad Prism (version 5.0f; GraphPad Software, La Jolla, CA). The logarithm of the minimal angle of resolution (LogMAR) was used to calculate visual acuity means.  $P$  values  $\leq 0.05$  were considered significant.

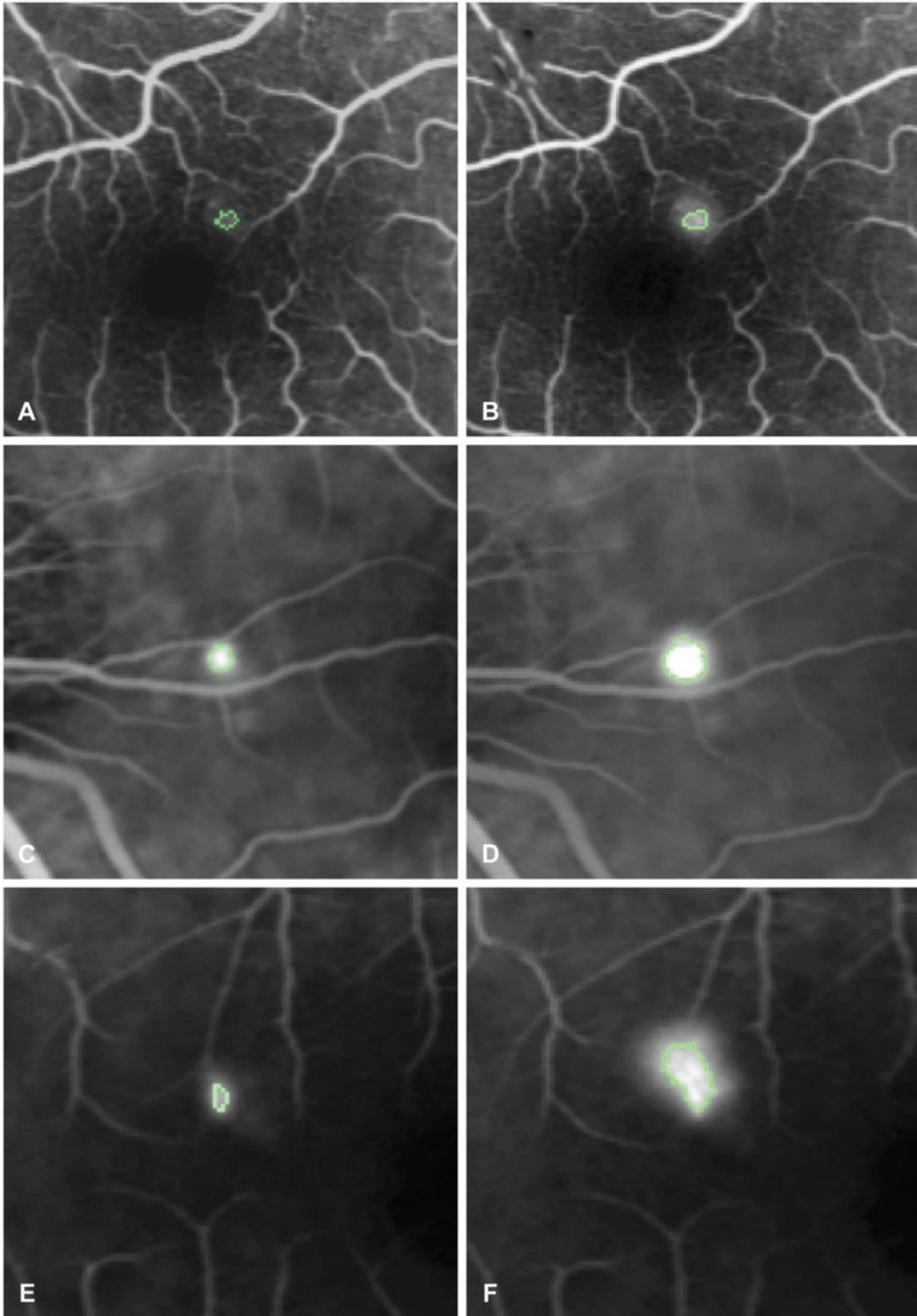


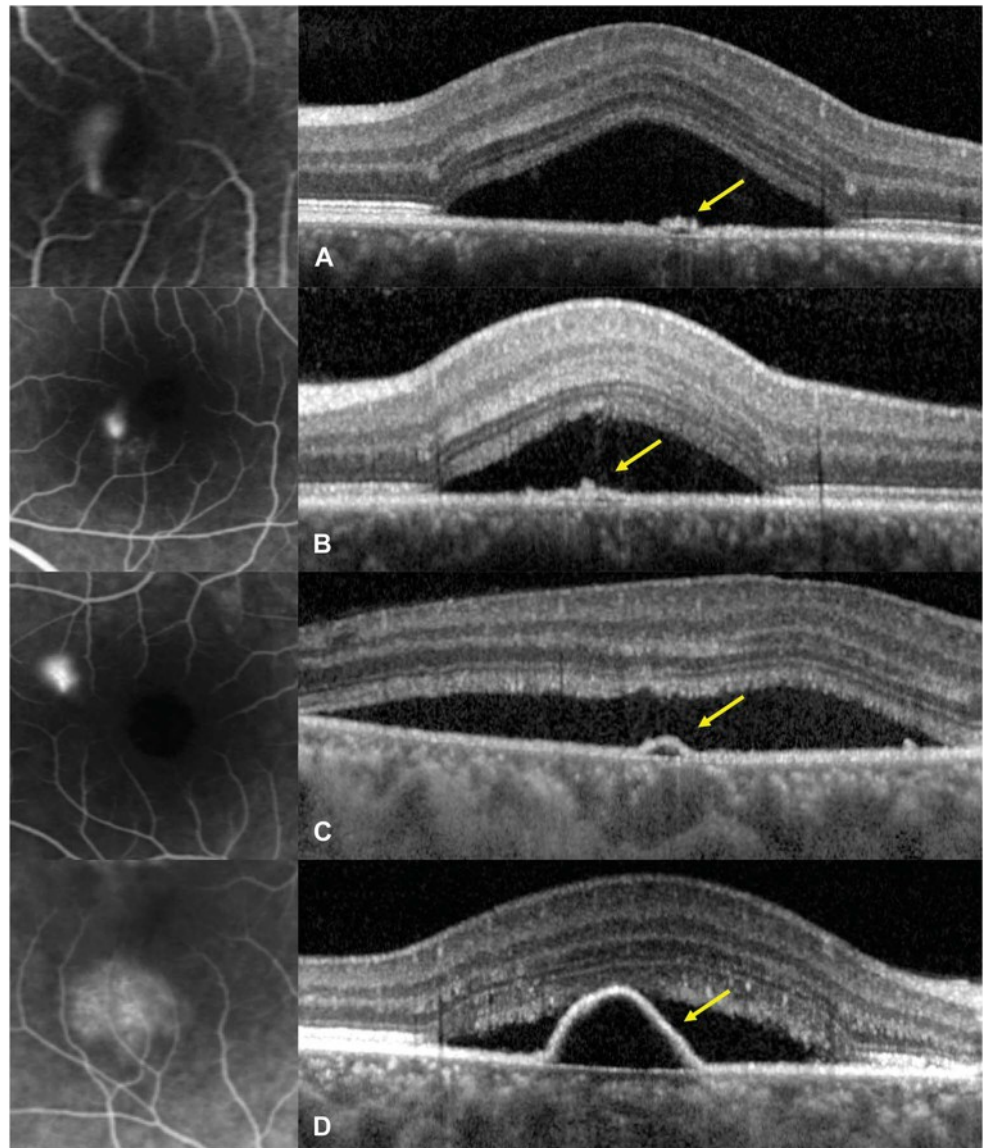
**Fig. 3.** Method to quantify fluorescein leakage expansion on fluorescein angiography from early phase (40–60 seconds) to midphase (2–2.5 minutes). **A** and **B**. Early phase (**A**) and midphase (**B**) angiograms in a case with a very weak leakage. The hyperfluorescent area corresponding to pixels whose intensity is comprised within 75% of the maximal hyperfluorescence is indicated by a green outline. The fluorescein expansion ratio was calculated as the ratio between the hyperfluorescent areas at midphase and early phase and was 1.32. **C** and **D**. Same method applied to early phase (**C**) and midphase (**D**) angiograms from a case with intermediate ink-blot leakage pattern, yielding a fluorescein expansion ratio of 3.98. **E** and **F**. Same method applied to early (**E**) and midphase (**F**) angiograms from a case with intense smokestack leakage pattern, yielding a fluorescein expansion ratio of 6.01.

## Results

Of 35 patients presenting with acute CSCR during the study period, 31 fulfilled the inclusion criteria. There were 26 men and 5 women, with a mean age of  $40.0 \pm 8.9$  years (median: 37.8 years, range: 24.3–58.3 years). After 6 months of follow-up, CRSC episodes were resolved in  $n = 26$  patients (83.9%) and persisted in  $n = 5$  patients (16.1%). Among

resolved cases, the mean time from the initial visit to resolution was  $83 \pm 46$  days (median: 83 days, range: 21–180 days). Four cases (12.9%) were resolved after 1 month, 9 cases (29.0%) after 2 months, 16 cases (51.6%) after 3 months, 21 cases (67.7%) after 4 months, and 23 cases (74.2%) after 5 months. A survival curve displaying the time-dependent resolution rate of the 31 cases is displayed in Figure 1.

**Fig. 4.** Optical coherence tomography of pigment epithelial lesions (right) at leaking sites on fluorescein angiograms (left) in acute central serous chorioretinopathy. A and B. Pigment epithelial bumps (yellow arrows) with estimated height of 25 mm in a 36-year-old man (A) and 41mm in a 28-year-old man (B). C and D. Pigment epithelial detachments (yellow arrows) with estimated height of 54 mm in a 39-year-old man (C) and 163 mm in a 52-year-old woman (D).



Clinical and imaging characteristics are summarized in Table 1. Subfoveal choroidal thickness ranged from 302  $\mu\text{m}$  to 619  $\mu\text{m}$  (mean: 479.9  $\mu\text{m}$ ) (Figure 2), the fluorescein expansion ratio ranged from 1.0 to 9.4 (mean: 2.8) (Figure 3), 13 patients had a PED, 14 had a RPE bump, and 4 had no RPE lesion at the leakage site, and the corresponding RPE elevation ranged from 0  $\mu\text{m}$  to 279  $\mu\text{m}$  (mean: 58.1  $\mu\text{m}$ ) (Figure 4). When analyzing the kinetics of subretinal fluid resorption using serial SRF volume segmentation on SD-OCT, a peak in SRF volume (higher than the initial value) was observed in  $n = 13$  subjects during follow-up (Figure 5), while  $n = 18$  subjects presented a progressive decrease in SRF volume from the initial visit (Figure 6). The mean time from the first visit to observed SRF volume peak was 42.6 days. A peak in

macular volume on SD-OCT was also detected at the same timepoints in these subjects ( $\text{kappa} = 1.0$ ,  $P < 0.0001$ ), but there was only a moderate agreement in peak detection between subretinal fluid volume and maximal height of subretinal detachment on SD-OCT ( $\text{kappa} = 0.49$ ,  $P = 0.0013$ ).

Using univariate survival analysis, the duration of CSCR episodes was longer in patients with SFCT  $\geq 500 \mu\text{m}$  ( $P = 0.0002$ ), those with RPE elevation at leakage sites higher than 50  $\mu\text{m}$  ( $P = 0.033$ ) and those with a peak in subretinal fluid observed during follow-up ( $P = 0.013$ ). There was a near-significant association of intense fluorescein leakage (fluorescein expansion ratio  $\geq 2$ ) with longer episodes ( $P = 0.074$ ). In contrast, patient age ( $P = 0.18$ ), initial subretinal fluid volume ( $P = 0.12$ ),

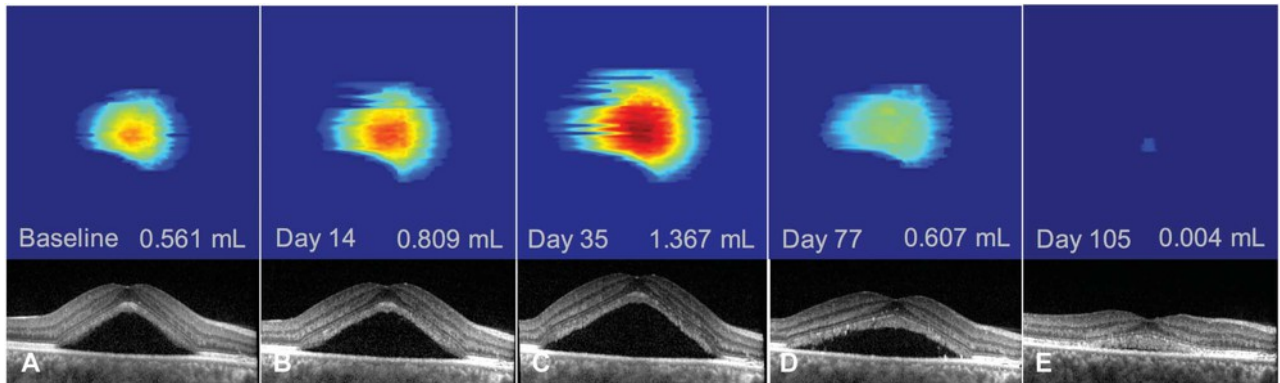


**Fig. 5.** Follow-up of an acute episode of central serous chorioretinopathy in a 52-year-old woman using subretinal fluid volume segmentation on optical coherence tomography. There was an initial increase in subretinal fluid from baseline (A–B) with a peak in subretinal fluid volume at Day 35 (C) and subsequent decrease (D–E) until subretinal fluid resolution at Day 132 (not shown). Note the shape of a pigment epithelial detachment visible on the segmented serous retinal detachment (same patient as Figure 4D).

focal/multifocal pattern of choroidal hyperpermeability on indocyanine-green angiography ( $P = 0.63$ ), history of corticosteroid intake ( $P = 0.98$ ), or mean arterial blood pressure ( $P = 0.67$ ) did not have a significant effect on episode durations.

Variables with a significance level  $\leq 0.2$  were selected for the Cox multivariate survival model, with the assumption of proportional hazard. After stepwise multivariate regression, SFCT ( $\geq 500 \mu\text{m}$ ,  $P = 0.017$ ), RPE elevation at leakage sites ( $\geq 50 \mu\text{m}$ ,  $P = 0.010$ ), and patient age ( $\geq 40$  years,  $P = 0.010$ ) remained independent significant contributors to longer duration of CSCR episodes. Comparative survival curves are displayed in Figures 7 and 8 and detailed survival results are reported in Table 2.

To confirm the robustness of these findings, we repeated the same analyses with the time from symptoms onset (as reported by the patient), instead of the time from the first visit. This modification did

not affect the results nor the significance levels in both the univariate and multivariate analyses.

To understand differences between univariate and multivariate results, we investigated possible correlations between variables. There were significant correlations between initial subretinal fluid volume and SFCT ( $r = 0.36$ ,  $P = 0.046$ ); between observation of a peak in subretinal fluid and SFCT ( $r = 0.45$ ,  $P = 0.010$ ); between the fluorescein expansion ratio and the observation of a peak in subretinal fluid ( $r = 0.39$ ,  $P = 0.036$ ), the RPE elevation at leakage sites ( $r = 0.46$ ,  $P = 0.026$ ), and the initial subretinal fluid volume ( $r = 0.58$ ,  $P = 0.001$ ). There was a near-significant trend between SFCT and fluorescein expansion ratio ( $r = 0.33$ ,  $P = 0.082$ ). There was also a near-significant, inverse correlation between patient age and SFCT ( $r = -0.31$ ,  $P = 0.09$ ), providing a likely explanation for the nonsignificance of age in the univariate analysis. However, both

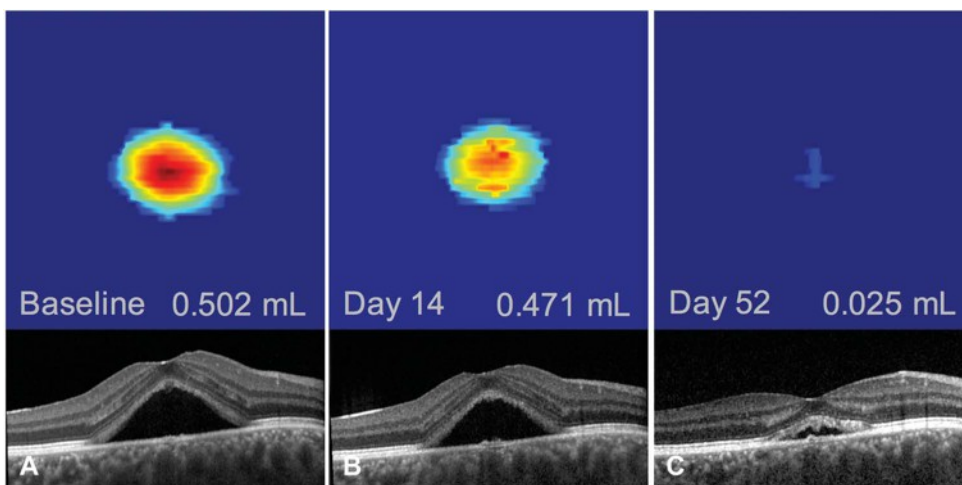


**Fig. 6.** Follow-up of an acute episode of central serous chorioretinopathy in a 35-year-old man using subretinal fluid volume segmentation on optical coherence tomography. No increase in subretinal fluid volume could be observed, with a progressive decrease from baseline (A) to all timepoints (B and C) and resolution at Day 75 (not shown).

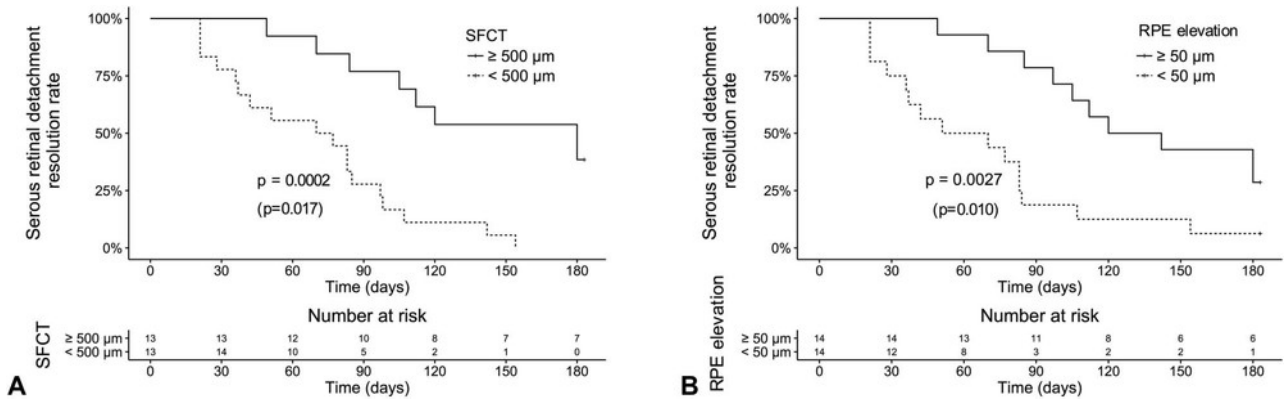


**Fig. 7.** Comparative survival curves showing the rate of subretinal detachment resolution over time about SFCT (A) and the height of RPE elevations at leakage sites (B) on optical coherence tomography. The duration from initial visit to episode resolution was significantly longer for subfoveal choroidal thickness  $\geq 500 \mu\text{m}$  (A) and pigment epithelium elevation  $\geq 50 \mu\text{m}$  (B) both in the univariate and multivariate analyses. *P*-values from the univariate (log-rank test) and the multivariate analysis (Cox proportional hazard model, between parenthesis) are reported.

parameters remained independent, consistently with the results of the multivariate model.

### Discussion

In acute CSCR, a serous retinal detachment of the macula is generally not considered a threat for visual function because visual acuity is not or mildly decreased and recovers completely in most cases. But altered quality of vision is a frequent complaint of patients despite normal visual acuity levels and macular microstructure. Electrophysiology studies of acute CSCR demonstrated that abnormal cone function observed during an active episode persists after resolution.<sup>24–27</sup> Poorer recovery is associated with longer symptom duration although the duration threshold before permanent functional damage has not been clearly deter-

mined.<sup>28</sup> This threshold would help to define the optimal treatment timing for nonresolving cases.

In this study, we have analyzed the natural history of acute, treatment-naïve first episodes of CSCR and have correlated the duration of subretinal fluid persistence with clinically available parameters. We have found that longer episode duration was independently associated with higher SFCT, higher elevation of RPE lesions at leakage sites, and older age.

Current hypotheses regarding the pathophysiology of CSCR include choroidal vascular dilation manifesting by choroidal thickening (or pachychoroid),<sup>29,30</sup> possibly because of inappropriate activation of the mineralocorticoid pathway,<sup>31,32</sup> with concurrent RPE alterations.<sup>33</sup> However, the mechanisms involved in SRF resolution or persistence are not fully understood. Genetic studies of nonresolving CSCR cases have reported an association with variants in the Complement Factor H, ARMS 2 and Cadherin 5 genes,<sup>34–36</sup> which

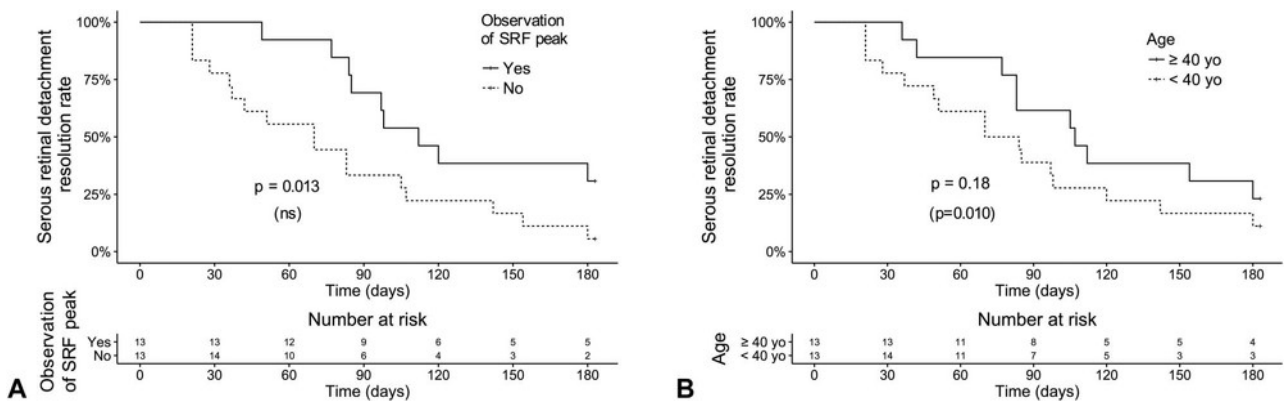


**Fig. 8.** Comparative survival curves showing the rate of subretinal detachment resolution over time about the observation of a peak in SRF on optical coherence tomography (A) and patient age (B). The duration from initial visit to episode resolution was significantly longer for cases with an observed peak in subretinal fluid volume in the univariate analysis only (A). Episodes were also longer for patients aged 40 years or older in the multivariate analysis only (B). *P*-values from the univariate (log-rank test) and the multivariate analysis (Cox proportional hazard model, between parenthesis) are reported. ns, nonsignificant contributor to the multivariate model.

Table 2. Factors Influencing the Duration of Acute, Treatment-Naive, First CSCR Episodes by Univariate and Multivariate Survival Analysis

	Univariate*		Multivariate†	
	HR (95% CI)	P	aHR (95% CI)	P
<b>Ocular factors</b>				
SFCT $\geq 500 \mu\text{m}$	0.19 (0.08–0.46)	0.0002	0.29 (0.10–0.80)	0.017
RPE elevation at leakage site $\geq 50 \mu\text{m}$	2.46 (1.07–5.65)	0.033	0.26 (0.09–0.73)	0.010
Peak in subretinal volume observed during follow-up	0.35 (0.16–0.80)	0.013	—	—
Initial serous retinal detachment volume $\geq 1 \text{ mL}$	1.88 (0.85–4.16)	0.12	—	—
Fluorescein leakage ratio $\geq 2$ on FA	2.22 (0.93–5.31)	0.074	—	—
Multifocal choroidal hyperpermeability on midphase ICGA	0.82 (0.37–1.82)	0.63	—	—
<b>Systemic factors</b>				
Age $\geq 40$ years	1.71 (0.78–3.74)	0.18	0.23 (0.07–0.70)	0.010
History of corticosteroid intake	0.99 (0.44–2.22)	0.98	—	—
Mean arterial blood pressure $\geq 110 \text{ mmHg}$	1.19 (0.54–2.61)	0.67	—	—

\*Log-Rank statistics.

†Cox proportional hazard model followed by stepwise multivariate regression.

aHR, adjusted hazard ratio; CI, confidence interval; FA, fluorescein angiography; HR, hazard ratio; ICGA, indocyanine green angiography; RPE, retinal pigment epithelium; SFCT, subfoveal choroidal thickness.

are expressed by RPE cells.<sup>37–39</sup> These findings suggest that RPE changes contribute to the evolution toward nonresolving CSCR. They are consistent with previous fluorescein angiography studies of CSCR<sup>40–42</sup> demonstrating that SRF originates from an abnormal passage from the choroid through the RPE, overwhelming the pumping outflow capacity of RPE cells. From this perspective, the association of longer episode duration with higher SFCT and higher elevation of RPE lesions at leakage sites are additional evidence that the degree of choroidal and RPE dysfunction is predictive of the final outcome.

Another interesting finding is the association of episode duration with older age. In aged human maculae, RPE cells increase in size and lose their regular hexagonal shape.<sup>43</sup> Studies of aging primate eyes have shown that mitochondrial elongation is observed within RPE cells located of the macular area, an indicator of increased metabolic stress.<sup>44</sup> In aged mouse eyes, RPE cells undergo multinucleation because of aborted mitosis, one of the mechanisms of cell death, and the contact with photoreceptor outer segments inhibits RPE cell proliferation.<sup>45</sup> Altogether, these observations indicate that the repair capacity of the RPE decreases with aging, particularly in the macula. This supports the notion that older age is associated with longer CSCR episodes, which may ultimately contribute to the chronic epitheliopathy frequently seen in older CSCR patients.<sup>46</sup>

We are unaware of previous reports relating the time-course of acute CSCR episodes to clinical and multimodal imaging features. In a study of 27 eyes

with acute CSCR performed before the OCT era, Klein et al<sup>1</sup> related the time-course of the disease to baseline and final fluorescein angiography and repeated fundus examinations. The mean time of resolution was 6 months after symptoms onset, with a maximal observed duration of 12 months. More recently, Pryds et al<sup>19</sup> have investigated the fluorescein leakage rate based on early FA frames in cases with typical smokestack leaks, using a method adapted in the present study. They observed variable leakage rates, a finding consistent with our results, but did not correlate with other clinical characteristics. Yang et al<sup>47</sup> have described the multimodal correlations between RPE alterations including PED on SD-OCT, FA, and indocyanine-green angiography in CSCR patients but did not relate these findings to the duration of episodes.

The present study may have practical consequences for the management of acute CSCR patients. Eighty-four percent of consecutive patients demonstrated spontaneous resolution of SRF within 6 months, confirming that observation for up to 6 months is an appropriate initial management. However, patients with SFCT  $\geq 500 \mu\text{m}$ , PED with elevation  $\geq 50 \mu\text{m}$ , or age  $\geq 40$  years may be identified and warned of a higher risk of longer CSCR duration, with a subsequent need for a longer follow-up and/or earlier treatment decision. Although they were not independent risk factors, observation of a peak in SRF during follow-up and to a lesser extent an intense leakage on the baseline FA may also contribute to identify clinically patients at risk of longer episodes. Further

studies are required to evaluate whether longer durations of macular serous detachment are associated with worse vision quality and higher risks of CSCR recurrence.

Limitations of this work include the size of the study population because of its prospective nature and the iterative subretinal fluid follow-up that prevented a continuous analysis of subretinal fluid evolution. As a result, peaks in subretinal fluid volume may have been missed, either between follow-up timepoints, or before the initial visit. To minimize this flaw, we excluded patients presenting more than 20 days after symptoms onset and densified the initial follow-up schedule. In addition, we did not consider recently described imaging signs in CSCR such as hyporeflective subretinal lucency,<sup>48</sup> loculation of fluid in the posterior choroid,<sup>49</sup> or presence of intraretinal hyperreflective foci.<sup>50</sup> Finally, SCFT were measured at a single time point at first visit and therefore diurnal variations of SFCT were not considered.

To summarize, we have identified clinical parameters that are significantly associated with longer duration of first acute CSCR episodes. Further functional analyses are required to determine whether these factors could help select patients who should benefit from earlier therapeutic interventions. These parameters could also be useful for the design of future randomized studies of CSCR to limit potential bias.

**Key words:** central serous chorioretinopathy, choroid, retinal pigment epithelium, choroidal thickness, optical coherence tomography, fluorescein angiography, indocyanine green angiography, age factors, time factors, steroids.

## References

1. Klein ML, Van Buskirk EM, Friedman E, et al. Experience with nontreatment of central serous choroidopathy. *Arch Ophthalmol* 1974;91:247–250.
2. Leaver P, Williams C. Argon laser photocoagulation in the treatment of central serous retinopathy. *Br J Ophthalmol* 1979;63:674–677.
3. Robertson DM, Ilstrup D. Direct, indirect, and sham laser photocoagulation in the management of central serous chorioretinopathy. *Am J Ophthalmol* 1983;95:457–466.
4. Daruich A, Matet A, Dirani A, et al. Central serous chorioretinopathy: recent findings and new physiopathology hypothesis. *Prog Retin Eye Res* 2015;48:82–118.
5. Malik KJ, Sampat KM, Mansouri A, et al. Low-intensity/high-density subthreshold micropulse diode laser for chronic central serous chorioretinopathy. *Retina* 2015;35:532–536.
6. Roisman L, Magalhães FP, Lavinsky D, et al. Micropulse diode laser treatment for chronic central serous chorioretinopathy: a randomized pilot trial. *Ophthalmic Surg Lasers Imaging Retina* 2013;44:465–470.
7. Salehi M, Wenick AS, Law HA, et al. Interventions for central serous chorioretinopathy: a network meta-analysis. *Cochrane Database Syst Rev* 2015:CD011841.
8. Lim JI, Glassman AR, Aiello LP, et al. Collaborative retrospective macula society study of photodynamic therapy for chronic central serous chorioretinopathy. *Ophthalmology* 2014;121:1073–1078.
9. Ma J, Meng N, Xu X, et al. System review and meta-analysis on photodynamic therapy in central serous chorioretinopathy. *Acta Ophthalmol* 2014;92:e594–e601.
10. Chan W-M, Lai TYY, Lai RYK, et al. Half-dose verteporfin photodynamic therapy for acute central serous chorioretinopathy: one-year results of a randomized controlled trial. *Ophthalmology* 2008;115:1756–1765.
11. Hagen S, Ansari-Shahrezaei S, Smreetschnig E, et al. Effect of photodynamic therapy on short-wavelength fundus autofluorescence in eyes with acute central serous chorioretinopathy. *Retina* 2015;35:223–230.
12. Shiode Y, Morizane Y, Kimura S, et al. Comparison of halving the irradiation time or the verteporfin dose in photodynamic therapy for chronic central serous chorioretinopathy. *Retina* 2015;35:2498–2504.
13. Bousquet E, Beydoun T, Rothschild P-R, et al. Spironolactone for nonresolving central serous chorioretinopathy: a randomized controlled crossover study. *Retina* 2015;35:2505–2515.
14. Herold TR, Prause K, Wolf A, et al. Spironolactone in the treatment of central serous chorioretinopathy - a case series. *Graefes Arch Clin Exp Ophthalmol* 2014;52:1985–1991.
15. Salz DA, Pitcher JD, Hsu J, et al. Oral eplerenone for treatment of chronic central serous chorioretinopathy: a case series. *Ophthalmic Surg Lasers Imaging Retina* 2015;46:439–444.
16. Singh RP, Sears JE, Bedi R, et al. Oral eplerenone for the management of chronic central serous chorioretinopathy. *Int J Ophthalmol* 2015;8:310–314.
17. Ghadiali Q, Jung JJ, Yu S, et al. Central serous chorioretinopathy treated with mineralocorticoid antagonists: a one-year pilot study. *Retina* 2016;36:611–618.
18. Daruich A, Matet A, Dirani A, et al. Oral mineralocorticoid-receptor antagonists: real-life experience in clinical subtypes of nonresolving central serous chorioretinopathy with chronic epitheliopathy. *Transl Vis Sci Technol* 2016;5:2.
19. Pryds A, Sander B, Larsen M. Characterization of subretinal fluid leakage in central serous chorioretinopathy. *Invest Ophthalmol Vis Sci* 2010;51:5853–5857.
20. Therneau TM, Grambsch PM. *Modeling Survival Data: Extending the Cox Model*. New York, NY: Springer; 2000.
21. Venables WN, Ripley BD. *Modern Applied Statistics With S*. 4th ed. New York, NY: Springer; 2002.
22. Wickham H. *ggplot2*. New York, NY: Springer New York; 2009. Available at: <http://link.springer.com/10.1007/978-0-387-98141-3>. Accessed June 16, 2016.
23. Cohen JA. Coefficient of agreement for nominal scales. *Educ Psychol Meas* 1960;20:37–46.
24. Goyal JL, Ghosh B, Sangit V, et al. Pattern ERG in central serous retinopathy. *Doc Ophthalmol* 2015;130:141–147.
25. Shimada Y, Imai D, Ota Y, et al. Retinal adaptability loss in serous retinal detachment with central serous chorioretinopathy. *Invest Ophthalmol Vis Sci* 2010;51:3210–3215.
26. Yip YWY, Ngai JWS, Fok ACT, et al. Correlation between functional and anatomical assessments by multifocal electroretinography and optical coherence tomography in central serous chorioretinopathy. *Doc Ophthalmol* 2010;120:193–200.
27. Chappelov AV, Marmor MF. Multifocal electroretinogram abnormalities persist following resolution of central

- serous chorioretinopathy. *Arch Ophthalmol* 2000;118:1211–1215.
28. Bae S, Jin K, Kim H, Bae SH. Clinical parameters related to metamorphopsia outcome in patients with resolved central serous chorioretinopathy using M-CHARTS: retrospective cohort study. *BMC Ophthalmol* 2015;15:180.
  29. Dansingani KK, Balaratnasingam C, Naysan J, Freund KB. En face imaging of pachychoroid spectrum disorders with swept-source optical coherence tomography. *Retina* 2016;36:499–516.
  30. Gallego-Pinazo R, Dolz-Marco R, Gómez-Ulla F, et al. Pachychoroid diseases of the macula. *Med Hypothesis Discov Innov Ophthalmol* 2014;3:111–115.
  31. Zhao M, Célérier I, Bousquet E, et al. Mineralocorticoid receptor is involved in rat and human ocular chorioretinopathy. *J Clin Invest* 2012;122:2672–2679.
  32. Daruich A, Matet A, Dirani A, et al. Central serous chorioretinopathy: recent findings and new physiopathology hypothesis. *Prog Retin Eye Res.* 2015;48:82–118.
  33. Yannuzzi LA. Central serous chorioretinopathy: a personal perspective. *Am J Ophthalmol* 2010;149:361–363.
  34. Schubert C, Pryds A, Zeng S, et al. Cadherin 5 is regulated by corticosteroids and associated with central serous chorioretinopathy. *Hum Mutat* 2014;35:859–867.
  35. Miki A, Kondo N, Yanagisawa S, et al. Common variants in the complement factor H gene confer genetic susceptibility to central serous chorioretinopathy. *Ophthalmology* 2014;121:1067–1072.
  36. de Jong EK, Breukink MB, Schellevis RL, et al. Chronic central serous chorioretinopathy is associated with genetic variants implicated in age-related macular degeneration. *Ophthalmology* 2015;122:562–570.
  37. Cheng Y, Huang L, Li X, et al. Genetic and functional dissection of ARMS2 in age-related macular degeneration and polypoidal choroidal vasculopathy. *PLoS One* 2013;8:e53665.
  38. Chu PG, Grunwald GB. Identification of an adhesion-associated protein of the retinal pigment epithelium. *Invest Ophthalmol Vis Sci* 1990;31:847–855.
  39. Kanan Y, Siefert JC, Kinter M, Al-Ubaidi MR. Complement factor H, vitronectin, and opticin are tyrosine-sulfated proteins of the retinal pigment epithelium. *PLoS One* 2014;9:e105409.
  40. Yoshioka H, Sugita T. Fluorescein fundus photographic studies on the central serous retinopathy. II. Fluorescein fundus photographic findings in the full course of this disease. *Kurume Med J* 1969;16:1–12.
  41. Gass JD. Pathogenesis of disciform detachment of the neuroepithelium. *Am J Ophthalmol* 1967;63:1–139.
  42. Coscas G, Aubry JP. Evolutive angiographic aspects of central serous chorioretinopathies [in French]. *Bull Mem Soc Fr Ophtalmol* 1972;85:169–187.
  43. Rashid A, Bhatia SK, Mazzitello KI, et al. RPE cell and sheet properties in normal and diseased eyes. *Adv Exp Med Biol* 2016;854:757–763.
  44. Gouras P, Ivert L, Neuringer M, Nagasaki T. Mitochondrial elongation in the macular RPE of aging monkeys, evidence of metabolic stress. *Graefes Arch Clin Exp Ophthalmol* 2016;254:1221–1227.
  45. Chen M, Rajapakse D, Fraczek M, et al. Retinal pigment epithelial cell multinucleation in the aging eye - a mechanism to repair damage and maintain homeostasis. *Aging Cell.* 2016;15:436–445.
  46. Spaide RF, Campeas L, Haas A, et al. Central serous chorioretinopathy in younger and older adults. *Ophthalmology* 1996;103:2070–2079; discussion 2079–2080.
  47. Yang L, Jonas JB, Wei W. Optical coherence tomography-assisted enhanced depth imaging of central serous chorioretinopathy. *Invest Ophthalmol Vis Sci* 2013;54:4659–4665.
  48. Yannuzzi NA, Mrejen S, Capuano V, et al. A central hyporeflective subretinal lucency correlates with a region of focal leakage on fluorescein angiography in eyes with central serous chorioretinopathy. *Ophthalmic Surg Lasers Imaging Retina* 2015;46:832–836.
  49. Spaide RF, Ryan EH. Loculation of fluid in the posterior choroid in eyes with central serous chorioretinopathy. *Am J Ophthalmol* 2015;160:1211–1216.
  50. Lee H, Lee J, Chung H, Kim HC. Baseline spectral domain optical coherence tomographic hyperreflective foci as a predictor of visual outcome and recurrence for central serous chorioretinopathy. *Retina* 2015;36:1372–1380.



[2b] Risk factors for recurrent central serous chorioretinopathy. *Retina 2017*

Matet A, Daruich A, Zola M, Behar-Cohen F

[Epub ahead of print] doi: 10.1097/IAE.0000000000001729.<sup>180</sup>

Contribution of PhD candidate:

- Patient follow-up
- Processing and analysis of multimodal imaging data
- Shared frailty survival statistical analysis
- Drafting the manuscript



# RISK FACTORS FOR RECURRENCES OF CENTRAL SEROUS CHORIORETINOPATHY

ALEXANDRE MATET, MD,\* ALEJANDRA DARUICH, MD,\* MARTA ZOLA, MD,\*  
FRANCINE BEHAR-COHEN, MD, PhD\*†

**Purpose:** To describe recurrence patterns and investigate candidate risk factors for recurrences of central serous chorioretinopathy.

**Methods:** In 46 patients with acute central serous chorioretinopathy and follow-up >12 months after first episode resolution, parameters influencing recurrences were retrospectively evaluated using a frailty Cox proportional hazard survival model. Covariates included baseline systemic findings: age, gender, corticosteroid use, stress, shift work, sleep disorder, depression, allergy, cardiovascular risk; baseline optical coherence tomography findings: subfoveal choroidal thickness, pigment epithelial detachment pattern (regular/bump/irregular), number of subretinal hyperreflective foci at leakage site; baseline angiographic findings: fluorescein leakage intensity (intense/moderate/subtle/absent), hyperpermeability pattern on indocyanine-green angiography (focal/multifocal); and episode-related findings: duration and treatment of previous episode.

**Results:** Twenty of 46 subjects (43%) presented  $\geq 1$  recurrences during a mean follow-up of  $29.9 \pm 9.5$  months (range, 15–54 months). Follow-up duration did not differ between cases with or without recurrences ( $P = 0.3$ ). Worse final visual acuity levels (logarithm of the minimal angle of resolution) were associated with a higher number of episodes during follow-up ( $P = 0.032$ ,  $r = 0.28$ ). In a univariate analysis, higher subfoveal choroidal thickness ( $P = 0.021$ ), nonintense fluorescein leakage (= moderate/subtle/absent,  $P = 0.033$ ), multiple subretinal hyperreflective foci ( $P = 0.026$ ), and shift work ( $P < 0.0001$ ) were significantly associated with recurrences, with a near-significant influence of irregular pigment epithelial detachment ( $P = 0.093$ ). In a multivariate analysis, higher subfoveal choroidal thickness ( $P = 0.007$ ), nonintense fluorescein leakage ( $P = 0.003$ ) and shift work ( $P < 0.0001$ ) remained significant and independent risk factors for recurrences.

**Conclusion:** Multiple factors influence the risk of central serous chorioretinopathy recurrence. These findings may contribute to identify patients at higher risk, who could benefit from earlier or more intensive treatment.

**RETINA** 0:1–12, 2017

Central serous chorioretinopathy (CSCR) consists in serous detachments of the neuroretina from the retinal pigment epithelium (RPE), most frequently occurring in middle-aged men.<sup>1–4</sup> It is favored by several widely agreed predisposing factors,<sup>5</sup> such as corticosteroid use,<sup>6,7</sup> psychological stress,<sup>8,9</sup> depression,<sup>10–12</sup> and cardiovascular disease,<sup>13–15</sup> or more recently advanced factors such as pachychoroid,<sup>16–18</sup> allergic disease,<sup>19</sup> disturbed sleep,<sup>20–22</sup> and shift work.<sup>21–23</sup> An association with *Helicobacter pylori* has also been postulated,<sup>24–26</sup> and pregnancy is known to favor episodes.<sup>19,27,28</sup> Other factors have been suggested and remain disputed.

During an active episode, multimodal imaging typically identifies one or multiple leakage sites of

varying intensity on fluorescein angiography (FA), focal or multifocal choroidal vascular hyperpermeability on midphase indocyanine green angiography (ICGA), and varying degrees of RPE abnormalities, ranging from RPE bumps to regular or irregular pigment epithelial detachments (PED).

Whilst acute episodes are usually self-resolving, ~20% to 50%<sup>29–31</sup> of affected eyes may later present one or several recurrences. Despite a remarkable resistance of photoreceptors to serous detachments during single CSCR episodes,<sup>32,33</sup> repeated episodes and prolonged serous detachment lead to irreversible photoreceptor/RPE damage, and vision loss.<sup>34</sup> Yet, little is known about the underlying mechanisms triggering

recurrences and leading to chronic forms of the disease. Whether recognized risk factors for CSCR or anatomical changes in the choroid, RPE and retina do also influence the recurrence rate of the disease has not been comprehensively explored. Identifying factors predisposing for CSCR recurrences would help detect patients at higher risk of recurrence, potentially needing preventive and/or more aggressive therapeutic interventions.

This retrospective case series describes recurrence patterns in CSCR patients, and investigates the influence of a panel of candidate systemic and ocular factors on the risk of recurrence.

## Methods

### Subjects

This observational, single-center, retrospective study was designed in accordance with the tenets of the Declaration of Helsinki. Data collection and analysis have been approved by the Ethics Committee of the Swiss Federal Department of Health (CER-VD no. 19/15).

Patients presenting with an active episode of CSCR at Jules-Gonin Eye Hospital from January 2012 to September 2015, followed by spontaneous or treatment-induced subretinal fluid resolution, and with a follow-up longer than 12 months after resolution of the initial episode, were included. Those presenting with fundus autofluorescence alterations suggestive of previous CSCR episodes, or chronic disease, such as hyperautofluorescent areas, possibly containing granular or confluent hypoautofluorescence, were excluded. In addition, the follow-up of patients who were maintained under oral mineralocorticoid-receptor antagonist therapy as prophylaxis after an episode resolution, was censored at the time of that resolution. Cases with

spherical equivalent  $\geq \pm 2$  D in the affected eye were excluded. In case of bilateral involvement, only the first eye affected by a recurrence was included in the study.

Patient medical and ocular history, including patient profession and specific risk factors detailed below, baseline clinical and imaging parameters, the number and chronology of recurrences, and the last available best-corrected visual acuity were recorded.

Based on clinical decisions by the senior consultant (F.B.-C.), patients with a first episode lasting  $>6$  months, or with a recurrence lasting  $>2$  months could receive either laser photocoagulation of extramacular leakage sites, or oral mineralocorticoid-receptor antagonist therapy.

### Retinal Imaging

Imaging was performed after standard pupillary dilation using tropicamide 0.5% drops with the Spectralis (Heidelberg Engineering, Heidelberg, Germany), and all visits occurred between 1 PM and 5 PM. A  $20^\circ \times 20^\circ$  97-sections map on spectral-domain optical coherence tomography (SD-OCT), a  $30^\circ$  enhanced-depth imaging SD-OCT horizontal scan through the fovea with an “automatic real time” averaging of 100 images, a  $30^\circ \times 30^\circ$  fundus infrared reflectance, and a  $30^\circ \times 30^\circ$  fundus autofluorescence image were acquired. FA and ICGA were performed at the baseline visit.

For each case, the degree of fluorescein leakage at the main leakage site on FA from early (40–60 seconds) to midphase (2–3 minutes) was graded as absent (no leakage), subtle (faint fluorescence increase), moderate (fluorescence increase without marked spatial diffusion) or intense (strong fluorescence increase and strong spatial diffusion). A quantitative assessment of leakage intensity was also obtained by calculating the ratio of fluorescein expansion at the leakage site between early and midphase angiograms, using a semiautomated algorithm on Matlab (Version R2015b; Mathworks, Natick, MA) as previously described.<sup>35</sup> Multifocal choroidal hyperpermeability was defined as the presence of two or more hypercyanescent areas on midphase ICGA (10–12 minutes after dye injection). The most advanced RPE defect observed within the subretinal detachment area on SD-OCT was categorized by incremental severity as: regular PED (curved elevation of the RPE with hyporeflective content), RPE bump (shallow irregular elevation of the RPE with hyperreflective content), or irregular PED (irregular elevation of the RPE with hyporeflective content). The height of this RPE lesion and its axial diameter on a horizontal SD-OCT scan were measured, and the PED height/diameter ratio was

From the \*Department of Ophthalmology, University of Lausanne, Jules-Gonin Eye Hospital, Fondation Asile des Aveugles, Lausanne, Switzerland; and †Inserm, U1138, Team 17, Physiopathology of Ocular Diseases to Clinical Development, Université Paris Descartes Sorbonne Paris Cité, Centre de Recherche des Cordeliers, Paris, France.

Supported by grants from the Swiss National Fund (#320030\_156401, F. Behar-Cohen), the Faculty of Biology and Medicine of the University of Lausanne (A. Matet) and from the Agence Nationale de la Recherche (Grant ANR-15-CE18-0032 “ROCK SUR MER”).

None of the authors has any conflicting interests to disclose.

Supplemental digital content is available for this article. Direct URL citations appear in the printed text and are provided in the HTML and PDF versions of this article on the journal’s Web site ([www.retinajournal.com](http://www.retinajournal.com)).

Reprint requests: Francine Behar-Cohen, MD, PhD, Faculty of Biology and Medicine, University of Lausanne, Rue du Bugnon 21, 1011 Lausanne, Switzerland; e-mail: francine.behar@gmail.com

calculated. Subjective gradings and measurements were performed on masked images by two independent observers (A.M., A.D.). In case of discrepancy between the two raters, the image was adjudicated by a senior retina specialist (F.B.-C.). The interrater agreement was assessed using the weighted Cohen's kappa statistics.

The subfoveal choroidal thickness (SFCT) was measured by two observers (A.M., A.D.) on baseline enhanced-depth imaging SD-OCT horizontal scans, as the axial distance from the RPE to the outer choroid/sclera interface, using the built-in Spectralis software (Heidelberg Eye Explorer, version 1.9.10.0). The mean of the two measures of each scan was retained, and the interrater agreement was assessed using the intraclass correlation coefficient.

Subretinal hyperreflective foci on SD-OCT were focal lesions with a reflectivity identical to the RPE signal, located between the outer tip of photoreceptor outer segments and the inner surface of the RPE, as defined by Lee et al.<sup>36</sup> Their number was determined by two observers (A.M., A.D.) within a 1,500- $\mu$ m area centered by the leakage site on a corresponding horizontal SD-OCT section, as reported by these authors, and the mean number of foci was considered for analysis. The interrater agreement was assessed using weighted Cohen's kappa statistics.

#### *Risk Factors of CSCR Recurrence*

Clinical and imaging parameters related to the pathophysiology of CSCR were evaluated as potential risk factors: age at first episode, gender, type of RPE alteration, number of subretinal hyperreflective foci at the leakage site, SFCT, intensity of fluorescein leakage, and pattern of choroidal hyperpermeability on ICGA. Additionally, previously reported systemic risk factors of CSCR were assessed: history of corticosteroid use (oral, intranasal, inhalational, topical skin application, intravenous, intramuscular), current or recent ( $\leq 2$  years) psychological stress (related to work: burden, responsibilities, layoff; or to life changes: death, divorce, familial strife), shift work (current or recent ( $\leq 2$  years) professional activity starting before 7:00 AM or finishing after 7:00 PM, which includes evening, night or early morning work), sleep disorder (patient-reported sleep-onset difficulties or frequent nocturnal awakening), history of depression, history of allergic disease, and cardiovascular risk (hypertension, diabetes mellitus or hypercholesterolemia).

#### *Statistical Analysis*

A shared frailty survival model was used to assess the effect of potential predictors on the risk of

recurrences, using the "frailtypack" package<sup>37,38</sup> and the R Software (Version 3.3.0, R Foundation for Statistical Computing, R Core Team, 2016, Vienna, Austria. <http://www.R-project.org/>). This model consists in a survival analysis of recurrence times, based on a Cox proportional hazard regression with an additional subject-specific random coefficient accounting for the fact that several recurrences will occur within single individuals. A series of univariate regressions, and a multivariate regression with covariates reaching  $P$  values  $\leq 0.2$  in the univariate analysis, were performed as previously described.<sup>39</sup> An additional analysis based on the first recurrences only was performed by a conventional Cox proportional hazard survival model on R, using the "survival" package,<sup>40</sup> and was used to plot survival curves using the "survminer" package.

Agreement between raters by weighted Cohen's Kappa, or intraclass correlation coefficient, were estimated using the R software with the "irr" package.<sup>41</sup>

Descriptive statistics, comparison of quantitative parameters (Mann-Whitney test) and correlations (Spearman) were performed on GraphPad Prism (version 5.0f; GraphPad Software, La Jolla, CA). The logarithm of the minimal angle of resolution (Log-MAR) was used to calculate visual acuity means.  $P$  values  $\leq 0.05$  were considered significant.

## Results

Amongst 62 patients presenting with an active episode of CSCR during the study period without knowledge of previous episodes, 16 were excluded ( $n = 5$  for follow-up  $\leq 12$  months and  $n = 11$  for fundus autofluorescence alterations at the first visit suggesting history of CSCR, including  $n = 6$  with hyperautofluorescent areas,  $n = 3$  with hyperautofluorescent areas containing granular hypoautofluorescence, and  $n = 2$  with confluent hypoautofluorescent areas). Of the remaining 46 patients, 20 presented CSCR recurrences (43%) during a mean follow-up of  $29.9 \pm 9.5$  months (range, 17–54 months). The follow-up of 2 subjects with recurrences was censored after resolution of the last episode, because they received prolonged oral mineralocorticoid-receptor antagonist therapy as prophylaxis after this episode. Three subjects with history or high risk of fluorescein allergy did not undergo FA or ICG.

Descriptive characteristics of nonrecurrent and recurrent cases are reported in Table 1, and a schematic chronology of episodes experienced by recurrent cases is displayed in Figure 1. On SD-OCT analysis, an excellent agreement was shown between observers

Table 1. Clinical and Time-dependent Characteristics for 46 Patients With Central Serous Chorioretinopathy According to the Observation of Recurrences During Follow-up

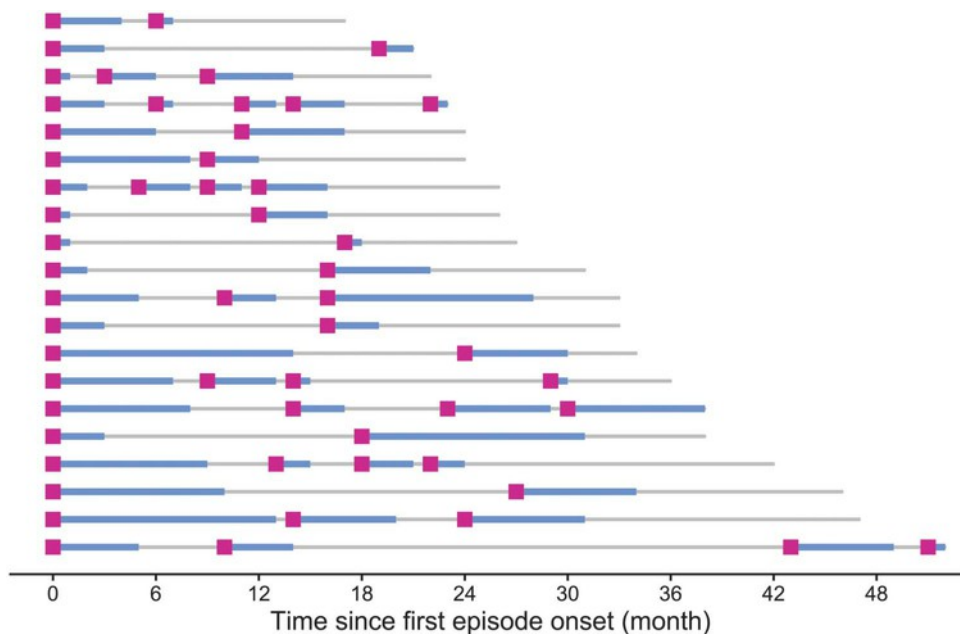
	No Recurrence	Recurrence
Subjects, N	26	20
Gender (male/female), N	21/5	18/2
Age at first episode, year (range)	43.3 ± 9.4 (28–56)	43.1 ± 7.7 (29–55)
Total follow-up duration, month (range)	28.3 ± 9.2 (15–54)	31.9 ± 9.8 (17–52)
Episode duration, month	4.4 ± 3.7	4.8 ± 3.3
No. of episodes during follow-up, per subject	1.0 ± 0.0	2.7 ± 0.9
Distribution of episode number:		
1 episode, N	26	0
2 episodes, N	0	11
3 episodes, N	0	3
4 episodes, N	0	5
5 episodes, N	0	1
BCVA at presentation, LogMAR (Snellen)	0.13 ± 0.14 (~20/27)	0.14 ± 0.13 (~20/28)
BCVA at the final visit, LogMAR (Snellen)	0.03 ± 0.08 (~20/21)	0.12 ± 0.21 (~20/26)
Treatment required during one episode or more, N	3	13
Laser photocoagulation, N	1	4
Oral MR antagonist, N	3	12
Prolonged MR antagonist after episode resolution, N	0	2

Quantitative variables are expressed as mean ± SD. BCVA, best-corrected visual acuity; MR, mineralocorticoid-receptor.

for SFCT measures using enhanced-depth imaging (intraclass correlation coefficient = 0.98), and for PED height/diameter ratios (intraclass correlation coefficient = 0.97), and a good agreement for the quantification of subretinal hyperreflective foci (Cohen’s

kappa = 0.67). A good-to-excellent agreement was also observed for the qualitative grading of PEDs, fluorescein leakage intensity and ICGA pattern (Cohen’s kappa = 0.65, 0.84, and 0.86, respectively). A clinical illustration of subtle/moderate/intense fluorescein leakages,

Fig. 1. Chronology of episodes in 20 patients with recurrent central serous chorioretinopathy. Onset of episodes (red squares), episode duration (blue segments), and total follow-up (gray lines) are displayed. For clarity, nonrecurrent cases were not represented.



regular PED/RPE bump/irregular PED, and focal/multifocal ICGA patterns are provided as **Supplemental Digital Content 1–3** (see **Figures**, <http://links.lww.com/IAE/A663>; <http://links.lww.com/IAE/A664>; <http://links.lww.com/IAE/A665>).

To assess the robustness of these gradings, multiple correlations were performed (see **Table, Supplemental Digital Content 4**, <http://links.lww.com/IAE/A666>), which revealed a significant correlation between PED type (regular PED, RPE bump, irregular PED) and PED height/diameter ratio ( $P = 0.027$ ,  $r = -0.33$ ), and between FA leakage intensity (none, subtle, moderate, intense), and fluorescein leakage expansion ratio ( $P = 0.0002$ ,  $r = 0.54$ ).

Follow-up duration ranged from 15 to 54 months and did not differ between the nonrecurrent and recurrent cases ( $P = 0.3$ ). Eleven cases (24%) presented 1 recurrence, 3 cases (7%) 2 recurrences, 5 cases 3 recurrences (11%), and 1 case 4 recurrences (2%), with a mean number of  $1.8 \pm 1.0$  recurrences per recurrent case. Among recurring patients, the mean time from resolution of the initial episode to the onset of the first recurrence was  $7.3 \pm 5.5$  months (range, 1–17 months), and the interepisode interval decreased with subsequent recurrences: 6.0 months between first and second recurrence, and 3.3 months between second and third recurrence.

When considering the whole cohort, the mean recurrence-free interval observed after resolution of the first episode was  $15.9 \pm 12.4$  months, and the absolute frequency of recurrences was 0.81 per patient-year. The risk of recurrence decreased with time elapsed since the previous episode (hazard ratio with 95% confidence interval: 0.86 (0.82–0.91),  $P < 0.0001$ ), indicating that the risk was highest immediately after a given episode and decreased as patients remained recurrence-free.

The initial BCVA did not differ between recurrent (LogMAR: 0.14, Snellen:  $\sim 20/28$ ) and nonrecurrent cases (LogMAR: 0.13, Snellen:  $\sim 20/27$ ) ( $P = 0.6$ ), but the final BCVA was near-significantly worse in recurrent (LogMAR: 0.12, Snellen:  $\sim 20/26$ ) than nonrecurrent cases (LogMAR: 0.03, Snellen:  $\sim 20/21$ ) ( $P = 0.07$ ). Using Spearman correlation, a higher number of recurrences was associated with worse visual outcome, assessed by the LogMAR BCVA ( $P = 0.032$ ,  $r = 0.28$ ). Yet, there was no correlation between the number of recurrences or the last LogMAR BCVA, and the duration of follow-up ( $P = 0.09$  and  $P = 0.11$ , respectively), ensuring that the number of observed recurrences was not a confounding factor linked to different follow-up durations.

Imaging and systemic features evaluated as potential risk factors are described in Table 2. Hazard ratios and

Table 2. Imaging and Systemic Parameters in 46 Patients With Central Serous Chorioretinopathy According to the Observation of Recurrences During Follow-up

	No Recurrence	Recurrence
Subjects, N	26	20
Imaging parameters at the first episode		
SFCT, $\mu\text{m}$	$439 \pm 88$	$498 \pm 74$
Degree of RPE alteration on OCT, N		
Regular PED	12	5
RPE bump	10	8
Irregular PED	4	7
PED height/diameter ratio	$0.116 \pm 0.067$	$0.134 \pm 0.108$
Subretinal hyperreflective foci at leakage site on OCT	$1.2 \pm 1.2$	$1.9 \pm 1.5$
Fluorescein leakage intensity, N		
Intense	12	2
Moderate	2	6
Subtle	7	10
Absent	2	2
NA*	3	0
Specific fluorescein leakage patterns		
Ink-blot	0	3
Smokestack	4	0
Fluorescein leak expansion ratio	$3.6 \pm 3.4$	$1.9 \pm 1.3$
Pattern of choroidal hyperpermeability on ICGA, N		
Multifocal	7	11
Focal	16	9
NA*	3	0
Systemic risk factors		
History of corticosteroid use, N	9	9
Stress, N	15	13
Shift work, N	5	9
Sleep disorder, N	9	10
Depression, N	5	5
Allergic disease, N	8	10
Cardiovascular risk, N	4	2

Quantitative variables are expressed as mean  $\pm$  SD.

\*Patients presenting fluorescein allergy.

95% confidence intervals representing the risk of CSCR recurrence associated with each of these parameters, obtained by uni- and multivariate analysis, are reported in Table 3. In the univariate analysis, SFCT ( $P = 0.021$ ), number of subretinal hyperreflective foci at the leakage site ( $P = 0.026$ ), nonintense fluorescein leakage (moderate, subtle, or absent;  $P = 0.033$ ), and shift work ( $P < 0.0001$ ) were significantly associated with an increased risk of recurrence. The univariate analysis also suggested that presence of an irregular PED may be associated with a higher risk of

Table 3. Factors Associated With Episode Recurrence in 46 Patients With Central Serous Chorioretinopathy

	Univariate		Multivariate	
	Hazard Ratio (95% CI)	<i>P</i>	Adjusted Hazard Ratio (95% CI)	<i>P</i>
Patient- and episode-related parameters				
Age at the initial episode (per 10-year interval)	1.14 (0.83–1.58)	0.4		
Gender (male vs female)	2.81 (0.80–9.89)	0.11	0.45 (0.08–2.40)	0.3
Total follow-up duration (per year)	1.27 (0.86–1.86)	0.23		
Treatment required for previous episode	0.88 (0.36–2.17)	0.8		
Duration of previous episode (≥6 vs <6 months)	1.16 (0.51–2.64)	0.7		
Imaging parameters at the first episode				
SFCT (per 100-μm)	1.75 (1.09–2.83)	0.021	1.92 (1.20–3.09)	0.007
RPE alteration on OCT (irregular PED vs regular PED or RPE bump)	2.21 (0.88–5.59)	0.093	1.19 (0.56–2.55)	0.6
Subretinal hyperreflective foci at leakage site on OCT (≥2 vs ≤1 foci)	2.44 (1.11–5.34)	0.026	0.66 (0.23–1.85)	0.4
Fluorescein leakage pattern on FA (intense vs moderate, subtle or absent)	0.30 (0.10–0.91)	0.033	0.16 (0.05–0.53)	0.003
Choroidal hyperpermeability on ICGA (multifocal vs focal or absent)	1.58 (0.67–3.72)	0.3		
Systemic risk factors				
Corticosteroid use	1.56 (0.65–3.73)	0.3		
Stress	2.00 (0.87–4.64)	0.10	1.70 (0.66–4.34)	0.3
Shift work	4.52 (2.25–9.07)	<0.0001	7.26 (2.78–18.98)	<0.0001
Sleep disorder	1.62 (0.67–3.96)	0.3		
Depression	1.87 (0.73–4.80)	0.19	0.46 (0.15–1.36)	0.16
Allergic disease	1.84 (0.79–4.31)	0.16	1.51 (0.55–4.14)	0.4
Cardiovascular risk	0.80 (0.22–2.99)	0.9		

CI, confidence interval.

recurrence ( $P = 0.093$ ), although it did not reach statistical significance. In the multivariate analysis, SFCT ( $P = 0.007$ ), nonintense fluorescein leakage ( $P = 0.003$ ) and shift work ( $P < 0.0001$ ) were significantly and independently associated with a higher risk of recurrence. When the multivariate model was run with fluorescein leakage intensity and PED type substituted by fluorescein expansion ratio and PED height/diameter ratio, SFCT ( $P = 0.006$ ), fluorescein expansion ratio ( $P = 0.020$ ), and shift work ( $P = 0.0008$ ) remained independent contributors.

Noticeably, follow-up duration did not influence the risk of recurrence in the univariate analysis ( $P = 0.23$ ) strongly suggesting that the results were not biased by the different follow-up durations among patients. To confirm this finding, we repeated the multivariate analysis with the follow-up duration as additional covariate, which did not alter the above-reported results and their significance levels. Treatment of a given episode by laser or mineralocorticoid-receptor antagonist did not influence the risk of ulterior recurrence ( $P = 0.8$ ).

To further confirm the robustness of these results, and to provide a graphical illustration of the contribution of the three above-mentioned parameters to the risk of recurrence, we performed a conventional Cox proportional hazard survival analysis, based on the disease-free interval following the initial episode, until the onset of the first recurrence (in recurring cases) or the end of follow-up (in nonrecurring cases). Higher SCFT (Figure 2), nonintense fluorescein leakage (Figure 3) and shift work (Figure 4) were all significantly associated with a higher risk of first recurrence in a univariate ( $P = 0.021$ ,  $P = 0.029$  and  $P = 0.009$ , respectively) and multivariate analysis ( $P = 0.005$ ,  $P = 0.016$  and  $P = 0.0003$ , respectively).

## Discussion

The exact link between acute, self-limited CSCR associated with good visual recovery and chronic forms of diffuse epitheliopathy leading to permanent visual loss, remains uncertain. It is suspected that

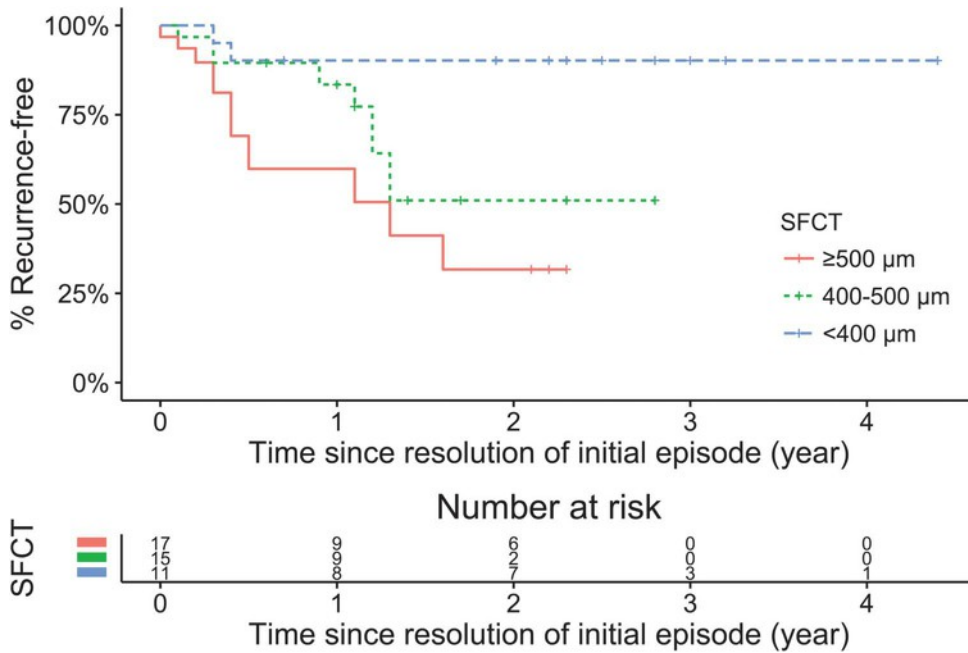


**Fig. 2.** Rate of first recurrence of central serous chorioretinopathy among 46 acute cases, with respect to subfoveal choroidal thickness. The disease-free interval from resolution of the initial episode was considered, and the survival curve was plotted after adjustment for fluorescein leakage intensity and shift work. Higher subfoveal choroidal thickness was associated with a higher rate of first recurrence ( $P = 0.005$ , multivariate Cox proportional hazard analysis), and with a higher global risk of recurrence ( $P = 0.007$ , multivariate shared frailty model). Since fluorescein angiography was not performed in 3 cases, 43 cases are displayed on this adjusted curve.

repeated and/or prolonged episodes of serous retinal detachments may lead to diffuse RPE dysfunction, which further contributes to incomplete subretinal fluid reabsorption and irreversible photoreceptor damage.<sup>42-44</sup> Yet, whether patients at risk for chronic disease do have specific ocular or systemic characteristics at baseline that distinguish them from patients experiencing only one acute episode has not been questioned. One way to explore this issue is to identify risk factors for CSCR recurrences. In addition to local

anatomical and biological factors triggering acute RPE barrier breakdown, endogenous or environmental factors such as genetic variations, stress, food regimen or other lifestyle habits might favor the maintenance of a pathologic state.

Recurrence rates of CSCR reported in the literature vary from ~20% to 50%,<sup>29-31</sup> a wide range probably because of the variable recording of asymptomatic episodes occurring outside the macula. In the present study, 43% of patients presented at least one recurrent

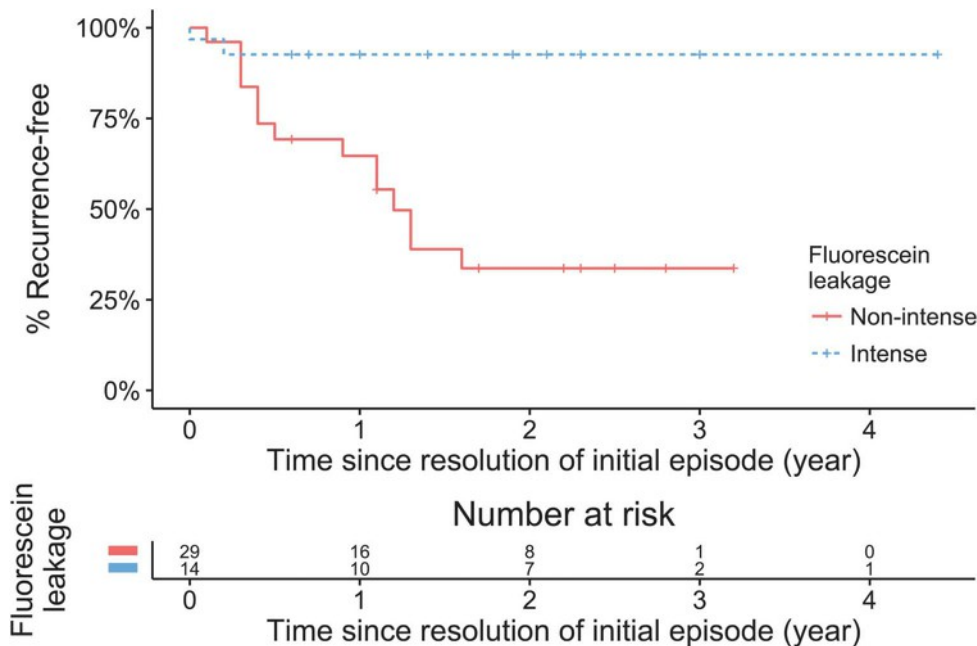


**Fig. 3.** Rate of first recurrence of central serous chorioretinopathy among 46 acute cases with respect to fluorescein leakage intensity. The disease-free interval from resolution of the initial episode was considered, and the survival curve was plotted after adjustment for subfoveal choroidal thickness and shift work. Nonintense fluorescein leakage patterns (absent, subtle, or moderate) were significantly associated with a higher rate of first recurrence ( $P = 0.016$ , multivariate Cox proportional hazard analysis), and significantly associated with a higher global risk of recurrence ( $P = 0.003$ , multivariate shared frailty model). Since fluorescein angiography was not performed in 3 cases, 43 cases are displayed on this adjusted curve.

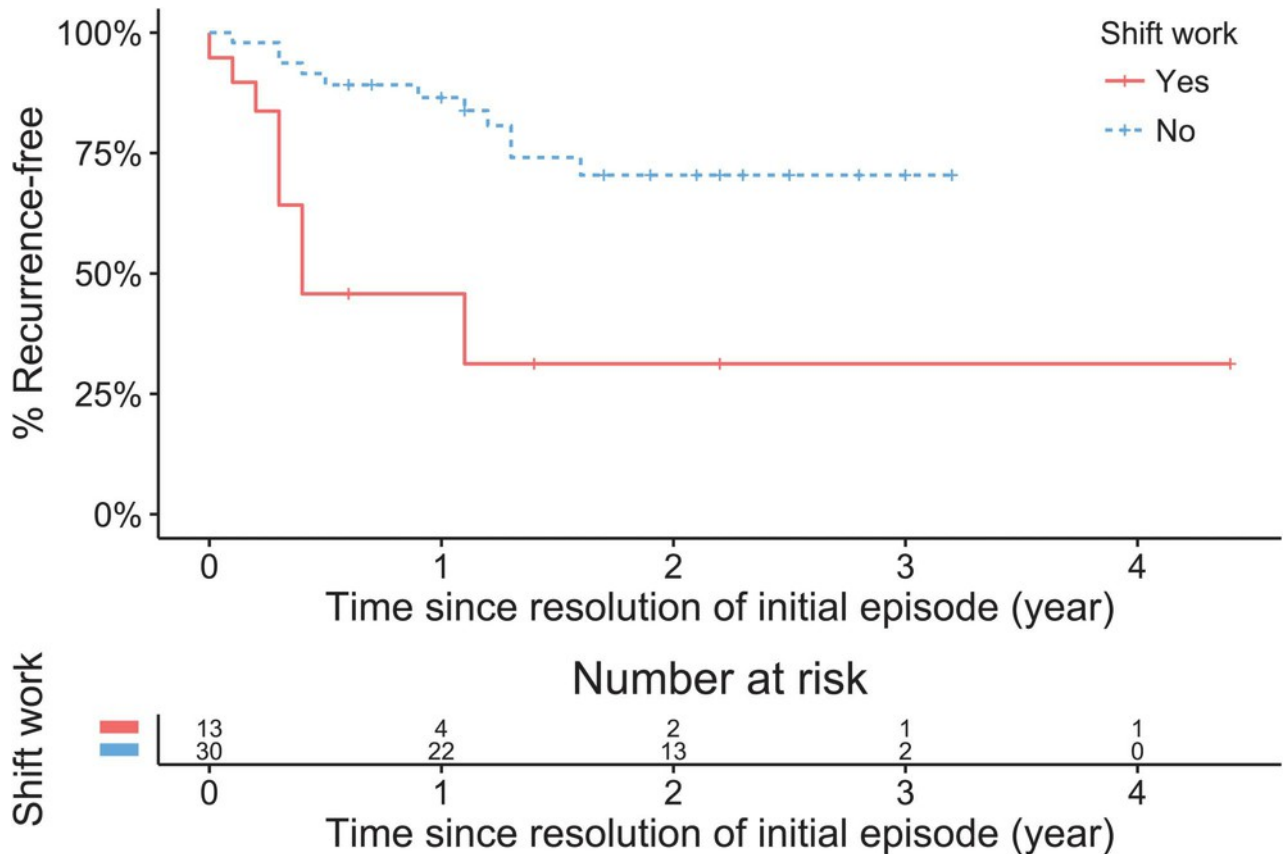


**Fig. 4.** Rate of first recurrence of central serous chorioretinopathy among 46 acute cases with respect to shift work. The disease-free interval from resolution of the initial episode was considered, and the survival curve was plotted after adjustment for subfoveal choroidal thickness and fluorescein leakage intensity. Shift work was associated with a higher rate of first recurrence ( $P = 0.0003$ , multivariate Cox proportional hazard analysis), and with a higher global risk of recurrence ( $P < 0.0001$ , multivariate shared frailty model). Since fluorescein angiography was not performed in 3 cases, 43 cases are displayed on this adjusted curve.

episode during follow-up. This relatively high ratio, at the upper range of reported recurrence rates, could result at least partly from the regular follow-up of these patients in a dedicated CSCR outpatient clinic, and their awareness of subtle symptoms suggestive of CSCR recurrence.

Whilst risk factors for acute CSCR have been extensively investigated and reported,<sup>2,5,45</sup> those associated with a higher risk of recurrence have been rarely addressed in the literature. In a retrospective analysis of 73 CSCR patients (52% of whom presented  $\geq 1$  recurrence over a mean follow-up of 72 months), Fok et al<sup>46</sup> identified that amongst gender, age, hypertension, peptic ulcer, smoking, and history of psychiatric illness, only the latter was associated with a higher rate of recurrence. In this series, clinical or imaging characteristics were not considered. In contrast, Lee et al<sup>36</sup> have retrospectively analyzed baseline imaging features in 62 patients (18% of whom presented  $\geq 1$  recurrence over a mean follow-up of 17 months), and have identified irregular PED and subretinal hyperreflective foci on baseline SD-OCT as predictors of disease recurrence.

In the present study, we evaluated a combined panel of systemic factors and baseline imaging parameters in 46 patients, 43% of whom presented  $\geq 1$  recurrence over a mean follow-up of 29.9 months. We found that SFCT, nonintense fluorescein leakage at baseline, and history of shift work were independent predictors of disease recurrence. In addition, a higher number of subretinal hyperreflective foci around leakage sites at baseline was associated with recurrences in the univariate analysis, which also suggested a near-significant association of irregular PED. These findings are consistent with the previous observations by Lee et al.<sup>36</sup> However, in our multivariate analysis, both parameters did not remain independent contributors, which is possibly explained by the strong effect of the three main contributing parameters. These results suggest that subretinal hyperreflective foci, and to a lesser extent irregular PED, may be risk markers rather than risk factors of disease recurrence. In contrast, SFCT was not mentioned in the assessment of the recurrence risk by Lee et al,<sup>36</sup> raising the possibility that SFCT was an unseen confounding factor in their model.

The type of fluorescein leak has not been previously suspected as a potential predictor for recurrence. We observed milder leakage at the first acute episode in cases who developed later recurrences. There was an ink-blot pattern in 3 of 20 recurring cases, and no smokestack pattern; in contrast, there was a smokestack pattern at this initial episode in 4 of 26 nonrecurrent cases, and no ink-blot pattern. The exact meaning of this observation is not clear. Interestingly, Bujarborua et al<sup>47</sup> analyzed how fluorescein fills the subretinal space during leakage, and identified amongst 479 CSCR cases, 14% of smokestack leak, of which 70% occurred in first acute episode, 27% during acute recurrent episodes, and only 3% at the chronic stage of the disease. This suggests that an intense leak of unbound fluorescein creating the smokestack effect, occurs essentially at the early stage of acute CSCR. On the other hand, Pryds et al<sup>48</sup> have estimated the flow of fluid leakage into the subretinal space of CSCR eyes, and have demonstrated that the smokestack was most likely because of bulk fluid flow from an underlying choroidal vessel through a RPE barrier break.

Together with our results, these observations suggest that, in patients at risk for recurrences, the choroid/RPE complex presents underlying pathogenic features predisposing to repeated subretinal fluid accumulation. We hypothesize that mechanical stress exerted by a modified choroidal vasculature on the RPE can induce a focal disruption in RPE cell junctions leading to an acute episode, as suggested by Dansingani et al in the recent description of pachyvessels in CSCR.<sup>17</sup> Subsequently, this RPE lesion may either heal, or form a scar of lower intercellular resistance that will not completely recover the barrier properties of intact RPE. The resulting focal RPE weaker resistance could favor recurrences, particularly if the underlying mechanical pressure from altered choroidal vessels persists. Consistently, it has been established that there is a focal hypoautofluorescence at the site of fluorescein leakage in CSCR eyes, suggesting a focal RPE disruption.<sup>49</sup> In a case series evaluating mineralocorticoid-receptor antagonist therapy in nonresolving CSCR (which included some of the patients from the present study), we had noticed that SFCT was higher in case of recurrent CSCR history, as compared with first episodes and to chronic diffuse epitheliopathy,<sup>50</sup> suggesting an association between pachychoroid and recurrences. In addition, we have previously observed that pachychoroid, defined as SFCT >395  $\mu\text{m}$ , was present in 50% of CSCR patients' relatives, suggesting that it could be an inherited condition and could predispose to CSCR.<sup>18</sup> The fact that elevated SFCT represents a risk factor for recurrences favors this hypothesis. Interestingly, we

have reported that pachychoroid is associated with longer duration of first acute episodes,<sup>35</sup> confirming a link between presence of choroidopathy and severity of CSCR in a time-dependent manner. Investigators have also observed a higher incidence of recurrences in eyes of patients with bilateral CSCR, strengthening the hypothesis that underlying risk factors may favor recurrences.<sup>51</sup>

Remarkably, shift work has been recognized in the present study as an independent risk factor for recurrences. Two recent studies (including one from our group on a different study population) have demonstrated that shift work was significantly associated with the occurrence of CSCR, as compared with control subjects.<sup>21,22</sup> As extensively discussed by the respective authors, shift work could induce CSCR through disruption of the circadian hormonal clock and dysregulation of cortisol and melatonin secretion. In addition, circadian rhythm disruption induced by exposure to artificial light at night in shift workers, or by frequent jet lag, is now recognized as a major cause of morbidity in multiple organ systems. Interestingly, amongst conditions presumably linked to circadian disruption,<sup>52</sup> several have also been associated with CSCR,<sup>5</sup> such as hypertension, insomnia/sleep disorders, peptic ulcer disease, depression, asthma or allergy, further supporting the potential implication of chronobiological factors in CSCR.

However, whether shift work is associated with clinical subtypes of CSCR has not been previously investigated. We hypothesize that biological clock deregulation induced by environmental factors triggers recurrences in individuals at risk, as those with pachychoroid or residual RPE weakness following a first CSCR episode.

In an attempt to link choroidal vasodilatation with cortisol levels, several studies have evaluated diurnal changes in SFCT in normal subjects with conflicting results, reporting an elevation of SFCT either in the morning,<sup>53–55</sup> or in the evening.<sup>56</sup> Other authors have concluded that cortisol may not have an effect on the choroid, since corticosteroid administration via different routes did not increase SFCT.<sup>54,57,58</sup> Consequently, the interaction between circadian rhythm, cortisol/melatonin levels and choroidal vasodilatation, if any, may involve more complex mechanisms. In addition, elevation of morning peak serum cortisol levels in CSCR patients remains controversial.<sup>59–62</sup> The cortisol cycle may also be disrupted without a detectable elevation in cortisol levels. In hormonal systems regulated by time-dependent phenomena, cyclical secretory patterns are more critical than levels at a given time point, which are submitted to multiple counterregulation loops. Moreover, it has been

recently proposed that the biological clock modulates the human cortisol response in a multiplicative fashion.<sup>63</sup> Exposure to stress at an unnatural phase of the circadian cycle, as in shift work, would result in abnormal cortisol regulation, providing a possible explanation for the recurrent nature of CSCR.

Limitations of this study include its retrospective nature, the limited sample size and follow-up duration, because of strict inclusion/exclusion criteria and the recent availability of standardized up-to-date imaging modalities for all patients. Noteworthy, although the shortest follow-up duration was 15 months, 16 of 20 (80%) recurring patients experienced at least 1 recurrence during this timeframe, and all patients experienced 1 recurrence or more within 29.9 months of the first episode, the mean follow-up duration in the study. The survival frailty approach partially compensated for the variable and limited follow-up, by comparing episode-free intervals in both recurring and nonrecurring cases. In addition, by taking into consideration the unobserved heterogeneity, this strategy identified efficiently significant covariates explaining the data variability.

A proportion of patients were treated during persisting active episodes, mostly with oral mineralocorticoid-receptor antagonists. However, treatments did not influence the risk of recurrence in our analysis although the number of treated episodes was limited. A decrease in SFCT has been reported after mineralocorticoid-receptor antagonist therapy,<sup>45</sup> but also after spontaneous resolution of CSCR episodes.<sup>64</sup> Whether such SFCT decrease would reduce the risk of further episodes remains to be determined in a larger study. This notion is consistent with recent findings by Herold et al<sup>65</sup> who observed 48% of recurrences over 1 year after a 3-month course of oral spironolactone for non-resolving CSCR. Also, quantitative evaluation and qualitative grading of multimodal retinal imaging were performed manually by investigators, but the degree of interrater agreement was estimated for each parameter, and a final adjudication was performed by a senior retinal specialist in case of disagreement. Moreover, a positive correlation was found between the qualitative and quantitative evaluations of certain parameters, such as FA leak intensity or RPE lesion severity.

In summary, these results suggest that recurrences of CSCR occur more frequently in patients presenting thicker choroids, nonintense fluorescein leakage, or with a history of shift work. Future studies are required to evaluate the benefits of preventive intervention in patients at risk, such as earlier or prolonged therapy, and adaptation of occupational schedule.

**Key words:** central serous chorioretinopathy, choroidal thickness, circadian rhythm, fluorescein angiog-

raphy, natural history, recurrences, retinal pigment epithelium, risk factors, shift work, time factors.

### Acknowledgments

The authors thank Virginie Rondeau, PhD for statistical counseling.

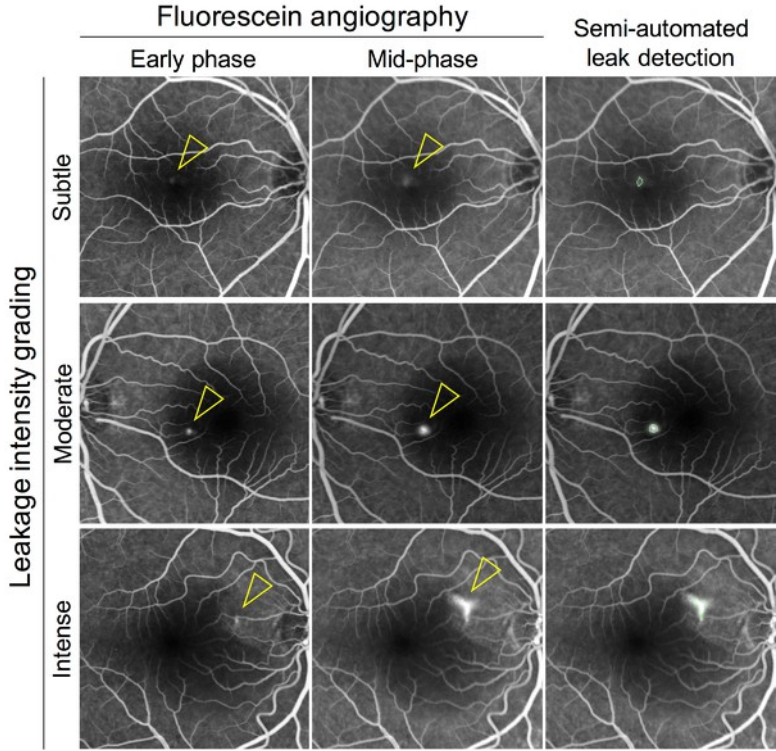
### References

1. Wang M, Sander B, la Cour M, Larsen M. Clinical characteristics of subretinal deposits in central serous chorioretinopathy. *Acta Ophthalmol Scand* 2005;83:691–696.
2. Liew G, Quin G, Gillies M, et al. Central serous chorioretinopathy: a review of epidemiology and pathophysiology: central serous chorioretinopathy. *Clin Exp Ophthalmol* 2013;41:201–214.
3. Quin G, Liew G, Ho IV, et al. Diagnosis and interventions for central serous chorioretinopathy: review and update. *Clin Exp Ophthalmol* 2013;41:187–200.
4. Nicholson B, Noble J, Forooghian F, Meyerle C. Central serous chorioretinopathy: update on pathophysiology and treatment. *Surv Ophthalmol* 2013;58:103–126.
5. Liu B, Deng T, Zhang J. Risk factors for central serous chorioretinopathy: a systematic review and meta-analysis. *Retina* 2016;36:9–19.
6. Wakakura M, Ishikawa S. Central serous chorioretinopathy complicating systemic corticosteroid treatment. *Br J Ophthalmol* 1984;68:329–331.
7. Polak BC, Baarsma GS, Snyers B. Diffuse retinal pigment epitheliopathy complicating systemic corticosteroid treatment. *Br J Ophthalmol* 1995;79:922–925.
8. Yannuzzi LA. Type-A behavior and central serous chorioretinopathy. *Retina* 1987;7:111–131.
9. Gelber GS, Schatz H. Loss of vision due to central serous chorioretinopathy following psychological stress. *Am J Psychiatry* 1987;144:46–50.
10. Sahin A, Bez Y, Kaya MC, et al. Psychological distress and poor quality of life in patients with central serous chorioretinopathy. *Semin Ophthalmol* 2014;29:73–76.
11. Conrad R, Weber NF, Lehnert M, et al. Alexithymia and emotional distress in patients with central serous chorioretinopathy. *Psychosomatics* 2007;48:489–495.
12. Conrad R, Geiser F, Kleiman A, et al. Temperament and character personality profile and illness-related stress in central serous chorioretinopathy. *ScientificWorldJournal* 2014;2014:631687.
13. Tewari HK, Gadia R, Kumar D, et al. Sympathetic-parasympathetic activity and reactivity in central serous chorioretinopathy: a case-control study. *Invest Ophthalmol Vis Sci* 2006;47:3474–3478.
14. Chen SN, Chen YC, Lian I. Increased risk of coronary heart disease in male patients with central serous chorioretinopathy: results of a population-based cohort study. *Br J Ophthalmol* 2014;98:110–114.
15. Tittl M, Polska E, Kircher K, et al. Topical fundus pulsation measurement in patients with active central serous chorioretinopathy. *Arch Ophthalmol* 2003;121:975–978.
16. Imamura Y, Fujiwara T, Margolis R, Spaide RF. Enhanced depth imaging optical coherence tomography of the choroid in central serous chorioretinopathy. *Retina* 2009;29:1469–1473.

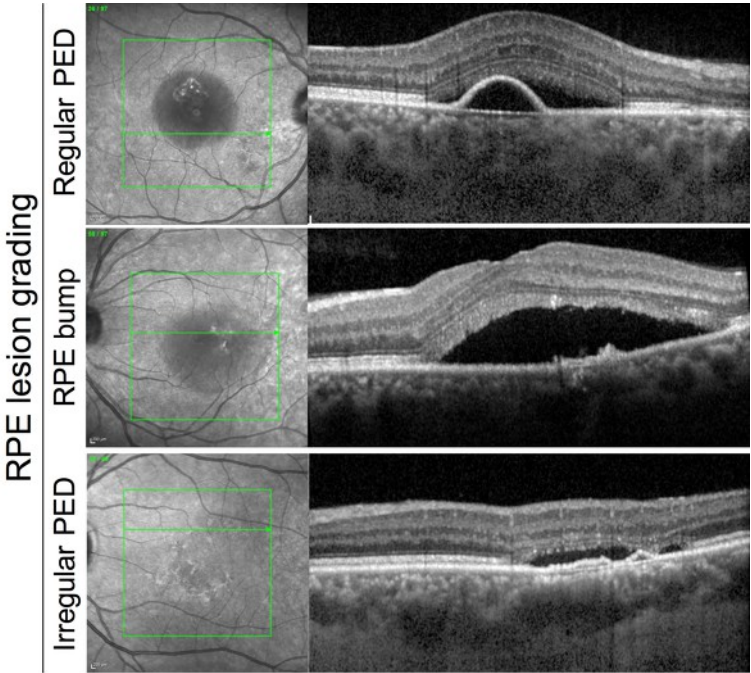
17. Dansingani KK, Balaratnasingam C, Naysan J, Freund KB. En face imaging of pachychoroid spectrum disorders with swept-source optical coherence tomography. *Retina* 2016;36:499–516.
18. Lehmann M, Bousquet E, Beydoun T, Behar-cohen F. Pachychoroid: an inherited condition? *Retina* 2015;35:10–16.
19. Haimovici R, Koh S, Gagnon DR, et al; Central Serous Chorioretinopathy Case-Control Study Group. Risk factors for central serous chorioretinopathy: a case-control study. *Ophthalmology* 2004;111:244–249.
20. Eom Y, Oh J, Kim SW, Huh K. Systemic factors associated with central serous chorioretinopathy in Koreans. *Korean J Ophthalmol* 2012;26:260–264.
21. Bousquet E, Dhundass M, Lehmann M, et al. Shift work: a risk factor for central serous chorioretinopathy. *Am J Ophthalmol* 2016;165:23–28.
22. Setrouk E, Hubault B, Vankemmel F, et al. Circadian disturbance and idiopathic central serous chorioretinopathy. *Graefes Arch Clin Exp Ophthalmol* 2016;254:2175–2181.
23. Zakir SM, Shukla M, Simi ZUR, et al. Serum cortisol and testosterone levels in idiopathic central serous chorioretinopathy. *Indian J Ophthalmol* 2009;57:419–422.
24. Cotticelli L, Borrelli M, D'Alessio AC, et al. Central serous chorioretinopathy and *Helicobacter pylori*. *Eur J Ophthalmol* 2006;16:274–278.
25. Giusti C. Association of *Helicobacter pylori* with central serous chorioretinopathy: hypotheses regarding pathogenesis. *Med Hypotheses* 2004;63:524–527.
26. Zhao M. The effect of eradicating *Helicobacter pylori* on idiopathic central serous chorioretinopathy patients. *Ther Clin Risk Manag* 2013;9:355–360.
27. Quillen DA, Gass DM, Brod RD, et al. Central serous chorioretinopathy in women. *Ophthalmology* 1996;103:72–79.
28. Errera M-H, Kohly RP, da Cruz L. Pregnancy-associated retinal diseases and their management. *Surv Ophthalmol* 2013;58:127–142.
29. Gilbert CM, Owens SL, Smith PD, et al. Long-term follow-up of central serous chorioretinopathy. *Br J Ophthalmol* 1984;68:815–820.
30. Ozkaya A, Alkin Z, Ozveren M, et al. The time of resolution and the rate of recurrence in acute central serous chorioretinopathy following spontaneous resolution and low-fluence photodynamic therapy: a case-control study. *Eye (Lond)* 2016;30:1005–1010.
31. Kitzmann AS, Pulido JS, Diehl NN, et al. The incidence of central serous chorioretinopathy in Olmsted County, Minnesota, 1980–2002. *Ophthalmology* 2008;115:169–173.
32. Yu J, Jiang C, Shi G, et al. Variable photoreceptor inner and outer segment junction appearance in central serous chorioretinopathy. *Retina* 2014;34:1492–1493.
33. Iacono P, Battaglia PM, Papayannis A, et al. Acute central serous chorioretinopathy: a correlation study between fundus autofluorescence and spectral-domain OCT. *Graefes Arch Clin Exp Ophthalmol* 2015;253:1889–1889.
34. Loo R, Scott IU, Flynn HW, et al. Factors associated with reduced visual acuity during long-term follow-up of patients with idiopathic central serous chorioretinopathy. *Retina* 2002;22:19–24.
35. Daruich A, Matet A, Marchionno L, et al. Acute central serous chorioretinopathy: factors influencing episode duration. *Retina* 2017; Jan 6 [Epub ahead of print].
36. Lee H, Lee J, Chung H, Kim C. Baseline spectral domain optical coherence tomographic hyperreflective foci as a predictor of visual outcome and recurrence for central serous chorioretinopathy. *Retina* 2016;36:1372–1380.
37. Rondeau V, Gonzalez JR. frailtypack: a computer program for the analysis of correlated failure time data using penalized likelihood estimation. *Comput Methods Programs Biomed* 2005;80:154–164.
38. Frailtypack: an R package for the analysis of correlated survival data with frailty models using penalized likelihood estimation or parametrical estimation. *J Stat Softw* 2012;47.
39. Holland GN, Crespi CM, ten Dam-van Loon N, et al. Analysis of recurrence patterns associated with toxoplasmic retinochoroiditis. *Am J Ophthalmol* 2008;145:1007–1013.
40. Therneau TM, Grambsch PM. *Modeling Survival Data: Extending the Cox Model*. New York, NY: Springer; 2000.
41. Cohen JA. Coefficient of agreement for nominal scales. *Educ Psychol Meas* 1960;20:37–46.
42. Yannuzzi LA, Shakin JL, Fisher YL, Altomonte MA. Peripheral retinal detachments and retinal pigment epithelial atrophic tracts secondary to central serous pigment epitheliopathy. *Ophthalmology* 1984;91:1554–1572.
43. Piccolino FC, Rigault R, Longrais DELA, et al. The foveal photoreceptor layer and visual acuity loss in central serous chorioretinopathy. *Am J Ophthalmol* 2005;139:87–99.
44. Eandi CM, Piccolino FC, Alovisi C, et al. Function in chronic central serous chorioretinopathy. *Am J Ophthalmol* 2015;159:652–658.e1.
45. Daruich A, Matet A, Dirani A, et al. Central serous chorioretinopathy: recent findings and new physiopathology hypothesis. *Prog Retin Eye Res* 2015;48:82–118.
46. Fok ACT, Chan PPM, Lam DSC, Lai TYY. Risk factors for recurrence of serous macular detachment in untreated patients with central serous chorioretinopathy. *Ophthalmic Res* 2011;46:160–163.
47. Bujarborua D, Nagpal PN, Deka M. Smokestack leak in central serous chorioretinopathy. *Graefes Arch Clin Exp Ophthalmol* 2010;248:339–351.
48. Pryds A, Sander B, Larsen M. Characterization of subretinal fluid leakage in central serous chorioretinopathy. *Invest Ophthalmol Vis Sci* 2010;51:5853–5857.
49. Eandi CM, Ober M, Iranmanesh R, et al. Acute central serous chorioretinopathy and fundus autofluorescence. *Retina* 2005;25:989–993.
50. Daruich A, Matet A, Dirani A, et al. Oral mineralocorticoid-receptor antagonists: real-life experience in clinical subtypes of nonresolving central serous chorioretinopathy with chronic epitheliopathy. *Transl Vis Sci Technol* 2016;5:2.
51. Lai FHP, Ng DS, Bakthavatsalam M, et al. A multicenter study on the long-term outcomes of half-dose photodynamic therapy in chronic central serous chorioretinopathy. *Am J Ophthalmol* 2016;170:91–99.
52. Smolensky MH, Hermida RC, Reinberg A, et al. Circadian disruption: new clinical perspective of disease pathology and basis for chronotherapeutic intervention. *Chronobiol Int* 2016;33:1101–1119.
53. Tan CS, Ouyang Y, Ruiz H, Sadda SR. Diurnal variation of choroidal thickness in normal, healthy subjects measured by spectral domain optical coherence tomography. *Invest Ophthalmol Vis Sci* 2012;53:261–266.
54. Lee SW, Yu S-Y, Seo KH, et al. Diurnal variation in choroidal thickness in relation to sex, axial length, and baseline choroidal thickness in healthy Korean subjects. *Retina* 2014;34:385–393.
55. Usui S, Ikuno Y, Akiba M, et al. Circadian changes in subfoveal choroidal thickness and the relationship with circulatory factors in healthy subjects. *Invest Ophthalmol Vis Sci* 2012;53:2300–2307.

56. Toyokawa N, Kimura H, Fukumoto A, Kuroda S. Difference in morning and evening choroidal thickness in Japanese subjects with no chorioretinal disease. *Ophthalmic Surg Lasers Imaging* 2012;43:109–114.
57. Lee TG, Yu SY, Kwak HW. Variations in choroidal thickness after high-dose systemic corticosteroid treatment in children with chronic glomerulonephritis. *Retina* 2015;35:2567–2573.
58. Lee EK, Han JM, Hyon JY, Yu HG. Changes in choroidal thickness after intravitreal dexamethasone implant injection in retinal vein occlusion. *Br J Ophthalmol* 2015;99:1543–1549.
59. Garg SP, Dada T, Talwar D, Biswas NR. Endogenous cortisol profile in patients with central serous chorioretinopathy. *Br J Ophthalmol* 1997;81:962–964.
60. Haimovici R, Rumelt S, Melby J. Endocrine abnormalities in patients with central serous chorioretinopathy. *Ophthalmology* 2003;110:698–703.
61. Tufan HA, Gencer B, Comez AT. Serum cortisol and testosterone levels in chronic central serous chorioretinopathy. *Graefes Arch Clin Exp Ophthalmol* 2013;51:677–680.
62. Natung T, Keditsu A. Comparison of serum cortisol and testosterone levels in acute and chronic central serous chorioretinopathy. *Korean J Ophthalmol* 2015;29:382–388.
63. van de Werken M, Booij SH, van der Zwan JE, et al. The biological clock modulates the human cortisol response in a multiplicative fashion. *Chronobiol Int* 2014;31:572–580.
64. Kang NH, Kim YT. Change in subfoveal choroidal thickness in central serous chorioretinopathy following spontaneous resolution and low-fluence photodynamic therapy. *Eye (Lond)* 2013;27:387–391.
65. Herold TR, Rist K, Priglinger SG, et al. Long-term results and recurrence rates after spironolactone treatment in non-resolving central serous chorio-retinopathy (CSCR). *Graefes Arch Clin Exp Ophthalmol* 2017;55:221–229.

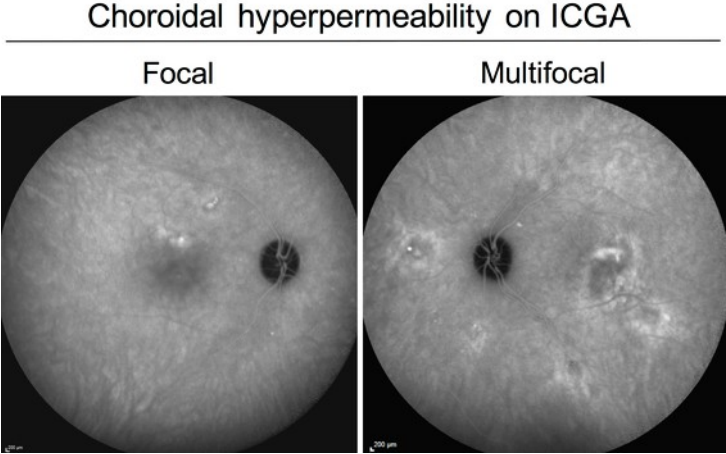
Suppl Fig 1



Suppl Fig 2



Suppl Fig 3



SUPPLEMENTAL DIGITAL CONTENT 4 (TABLE).

Correlation matrix between imaging parameters at baseline among 46 patients with recurrent or non-recurrent central serous chorioretinopathy.

P values (Spearman <i>r</i> reported when $P < 0.05$ )	PED type (categorized as regular PED, RPE bump, irregular PED)	PED height/diameter ratio	Fluorescein leakage intensity (categorized as absent, subtle, moderate, intense)	Fluorescein leakage expansion ratio	Subretinal hyperreflective foci (N.)	Hyperpermeability pattern on ICGA (categorized as focal, multifocal)
SFCT	0.7	0.17	0.9	1.0	0.8	0.9
PED type	-	0.027 ( $r = -0.33$ )	0.7	0.8	0.8	0.3
PED height/diameter ratio	-	-	0.8	0.4	0.4	0.9
Fluorescein leakage intensity	-	-	-	0.0002 ( $r = 0.54$ )	0.8	0.5
Fluorescein leakage expansion ratio	-	-	-	-	0.7	0.18
Subretinal hyperreflective foci	-	-	-	-	-	0.19

SFCT= subfoveal choroidal thickness; PED= pigment epithelial detachment; RPE= retinal pigment epithelium



[2c] Choriocapillaris flow voids in central serous chorioretinopathy: an optical coherence tomography angiography study (submitted)

Matet A, Daruich A, Hardy S, Behar-Cohen F

Submitted in August 2017

Contribution of PhD candidate:

- Patient follow-up
- Processing and analysis of OCT and OCT angiography data
- Statistical analyses
- Drafting the manuscript



Patterns of choriocapillaris flow voids in central serous chorioretinopathy

Alexandre Matet,<sup>1</sup> Alejandra Daruich,<sup>1</sup> Samuel Hardy,<sup>1</sup> Francine Behar-Cohen<sup>2,3</sup>

<sup>1</sup> Department of ophthalmology, University of Lausanne, Jules-Gonin Eye Hospital, Fondation Asile des Aveugles, Avenue de France 15, 1004 Lausanne, Switzerland

<sup>2</sup> Inserm, U1138, Team 17, From physiopathology of ocular diseases to clinical development, Université Paris Descartes Sorbonne Paris Cité, Centre de Recherche des Cordeliers, 15 rue de l'Ecole de Médecine, 75006 Paris, France

<sup>3</sup> Faculty of Biology and Medicine, Lausanne University, rue du Bugnon 21, CH-1011, Lausanne, Switzerland

Corresponding author:

Francine Behar-Cohen

Inserm UMR1138

15 rue de l'Ecole de Médecine

75006 Paris, France

Tel: +33-144278169

Email: francine.behar@gmail.com

Grant information:

This work was supported by grants from the Swiss National Fund (#320030\_156401, F. Behar-Cohen) and from the Faculty of Biology and Medicine Research Commission Fund, University of Lausanne, Switzerland (A. Matet).

Keywords:

central serous chorioretinopathy; optical coherence tomography; choriocapillaris; blood flow

Word count: 3156

Short title: Choriocapillaris flow voids in CSCR

## ABSTRACT

**PURPOSE:** To investigate choriocapillaris flow void distribution on optical coherence tomography (OCT) angiography (OCTA) in central serous chorioretinopathy (CSCR), and its correlation to choroidal vessel morphology.

**METHODS:** Fifty-three CSCR eyes (48 patients) and 34 healthy control eyes were retrospectively included. Exclusion criteria were refractive error >2D, previous laser or photodynamic therapy, low-quality OCTA or excessive shadowing artifacts. Choriocapillaris OCTA scans were processed by local-threshold binarization to identify flow voids, and extract their cumulative total area. The locations of the two largest voids in each eye were reported on the corresponding enhanced-depth imaging OCT (EDI-OCT) raster scan. Choriocapillaris thickness and diameter of underlying outer choroidal vessels were measured at flow voids and at adjacent “normal” outer choroidal vessels.

**RESULTS:** There was 22 acute, 16 recurrent and 15 chronic CSCR eyes. Total flow void area was larger in CSCR than control eyes. In a univariate analysis, the total flow void area on OCTA increased with age ( $P=0.0002$ ), duration since CSCR diagnosis ( $P=0.004$ ) and more severe CSCR type ( $P<0.0001$ ). In a multivariate analysis, age ( $P=0.023$ ) and CSCR type ( $P=0.007$ ) were the only independent contributors to total flow void area. Using EDI-OCT, outer choroidal vessel diameter was higher ( $P<0.0001$ ), and choriocapillaris was thinner ( $P<0.0001$ ) at flow voids compared to adjacent sites, independently from eccentricity of sites from the fovea.

**CONCLUSIONS:** Choriocapillaris flow voids colocalize with choriocapillaris thinning and deep choroidal vessel dilation in CSCR eyes. Age and CSCR severity influence choriocapillaris flow, a key contributor to CSCR pathophysiology, which has clinical and therapeutic consequences.

## INTRODUCTION

Central serous chorioretinopathy (CSCR) manifests with serous retinal detachments, that self-resolve in 80% of acute cases<sup>1</sup> but may recur<sup>2-4</sup> or persist,<sup>5,6</sup> leading in chronic cases to permanent retinal pigment epithelium (RPE) damage.<sup>7,8</sup>

Although leakage through the RPE is the direct cause of subretinal fluid accumulation,<sup>9,10</sup> as evidenced by fluorescein angiography, choroidal vasodilation and hyperpermeability are considered the primary underlying mechanisms in the disease pathophysiology.<sup>11</sup> These changes have long been recognized on indocyanine green (ICG) angiography.<sup>12,13</sup> Subsequently, the morphology of choroidal vessels in CSCR was further explored by enhanced-depth imaging (EDI) optical coherence tomography (OCT), that identified an increase in choroidal thickness resulting from the dilation of deep choroidal vessels,<sup>14</sup> termed “pachyvessels”.<sup>15</sup> Recently, en face swept-source OCT further detailed the morphology of the thickened choroid in CSCR and the associated “pachychoroid-spectrum” disorders,<sup>15</sup> and focal choriocapillaris thinning was revealed by choroidal layer segmentation.

The advent of OCT angiography (OCTA) has allowed to visualize non-invasively the distribution of blood flow within the choriocapillaris, the only choroidal layer properly imaged by current OCTA technology,<sup>16</sup> providing novel dynamic information on choroidal physiology. Moreover, choriocapillaris flow is not adequately visualized on ICG angiography. Multiple focal alterations in the choriocapillaris flow pattern of CSCR eyes have been recognized, and termed “foci of reduced flow”,<sup>17</sup> “dark areas” or “dark spots,”<sup>18</sup> although a proportion of these lesions may originate from shadowing artifacts by overlying structures, such as pigment epithelial detachments or subretinal hyperreflective material.<sup>18,19</sup> Recently, Spaide has advanced that the vascular segments forming the choriocapillaris are below the current resolution of OCTA devices, whereas areas of absent flow signal in the choriocapillaris are resolvable on OCTA, appearing as hyporefective spaces. The author demonstrated by means of image processing techniques, that their area follows a power law distribution in normal eyes, mostly influenced by age and the presence of hypertension.<sup>20</sup> Yet, the pattern of choriocapillaris flow voids in CSCR eyes has not been investigated with similar processing tools, which has the potential to bring insight into choroidal changes occurring in CSCR, guide therapeutic strategies and monitor treatments effects with respect to choroidal perfusion.

The aim of this study is to investigate the distribution of choriocapillaris flow voids in CSCR eyes imaged by OCTA, and its correlation to choroidal morphology.

## METHODS

### *Study subjects*

This observational, single-center, retrospective study was designed in accordance with the tenets of the Declaration of Helsinki. Data collection and analysis have been approved by the Ethics Committee of the Swiss Federal Department of Health (CER-VD n°19/15). Consecutive patients presenting with CSCR between September 2015 and March 2017, and who underwent OCTA imaging, were retrospectively included. Patients with refractive error > 2D, history of laser or photodynamic therapy treatment, with low-quality OCTA images (signal strength index, SSI <50) or those with excessive shadowing artifacts, as detailed below, were excluded. In patients who underwent OCTA at several visits, the highest quality OCTA image of the choriocapillaris was selected. When possible, we selected a visit when subretinal detachment, a frequent cause of shadowing,<sup>18</sup> had resolved.

Subjects were categorized according to the clinical form of CSCR, as acute (first episode, within 12 months of symptom onset), recurrent (same criteria as acute, with history of previous episodes) or chronic CSCR (subretinal fluid lasting for 12 months or more).

In addition, 34 eyes from 34 age-matched healthy control subjects imaged by OCTA were included.

#### *Image acquisition*

Subjects underwent spectral-domain optical coherence tomography (SD-OCT) on Spectralis (Heidelberg Engineering, Heidelberg, Germany). A 20×20° 97-section raster scan was acquired in enhanced-depth imaging (EDI) mode, enhancing the visualization of choroidal features, with automated real time (ART) averaging set at 16 images.

The Angiovue RTx 100 (Optovue Inc., Fremont, CA) was used to acquire 3×3-mm OCTA images. The built-in AngioAnalytics software (v2016.1.0.26) was used to segment automatically the choriocapillaris, with the manufacturer's parameter: a 28-µm-thick slab parallel to, and located 31 µm beneath the retinal pigment epithelium (RPE). The correct segmentation of the choriocapillaris was visually controlled in each patient. In addition to SSI<50, imaging exclusion criteria based on OCTA were: excessive motion artifacts, and excessive shadowing artifacts in the choriocapillaris by subretinal material, pigment epithelial or serous retinal detachments. These artifacts were differentiated from actual flow void lesions by visually comparing the corresponding 'en face' OCT scan acquired by the Angiovue device and detecting hyporeflective lesions in both the flow and the 'en face' signals.

#### *Image analysis*

A 3-step image analysis was performed to extract relevant parameters from the distribution of blood flow in the choriocapillaris and its relationship to choroidal morphology.

- First, OCTA images of the choriocapillaris were extracted as .jpg files using a screen capture tool, and their size was increased from 304×304 to 608×608 pixels in order to prevent any loss in image resolution. Images were processed with an automated custom algorithm developed on MatLab (Version 2017b, Matworks, Natick, MA), aimed at detecting choriocapillaris flow voids. This is an automated, batch-processing version of the method recently described by Spaide.<sup>21</sup> Briefly, the algorithm used the local thresholding function ('adaptthresh') embedded in MatLab Image Processing Toolbox to detect flow voids, that manifest as hyporeflective ("dark") spaces within the hyperreflective choriocapillaris flow signal (Figure 1). The algorithm provides a binarized image of the voids (Figure 2, Bottom Left), extracts a list of areas of all detected flow voids larger than  $0.2 \times 10^3 \mu\text{m}^2$  (corresponding to 4 pixel<sup>2</sup> in the original 304×304 scans), and computes the cumulative area of flow voids larger than 10,000  $\mu\text{m}^2$  (Figure 2, Bottom Right), termed "total flow void area", as proposed in the above-mentioned publication.<sup>21</sup>

- Second, the localization of the three largest flow void lesions identified in each eye by the automated algorithm were labelled on the AngioAnalytics software using the horizontal/vertical lines, and the display was changed to the superficial plexus to localize the lesion with respect to retinal vessels. This image was recorded (Figure 3, Left), and the corresponding location was identified on the infrared fundus image acquired along the Spectralis OCT raster scan on the Heidelberg Eye Explorer software (version 1.9.10.0) (Figure 3, Right). Finally, the horizontal EDI SD-OCT section containing this lesion was identified from the dense 97 scans, and the lesion localization was reported on this section. Images of these sections were exported, with "overlays" displaying the sites of flow void, and overlays were deleted from the software (Supplemental Figure 1). All images were processed by the same operator (AM).

- Third, measures of the choriocapillaris and deep choroidal vessels from Haller's layer were carried out on these EDI SD-OCT scans where overlays were removed, on the Heidelberg Eye Explorer software, by an independent observer (AD) masked to the set of exported images with overlays labelling the sites of flow voids. The built-in caliper function was used after setting the scale to 1  $\mu\text{m}$ :1  $\mu\text{m}$  according to the manufacturer's recommendations, and magnifying images at 300%. The observer identified the choriocapillaris borders as recently determined by the OCT nomenclature of the "IN•OCT Consensus",<sup>22</sup> and all visible choroidal vessels from Haller's layer, as the outermost vessels contacting with the sclera. The anteroposterior diameter of each vessel identified in Haller's layer was measured, as

well as the thickness of the overlying choriocapillaris at the corresponding locations, resulting in ~6-8 measures per EDI SD-OCT section, that was exported with “overlays” (calipers and measurements) (Supplemental Figure 1). Finally, a dataset was created by the unmasked observer (AM) where choriocapillaris and deep choroidal vessel measurements were reported, along with the type of site (“Flow void” or “Normal”) and its eccentricity with respect to the fovea (750  $\mu\text{m}$ , 750-1500  $\mu\text{m}$ , >1500  $\mu\text{m}$ ).

### *Statistical analyses*

Descriptive and comparative statistics were performed on GraphPad Prism (version 5.0f, GraphPad Software, La Jolla, CA). Quantitative continuous values were reported as mean  $\pm$  standard deviation (SD). The distribution of flow void areas was represented by the total area and the number of flow void lesions larger than 10,000  $\mu\text{m}^2$ . The Mann-Whitney test for comparisons, and the Chi-square test for contingency analysis were used where appropriate.

Univariate and multivariate analysis (including variable with  $P < 0.3$  in the univariate assessment) followed by stepwise forward regression were performed, using the ‘MASS’ package<sup>23</sup> on the R Software (Version 3.3.0, R Foundation for Statistical Computing, R Core Team, 2016, Vienna, Austria. <http://www.R-project.org>).

Measurements of choriocapillaris /choroidal vessel thickness were compared with the Kruskal-Wallis test on R and the “pgirmess” package for post-tests (Version 1.6.7, Patrick Giraudoux, 2017; <https://CRAN.R-project.org/package=pgirmess>). Plots were created using the ‘ggplot’ package<sup>24</sup> on R.  $P$  values  $< 0.05$  were considered significant.

## RESULTS

Fifty-three eyes from 48 subjects were included in the study (age:  $47.6 \pm 18.7$  years; 39 men and 9 women). Twenty-two eyes were classified as acute, 16 eyes as recurrent and 15 eyes as chronic CSCR. Their clinical characteristics are detailed in Table 1.

At the level of the choriocapillaris, a qualitative analysis of OCTA showed that flow void lesions were less frequent in healthy eyes from control age-matched individuals than in CSCR eyes, as illustrated in Figure 1.

The analysis of choriocapillaris OCTA scans by a custom algorithm, that detects hyporeflective areas corresponding to flow void lesions (above a de-noising threshold of 10,000  $\mu\text{m}^2$ ), confirmed their differential distribution between healthy and CSCR eyes. CSCR eyes presented a higher total flow void area, and a higher number of flow void lesions as compared to healthy eyes ( $P = 0.0004$  and  $0.003$ , respectively) (Table 2).

The total area of flow voids was significantly higher in chronic as compared to acute or recurrent CSCR eyes ( $P=0.0007$  and  $0.012$ , respectively) and there was a trend towards significance between acute and recurrent eyes ( $P=0.09$ ). To further investigate the influence of CSCR type and other potential confounding clinical factors on the distribution of choriocapillaris flow voids, a uni- and multivariate analysis was performed (Table 3). In the univariate analysis, age ( $P=0.0002$ ), duration since CSCR diagnosis ( $P=0.004$ ) and CSCR type (categorized as acute, recurrent, chronic) ( $P<0.0001$ ) had a significant influence on the total flow void area. In the multivariate analysis, age ( $P=0.023$ ) and CSCR type ( $P=0.007$ ) remained the only independent contributors to the total area of flow voids ( $R^2=0.35$ ).

Finally, the two larger choriocapillaris flow void areas identified on each OCTA scan were reported on the corresponding location of Spectralis EDI SD-OCT horizontal scans, where the diameter of all visible deeper choroidal vessels and the thickness of the overlying choriocapillaris were measured by a masked observer. A total of 756 choroidal vessels were correctly visualized, corresponding to an average of 7.1 vessel per EDI scan. Using Kruskal-Wallis test with multiple comparison post-tests, the diameter of deep choroidal vessels was higher ( $328\pm110$  vs  $234\pm91$   $\mu\text{m}$ ,  $P<0.0001$ ), and the choriocapillaris was significantly thinner ( $14\pm7$  vs  $34\pm29$   $\mu\text{m}$ ,  $P<0.0001$ ) at sites co-localizing with flow voids compared to non-flow-void "normal" sites (Figure 4 and 5, respectively). Regarding the distribution of assessed choroidal vessels, those corresponding to flow voids were located more centrally than non-flow-void sites ( $67$  vs  $37\%$ ,  $P<0.0001$ , Chi-Square test) in a  $3\times3$ -mm macular area. Given the morphology of the choroid on EDI SD-OCT, that is thickest at the foveal center, and thinner towards the periphery, we assessed whether eccentricity to the fovea could have influenced the results, by using the same method. A Kruskal-Wallis test with multiple comparison post-tests showed that eccentricity was related to the diameter of deep choroidal vessels ( $P<0.0001$ ), but not to choriocapillaris thickness ( $P=0.14$ ) (Supplementary Figure 2). Multivariate regression was used to better assess the effect of these observations on the relationship between choroidal metrics and flow void sites. It showed that the diameter of large choroidal vessels was thicker at flow void sites ( $P<0.0001$ ), independently from eccentricity ( $P<0.0001$ ) ( $R^2=0.53$ ). No relevant multivariate model of choriocapillaris thickness based on colocalization with flow voids and eccentricity could be fitted ( $R^2=0.07$ ).

## DISCUSSION

In the present study, we analyzed the distribution of flow voids in the choriocapillaris on OCTA, and found that the total area of flow voids was higher in CSCR eyes than age-matched control eyes, and that among CSCR eyes it was higher in older subjects and in more chronic cases. Moreover, we assessed the morphology of choroidal vessels at flow

void sites and observed that the choriocapillaris was thinner, and deep choroidal vessels were thicker at these sites than at adjacent sites.

In healthy eyes, flow voids in OCTA images of the choriocapillaris have been reported, and are likely to result from progressive occlusion of small segments of the interconnected choriocapillaris meshwork, at sub-lobular level, as suggested by their increased density with age.<sup>20</sup> This observation is consistent with the canonical description of the segmental nature of the choroidal vasculature organized in lobular subunits by Hayreh.<sup>25</sup> In CSCR, several groups have described choriocapillaris flow voids,<sup>17,18</sup> in accordance with the present results, but there has been to date no report of their distribution and relationship with the morphology of the choriocapillaris and underlying large choroidal vessels. Moreover, the exact significance of these voids remains unclear.

Spaide reported that factors related to more extended choriocapillaris flow voids in healthy eyes include age, and hypertension, and presence of late AMD or pseudodrusen in the fellow eye.<sup>20</sup> In the present series of CSCR eyes, a similar effect of age was observed, but hypertension was not associated with more extended flow void areas, probably due to the low prevalence of hypertension in this younger cohort (Table 1). Of importance, more advanced CSCR chronicity was linked to more extended total flow void area, confirming that not only large choroidal vessels, or “pachyvessels”, are involved in CSCR but that decreased choriocapillaris perfusion could be a local consequence of these pachyvessels and interfere negatively with RPE homeostasis.

Using ICG angiography combined to OCT, several authors had previously established that large dilated choroidal vessels localize within areas of increased choroidal vascular permeability.<sup>26–31</sup> In addition, ICG angiography also identified areas of choriocapillaris non-perfusion in CSCR during early frames,<sup>32</sup> best visible in confocal video mode. However, the reliable imaging of this phenomenon on ICG angiography is limited by its low reproducibility depending on intravenous injection velocity, heart rate, image exposition, and patient fixation; by its invasiveness preventing repeated imaging; and finally, its low resolution compared to OCTA, that overcomes most of these limitations.

A focally decreased or absent blood flow in the choriocapillaris is likely to result in focal RPE ischemia and alterations of RPE bidirectional transport functions. Mechanical stress directly applied on the RPE by pachyvessels could further alter cytoskeleton organization and polarization, enhancing transport dysfunction and ultimately favoring leakage of fluid from the choroid to the subretinal space, as observed on fluorescein angiography.<sup>10</sup> Yet, by correlating OCTA from CSCR eyes to multimodal imaging findings, including fluorescein and ICG angiography, Feucht *et al* have established that choriocapillaris flow voids do not colocalize with fluorescein leakage sites.<sup>33</sup> Consistently, there are numerous visible flow void

sites in CSCR (Figure 1), and yet there is usually one, and rarely two or more leakage sites in acute CSCR eyes.

Given that the distribution of flow voids in normal eyes follows a power law,<sup>20</sup> it cannot be represented and compared between different subjects by computing mean and standard deviation as in Gaussian or near-Gaussian distributions.<sup>34</sup> Therefore, the cumulative area of hyporeflective spaces (above a threshold of 10,000  $\mu\text{m}^2$  to reduce noise) has been proposed as a relevant parameter<sup>20</sup> since it accounts for the total of all hyporeflective spaces without providing a distorted representation of the distribution as would the mean and standard deviation.

The present work confirms the relevance of the algorithm employed to extract flow voids from OCTA scans, by showing that these lesions were significantly more extended in CSCR eyes than in age-matched control eyes. This external validation confirmed that flow voids participate indeed to pathological processes occurring in the choroid of CSCR eyes. Furthermore, we analyzed choroidal morphology at sites of flow voids by combining OCTA and EDI SD-OCT data, and observed that the choriocapillaris was thinner, and deep choroidal vessels were thicker at sites of flow voids. While eccentricity had no significant impact on choriocapillaris thickness within the assessed 3×3-mm macular area, deep choroidal vessels were thinner in the peripheral macula, but the relationship between deep vessel thickness and flow voids was independent from their localization.

Altogether, these results provide a quantitative confirmation of the inner choroidal thinning that occurs in CSCR and colocalizes with enlarged deep choroidal vessels, as advanced previously by Yang *et al* using EDI-OCT,<sup>30</sup> and by Dansingani *et al* using swept-source OCT choroidal thickness maps.<sup>15</sup> Additionally, the present study demonstrates that choriocapillaris flow is altered at sites of choriocapillaris thinning. Whether thinning, resulting for instance from compression from inwardly displaced large choroidal vessels,<sup>15</sup> induces flow decrease, or the converse, remains to be elucidated. Advancements in quantitative flow velocity detection by OCTA, in segmentation algorithm, and in artifact removal should contribute to further investigate *in vivo* choriocapillaris blood flow kinetics.

This study has several limitations, including the limited size of the cohort resulting from strict exclusion criteria. One of the drawbacks of choriocapillaris imaging by OCTA is the frequency of shadowing artifacts, manifesting as hyporeflective areas resembling flow voids. Subretinal material, pigment epithelial or serous retinal detachments frequently cause “dark spots” within the choriocapillaris on OCTA.<sup>18</sup> Here, we have reduced this flaw by visually reviewing all OCTA scans, selecting for each patient the available OCTA scan with the least artifacts, and by excluding those with evident shadowing artifacts. In addition to pigment epithelial detachments, a frequent cause of shadowing was the presence of serous retinal detachment, either due to the composition of the protein-rich subretinal fluid, or more likely,

to the shadowing effect provoked by elongated photoreceptor outer segments. We attempted to reduce these artifacts by selecting timepoints when subretinal fluid had resolved, or was inferiorly displaced beyond the 3×3-mm area imaged by OCTA. In addition, the adaptive thresholding method employed to detect hyporeflective spaces reduced the impact of artifacts, by detecting these lesions equally within darker areas due to shadowing.

This study opens several perspectives for the better understanding of CSCR mechanisms, and ultimately the improvement of treatment alternatives. First, the possible variation of choriocapillaris flow voids during the course of the disease, suggested by the more extended lesions found in chronic than recurrent or acute cases in this cross-sectional analysis, should be investigated. In our view, this analysis is currently impeded by the excessive above-mentioned artifacts, that may exceed the magnitude of choriocapillaris change over the course of a CSCR episode. Second, whether flow voids partially recover after episode resolution should also be assessed. Third, the dynamic consequences on choriocapillaris flow of photodynamic therapy, a common treatment strategy for non-resolving CSCR targeting choroidal hyperpermeability, and putatively leading to micro-occlusions in the choroidal vasculature, should be evaluated. Recently, Xu *et al* evidenced choriocapillaris flow modifications on OCTA after photodynamic therapy. Finally, given the complex, unique morphology of the choriocapillaris, its difficult accessibility by *in vivo* imaging, and the rarity of validated animal models of CSCR,<sup>35</sup> computerized models reproducing the human choriocapillaris structure, such as the Ising model of magnetism recently proposed by Spaide,<sup>36</sup> may contribute to evaluate its physiological properties and response to pathological dilation or compression by underlying vessels.

## ACKNOWLEDGEMENTS

The authors thank Richard F. Spaide (New York, NY) for previous developments of image processing strategy and fruitful discussions.

## REFERENCES

1. Daruich A, Matet A, Marchionno L, et al. Acute central serous chorioretinopathy: factors influencing episode duration. *Retina*. January 2017;1. doi:10.1097/IAE.0000000000001443.
2. Matet A, Daruich A, Zola M, Behar-Cohen F. Risk factors for recurrences of central serous chorioretinopathy. *Retina*. May 2017;1. doi:10.1097/IAE.0000000000001729.
3. Fok ACT, Chan PPM, Lam DSC, Lai TYY. Risk factors for recurrence of serous macular detachment in untreated patients with central serous chorioretinopathy. *Ophthalmic Res*. 2011;46(3):160-163. doi:10.1159/000324599.
4. Lee H, Lee J, Chung H, Kim C. Baseline spectral domain optical coherence tomographic hyperreflective foci as a predictor of visual outcome and recurrence for central serous chorioretinopathy. *Retina*. 2016;36:1372-1380.
5. Daruich A, Matet A, Dirani A, Bousquet E. Central serous chorioretinopathy : Recent findings and new physiopathology hypothesis. *Prog Retin Eye Res*. 2015;48. doi:10.1016/j.preteyeres.2015.05.003.
6. Gilbert CM, Owens SL, Smith PD, et al. Long-term follow-up of central serous chorioretinopathy. *Br J Ophthalmol*. 1984;68(11):815-820. doi:10.1136/bjo.68.11.815.
7. von Winning CH, Oosterhuis JA, Renger-van Dijk AH, Hornstra-Limburg H, Polak BC. Diffuse retinal pigment epitheliopathy. *Ophthalmologica*. 1982;185(1):7-14.
8. Cohen D, Gaudric A, Coscas G, Quentel G, Binaghi M. [Diffuse retinal epitheliopathy and central serous chorioretinopathy]. *J Fr Ophthalmol*. 1983;6(4):339-349.
9. Gass JD. Pathogenesis of disciform detachment of the neuroepithelium. *Am J Ophthalmol*. 1967;63(3):Suppl:1-139.
10. Pryds A, Sander B, Larsen M. Characterization of subretinal fluid leakage in central serous chorioretinopathy. *Investig Ophthalmol Vis Sci*. 2010;51(11):5853-5857. doi:10.1167/iovs.09-4830.
11. Liew G, Quin G, Gillies M, et al. Central serous chorioretinopathy: a review of epidemiology and pathophysiology: Central serous chorioretinopathy. *Clin Experiment Ophthalmol*. 2013;41(2):201-214. doi:10.1111/j.1442-9071.2012.02848.x.
12. Scheider A, Nasemann JE, Lund OE. Fluorescein and indocyanine green angiographies of central serous choroidopathy by scanning laser ophthalmoscopy. *Am J Ophthalmol*. 1993;115(1):50-56.

13. Guyer DR, Yannuzzi LA, Slakter JS, Sorenson JA, Ho A, Orlock D. Digital indocyanine green videoangiography of central serous chorioretinopathy. *Arch Ophthalmol*. 1994;112(8):1057-1062.
14. Imamura Y, Fujiwara T, Margolis R, Spaide RF. Enhanced depth imaging optical coherence tomography of the choroid in central serous chorioretinopathy. *Retina*. 2009;29:1469-1473. doi:10.1097/IAE.0b013e3181be0a83.
15. Dansingani KK, Balaratnasingam C, Naysan J, Freund KB. En face imaging of pachychoroid spectrum disorders with swept-source optical coherence tomography. *Retina*. August 2015. doi:10.1097/IAE.0000000000000742.
16. Ferrara D, Waheed NK, Duker JS. Investigating the choriocapillaris and choroidal vasculature with new optical coherence tomography technologies. *Prog Retin Eye Res*. 2016;52:130-155. doi:10.1016/j.preteyeres.2015.10.002.
17. Teussink MM, Breukink MB, Van Grinsven MJJP, et al. OCT Angiography Compared to Fluorescein and Indocyanine Green Angiography in Chronic Central Serous Chorioretinopathy. *Investig Ophthalmology Vis Sci*. 2015;56(9):5229. doi:10.1167/iovs.15-17140.
18. Costanzo E, Cohen SY, Miere A, et al. Optical Coherence Tomography Angiography in Central Serous Chorioretinopathy. *J Ophthalmol*. 2015;2015:1-10. doi:10.1155/2015/134783.
19. Spaide RF, Fujimoto JG, Waheed NK. Image artifacts in optical coherence tomography angiography. *Retina*. 2015;35(11):2163-2180. doi:10.1097/IAE.0000000000000765.
20. Spaide RF. Choriocapillaris Flow Features Follow a Power Law Distribution: Implications for Characterization and Mechanisms of Disease Progression. *Am J Ophthalmol*. 2016. doi:10.1016/j.ajo.2016.07.023.
21. Spaide RF. Choriocapillaris Flow Features Follow a Power Law Distribution: Implications for Characterization and Mechanisms of Disease Progression. 2016. doi:10.1016/j.ajo.2016.07.023.
22. Staurengi G, Sadda S, Chakravarthy U, Spaide RF, International Nomenclature for Optical Coherence Tomography (IN•OCT) Panel. Proposed Lexicon for Anatomic Landmarks in Normal Posterior Segment Spectral-Domain Optical Coherence Tomography. *Ophthalmology*. 2014;121(8):1572-1578. doi:10.1016/j.ophtha.2014.02.023.
23. Venables WN, Ripley BD. *Modern Applied Statistics with S*. Fourth Ed. New York: Springer; 2002.
24. Wickham H. *ggplot2*. New York, NY: Springer New York; 2009.

25. Hayreh SS. Segmental nature of the choroidal vasculature. *Br J Ophthalmol*. 1975;59(11):631-648. doi:10.1136/bjo.59.11.631.
26. Jirarattanasopa P, Ooto S, Tsujikawa A, et al. Assessment of macular choroidal thickness by optical coherence tomography and angiographic changes in central serous chorioretinopathy. *Ophthalmology*. 2012;119(8):1666-1678. doi:10.1016/j.ophtha.2012.02.021.
27. Kuroda S, Ikuno Y, Yasuno Y, et al. Choroidal thickness in central serous chorioretinopathy. *Retina*. 2013;33:302-308. doi:10.1097/IAE.0b013e318263d11f.
28. Maruko I, Iida T, Sugano Y, Ojima A, Sekiryu T. Subfoveal choroidal thickness in fellow eyes of patients with central serous chorioretinopathy. *Retina*. 2011;31(8):1603-1608. doi:10.1097/IAE.0b013e31820f4b39.
29. Razavi S, Souied EH, Cavallero E, Weber M, Querques G. Assessment of choroidal topographic changes by swept source optical coherence tomography after photodynamic therapy for central serous chorioretinopathy. *Am J Ophthalmol*. 2014. doi:10.1016/j.ajo.2013.12.029.
30. Yang L, Jonas JB, Wei W. Optical coherence tomography-assisted enhanced depth imaging of central serous chorioretinopathy. *Investig Ophthalmol Vis Sci*. 2013;54(7):4659-4665. doi:10.1167/iovs.12-10991.
31. Ferrara D, Mohler KJ, Waheed N, et al. En Face Enhanced-Depth Swept-Source Optical Coherence Tomography Features of Chronic Central Serous Chorioretinopathy. *Ophthalmology*. 2014;121(3):719-726. doi:10.1016/j.ophtha.2013.10.014.
32. Prünte C. Indocyanine green angiographic findings in central serous chorioretinopathy. *Int Ophthalmol*. 1995;19(2):77-82.
33. Feucht N, Maier M, Lohmann CP, Reznicek L. OCT Angiography Findings in Acute Central Serous Chorioretinopathy. *Ophthalmic Surgery, Lasers Imaging Retin*. 2016;47(4):322-327. doi:10.3928/23258160-20160324-03.
34. Spaide RF. Choriocapillaris Flow in Myopia. *Investig Ophthalmology Vis Sci*. 2017;58(9):3563. doi:10.1167/iovs.17-22042.
35. Zhao M, Célérier I, Bousquet E, et al. Mineralocorticoid receptor is involved in rat and human ocular chorioretinopathy. 2012;122(7):1-8. doi:10.1172/JCI61427DS1.
36. Spaide RF. Ising model of choriocapillaris flow. *Retina*. 2017;in press.

## FIGURE CAPTIONS

FIGURE 1. Optical coherence tomography angiography of the choriocapillaris in three cases of central serous chorioretinopathy and one healthy control eye.

A. Healthy eye. B. Acute CSCR. C. Recurrent CSCR. D. Chronic CSCR. Hyporeflective flow void lesions were more numerous and extended in CSCR eyes than in the healthy eye, and the number and area of lesions increased with the severity of CSCR.

FIGURE 2. Image processing algorithm extracting choriocapillaris flow voids from optical coherence tomography angiography images of the choriocapillaris.

A. Original optical coherence tomography angiography scan of a 54-year old woman with central serous chorioretinopathy, after choriocapillaris segmentation and exportation from the Angiovue device, showing hyporeflective flow voids. B. Binarized image using local thresholding, resulting in the flow signal appearing white and flow voids appearing black. C. Morphological opening and image inversion resulting in flow voids appearing white. D. Filtering of flow void lesions to compute the total area of voids larger than  $10,000 \mu\text{m}^2$ .

FIGURE 3. Identification of the corresponding site of flow voids in the choriocapillaris and the superficial plexus.

Screen capture showing the labelling of choriocapillaris flow voids by crossed lines tool (A) and identification of the corresponding location in the superficial plexus (B) on the Angiovue device, that was subsequently visually identified on the Spectralis infrared reflectance image with respect to retinal vessels.

FIGURE 4. Analysis of deep choroidal vessel diameter at sites of flow voids and adjacent outer choroidal vessels.

Plot showing that the anteroposterior diameter of deep choroidal vessels was higher at flow void sites than at other “normal” sites, on enhanced-depth imaging optical coherence tomography horizontal scans through flow voids identified on optical coherence tomography angiography.

\*\*\*  $P < 0.001$

FIGURE 5. Analysis of choriocapillaris thickness at sites of flow voids and adjacent outer choroidal vessels

Plot showing that the choriocapillaris was thinner at flow void sites than at other “normal” sites, on enhanced-depth imaging optical coherence tomography horizontal scans through flow voids identified on optical coherence tomography angiography.

\*\*\*  $P < 0.001$

SUPPLEMENTAL FIGURE 1. Exported images from EDI-OCT with overlays indicating the site of choriocapillaris flow void detected on OCTA (A), and the measurements of choriocapillaris and deep choroidal vessels by the masked observer (B).

SUPPLEMENTARY FIGURE 2. Influence of eccentricity from the fovea on choriocapillaris and outer choroidal vessel thickness.

A. Plot showing that eccentricity to the fovea had a significant effect on the diameter of deep choroidal vessels thickness within the 3×3-mm macular area evaluated. However, multivariate analysis showed that both parameters influenced the diameter of deep choroidal vessels independently.

B. Plot showing that eccentricity to the fovea had no significant effect on choriocapillaris thickness within the 3×3-mm macular area evaluated.

\*\*\*  $P < 0.001$

TABLE 1. Clinical characteristics of N patients with CSCR who underwent optical coherence tomography angiography imaging of the choriocapillaris

	Acute CSCR (n=22 eyes)	Recurrent CSCR (n=16 eyes)	Chronic CSCR (n=15 eyes)
Subjects, N.	20	15	13
Age, year	41 ± 16	49 ± 16	57 ± 23
Sex, N. (male/female)	17/3	13/2	9/4
Axial length, mm	22.8 ± 0.8	23.8 ± 1.1	23.3 ± 1.1
Hypertension, N. (%)	2 (10%)	2 (13%)	4 (31%)
Duration since CSCR diagnosis, month	4.8 ± 3.0	18.4 ± 10.7	30.9 ± 11.9
Subfoveal choroidal thickness, µm	463 ± 99	474 ± 103	448 ± 87
Total flow void area, ×10 <sup>3</sup> µm <sup>2</sup>	1800 ± 222	1900 ± 236	2234 ± 390
Number of flow void lesions ≥ 10,000 µm <sup>2</sup>	95 ± 9	95 ± 7	101 ± 10

Quantitative values are reported as mean ± standard deviation.

CSCR= central serous chorioretinopathy

TABLE 2. Comparison of choriocapillaris flow voids on optical coherence tomography angiography scans between CSCR eyes and age-matched control eyes

	CSR (n=53 eyes)	Controls (n=34 eyes)	<i>P</i> *
Total flow void area, $\times 10^3 \mu\text{m}^2$	1953 $\pm$ 332	1698 $\pm$ 226	.0004
Number of flow void lesions ( $\geq 10,000 \mu\text{m}^2$ )	96.3 $\pm$ 8.8	91.1 $\pm$ 6.7	.003

The total area of flow voids refers to the cumulative areas of flow voids larger than 10,000  $\mu\text{m}^2$ .

\* Mann-Whitney test

CSCR= central serous chorioretinopathy

TABLE 3. Parameters influencing the total area of choriocapillaris flow voids on optical coherence tomography angiography scans of CSCR eyes.

Parameter	Univariate			Multivariate		
	Estimate	Standard error	<i>P</i> <sup>*</sup>	Estimate	Standard error	<i>P</i> <sup>†</sup>
Age, year	13.1	3.2	.0002	8.2	3.5	.023
Sex (male versus female)	-196.0	119.6	.11	-	-	-
Axial length, mm	-21.6	45.2	.63	-	-	-
Hypertension	141.6	127.2	.27	-	-	-
Duration since CSCR diagnosis, month	9.3	3.1	.004	-	-	-
Type of CSCR (acute, recurrent, chronic)	210.0	47.5	<0.0001	148.9	52.4	.007

\* Univariate linear regression

† Multivariate linear regression followed by stepwise regression

The total area of flow voids refers to the cumulative areas of flow voids larger than 10,000  $\mu\text{m}^2$ .

Multivariate analysis:  $R^2=0.35$

CSCR= central serous chorioretinopathy

Fig 1

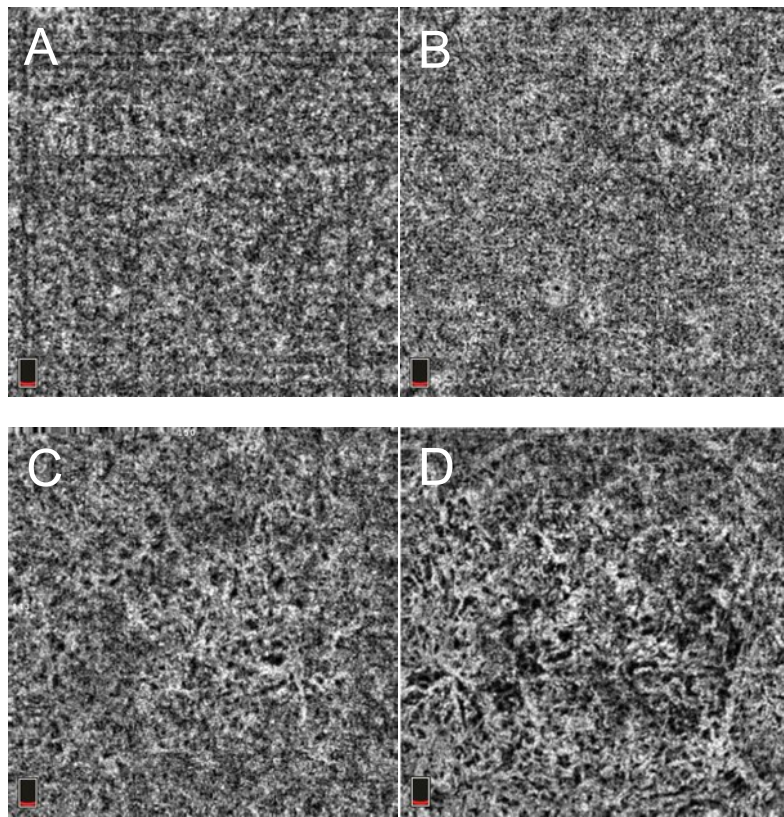


Fig 2

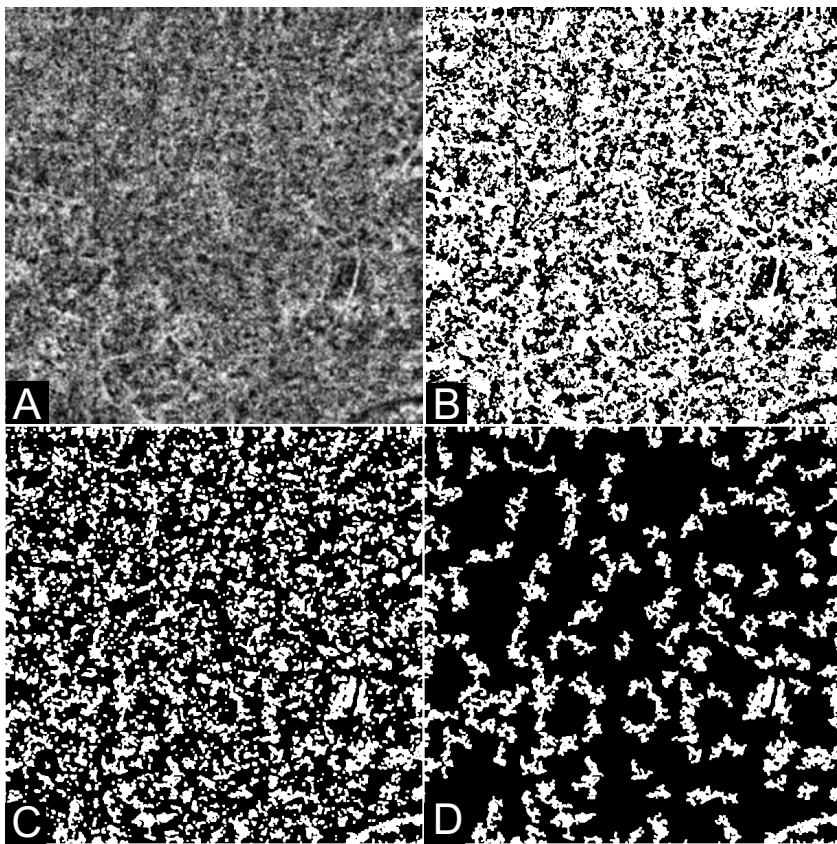


Fig 3

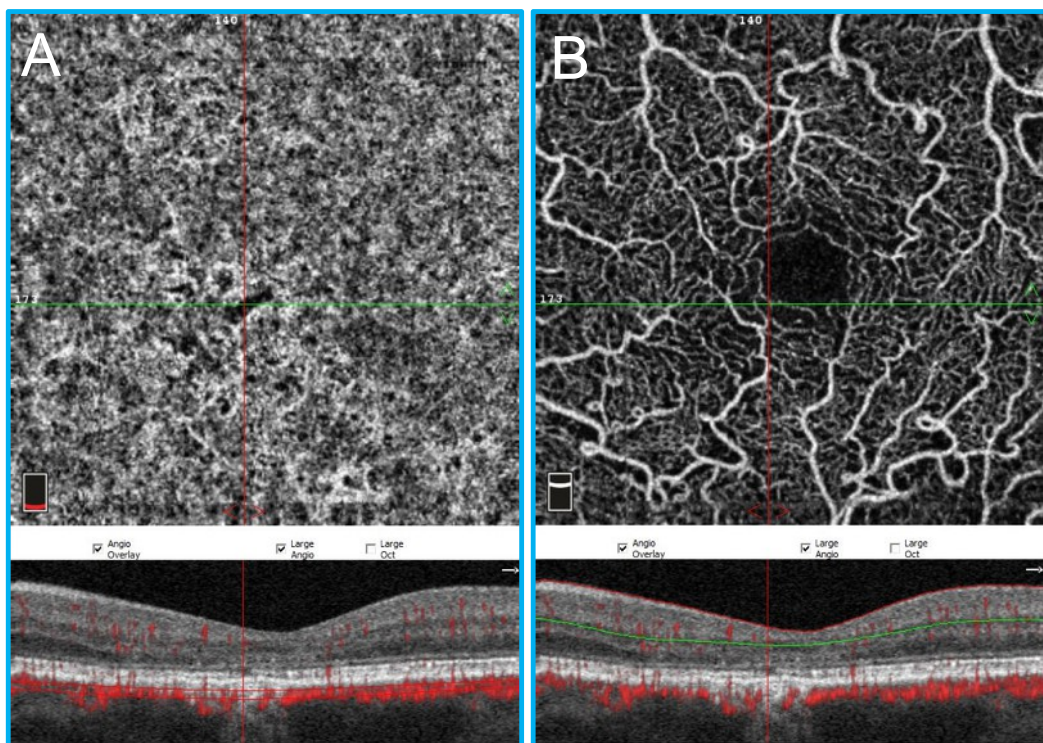


Fig 4

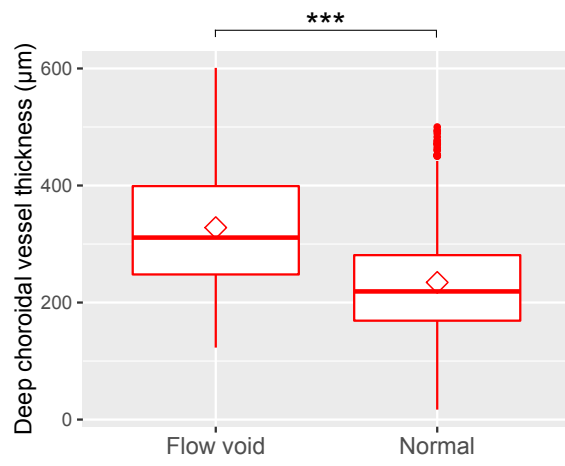
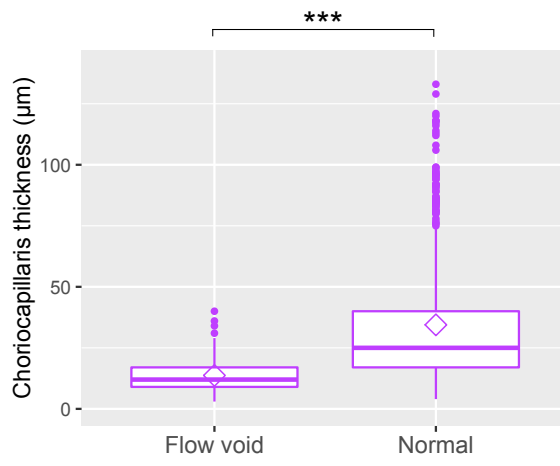
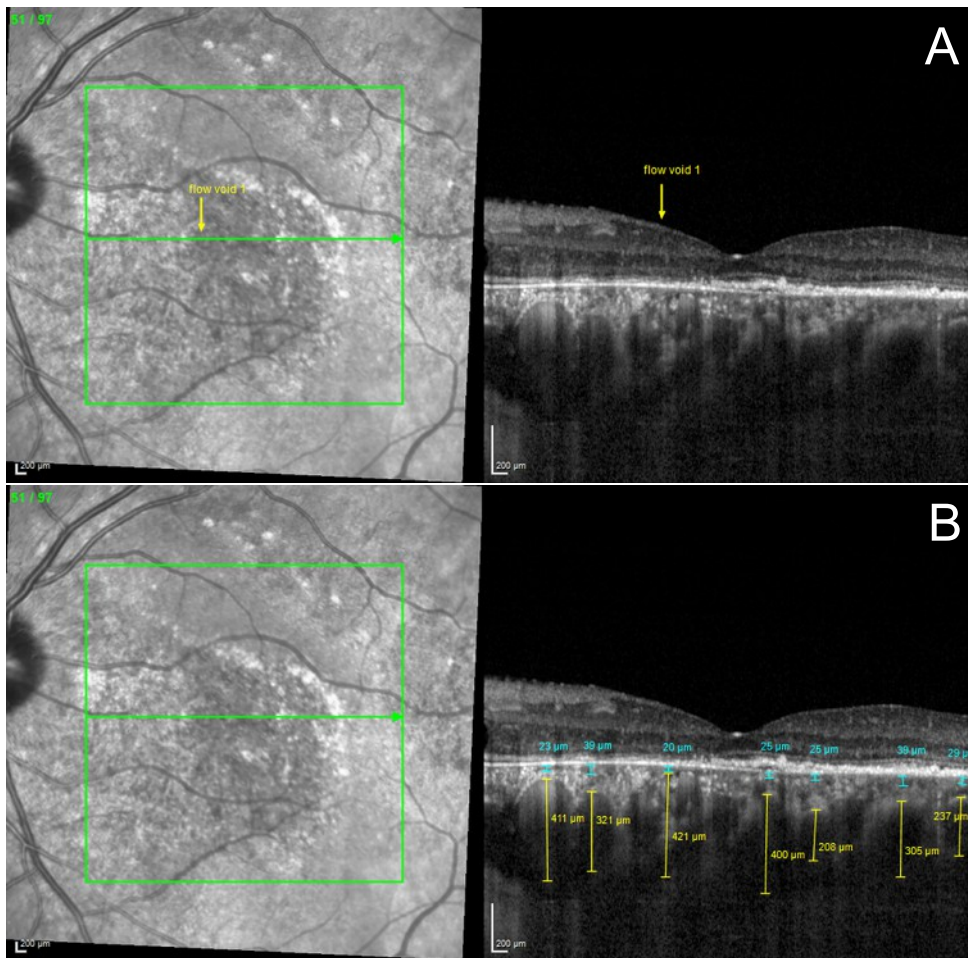


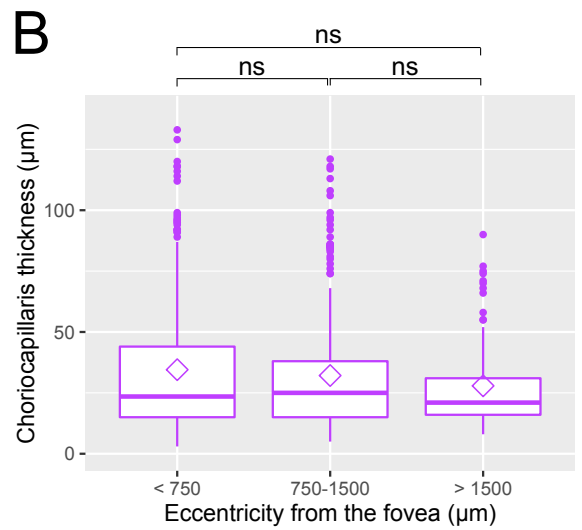
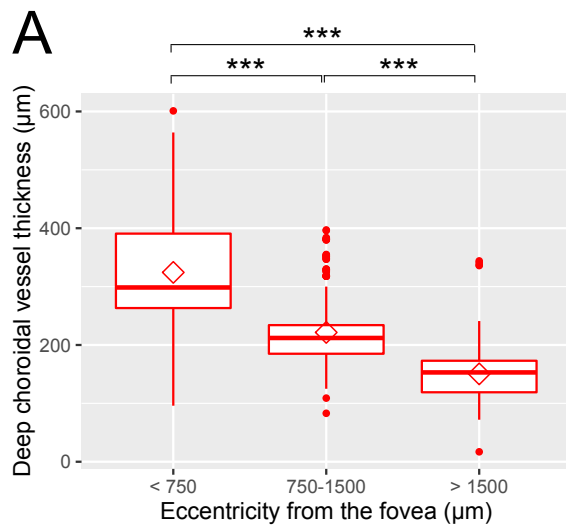
Fig 5



Suppl Fig 1



Suppl Fig 2





[2d] Proteome and metabolome of subretinal fluid in central serous chorioretinopathy and rhegmatogenous retinal detachment: a pilot case study (submitted)

Kowalczuk L\*, Matet A\*, Dor M, Bararpour N, Daruich A, Dirani A, Behar-Cohen F, Thomas A, Turck N

Submitted in June 2017

Status: post-revision

\*= co-first authors

Contribution of PhD candidate:

- Patient follow-up
- Interpretation of results
- Co-drafting the manuscript



## **Proteome and metabolome of subretinal fluid in central serous chorioretinopathy and rhegmatogenous retinal detachment: a pilot case study**

Laura Kowalczuk<sup>1\*</sup>, Alexandre Matet<sup>1\*</sup>, Marianne Dor<sup>2</sup>, Nasim Bararpour<sup>3</sup>, Alejandra Daruich<sup>1</sup>, Ali Dirani<sup>1</sup>, Francine Behar-Cohen<sup>4,5</sup>, Aurélien Thomas<sup>3,4†</sup>, Natacha Turck<sup>2†</sup>

<sup>1</sup> Department of Ophthalmology, University of Lausanne, Jules-Gonin Eye Hospital, Fondation Asile des Aveugles, Lausanne, Switzerland

<sup>2</sup> OPTICS Laboratory, Department of Human Protein Science, University of Geneva, Geneva, Switzerland

<sup>3</sup> Unit of Toxicology, CURML, Lausanne-Geneva, Switzerland

<sup>4</sup> Faculty of Biology and Medicine, Lausanne University Hospital, University of Lausanne, Lausanne, Switzerland

<sup>5</sup> Inserm, U1138, Team 17, From physiopathology of ocular diseases to clinical development, Université Paris Descartes Sorbonne Paris Cité, Centre de Recherche des Cordeliers, Paris, France

\* Both authors contributed equally to this work.

† Both authors contributed equally to this work

### **Corresponding author:**

Francine Behar-Cohen  
Inserm U1138, Team 17, Centre de Recherche des Cordeliers  
15 rue de l'École de Médecine  
75006 Paris, France  
Tel : +33-144278169  
E-mail: francine.behar@gmail.com

**Grant information:** This work was supported by grants from the Swiss National Science Foundation to NT (#PMPDP3\_158370), AT (#310030-156771), and FBC (#320030\_156401), from the Agence Nationale de la Recherche to FBC (ANR-15-CE18-0032 “ROCK SUR MER”) and from the Faculty of Biology and Medicine Research Commission Fund, University of Lausanne, to AM. The funders had no role in study design, data collection and analysis, decision to publish, or preparation of the manuscript.

**Competing Interests:** The authors have declared that no competing interests exist.

**Running head:** Multi-omics of subretinal fluid

**Word count:** 3859

**Key words:** Subretinal space; Retinal pigment epithelium; Retinal Detachment; Retinal Metabolism; vitreoretinal surgery

**ABSTRACT**

**Purpose:** To evaluate the feasibility of proteomics and metabolomics to investigate the molecular composition of subretinal fluid (SRF) in central serous chorioretinopathy (CSCR) and rhegmatogenous retinal detachment (RRD).

**Methods:** SRF was obtained from one patient with severe non-resolving bullous CSCR requiring surgical subretinal fibrin removal, and two patients with long-standing RRD. Proteins were trypsin-digested, labeled with Tandem-Mass-Tag and fractionated according to their *pI* for identification and quantification by tandem mass spectrometry. Independently, metabolites were extracted on cold methanol/ethanol, and identified by untargeted ultra-high-performance liquid chromatography and high-resolution mass spectrometry. Bioinformatics analyses were conducted.

**Results:** In total, 291 proteins and 651 metabolites were identified in SRF samples. One-hundred twenty-eight proteins (77 down-regulated; 51 up-regulated) and 76 metabolites (43 down-regulated; 33 up-regulated) differed in the SRF from CSCR compared to RRD. Protein and metabolites notably deregulated in CSCR were related to glycolysis/gluconeogenesis, inflammation (including serum amyloid P component, versican), alternative complement pathway (complement factor H and complement factor H-related protein), cellular adhesion, biliary acid metabolism (farnesoid X receptor/retinoid X receptor), and gluco- and mineralocorticoid systems (aldosterone, angiotensin and corticosteroid-binding globulin).

**Conclusions:** Proteomics and metabolomics can be performed on SRF. A unique SRF sample from CSCR exhibited a distinct molecular profile compared to RRD.

**Translational relevance:** This first comparative multi-omics analysis of SRF improved the understanding of CSCR and RRD pathophysiology. It identified pathways potentially involved in the better photoreceptor preservation in CSCR, suggesting neuroprotective targets that will require additional confirmation.

## INTRODUCTION

Central serous chorioretinopathy (CSCR) is characterized by serous detachments of the neurosensory retina, frequently affecting the macula, focal pigment epithelial detachments, increased choroidal thickness and choroidal vascular hyper-permeability. Severe CSCR can present as bullous exudative retinal detachment with persistence of subretinal material,<sup>1</sup> that may exceptionally require surgery.<sup>2</sup> During the procedure, subretinal fluid (SRF) can be collected, but to the best of our knowledge, the composition of SRF from a CSCR patient has never been analyzed. Mechanisms of SRF accumulation in CSCR are still uncertain. Several theories have been proposed to explain fluid entry from the choroid towards the subretinal space: dilated and hyper-permeable choroidal vessels favoring trans- or inter-retinal pigment epithelium (RPE) entry flow,<sup>3</sup> changes in RPE cell polarity altering hydro-ionic pumping direction,<sup>4</sup> uni- or multifocal rupture of the RPE barrier,<sup>5</sup> or active reverse flow by unknown triggering mechanisms.<sup>6</sup>

Although serous macular detachments form rapidly and last for 3-6 months in most cases,<sup>7</sup> visual acuity is usually preserved, suggesting a good preservation of photoreceptors function and structure.<sup>8</sup> This differs strikingly with macula-off rhegmatogenous retinal detachment (RRD), in which detachments lasting more than 3-5 days lead to irreversible visual impairment.<sup>9</sup> Mechanisms of photoreceptor cell death after RRD are multiple, triggered by oxidative and metabolic stress, complement alternative pathway activation, immune response and inflammation.<sup>10,11</sup> In RRD, SRF originates mainly from liquefied vitreous, which diffuses through a retinal tear under the neuroretina. In response to neuroretinal detachment, RPE cells proliferate and migrate into the subretinal space,<sup>12</sup> which may contribute to SRF accumulation. Whether SRF composition influences the differential photoreceptor survival and visual prognosis in different types of neuroretinal detachment is not known.

The aim of this study was to investigate the molecular composition of subretinal fluid in CSCR and RRD using proteomics and metabolomics. We compared the SRF profile from one case with severe CSCR and two cases with chronic RRD. Due to the rarity of SRF samples from CSCR, we opted for an untargeted proteomic approach, with independent cross-assessment by metabolomics analysis.

## **PATIENTS AND METHODS**

### **Study subjects**

This study involving human subjects adhered to the tenets of the Declaration of Helsinki, and was approved by the local Ethics Committee of the Swiss Department of Health on research involving human subjects (CER-VD N°340/15 and CER-VD N°19/15). Patients signed an informed consent. A 48-year-old male patient with persistent bullous CSCR underwent vitrectomy for sub-retinal fibrinous clot removal. Two patients aged 58 and 82 years, presenting macula-off RRD lasting more than 15 days since central vision loss, underwent vitrectomy for RRD repair. In all cases, 23-Gauge trocars were inserted at the pars plana and SRF was collected using a back flush cannula connected to a syringe. The CSCR patient underwent multimodal retinal imaging at regular intervals, consisting in spectral-domain optical coherence tomography (SD-OCT), fundus autofluorescence, fluorescein and indocyanine green (ICG) angiography on Spectralis (Heidelberg Engineering, Heidelberg, Germany).

### **Proteomic analysis**

The proteome of the SRF was compared between samples from the CSCR patient and the two patients with chronic RRD. The total protein concentration in each sample was determined using a Bradford protein assay (Protein assay Dye reagent concentrate, Biorad, US-CA) according to the manufacturer's instructions.

#### *Sample preparation*

In order to reduce the impact of potential blood contamination during sample collection, 100 µg of SRF from the CSCR patient and 100 µg of SRF pooled from the two RRD patients (a 1:1 volume/volume ratio) were filtered using a commercial resin according to the manufacturer's recommendations (Proteome Purify 12 Human Serum Protein Immunodepletion Resin, R&D Systems, UK). The classical top-12 most abundant proteins in the serum were then depleted (alpha-1-Acid Glycoprotein, Alpha-1-Antitrypsin, alpha-2-Macroglobulin, Albumin, Apolipoprotein A-I, Apolipoprotein A-II, Fibrinogen, Haptoglobin, IgA, IgG, IgM, Transferrin). Using Bradford method,

the total protein concentration after depletion was estimated at 9.5 µg/mL in the CSCR sample and 9.6 µg/mL in the pooled RRD samples. Subsequently, 5 µg of samples (CSCR and RRD) were reduced using 33µl of 6M urea (Merk, Germany) and 2µl of 50mM tris-(2-carboxyethyl)phosphine (TCEP, Sigma-Aldrich, US-MO). After incubation at 37°C during 1 hour, 1 µl of 400mM iodoacetamid (Sigma-Aldrich, US-MO) was added and samples were incubated for 30 minutes and 67 µl of 0.1M TEAB (Triethylammonium bicarbonate buffer, Sigma-Aldrich, US-MO) were added before trypsin (1 µg/50 µg of proteins, porcine origin, Promega Corporation, US-WI) digestion overnight at 37°C. Samples were labeled with one of the 6 TMT reagents (Tandem Mass Tag; isobaric label reagent sets, ThermoFisher Scientific, US-IL) applying the Simultaneous Marker discovery And verification for the Rapid Translation of Exogeneous Reference material (SMARTER)-based approach,<sup>13</sup> according to manufacturer's instructions. Briefly, tag 128 was attributed to pooled SRFs (used as clinical controls) from RRD patients and tag 130 to the case study CSCR. Tags 126 and 127 were used to label vitreous pool of RRD patients and commercial tears (HMTEARS, Seralab, UK) both used as biological controls. Finally, the 2 remaining tags (129 and 131) were used as internal technical controls. The total quantity of each labeled sample (30 µg) was pooled and dried in a speed-vacuum.

#### *Off-gel electrophoresis (OGE)*

Previously dried samples were resuspended in 5% CAN and 0.1%FA and purified under Macrospin columns (Harvard Apparatus, US-MA). A 3100 OFFGEL Fractionator (Agilent technologies, US-CA) was then used to separate peptides according to their *pI*, as reported previously<sup>14</sup> with a 13 cm IPG strip (immobiline Dry strip pH 3-10, 13 cm, GE Healthcare, UK) and 12 OGE wells. The focusing parameters were 20Kvh, 800v, 50uA, 200mW and 100s. The hold parameters were 500V, 20uA and 50 mW. After overnight fractionation, microspin columns (Harvard Apparatus, US-MA) were performed according to manufacturer's recommendations and the 12 fractions were dried under speed-vacuum.

### *Mass spectrometry analysis*

For each fraction, 0.5 µg of sample was injected 4 times (final amount injected: 2 µg) and then analyzed in gas-phase fractionation (GPF4) mode<sup>15</sup> by tandem mass spectrometry (MS) (Liquid Chromatography(LC)-MS/MS) using a LTQ Orbitrap Velos Pro (Thermo Fisher instrument, US-CA) coupled to a nanoflow high pressure liquid chromatography (HPLC, nanoaquity system from Waters, US-MA). LC-MS/MS analyses were performed as described elsewhere.<sup>16</sup>

### *Data analyses*

Peak lists and resulting files were searched against the UniProt-Swiss-Prot database (2014\_10 version Homo sapiens taxonomy) using Phenyx 2.6 software (Gene Bio, Geneva, Switzerland). Variable amino acid modifications were oxidized methionine, glutamine and asparagine deamidation and TMT®-labeled peptides amino terminus (+229.1629 Da if required). TMT®-labeled lysine (if concerned) and carbamidomethylation of cysteines were set as fixed modification.<sup>16</sup> Trypsin was selected as the enzyme, with one potential missed cleavage. Only proteins matching two different and unique peptide sequences were selected for identification and quantification. A false discovery rate of 1% was selected. Protein quantification was obtained from Mascot method in Easyprot (version 2.3) as statistical tools in order to calculate the proteins ratios between the CSCR SRF (tag 130) and the RRD SRFs (tag 128).<sup>17</sup> Briefly, to obtain the ratio of a protein, Mascot computes the geometric mean of all peptide ratios linked to this protein. Proteins were considered as significantly different if the 130/128 ratio were above 1.50 or below 0.67, with a p-value <0.05.<sup>18</sup> For more details about quantification and statistical criteria, please refer to the previously reported methods.<sup>17, 18</sup> The 12 proteins that were initially resin-depleted were removed from the final lists, if identified.

### **Metabolomics analysis**

Similarly, independent untargeted metabolomics was performed to compare SRF metabolome in the CSCR patient with the two RRD patients. Metabolites were extracted from 50 µL of SRF samples using cold methanol/ethanol (1:1, v/v) in a 1:3 ratio.<sup>19</sup>

*Untargeted ultra-high-performance liquid chromatography (UHPLC) – high-resolution mass spectrometry (HRMS) analysis*

For comparison of CSCR and RRD, two independent analyses were performed on two different days. These analyses were performed on UHPLC (UltiMate 3000 RSLCnano System, Thermo Scientific) hyphenated with HRMS (Q Exactive Plus MS, Thermo Scientific). The metabolites were separated by reversed phase chromatography on a Kinetex C18 (2.6µm, 50mm x 2.1mm I.D) column (Phenomenex, PA) using MeOH:H<sub>2</sub>O 0.1% formic acid solvent in a gradient elution mode with fixed flow rate at 0.3mL/min. Quality controls (i.e. representative pool of samples) and internal standards were used to assess the over-batch repeatability. Data acquisition was performed in full scan mode in both negative and positive polarities considering suitable tuning methods.<sup>19</sup> Subsequently, MS/MS spectra were acquired in a data dependent acquisition mode. Resolutions were fixed at 70,000 and 17,000 for full scan and MS/MS acquisitions, respectively.

*Chemometric analysis*

Raw UHPLC-HRMS data were converted to appropriate format to be processed by XCMS online software for peak detection, chromatogram alignment and isotope annotation.<sup>20</sup> Pre-processed data were normalized by using sample-wise mean normalization as well as feature-wise pareto-scaling. The assessment of the metabolic patterns was driven by the use of unsupervised and supervised learning approaches, including prediction analysis for microarrays data mining (PAM) into the R software (Version 3.3.0, R Foundation for Statistical Computing, R Core Team, 2016, Vienna, Austria. <http://www.R-project.org>) and the ‘pamr’ package, as well as the online Metaboanalyst tool (<http://www.metaboanalyst.ca/>). PAM classifier gives the opportunity to keep only the subset of features that maximized the model performance in predicting class membership.<sup>21</sup>

*Metabolite identification*

Differential metabolites were confirmed based on their retention time and MS<sup>2</sup> fragmentation pattern<sup>19</sup> using open-access libraries, including the HMDB database ([www.hmdb.ca](http://www.hmdb.ca)), lipidmaps ([www.lipidmaps.org](http://www.lipidmaps.org)), metlin (<http://metlin.scripps.edu/index.php>) and mzcloud ([www.mzcloud.org](http://www.mzcloud.org)).<sup>22</sup>

### **Biological process and pathway analysis**

The Panther software (Protein Analysis Through Evolutionary Relationships, version 10.0, release date April, 2015) was used to analyze the protein lists in order to generate the gene ontology categories (protein class).<sup>23</sup> The overrepresentation of the pathways in which the differential proteins of the CSCR SRF compared to the RRD SRF are involved was performed with QIAGEN's Ingenuity Pathway Analysis (IPA, QIAGEN Redwood City, [www.qiagen.com/ingenuity](http://www.qiagen.com/ingenuity)).

Over-representation analysis on the metabolomics data was performed by Consensuspathdb (<http://consensuspathdb.org>) to obtain accurate insight into the underlying biology of differentially expressed metabolites exploiting the KEGG database. Enrichment set analysis was appreciated by 4150 IDs for human species included in the KEGG library. Cytoscape software (Version 3.2.1, <http://cytoscape.org>) and the MetScape plugin (Version 3.1.2) were used to build the compound-gene metabolic network.<sup>24</sup> From the set of genes obtained in the compound-gene network, gene ontology terms were integrated and functionally organized in a gene ontology network function using the ClueGO plugin (Version 2.2.5).<sup>25</sup>

## **RESULTS**

### **Clinical history of the CSCR patient**

A 48-year old man was referred with right eye vision loss for three months. He reported steroid nasal spray use for allergic rhinitis, and no remarkable medical history. Best-corrected visual acuity of his right eye was decreased to 20/200. No ocular inflammation was observed, and intraocular pressure was normal. Fundus examination showed a posterior serous retinal detachment with multiple retinal folds and presence of focal subretinal yellowish material (Figure 1A). On fundus autofluorescence, extensive hyper-autofluorescent gravitational tracks contrasted with central hypo-autofluorescence due to subretinal material masking effect (Figure 1B, arrows). SD-OCT showed a serous retinal detachment with retinal folds, hyper-reflective material in the subretinal space (Figures 1C-D) and flat irregular pigment epithelial detachments (Figures 1C-D). Subfoveal choroidal thickness, using enhanced depth imaging SD-OCT was 548 $\mu$ m in the right eye and 661 $\mu$ m in the left eye, superior to

choroidal thickness reported in normal subjects.<sup>8</sup> In the left eye a regular pigment epithelial detachment temporal to the fovea was observed on SD-OCT (Figure 1E). On fluorescein angiography, multiple leakage sites were observed in the right eye, temporal to the fovea and along the superior and inferior temporal vessels (Figures 1F-G), and pigment epithelial alterations, suggestive of previous CSCR episodes, were visible in the left eye (Figure 1K). On ICG angiography, choroidal hyperpermeability was clearly observed in both eyes (Figures 1H-J).

After a two-month observation period without any SRF resolution, this refractory CSCR patient with signs of chronic epitheliopathy was treated with the oral mineralocorticoid-receptor antagonist spironolactone (25mg/day for a week and then with 50mg/day) as previously reported.<sup>26-28</sup> After three months, visual acuity had improved to 20/50. SRF and subretinal protein exudates decreased dramatically (Figures 2A-B), but a globular fibrous clot persisted just temporal to the fovea, preventing complete macular reattachment (Figure 2A, arrow). Pars-plana vitrectomy with retinotomy and subretinal clot removal was performed, and SRF was collected prior to clot removal. One month later, visual acuity had improved to 20/25, and the macular detachment had resolved without remnants of subretinal material (Figs 2 C-D). Visual acuity remained unchanged without CSCR recurrence over an additional 2-year follow-up.

### **Subretinal fluid proteome**

The quantitative proteomics analysis identified 291 proteins in all SRF samples, among which 128 were differentially regulated between the CSCR and RRD samples (See Supplementary Table 1 for the complete list of identified proteins). Seventy-seven proteins were down-regulated ( $<0.67$ ) and 51 were up-regulated ( $>1.5$ ) in CSCR compared to RRD (see Supplementary Table 2 for the list of up- and down-regulated proteins). Using gene ontology, these differentially regulated proteins were categorized as enzymes (41.5%, 55 proteins including complement factors, peptidases and protease inhibitors), receptors (15.4%, 32 proteins), cell adhesion molecules (15%, 29 proteins), defense/immunity proteins (8.9%, 19 proteins) and transporters (8.4%, 17 proteins) (Figure 3A).

Among the 15 most up-regulated proteins in the CSCR sample (ratio $>10$ ), 10 were involved in glycolysis and gluconeogenesis: Fructose-bisphosphate aldolase A, Beta-enolase, Glycerol-3-

phosphate dehydrogenase [NAD(+)], cytoplasmic L-lactate dehydrogenase A chain, Phosphoglucomutase-1, Alpha-enolase, Pyruvate kinase, Phosphoglycerate kinase-1, Triosephosphate isomerase and Glyceraldehyde-3-phosphate dehydrogenase. The most down-regulated proteins were mainly involved in cell adhesion or extracellular matrix interaction, including opticin, myocilin, calsyntenin-1, versican, metalloproteinase-2, osteopontin, neurexin-3, cell adhesion molecule 1 and 2 and insulin-like growth factor-binding protein 7 (see Supplementary Table 2 for *P*-values). Among proteins involved in cell adhesion, galectin-3 binding protein was the only up-regulated molecule.

The over-representation analysis of differentially regulated pathways is displayed in Figure 3B, and the corresponding up- and downregulated proteins within over-represented pathways are displayed in Table 1. The following pathways were over-represented in CSCR, as compared to RRD:

- the immune and inflammatory response (acute phase response signaling,  $P=5.85E^{-19}$ ; complement system,  $P=1.49E^{-14}$ ), with a majority of down-regulated proteins in CSCR (68% and 60% respectively),
- lipid transport and macrophage activation (liver X receptor/retinoid X receptor pathway, LXR/RXR, with 69% of down-regulated proteins in CSCR,  $P=2.86E^{-18}$ ),
- metabolism of biliary acids (farnesoid X receptor/retinoid X receptor pathway, FXR/RXR, with 75% of down-regulated proteins in CSCR,  $P=5.57E^{-17}$ ),
- the glycolysis ( $P=1.16E^{-10}$ ) and gluconeogenesis ( $P=3.74E^{-7}$ ) pathways, in which all proteins were up-regulated in CSCR compared to RRD (Aldolase, fructose-bisphosphate A, enolase 1, 3, glyceraldehyde-3-phosphate dehydrogenase, phosphoglycerate kinase 1, pyruvate kinase, muscle, triosephosphate isomerase 1),
- coagulation system ( $P=2.18E^{-6}$ ),
- atherosclerosis signaling ( $P=1.1E^{-5}$ ; up-regulation of apolipoprotein B, C-III, lysozyme, paraoxonase 1 and down-regulation of apolipoprotein A-IV, retinol binding protein 3, serpin family A member 1),
- IL-12 signaling ( $P=1.74E^{-5}$ )
- clathrin-mediated endocytosis ( $P=1.81E^{-5}$ )

### Subretinal fluid metabolome

After matching against known metabolites in the HMDB database using the mass to charge ratio ( $m/z$ ), the putative metabolite list was reduced to 651 single molecules. The supervised learning approach was successful in reconstructing sample classes, based on the differentially expressed metabolites between CSCR and RRD. Seventy-six metabolites were differentially regulated in the SRF sample from the CSCR patient, as compared to RRD, of which 43 were down-regulated and 33 were up-regulated (see Supplemental Table 3 for a list of differentially regulated metabolites).

Over-representation pathway analysis was performed on the deregulated metabolites (Figure 4A). It confirmed the proteomics results with the protein digestion and absorption pathway ( $P=3E^{-09}$ ) defined by approximately 20% coverage of inputted metabolites (specifically methionine, phenylalanine, valine, tyrosine, leucine, glutamine, arginine, isovalerylcarnitine and tyramine-*o*-sulfate), which is in accordance with the peptidase and protease inhibitor activity differentially regulated within the enzyme in the proteomics analysis.

Interestingly, additional pathways were also highlighted in CSCR compared to RRD samples, including:

- the choline pathway, containing exclusively over-regulated metabolites, such as phosphatidylcholine (P-16:0/18:4) ( $FC=5.8$ ,  $P=4E^{-5}$ ) and phosphatidylglycerol (18:0/18:1) ( $FC= 1.58$ ,  $P =6E^{-3}$ ), with 18% metabolite coverage,
- the aminoacyl tRNA biosynthesis, arginine biosynthesis and pantothenate/CoA biosynthesis pathways, determined exclusively by down-regulated metabolites,
- the mineral absorption and ABC transporters pathways were mostly down-regulated, which is consistent with the reduced expression of transporter proteins in the CSCR SRF.
- phosphoric acid, also involved in ATP production, was the only up-regulated metabolite in the mineral absorption pathway ( $FC=4.22$ ).

The chemical sub-classification of metabolites deregulated in CSCR, as compared to RRD, was obtained from the HMDB library. The largest subgroup (30%) belonged to the amino acid/peptide subclass, confirming the over-representation pathway analysis (see Supplementary Figure 1 for a chart

of deregulated metabolites). Using this classification system, the next highly susceptible metabolite classes were phosphosphingolipids (12%), fatty acids/conjugates (7%) and fatty acid esters (6%), which demonstrated alterations in lipid metabolism, in agreement with the proteomic results showing deregulation of the LXR/RXR pathway.

Finally, the pathway-based network was explored to create a compound-gene network on the MetScape software (Figure 4B), providing a comprehensive overview of the specific SRF metabolic signature in the CSCR sample. Among sub-networks, branch-chain amino acid degradation pathway, glycolysis and gluconeogenesis, steroid hormone biosynthesis and metabolism, and bile acid biosynthesis were remarkably deregulated, showing a high consistency with the proteomics results.

## DISCUSSION

The present study reports the first proteomic and metabolomic investigation of SRF, to the best of our knowledge. Applied comparatively to CSCR and RRD, this approach provided unique molecular information, given the rarity of bullous variants of CSCR requiring subretinal surgery,<sup>1,2</sup> the difficulty of SRF collection, and the limited volume of SRF available. Although proteomics results were based on a single CSCR case, they were supported by an independent and orthogonal metabolomics analysis, and by the biological consistence with current understanding of CSCR pathophysiology.

In addition to demonstrating the feasibility of multi-omics exploration of SRF, this study suggests that inflammatory and immune responses in the subretinal space are differentially regulated in CSCR and RRD. Regarding the complement pathway, the up-regulation of CFH confirms its involvement in CSCR pathogenesis. This finding is consistent with previous reports that genetic variants of CFH are associated to a higher risk of developing CSCR,<sup>29-31</sup> and that other variants could protect from the disease.<sup>31</sup> The up-regulation of CFH and CFH-related protein-1, and the decrease in complement factors B and 4B in the SRF of CSCR may indicate a lower activation of the alternative complement pathway, subsequent reduction of membrane attack complex and reduced photoreceptor cell death.<sup>32,33</sup> Noticeably, the C4B genomic copy number is related to the risk of developing chronic CSCR, with absent C4B conferring a higher risk and presence of 3 copies decreasing this risk.<sup>34</sup> On the other hand, the alternative complement pathway contributes to physiologic transport of ions and macromolecules

through pores formation such as C5b-8 and C5b-9.<sup>33</sup> This mechanism involves CD59 protein, also found in our study as down-regulated. Impaired activation of this mechanism could result in fluid and macromolecule accumulation in the sub retinal space of patients with CSCR.

Among proteins differentially regulated in the acute phase response signaling pathway, Serum amyloid P component (SAP or pentraxin-2) is of specific interest. SAP interacts with complement factors<sup>35</sup> and inhibits the recruitment of pro-fibrotic macrophages.<sup>36</sup> In addition, it protects from cell damage induced by histone H3,<sup>37</sup> a potential mechanism contributing to photoreceptor cell death.<sup>38</sup>

Regarding proteins related to gluco- and mineralocorticoid hormonal systems, the CSCR sample showed a moderate elevation of galectin-3, a biomarker linked to mineralocorticoid activation and vascular fibrosis,<sup>39,40</sup> and a reduction in cortisol binding globulin and angiotensin (Supplementary Table 2). In addition, the identification of the C21 steroid hormone biosynthesis metabolic subnetwork (Figure 4), which includes critical gluco- and mineralocorticoid molecules such as cortisol and aldosterone (both having 21 carbons), reflects the deregulation of steroid metabolism, as previously identified in CSCR patients.<sup>41,42</sup> This increase in C21 steroids and the reduced cortisol binding globulin in the SRF of CSCR could also modulate photoreceptor cell death and survival.<sup>43</sup>

Clathrin-mediated endocytosis, one of the differentially regulated pathways between CSCR and RRD, could be an additional mechanism for controlling C5b-8 or C5b-9 levels at the RPE cell membrane, and regulating their lytic threshold.<sup>32</sup> Interestingly, five out of seven proteins of the clathrin-mediated endocytosis pathway have functions in lipid transport and are involved in vascular diseases (apolipoprotein A-IV, retinol binding protein 3, serpin family A member 1, apolipoprotein B, C-III, paraoxonase 1). The LXR/RXR pathway, involved in lipid transport, also regulates macrophage-mediated inflammatory response in atherosclerosis,<sup>44</sup> and induces microglial activation in the subretinal space.<sup>45</sup> Taken together, these results indicate that microglia/macrophage and lipid metabolism are differentially regulated during rhegmatogenous or serous retinal detachments, and are potentially involved in CSCR pathophysiology.

The difference in glycolysis and gluconeogenesis pathways between CSCR and RRD is also emphasized by both proteomics and metabolomics approaches. Compared to RRD, all proteins involved in glycolysis and gluconeogenesis pathways were up-regulated in the SRF from CSCR,

which could point to differential neuronal survival mechanisms. Indeed, gluconeogenesis products contribute to protecting the retina against oxidative and nitrosative stress,<sup>46,47</sup> and increased glucose levels may promote cone photoreceptor survival by stimulation of aerobic glycolysis.<sup>48</sup>

The FXR pathway identified by proteomics analysis is directly linked to the bile acid pathway identified by metabolomics. Bile acids, increased in the SRF of CSCR as compared to RRD are potent anti-apoptotic components for photoreceptors in various models.<sup>49</sup> For example, tauroursodeoxycholic acid (TUDCA) prevents photoreceptors cell death after experimental retinal detachment.<sup>50</sup> Similarly, the pentothenate and CoA pathways have a protective effect against retinal degeneration, and were also activated in CSCR, pointing out another potential neuroprotective mechanism.<sup>51</sup>

Proteins involved in cell migration and adhesion, essential to cellular movement, accounted for 15% of the differentially regulated proteins in the SRF of CSCR, compared to RRD. Consistently, most proteins usually found in the vitreous<sup>52,53</sup> were less abundant in the SRF from CSCR, which is not expected to be contaminated by vitreous fluid, such as opticon,<sup>54</sup> osteopontin<sup>55</sup> and versican.<sup>56</sup> Proteins involved in retinal structure were also reduced in the SRF of CSCR as compared to RRD (such as contactin 1,<sup>57</sup> SYNCAM and lumican<sup>58</sup>) which may be related to the better architecture preservation of the detached retina in CSCR. A clear reduction in the choline metabolic pathway, which intervenes in the photoreceptor outer segment/RPE microvilli interaction,<sup>59</sup> may also be related to the better preservation of photoreceptor outer segments in CSCR as compared to RRD.<sup>60</sup>

Finally, a recent proteomics analysis of intraretinal schisis fluid from two subjects with X-linked retinoschisis highlighted canonical pathways also identified in the present study, such as LXR/RXR activation, complement system and acute phase response signaling.<sup>61</sup> Since chronic CSCR may also manifest with retinoschisis-like cavities,<sup>62</sup> similar biochemical changes may occur in both diseases. These convergent results support the involvement of the identified pathways in a range of retinal disorders, and show the emerging potential of ocular proteomics.

To summarize, this work demonstrated the feasibility and power of proteomics, combined to metabolomics, for the analysis of SRF. This approach opens perspectives for the comprehensive analysis of ocular biomarkers in retinal diseases, and for the screening of neuroprotective therapeutic targets. The main weakness of this study was the limited number of SRF samples analyzed. Although

results from proteomics and metabolomics were largely consistent with each other, and highlighted key molecular players in CSCR pathophysiology previously reported in the literature, they must be interpreted with caution. Although the indication of subretinal surgical procedures in CSCR is exceptional, these translational results will require confirmation with additional samples. This first comparative molecular analysis of SRF in CSCR and RRD improved the understanding of both disorders, and identified pathways involved in the better photoreceptor preservation in CSCR.

#### **ACKNOWLEDGMENTS**

Authors thank Cindy Salvisberg for technical assistance.

## References

1. Balaratnasingam C, Freund KB, Tan AM, et al. Bullous Variant of Central Serous Chorioretinopathy: Expansion of Phenotypic Features Using Multimethod Imaging. *Ophthalmology* 2016;123:1541-1552.
2. Bondalapati S, Pathengay A, Chhablani J. External drainage for exudative retinal detachment secondary to central serous chorioretinopathy. *Eye Sci* 2015;30:204-208.
3. Prunte C, Flammer J. Choroidal capillary and venous congestion in central serous chorioretinopathy. *Am J Ophthalmol* 1996;121:26-34.
4. Ferrara D, Mohler KJ, Waheed N, et al. En face enhanced-depth swept-source optical coherence tomography features of chronic central serous chorioretinopathy. *Ophthalmology* 2014;121:719-726.
5. Spitznas M. Pathogenesis of central serous retinopathy: a new working hypothesis. *Graefes Arch Clin Exp Ophthalmol* 1986;224:321-324.
6. Marmor MF. New hypotheses on the pathogenesis and treatment of serous retinal detachment. *Graefes Arch Clin Exp Ophthalmol* 1988;226:548-552.
7. Daruich A, Matet A, Marchionno L, et al. Acute central serous chorioretinopathy: factors influencing episode duration. *Retina* 2017;In press.
8. Daruich A, Matet A, Dirani A, et al. Central serous chorioretinopathy: Recent findings and new physiopathology hypothesis. *Prog Retin Eye Res* 2015;48:82-118.
9. van Bussel EM, van der Valk R, Bijlsma WR, La Heij EC. Impact of duration of macula-off retinal detachment on visual outcome: a systematic review and meta-analysis of literature. *Retina* 2014;34:1917-1925.
10. Murakami Y, Notomi S, Hisatomi T, et al. Photoreceptor cell death and rescue in retinal detachment and degenerations. *Prog Retin Eye Res* 2013;37:114-140.
11. Sweigard JH, Matsumoto H, Smith KE, et al. Inhibition of the alternative complement pathway preserves photoreceptors after retinal injury. *Sci Transl Med* 2015;7:297ra116.
12. Anderson DH, Stern WH, Fisher SK, Erickson PA, Borgula GA. The onset of pigment epithelial proliferation after retinal detachment. *Invest Ophthalmol Vis Sci* 1981;21:10-16.
13. Azurmendi L, Degos V, Tiberti N, et al. Measuring Serum Amyloid A for Infection Prediction in Aneurysmal Subarachnoid Hemorrhage. *J Proteome Res* 2015;14:3948-3956.
14. Dayon L, Turck N, Kienle S, et al. Isobaric tagging-based selection and quantitation of cerebrospinal fluid tryptic peptides with reporter calibration curves. *Anal Chem* 2010;82:848-858.
15. Scherl A, Shaffer SA, Taylor GK, Kulasekara HD, Miller SI, Goodlett DR. Genome-Specific Gas-Phase Fractionation Strategy for Improved Shotgun Proteomic Profiling of Proteotypic Peptides. *Analytical Chemistry* 2008;80:1182-1191.
16. Dayon L, Pasquarello C, Hoogland C, Sanchez JC, Scherl A. Combining low- and high-energy tandem mass spectra for optimized peptide quantification with isobaric tags. *J Proteomics* 2010;73:769-777.
17. Gluck F, Hoogland C, Antinori P, et al. EasyProt--an easy-to-use graphical platform for proteomics data analysis. *J Proteomics* 2013;79:146-160.
18. Salvisberg C, Tajouri N, Hainard A, Burkhard PR, Lalive PH, Turck N. Exploring the human tear fluid: discovery of new biomarkers in multiple sclerosis. *Proteomics Clin Appl* 2014;8:185-194.
19. Dunn WB, Broadhurst D, Begley P, et al. Procedures for large-scale metabolic profiling of serum and plasma using gas chromatography and liquid chromatography coupled to mass spectrometry. *Nat Protoc* 2011;6:1060-1083.

20. Wolfender J-L, Marti G, Thomas A, Bertrand S. Current approaches and challenges for the metabolite profiling of complex natural extracts. *Journal of Chromatography A* 2015;1382:136-164.
21. Guo Y, Graber A, McBurney RN, Balasubramanian R. Sample size and statistical power considerations in high-dimensionality data settings: a comparative study of classification algorithms. *BMC Bioinformatics* 2010;11:447.
22. Thomas A, Deglon J, Lenglet S, et al. High-Throughput Phospholipidic Fingerprinting by Online Desorption of Dried Spots and Quadrupole-Linear Ion Trap Mass Spectrometry: Evaluation of Atherosclerosis Biomarkers in Mouse Plasma. *Anal Chem* 2010;82:6687-6694.
23. Mi H, Poudel S, Muruganujan A, Casagrande JT, Thomas PD. PANTHER version 10: expanded protein families and functions, and analysis tools. *Nucleic Acids Res* 2016;44:D336-342.
24. Karnovsky A, Weymouth T, Hull T, et al. Metscape 2 bioinformatics tool for the analysis and visualization of metabolomics and gene expression data. *Bioinformatics* 2012;28:373-380.
25. Bindea G, Mlecnik B, Hackl H, et al. ClueGO: a Cytoscape plug-in to decipher functionally grouped gene ontology and pathway annotation networks. *Bioinformatics* 2009;25:1091-1093.
26. Bousquet E, Beydoun T, Zhao M, Hassan L, Offret O, Behar-Cohen F. Mineralocorticoid receptor antagonism in the treatment of chronic central serous chorioretinopathy: a pilot study. *Retina* 2013;33:2096-2102.
27. Singh RP, Sears JE, Bedi R, Schachat AP, Ehlers JP, Kaiser PK. Oral eplerenone for the management of chronic central serous chorioretinopathy. *Int J Ophthalmol* 2015;8:310-314.
28. Daruich A, Matet A, Dirani A, et al. Oral Mineralocorticoid-Receptor Antagonists: Real-Life Experience in Clinical Subtypes of Nonresolving Central Serous Chorioretinopathy With Chronic Epitheliopathy. *Transl Vis Sci Technol* 2016;5:2.
29. Miki A, Kondo N, Yanagisawa S, Bessho H, Honda S, Negi A. Common variants in the complement factor H gene confer genetic susceptibility to central serous chorioretinopathy. *Ophthalmology* 2014;121:1067-1072.
30. Moschos MM, Gazouli M, Gatzoufas Z, et al. Prevalence of the Complement Factor H and Gstm1 Genes Polymorphisms in Patients with Central Serous Chorioretinopathy. *Retina* 2016;36:402-407.
31. de Jong EK, Breukink MB, Schellevis RL, et al. Chronic central serous chorioretinopathy is associated with genetic variants implicated in age-related macular degeneration. *Ophthalmology* 2015;122:562-570.
32. Georgiannakis A, Burgoyne T, Lueck K, Futter C, Greenwood J, Moss SE. Retinal Pigment Epithelial Cells Mitigate the Effects of Complement Attack by Endocytosis of C5b-9. *J Immunol* 2015;195:3382-3389.
33. Farkas I, Baranyi L, Ishikawa Y, et al. CD59 blocks not only the insertion of C9 into MAC but inhibits ion channel formation by homologous C5b-8 as well as C5b-9. *J Physiol* 2002;539:537-545.
34. Breukink MB, Schellevis RL, Boon CJ, et al. Genomic Copy Number Variations of the Complement Component C4B Gene Are Associated With Chronic Central Serous Chorioretinopathy. *Invest Ophthalmol Vis Sci* 2015;56:5608-5613.
35. Bottazzi B, Inforzato A, Messa M, et al. The pentraxins PTX3 and SAP in innate immunity, regulation of inflammation and tissue remodelling. *J Hepatol* 2016;64:1416-1427.
36. Horgan SJ, Watson CJ, Glezeva N, et al. Serum Amyloid P-Component Prevents Cardiac Remodeling in Hypertensive Heart Disease. *J Cardiovasc Transl Res* 2015;8:554-566.
37. Iba T, Hamakubo T, Nagaoka I, Sato K, Thachil J. Physiological Levels of Pentraxin 3 and Albumin Attenuate Vascular Endothelial Cell Damage Induced by Histone H3 In Vitro. *Microcirculation* 2016;23:240-247.

38. Kawano H, Ito T, Yamada S, et al. Toxic effects of extracellular histones and their neutralization by vitreous in retinal detachment. *Lab Invest* 2014;94:569-585.
39. Calvier L, Miana M, Reboul P, et al. Galectin-3 mediates aldosterone-induced vascular fibrosis. *Arteriosclerosis, thrombosis, and vascular biology* 2013;33:67-75.
40. Martinez-Martinez E, Calvier L, Fernandez-Celis A, et al. Galectin-3 blockade inhibits cardiac inflammation and fibrosis in experimental hyperaldosteronism and hypertension. *Hypertension (Dallas, Tex : 1979)* 2015;66:767-775.
41. Garg SP, Dada T, Talwar D, Biswas NR. Endogenous cortisol profile in patients with central serous chorioretinopathy. *Br J Ophthalmol* 1997;81:962-964.
42. Haimovici R, Rumelt S, Melby J. Endocrine abnormalities in patients with central serous chorioretinopathy. *Ophthalmology* 2003;110:698-703.
43. Cubilla MA, Castaneda MM, Bachor TP, Suburo AM. Glucocorticoid-dependent mechanisms in photoreceptor survival. *Adv Exp Med Biol* 2012;723:101-106.
44. Lee SD, Tontonoz P. Liver X receptors at the intersection of lipid metabolism and atherogenesis. *Atherosclerosis* 2015;242:29-36.
45. Choudhary M, Malek G. A Brief Discussion on Lipid Activated Nuclear Receptors and their Potential Role in Regulating Microglia in Age-Related Macular Degeneration (AMD). *Adv Exp Med Biol* 2016;854:45-51.
46. Mamczur P, Mazurek J, Rakus D. Ubiquitous presence of gluconeogenic regulatory enzyme, fructose-1,6-bisphosphatase, within layers of rat retina. *Cell Tissue Res* 2010;341:213-221.
47. Frenzel J, Richter J, Eschrich K. Pyruvate protects glucose-deprived Muller cells from nitric oxide-induced oxidative stress by radical scavenging. *Glia* 2005;52:276-288.
48. Ait-Ali N, Fridlich R, Millet-Puel G, et al. Rod-derived cone viability factor promotes cone survival by stimulating aerobic glycolysis. *Cell* 2015;161:817-832.
49. Lawson EC, Bhatia SK, Han MK, et al. Tauroursodeoxycholic Acid Protects Retinal Function and Structure in rd1 Mice. *Adv Exp Med Biol* 2016;854:431-436.
50. Mantopoulos D, Murakami Y, Comander J, et al. Tauroursodeoxycholic acid (TUDCA) protects photoreceptors from cell death after experimental retinal detachment. *PLoS One* 2011;6:e24245.
51. Hayflick SJ. Defective pantothenate metabolism and neurodegeneration. *Biochem Soc Trans* 2014;42:1063-1068.
52. Aretz S, Krohne TU, Kammerer K, et al. In-depth mass spectrometric mapping of the human vitreous proteome. *Proteome science* 2013;11:22.
53. Skeie JM, Roybal CN, Mahajan VB. Proteomic insight into the molecular function of the vitreous. *PLoS One* 2015;10:e0127567.
54. Reardon AJ, Le Goff M, Briggs MD, et al. Identification in vitreous and molecular cloning of opticin, a novel member of the family of leucine-rich repeat proteins of the extracellular matrix. *J Biol Chem* 2000;275:2123-2129.
55. Deeg CA, Eberhardt C, Hofmaier F, Amann B, Hauck SM. Osteopontin and fibronectin levels are decreased in vitreous of autoimmune uveitis and retinal expression of both proteins indicates ECM re-modeling. *PLoS One* 2011;6:e27674.
56. Keenan TD, Clark SJ, Unwin RD, Ridge LA, Day AJ, Bishop PN. Mapping the differential distribution of proteoglycan core proteins in the adult human retina, choroid, and sclera. *Invest Ophthalmol Vis Sci* 2012;53:7528-7538.

57. D'Alessandri L, Ranscht B, Winterhalter KH, Vaughan L. Contactin/F11 and tenascin-C co-expression in the chick retina correlates with formation of the synaptic plexiform layers. *Curr Eye Res* 1995;14:911-926.
58. Ribic A, Liu X, Crair MC, Biederer T. Structural organization and function of mouse photoreceptor ribbon synapses involve the immunoglobulin protein synaptic cell adhesion molecule 1. *J Comp Neurol* 2014;522:900-920.
59. Matsumoto H, Shibasaki K, Uchigashima M, et al. Localization of acetylcholine-related molecules in the retina: implication of the communication from photoreceptor to retinal pigment epithelium. *PLoS One* 2012;7:e42841.
60. Fisher SK, Lewis GP, Linberg KA, Verardo MR. Cellular remodeling in mammalian retina: results from studies of experimental retinal detachment. *Prog Retin Eye Res* 2005;24:395-431.
61. Sudha D, Kohansal-Nodehi M, Kovuri P, et al. Proteomic profiling of human intraschisis cavity fluid. *Clin Proteomics* 2017;14:13.
62. Lee JH, Park H-YL, Baek J, Lee WK. Alterations of the Lamina Cribrosa Are Associated with Peripapillary Retinoschisis in Glaucoma and Pachychoroid Spectrum Disease. *Ophthalmology* 2016;123:2066-2076.

### Figure legends

**Figure 1: Retinal imaging findings in a 48-year old patient with severe fibrinous central serous chorioretinopathy.**

**Right eye:** (A) Multicolor fundus imaging showing a posterior serous retinal detachment with multiple folds and focal subretinal protein deposits. (B) Fundus autofluorescence showing a large hyper-autofluorescent area covering the posterior pole and extending towards the superior and inferior temporal vascular arcades, due to recent exudative detachment, with central autofluorescence masking due to protein deposits (arrows). (C-D) Spectral-Domain optical coherence tomography (SD-OCT) showing a serous retinal detachment with retinal folds, and hyperreflective material partially occupying the subretinal space. (F-G) Fluorescein angiography showing leakage sites, temporal to the fovea and along the superior and inferior temporal vessels. (H-I) Mid- and late phase indocyanine green angiography (ICGA) showing choroidal vascular hyperpermeability.

**Left eye:** (E) SD-OCT showing a serous pigment epithelial detachment temporal to the fovea. (J) Midphase ICGA angiography demonstrating choroidal hyperpermeability. (K) Fluorescein angiography showing multifocal retinal pigment epithelium alterations and progressive dye filling of the pigment epithelial detachment.

**Figure 2: Resolution of residual retinal detachment after surgical subretinal fibrin removal in a 48-year old patient with severe fibrinous central serous chorioretinopathy.**

(A) Three months after initiation of oral spironolactone, spectral-domain optical coherence tomography (SD-OCT) showed persistence of subretinal material preventing complete retinal reattachment, which prompted to perform vitrectomy with retinotomy and internal removal of a subretinal fibrin clot.

(B) One month after the procedure, SD-OCT showed disappearance of the subretinal deposit and complete macular reattachment (arrow).

**Figure 3. Differential subretinal fluid proteome in central serous chorioretinopathy compared to rhegmatogenous retinal detachment.**

**(A)** Circle chart of differentially regulated protein classes obtained with the Panther software. Some classes contain several subclasses (cell adhesion and extracellular matrix protein: cell adhesion molecule, cytoskeletal protein, extracellular matrix protein, structural protein, surfactant; enzyme: enzyme modulator, hydrolase, isomerase, kinase, lyase, oxidoreductase, phosphatase, protease, transferase; transporter: membrane traffic protein, transfer/carrier protein, transporter). Twenty-nine proteins from the list were not taken into account by Panther.

**(B)** Protein pathways differentially represented using over-representation pathway analysis in CSCR subretinal fluid compared to RRD. The 10 most significant pathways provided by the Ingenuity Pathway Analysis software were selected based on right-tailed Fisher's exact test significance levels. Red and green bars represent up- and down-regulated proteins, respectively. The orange line represents the *P*-value corresponding to each pathway.

CSCR= central serous chorioretinopathy; RRD= rhegmatogenous retinal detachment

**Figure 4. Differential metabolome of the central serous chorioretinopathy subretinal fluid compared to rhegmatogenous retinal detachment.**

**(A)** Over-representation pathway analysis of differentially represented metabolites in the CSCR subretinal fluid sample compared to RRD. A minimum of 2 metabolites per pathway and a significant association cut-off ( $P < 0.01$  and  $q\text{-value} < 0.05$ ) were used. Red and green bars represent metabolites up- and down-regulated, respectively. The orange line represents the associated *P*-value corresponding to each pathway.

**(B)** Compound-gene metabolic network in the CSCR sample compared to RRD. Major pathways altered in the network are outlined by dashed lines.

CSCR= central serous chorioretinopathy; RRD= rhegmatogenous retinal detachment

## Supplementary material

**Figure S1. Circle chart of chemical sub-class taxonomy for deregulated metabolites in the central serous chorioretinopathy subretinal fluid sample, compared to rhegmatogenous retinal detachment.**

Metabolites without sub-class taxonomy are assigned as non-attributed.

**Table S1. List of proteins identified in the subretinal fluid samples from central serous chorioretinopathy and rhegmatogenous retinal detachment.**

**Table S2. List of proteins differentially expressed in the subretinal fluid from the central serous chorioretinopathy case, compared to rhegmatogenous retinal detachment.**

**Table S3. List of discriminant metabolites obtained using the prediction analysis for microarrays (PAM) classification.**

The HMDB ID of each identified metabolite is proposed according to the characterization process based on mass accuracies, MS/MS library searching and *in-silico* fragmentation tool as described in the “metabolite identification” section. Compounds confirmed by the three criteria are notified in bold.

Figure 1

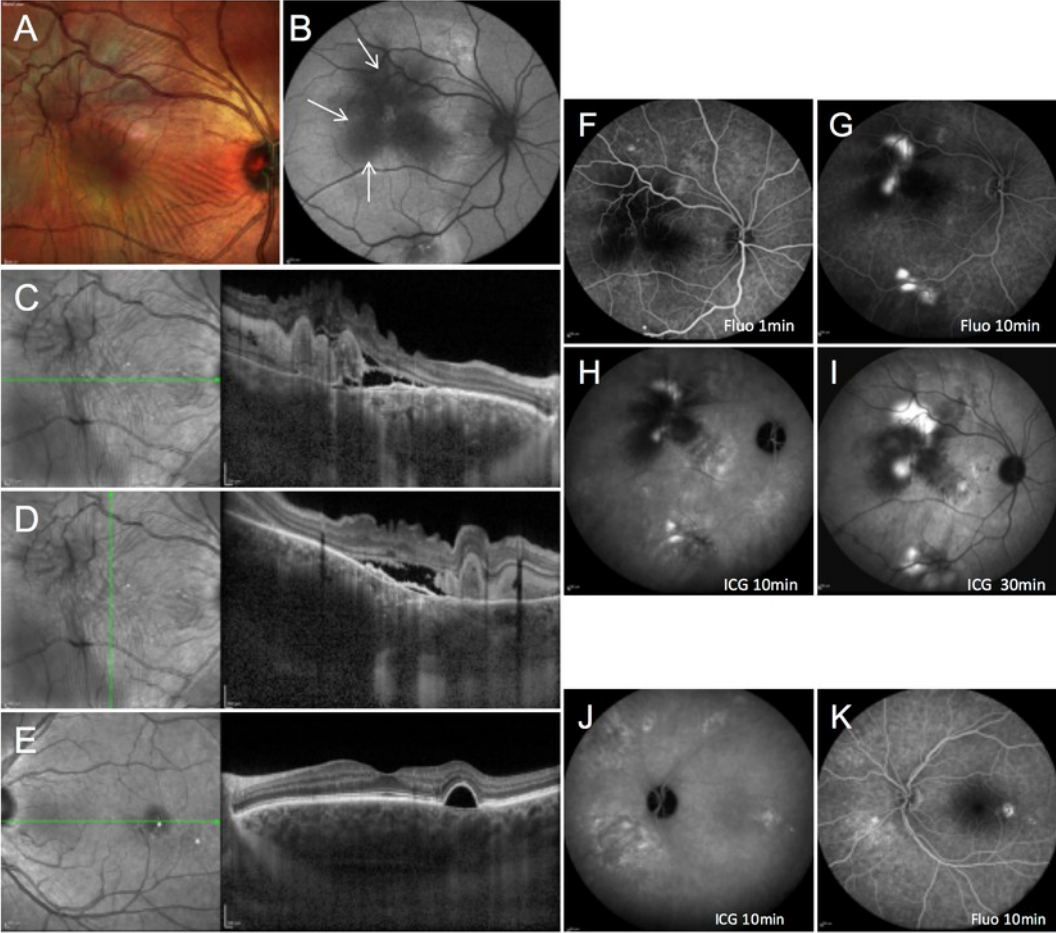


Figure 2

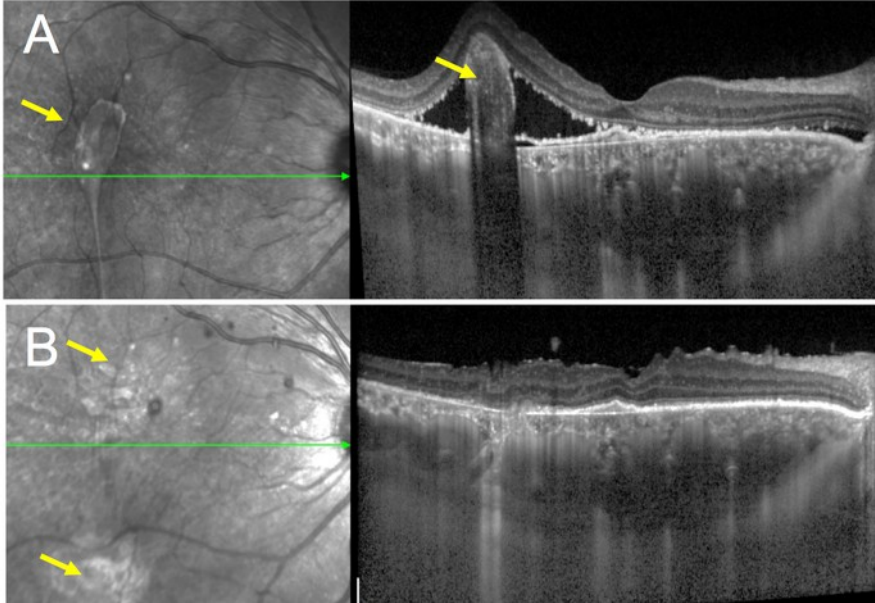
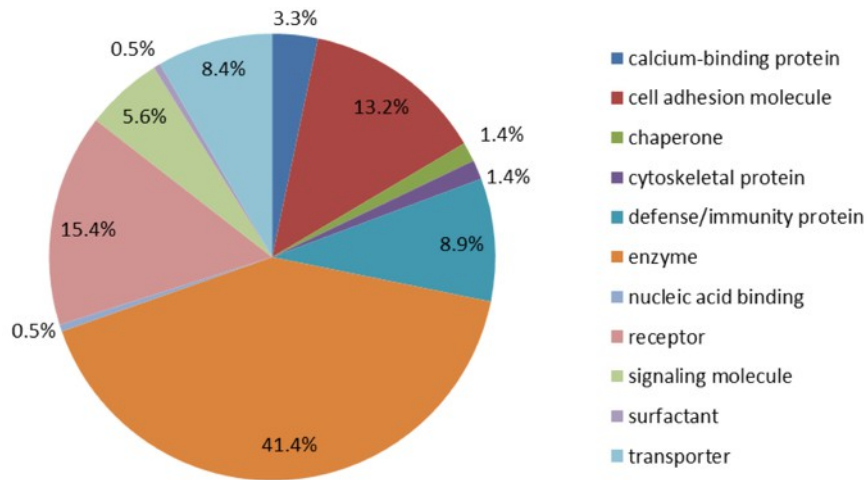


Figure 3

**A Protein classes differentially regulated in CSCR subretinal fluid compared to RRD**



**B Protein pathways differentially represented in CSCR subretinal fluid compared to RRD**

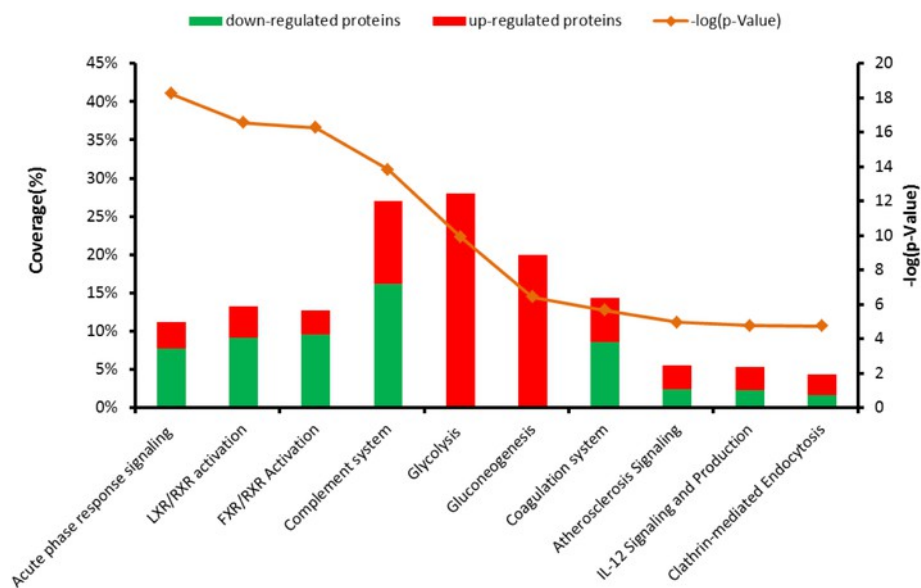
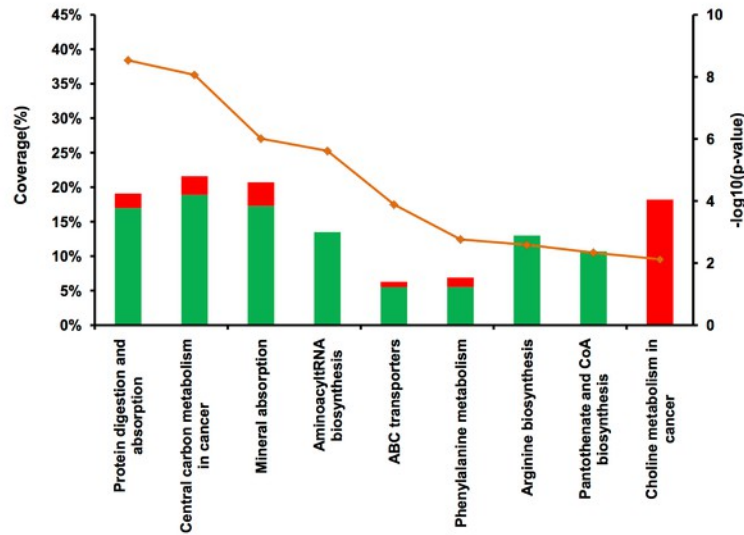
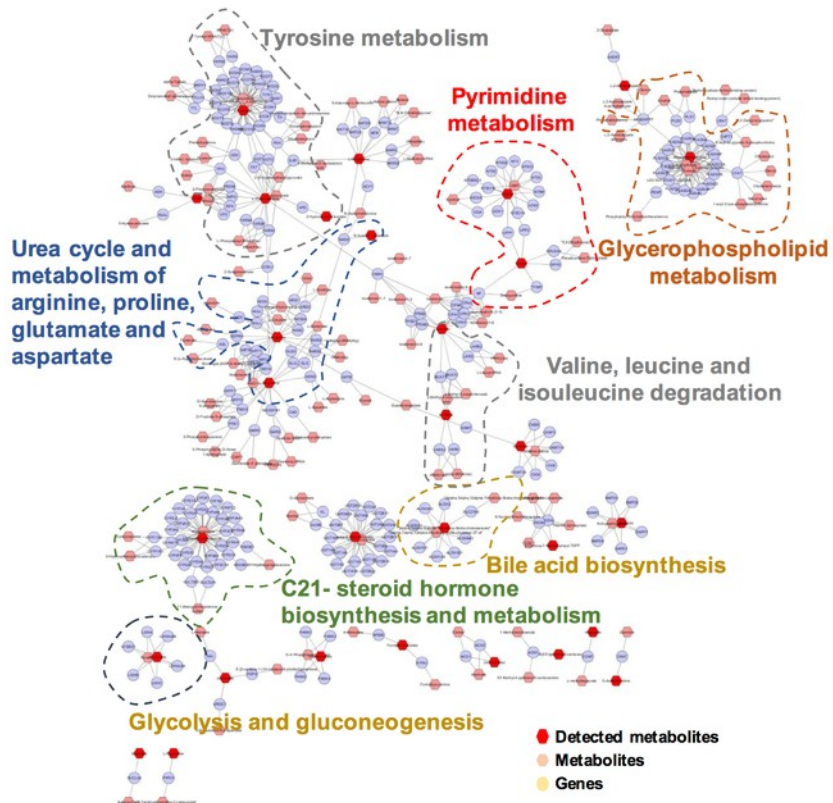


Figure 4

**A** Metabolite pathways differentially represented in CSCR subretinal fluid compared to RRD



**B** Compound-gene metabolic network in CSCR subretinal fluid compared to RRD



Suppl Figure 1

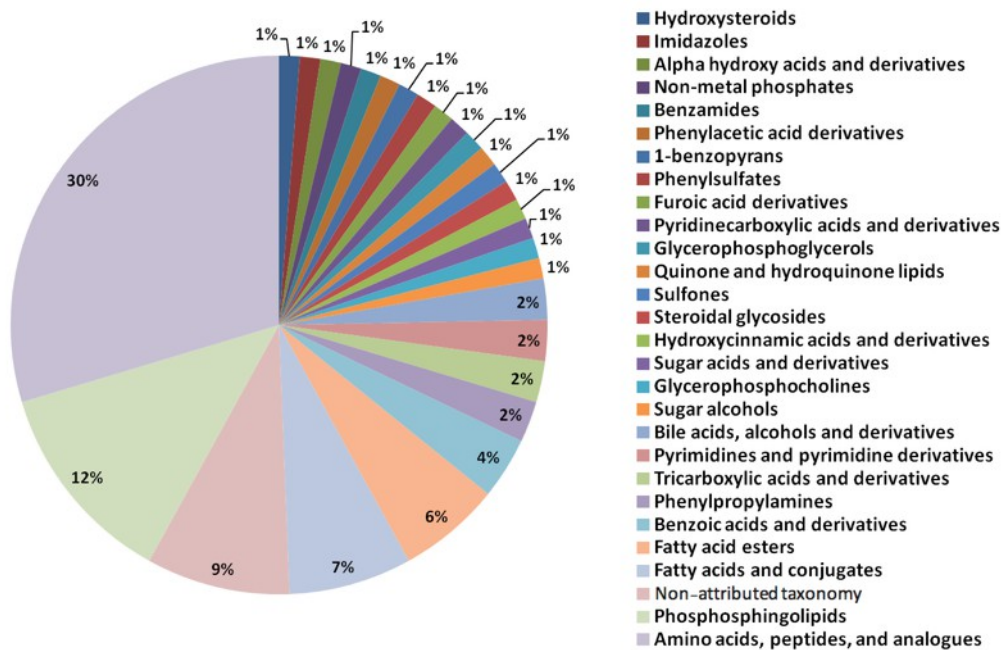


**Table 1. Proteins identified in the subretinal fluid and differentially expressed in central serous chorioretinopathy compared to rhegmatogenous retinal detachment.**

	Up-regulated proteins		Down-regulated proteins	
Canonical pathway	Protein	Ratio*	Protein	Ratio*
<b>Acute phase response signaling</b>	Amyloid P component, serum	4.42	Angiotensinogen	0.51
	Complement component 3	1.93	Alpha-2-HS-glycoprotein	0.59
	Complement component 4	3.18	Complement component 9	0.29
	Fibronectin 1	2.68	Complement component 1r	0.38
	Kallikrein B1	1.67	Complement component 4B	0.49
	Serpin family D member 1	2.58	Complement factor B	0.45
			Hemopexin	0.23
			Histidine-rich glycoprotein	0.31
			Inter-alpha-trypsin inhibitor	0.44
			Plasminogen	0.36
			Retinol binding protein 3	0.63
			Retinol binding protein 4	0.64
			Serpin family A member 1	0.31
<b>LXR/RXR and FXR/RXR activations</b>	Apolipoprotein B	5.28	Alpha-1-B glycoprotein	0.65
	Apolipoprotein C-III	3.79	Angiotensinogen	0.51
	Complement component 3	1.93	Alpha-2-HS-glycoprotein	0.59
	Lysozyme	1.64	Apolipoprotein A-IV	0.15
	Paraoxonase 1	1.95	Complement component 9	0.29
			Complement component 4B	0.49
			Group-specific component (vitamin D binding protein)	0.21
			Fetuin B	0.36
			Hemopexin	0.23
			Inter-alpha-trypsin inhibitor	0.44
			Retinol binding protein 4	0.64
		Serpin peptidase inhibitor, clade A	0.31	
<b>Complement system</b>	Complement component 3	1.93	Complement component 7	0.34
	Complement component 4	3.18	Complement component 9	0.29
	Complement component 8	1.59	Complement component 1r	0.38
	Complement factor H	2.99	Complement component 4B	0.49
			CD59 molecule	0.43
		Complement factor B	0.45	
<b>Glycolysis I</b>	Aldolase, fructose-bisphosphate A	39.3		
	Enolase 1	12.68		
	Enolase 3	24.59		
	Glyceraldehyde-3-phosphate dehydrogenase	10.12		
	Phosphoglycerate kinase 1	10.83		
	Pyruvate kinase, muscle	11.86		
	Triosephosphate isomerase 1	10.41		
<b>Gluconeogenesis</b>	Fructose-bisphosphate aldolase A	39.3		
	Enolase 1	12.68		

	Enolase 3	24.59		
	Glyceraldehyde-3-phosphate dehydrogenase	10.12		
	Phosphoglycerate kinase 1	10.83		
<b>Coagulation system</b>	Kallikrein B1	1.67	Plasminogen	0.36
	Serpin family D member 1	2.58	Serpin family A member 1	0.31
			Serpin family C member 1	0.32
<b>Atherosclerosis signaling</b>	Apolipoprotein B	5.28	Apolipoprotein A-IV	0.15
<b>IL-12 Signaling and Production in Macrophages</b>	Apolipoprotein C-III	3.79	Retinol binding protein 3	0.63
	Lysozyme	1.64	Serpin family A member 1	0.31
	Paraoxonase 1	1.95		
	Heat shock protein family A (only for Clathrin mediated Endocytosis Signaling)	5.62		
<b>Clathrin-mediated Endocytosis Signaling</b>				

Pathway analysis was performed using the ‘Ingenuity Pathway Analysis’ software. LXR/RXR, liver X receptor/retinoid X receptor; FXR/RXR, farnesoid X receptor/retinoid X receptor.

\* Ratio of subretinal fluid protein concentrations between central serous chorioretinopathy and rhegmatogenous retinal detachment samples. Only upregulated (>1.5) or downregulated (<0.67) proteins are reported.

Supplementary Tables 1, 2 and 3 were not included in this thesis dissertation because their format did not allow it (lists of identified molecules in Excel data files).

They are available upon request.

[3a] Macular telangiectasia type 1: capillary density and microvascular abnormalities assessed by optical coherence tomography angiography. *Am J Ophthalmol* 2016

Matet A, Daruich A, Dirani A, Ambresin A, Behar-Cohen F<sup>212</sup>

doi: 10.1016/j.ajo.2016.04.005.

Contribution of PhD candidate:

- Patient follow-up
- Processing and analysis of OCT angiography and multimodal imaging data
- Statistical analyses
- Drafting the manuscript

NB: a figure from this Article was selected as cover illustration (one of four small cover figures)



# Macular Telangiectasia Type 1: Capillary Density and Microvascular Abnormalities Assessed by Optical Coherence Tomography Angiography



ALEXANDRE MATET, ALEJANDRA DARUICH, ALI DIRANI, AUDE AMBRESIN, AND FRANCINE BEHAR-COHEN

- **PURPOSE:** To describe microvascular abnormalities and capillary density in macular telangiectasia type 1 (MT1) using optical coherence tomography angiography (OCTA), and correlate them with fluorescein angiography (FA).
- **DESIGN:** Observational case series.
- **METHODS:** Seven patients with MT1 and 12 age-matched controls were included. Focal microvascular dilations were identified on  $3 \times 3$  mm OCTA and early-frame FA images. OCTA images were processed to determine the global capillary density after subtraction of larger vessels and cystoid edema cavities. Local capillary densities were calculated inside 100- $\mu$ m circles around telangiectasias, projected over superficial (SCP) and deep capillary plexuses (DCP). They were compared to a random sample of 100- $\mu$ m circles generated in each OCTA image. FA images were processed to measure mean perifoveal intercapillary areas (PIA), inversely reflecting capillary density.
- **RESULTS:** In MT1 eyes, fewer telangiectasias were identified with OCTA than with FA ( $P = .016$ ), exclusively localized in the DCP ( $P = .016$ ). Rarefaction of both capillary plexus and abnormal microvascular morphology were better identified by OCTA than by FA. The global capillary density on OCTA was significantly lower in MT1 eyes than in fellow and control eyes, respectively: SCP, 0.347 vs 0.513 ( $P = .004$ ) and 0.560 ( $P = .0005$ ); DCP, 0.357 vs 0.682 ( $P = .016$ ) and 0.672 ( $P = .0005$ ). Capillary density was significantly reduced around telangiectasias in both SCP ( $P = .021$ ) and DCP ( $P = .042$ ). Capillary density of the SCP correlated inversely with the mean PIA on FA ( $r = -0.94$ ,  $P = .017$ ). LogMAR visual acuity was

inversely correlated with SCP ( $r = -0.88$ ,  $P = .012$ ) and DCP capillary densities ( $r = -0.79$ ,  $P = .048$ ).

- **CONCLUSIONS:** OCTA confirmed that global and focal capillary depletion is associated with MT1. (Am J Ophthalmol 2016;167:18–30. © 2016 Elsevier Inc. All rights reserved.)

**M**ACULAR TELANGIECTASIA TYPE 1 (MT TYPE 1) IS a congenital or developmental vascular disorder affecting mostly male subjects and consisting of focal, exudative dilations of perifoveal retinal capillaries.<sup>1</sup> It is usually unilateral, may extend beyond the macula, and therefore may be part of the larger spectrum of Coats disease.<sup>2</sup> Historically, the condition has been termed “miliary aneurysms” by Leber,<sup>3</sup> “idiopathic juxtafoveal telangiectasis” (group 1A-1B) by Gass and Blodi,<sup>1</sup> “Type 1 aneurysmal telangiectasia” by Yannuzzi and associates,<sup>4</sup> and finally MT type 1 in the recent classification by the MacTel Study Group.<sup>5</sup>

In contrast with type 2 idiopathic macular telangiectasia or “MacTel2,” in which telangiectasias develop along with pathognomonic degenerative alterations of the retinal architecture linked to Müller cell depletion,<sup>6,7</sup> MT type 1 is primarily a vascular disease, complicated by macular edema originating from the exudative telangiectasias.<sup>4</sup> Fluorescein angiography (FA) allows the visualization of telangiectasias, but its ability to image the fine perifoveal capillaries at high resolution and to discriminate between the superficial and deep capillary plexuses is limited. Moreover, these lesions and the surrounding perifoveal capillaries are visible exclusively during the early frames of the sequence, since details are progressively submerged by dye diffusion from telangiectasias.

Optical coherence tomography angiography (OCTA) is a recent noninvasive imaging technology based on the detection of flows that provides a representation of the microvascular morphology. Absence of dye diffusion and higher resolution help to overcome limitations of FA to image the perifoveal capillary network.<sup>8,9</sup> Moreover, the segmentation of volumes acquired by OCTA produces a separate visualization of the superficial and the deep retinal capillary plexuses. To date, several groups have employed OCTA to describe normal features of the

AJO.com

Supplemental Material available at [AJO.com](http://AJO.com).

Accepted for publication Apr 3, 2016.

From the Department of Ophthalmology, University of Lausanne, Jules-Gonin Eye Hospital, Fondation Asile des Aveugles, Lausanne, Switzerland (A.M., A.Daruich, A.Dirani, A.A., F.B.-C.); and Inserm, U1138, Team 17, From Physiopathology of Ocular Diseases to Clinical Development, Université Paris Descartes Sorbonne Paris Cité, Centre de Recherche des Cordeliers, Paris, France (F.B.-C.).

Inquiries to Francine Behar-Cohen, Hôpital Ophtalmique Jules-Gonin, Avenue de France 15, CP 133, 1000 Lausanne 7, Switzerland; e-mail: [francine.behar@gmail.com](mailto:francine.behar@gmail.com)

macular microvasculature<sup>10–14</sup> and to describe fine alterations involving both plexuses in several vascular disorders, such as retinal vein occlusion,<sup>15–17</sup> diabetic retinopathy,<sup>18–20</sup> and MT type 2.<sup>21,22</sup> Furthermore, the recent adjunction of quantitative tools has expanded the ability of OCTA to investigate highly detailed abnormalities of the retinal microvasculature, such as vessel density or non-flow areas.<sup>9,23</sup>

Imaging MT type 1 eyes with OCTA, we have described the vascular abnormalities (“telangiectasias”) and their vascular microenvironment. We used a quantitative analysis of OCTA images to compare the macular capillary density of MT type 1 eyes with fellow eyes and with healthy control eyes. We then correlated OCTA findings with FA imaging.

---

## METHODS

• **SUBJECTS:** This observational case series adhered to the tenets of the Declaration of Helsinki and Swiss federal regulations and was approved by the local Ethics Committee of the Swiss Department of Health (CER-VD no. 19/15). The study was conducted from June 1 to October 1, 2015, at Jules-Gonin Eye Hospital, Lausanne, Switzerland.

Medical records, optical coherence tomography (OCT), OCTA, FA, and indocyanine green angiography (ICGA) images from 7 consecutive subjects presenting with MT type 1 were retrospectively analyzed. The diagnosis of MT type 1 was based on the presence of unilateral, exudative telangiectasia affecting the macular area, without any clinical sign or history suggestive of vascular occlusion, posterior segment inflammation, or other causes of secondary macular telangiectasia. Exclusion criteria were age <18 years and spherical equivalent <−2 diopter (D) or >+2 D.

Twelve eyes from 12 healthy subjects imaged by OCTA were selected from the local OCTA database based on age and sex to serve as a control group.

• **IMAGE ACQUISITION AND SEGMENTATION:** The instrument used for en face OCT and OCTA images, Angiovue RTx 100, is based on the AngioVue Imaging System (Optovue, Inc, Fremont, California, USA) to obtain amplitude decorrelation angiography images. This instrument has an A-scan rate of 70 000 scans per second, using a light source centered on 840 nm and a bandwidth of 50 nm. Each OCTA volume contains 304 × 304 A-scans with 2 consecutive B-scans captured at each fixed position before proceeding to the next sampling location. Split-spectrum amplitude-decorrelation angiography (SSADA) was used to extract the OCT angiography information. Each OCTA volume is acquired in 3 seconds and 2 orthogonal OCTA volumes were acquired in order to perform motion correction to minimize motion artifacts arising from microsaccades and fixation changes. Angiography

information displayed is the average of the decorrelation values when viewed perpendicularly through the thickness being evaluated.

In order to obtain comparable 3 × 3-mm OCTA scans between subjects, volumes were automatically segmented by the software provided by the manufacturer to provide images of the superficial plexus (3 μm below the inner limiting membrane to 16 μm below the outer border of the inner plexiform layer) and deep plexus (16–69 μm below the outer border of the inner plexiform layer). We controlled the correct segmentation for each patient before reporting the data.

The central macular thickness was measured on the Angiovue RTx 100 OCT in the central subfield of an Early Treatment Diabetic Retinopathy Study (ETDRS) grid centered on the fovea.

FA and ICGA were performed on Spectralis (Heidelberg Engineering, Heidelberg, Germany). Early frames (≤50 seconds after dye injection) were acquired with a 30-degree lens to visualize the macular microvasculature. Image quality was optimized using the “sharpen” tool of the Heidelberg Eye Explorer software (Version 1.9.10.0; Heidelberg Engineering). Angiograms were rotated and cropped to match the 3 × 3-mm OCTA scans centered on the fovea, using ImageJ (Version 1.50c4, Wayne Rasband; National Institutes of Health, Bethesda, Maryland, USA).

• **IDENTIFICATION OF MICROVASCULAR ABNORMALITIES:** OCTA images from normal and MT type 1 subjects and FA and ICGA images from MT type 1 eyes were presented randomly to 3 masked independent observers (A.A., A.Da., F.B.C.) during separate sessions for each imaging modality. Lesions identified as microvascular abnormalities were labeled by each observer, and those labeled by 2 observers or more were retained. The interobserver reliability was assessed using a 2-way, mixed-model intraclass correlation coefficient based on the number of lesions identified per OCTA, FA, or ICGA image. Numbers of lesions in the deep and superficial capillary plexuses on OCTA were compared using a Wilcoxon signed-rank paired test.

• **QUANTITATIVE DETERMINATION OF CAPILLARY VESSEL DENSITY ON OPTICAL COHERENCE TOMOGRAPHY ANGIOGRAPHY:** The vascular densities of the capillary network in the superficial and deep plexuses were assessed by a custom semi-automated, intensity-based algorithm on Matlab (Mathworks, Natick, Massachusetts, USA).

First, original grayscale OCTA images were processed to detect pixels corresponding to vascular flow. In each image (Figure 1, Top and Bottom left), a region of interest (ROI) inside the foveal avascular zone that did not include dark areas corresponding to intraretinal cystoid cavities was manually outlined to define the background intensity of the intervacular retinal tissue. Using the threshold intensity  $I_{threshold} = Mean(ROI\ pixels) + 2 \times$

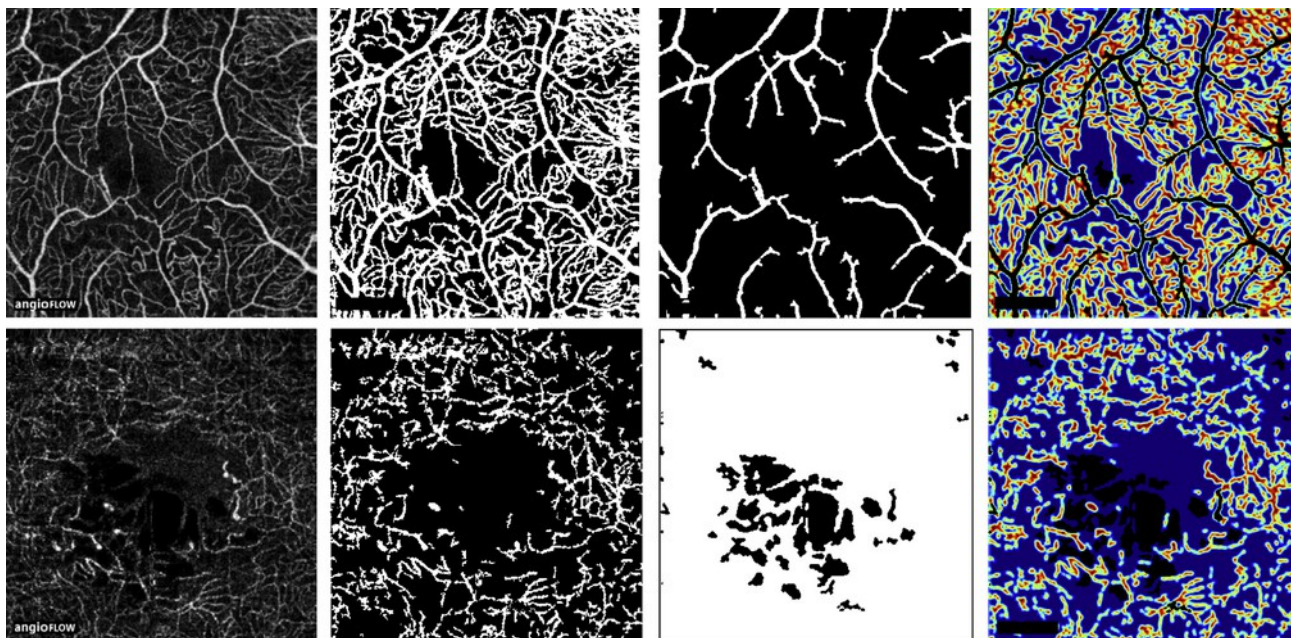


FIGURE 1. Illustration of the semi-automated method to estimate capillary density and produce capillary density maps from optical coherence tomography angiography images. Original optical coherence tomography angiography image of (Top left) the superficial capillary plexus (Case 3) and (Bottom left) the deep capillary plexus (Case 5), with (Top and Bottom middle left) their respective binary transform. (Top middle right) Extraction of large retinal vessels and (Bottom middle right) areas corresponding to cystoid spaces were extracted from the binary images. (Top and Bottom right) Final capillary density maps after subtraction of larger vessels and cystoid spaces.

Standard Deviation (ROI pixels), a binary transform of the OCTA image was performed, resulting in a “skeleton” of the vascular network (Figure 1, Top and Bottom middle left). In order to extract larger arterioles and venules that appear brighter owing to their higher flow, another binary transform was applied to the original OCTA images with a threshold set arbitrarily at 50% of the maximum pixel intensity value ( $122.5 = 0.5 \times 255$ ) (Figure 1, Top middle right).

Second, pixels corresponding to the en face visualization of cystoid edema were identified on OCTA images. These areas appear slightly darker than the surrounding retinal tissue that is detected by the SSADA algorithm, most likely because of imperceptible retinal motion during acquisition originating from arterial pulsations, breathing, tremors, or microsaccades.<sup>24</sup> Cystoid spaces were identified using a low threshold intensity value of 5% ( $12.5 = 0.05 \times 255$ ) (Figure 1, Bottom middle left).

The capillary network density was calculated over an area defined by subtracting from the total OCTA binary image the areas corresponding to larger vessels and cystoid edema. A  $12 \times 89$ -pixel rectangle located in the lower left corner and corresponding to the “Angioflow” sign embedded in native OCTA images was also subtracted. Over this final binary image, the total capillary network density was defined as the ratio of 1-pixels to total pixels. For graphical purposes, vessel density maps were produced

by plotting the local mean intensity values in a sliding  $5 \times 5$ -pixel square area (Figure 1, Top and Bottom right).

Total capillary vessel densities in the deep and superficial plexuses were compared between affected and fellow eyes of MT type 1 subjects and control eyes from healthy subjects, using Mann-Whitney test and Wilcoxon signed-rank paired test (for fellow eyes). Correlations of capillary densities with multimodal imaging findings and visual acuity were performed using the Spearman rank correlation coefficients.

• **QUANTITATIVE DETERMINATION OF LOCAL CAPILLARY VESSEL DENSITY AROUND MICROVASCULAR LESIONS ON OPTICAL COHERENCE TOMOGRAPHY ANGIOGRAPHY:** In MT type 1 eyes a local capillary vessel density was calculated inside  $100\text{-}\mu\text{m}$ -radius circles centered by each previously identified microvascular lesion, using a semi-automated algorithm on Matlab. These lesions were labeled manually on original OCTA images by a single operator (A.M.) and local capillary densities were computed automatically on the previously generated binary images where cystoid edema and larger vessels (and the “Angioflow” label) had been excluded. In each plexus, these local densities were computed around the microvascular lesions of both plexuses, whenever present.

In order to compare local densities to an analogous measurement reflecting the average density of OCTA images, a random distribution of 1000 local areas of similar size

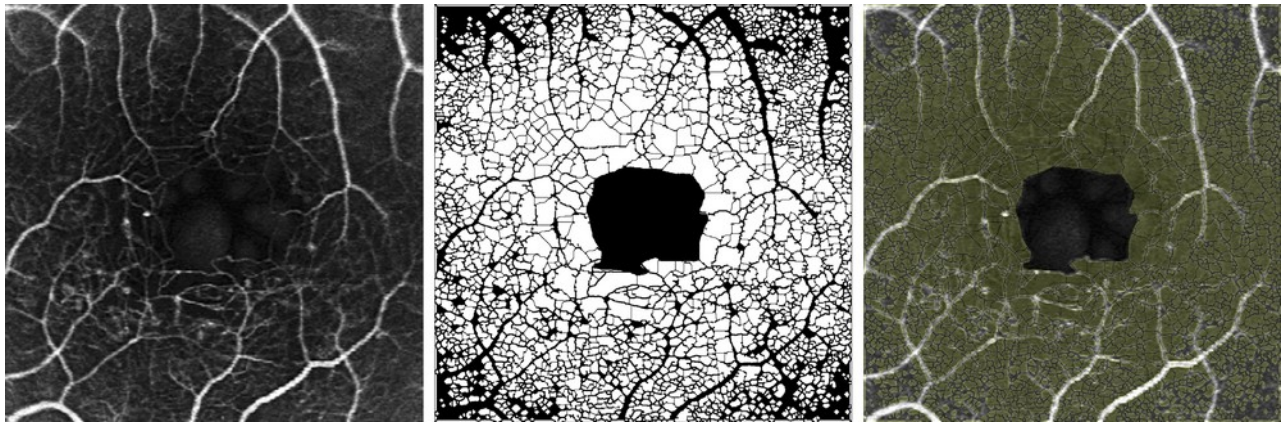


FIGURE 2. Quantitative determination of perifoveal intercapillary areas to estimate capillary density on fluorescein angiograms. (Left) A 3 × 3-mm section of an early-frame fluorescein angiogram in a 54-year-old man (Case 5) with macular telangiectasia type 1. (Middle) Following skeletonization, perifoveal intercapillary areas were automatically identified and (Right) reported on the fluorescein angiogram.

(100- $\mu$ m-radius circles) was generated in each OCTA image. Areas overlapping a 100- $\mu$ m-radius local region around a labeled microvascular lesion, another randomly generated area, or a central disc of 0.250 mm<sup>2</sup> (corresponding to the area of the foveal avascular zone reported by independent groups on OCTA<sup>14,25</sup>) were excluded (Supplemental Figure 1, available at [AJO.com](http://AJO.com)). The distributions of perilesional and randomly distributed local densities were compared within each plexus by a Kruskal-Wallis test and a multiple comparison post-test.

• **QUANTITATIVE ESTIMATION OF CAPILLARY DENSITY ON FLUORESCEIN ANGIOGRAPHY:** To provide an estimate of the capillary density on FA, a quantification of *perifoveal intercapillary areas* was performed on Matlab by adapting a method previously described in detail<sup>26</sup> and applied to digital FA.<sup>27</sup> Briefly, after manual outlining of the foveal avascular zone border and automated intensity-based skeletonization of the perifoveal microvasculature, intercapillary spaces were automatically detected and their areas were measured over the 3 × 3-mm angiograms, which corresponds approximately to the perifoveal 5-degree region reported in the original method<sup>26</sup> (Figure 2). For each angiogram, the mean perifoveal intercapillary area was calculated and was considered an inverse estimate of capillary density.

• **STATISTICAL ANALYSES:** Comparative tests and correlation analyses were performed on GraphPad Prism (Version 5.0f; GraphPad Software, San Diego, California, USA). Intraclass correlation coefficients, Kruskal-Wallis test, and post-tests were calculated on R software (Version 3.2.2; R Foundation for Statistical Computing, R Core Team, 2015, Vienna, Austria; <http://www.R-project.org/>) using the “irr” package (Version 0.84, 2012, M. Gamer, J. Lemon, I. Fellows, P. Singh, <http://CRAN.R-project.org/package=irr>) and the “pgirmess” package (2015, Version 1.6.3, P. Giraudoux, <http://CRAN.R-project.org/package=pgirmess>). Visual acuities were converted to the logarithm of the minimal angle of resolution (logMAR) for calculations. *P* values inferior to .05 were considered statistically significant.

## RESULTS

THERE WAS NO DIFFERENCE BETWEEN THE 7 PATIENTS presenting MT type 1 and the 12 healthy controls in terms of age (57.1 ± 10.2 vs 57.8 ± 6.9 years, *P* > .99) and sex (all male subjects).

• **IDENTIFICATION OF MICROVASCULAR ABNORMALITIES:** In MT type 1 eyes imaged by OCTA, microvascular abnormalities consisting of focal capillary dilations were detected exclusively in the deep capillary plexus by the 3 independent observers. There was a mean of 6.9 (range, 2–14) lesions in the deep plexus and 0 lesions in the superficial plexus (*P* = .016) (Table 1). Microvascular abnormalities were not observed in fellow eyes of MT type 1 subjects or in control healthy eyes.

On early-frame 3 × 3-mm FA images, a higher number of lesions was identified by the 3 independent observers (mean: 21.8, range, 6–54) than on OCTA (*P* = .016). Early-frame confocal ICGA was obtained in 5 MT type 1 subjects. Lesions suggestive of telangiectasia were observed in all 5 subjects (mean: 13.2, range, 3–36), but their number was variably higher or lower than observed using OCTA or FA, with no difference in mean number (*P* = .13 and *P* = .31, respectively).

The resulting intraclass correlation coefficient was 0.97 (95% confidence interval [CI]: 0.89–0.99) for OCTA,

**TABLE 1.** Clinical and Imaging Findings by Optical Coherence Tomography Angiography, Fluorescein Angiography, Indocyanine Green Angiography, and Optical Coherence Tomography in 7 Patients With Macular Telangiectasia Type 1

Case, Sex (Age, y)	OCTA - Superficial Capillary Plexus				OCTA - Deep Capillary Plexus				FA	ICGA	OCT	Best-Corrected Visual Acuity	
	Abnormal Microvascular Lesions, n	Observed Capillary Density of OCTA Image	Local Capillary Density in Random Regions	Observed Perilesional Capillary Density	Abnormal Microvascular Lesions, n	Observed Capillary Density of OCTA Image	Local Capillary Density in Random Regions	Observed Perilesional Capillary Density	Abnormal Microvascular Lesions, n	Mean Perifoveal Intercapillary Area, 10 <sup>-3</sup> mm <sup>2</sup>	Abnormal Microvascular Lesions, n	Central Macular Thickness, μm	LogMAR (Snellen)
1, M (52)	0	0.377	0.379	0.302	9	0.542	0.564	0.396	54	3.75	36	343	+0.1 (20/25)
2, M (51)	0	0.380	0.374	0.291	5	0.318	0.332	0.0978	7	3.59	3	402	+0.1 (20/25)
3, M (68)	0	0.378	0.390	0.280	14	0.527	0.549	0.412	32	3.64	NA	377	0.0 (20/20)
4, M (56)	0	0.212	0.204	0.162	2	0.230	0.234	0.153	6	NA	4	305	+0.5 (20/63)
5, M (54)	0	0.306	0.309	0.372	7	0.206	0.214	0.281	12	3.79	17	304	+0.2 (20/32)
6, M (74)	0	0.319	0.311	0.310	8	0.235	0.251	0.267	28	4.99	NA	342	+0.2 (20/32)
7, M (45)	0	0.455	0.430	0.400	3	0.441	0.461	0.355	13	2.15	6	282	0.0 (20/20)
Mean ± SD	0	0.347 ± 0.077	0.349 ± 0.149	0.302 ± 0.076	6.9 ± 4.1	0.357 ± 0.145	0.372 ± 0.232	0.280 ± 0.170	21.8 ± 17.4	3.65 ± 0.90	13.2 ± 13.9	326 ± 40	+0.16
<i>P</i> value			<i>P</i> = .021 <sup>a</sup>				<i>P</i> = .042 <sup>a</sup>						

FA = fluorescein angiography; ICGA = indocyanine green angiography; LogMAR = logarithm of the minimal angle of resolution; OCT = optical coherence tomography; OCTA = optical coherence tomography angiography.

<sup>a</sup>Kruskal-Wallis test with multiple comparison post-tests.

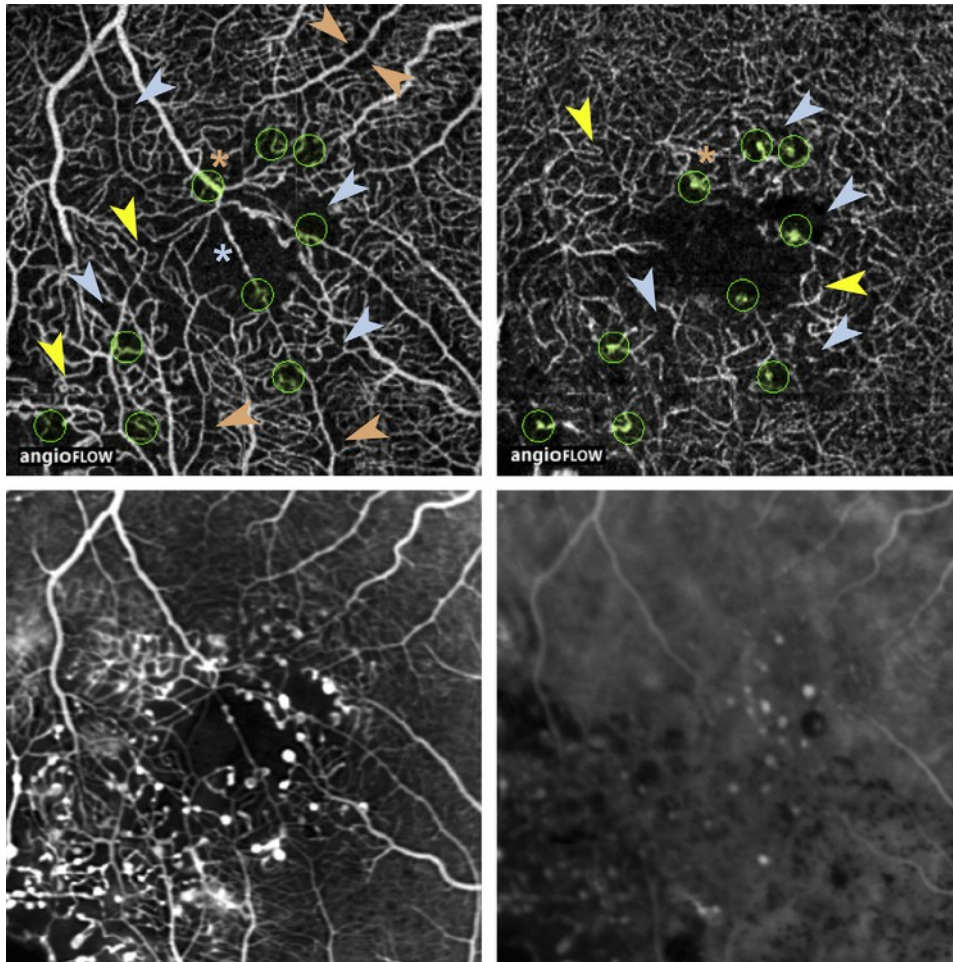


**FIGURE 3.** Multimodal imaging in a 52-year-old man with macular telangiectasia type 1 (Case 1) showing severe alterations of the perifoveal microvasculature. (Top left) Optical coherence tomography angiography of the superficial capillary plexus showed a rarefied capillary network with numerous patchy areas of severe capillary depletion (blue arrows), close to the localization of focal microvascular dilations in the deep plexus (green circles). Exacerbated capillary loops (yellow arrows), enlarged capillary-free areas along arterioles (orange arrows), and an abnormal capillary vessel crossing the foveal avascular zone (blue star) were also visible. (Top right) The deep capillary plexus harbored a number of focal microvascular dilations (green circles), diffuse capillary depletion with focal areas of severe depletion located in the vicinity of the microvascular dilations (blue arrows). Note that certain microvascular lesions in the deep plexus were close to the termination of an arteriole/venule in the superficial plexus (orange star). (Bottom left) Early-frame fluorescein angiography showed a higher number of telangiectasias than identified by optical coherence tomography angiography, diffuse and focal capillary depletion, an abnormal capillary vessel crossing the foveal avascular zone, capillary loops, and enlarged capillary-free areas along arterioles. (Bottom right) Early-frame indocyanine green angiography did not visualize details of the macular microvasculature, except for focal telangiectasia, but their number was lower than on fluorescein angiography and was comparable to optical coherence tomography angiography.

0.96 (95% CI: 0.81–0.99) for FA, and 0.99 (95% CI: 0.98–1.00) for ICGA, indicating excellent consistency between the 3 independent observers, with a greater agreement for OCTA and ICGA than for FA. The detailed number of lesions identified by each observer is given in [Supplemental Table 1](#) (Supplemental Material available at [AJO.com](#)).

• **QUALITATIVE DESCRIPTION OF CAPILLARY NETWORK CHANGES:** A qualitative visual assessment of OCTA images revealed a rarefied capillary network in the superficial and deep plexuses. Enlarged capillary-free areas along

arterioles and exacerbated capillary loops were mostly observed in the superficial plexus ([Figures 3–5](#)). In 5 out of 7 patients, a proportion of focal microvascular dilations suggestive of telangiectasias were located close to a termination or branching of a venule or arteriole (Cases 1–3 and 5–6, [Figures 3–5](#)). In addition, the foveal avascular zone morphology was severely altered in OCTA images of the superficial plexus, and showed an abnormal capillary vessel crossing linearly this area in 4 out of 7 eyes (Cases 1–3 and 6, [Figures 3–5](#)). Similar abnormal features were partly visible on early-frame FA,

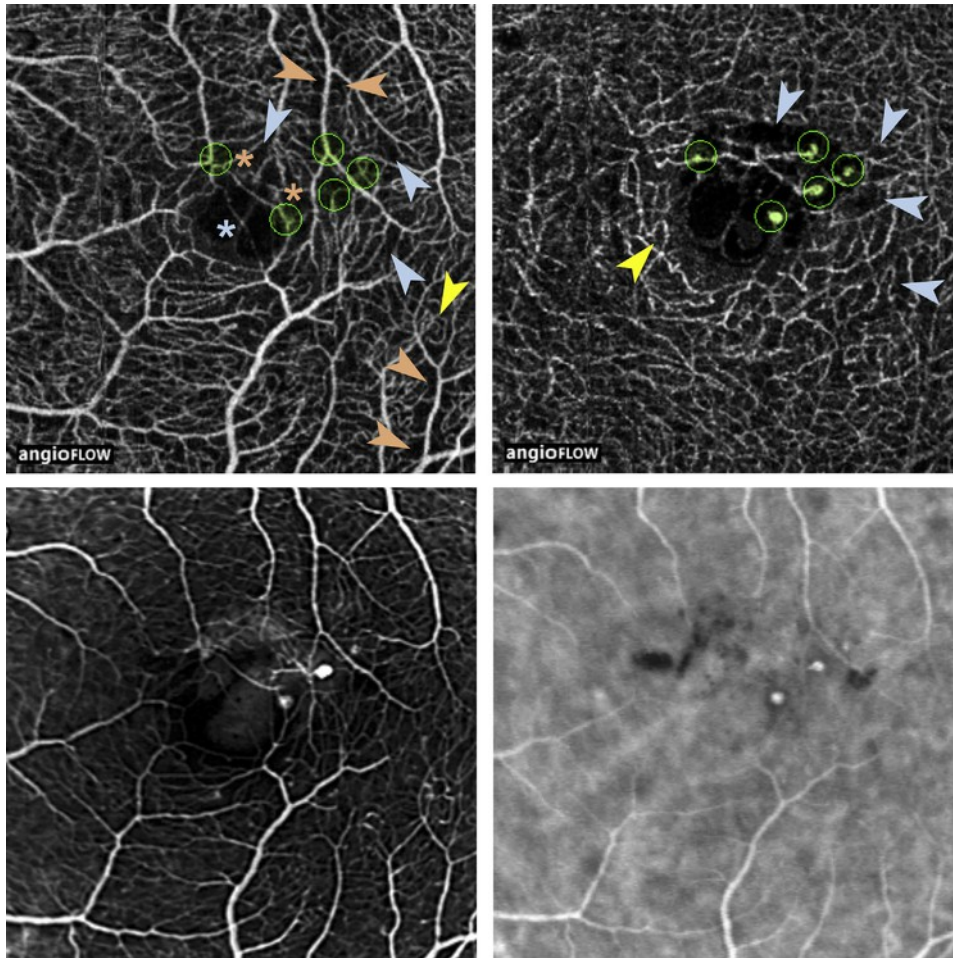


**FIGURE 4.** Multimodal imaging in a 51-year-old man with macular telangiectasia type 1 (Case 2) showing mild alterations of the perifoveal microvasculature. (Top left) Optical coherence tomography angiography of the superficial capillary plexus showed a mild decrease in capillary network density with few focal areas of increased depletion (blue arrows), close to the localization of focal microvascular dilations in the deep plexus (green circles). Capillary loops (yellow arrows), moderately enlarged capillary-free areas along arterioles (orange arrows), and an abnormal capillary vessel crossing the foveal avascular zone (blue star) were also visible. (Top right) The deep capillary plexus presented focal microvascular dilations (green circles), diffuse capillary depletion with a few focal areas of more severe depletion located in the vicinity of the microvascular dilations (blue arrows). Note that certain microvascular lesions in the deep plexus were close to the termination of an arteriole/venule in the superficial plexus (orange stars). (Bottom left) Early-frame fluorescein angiography showed a comparable number of telangiectasias as identified by optical coherence tomography angiography, mild diffuse and focal capillary depletion, an abnormal capillary vessel crossing the foveal avascular zone, a few capillary loops, and moderately enlarged capillary-free areas along arterioles. (Bottom right) Early-frame indocyanine green angiography did not visualize details of the macular microvasculature, except for 3 focal telangiectasia corresponding to lesions visible by both fluorescein angiography and optical coherence tomography angiography.

although it did not discriminate between superficial and deep plexus alterations (Figures 3–5). In addition, the definition of the perifoveal microvasculature on early FA images was variable and qualitatively lower than on OCTA. This discrepancy was caused by leakage from telangiectasias (Case 3, Figure 5), fluorescein filling of cystoid edema cavities (Case 2, Figure 4 and Cases 5–6, Figure 5), or long-standing retinal pigment epithelium alterations secondary to retinal edema and subretinal exudates (Case 4, Figure 5).

- **CAPILLARY VESSEL DENSITY:** The capillary vessel density was estimated by a semi-automated method over the entire OCTA images after subtraction of areas corresponding to arterioles, venules, and cystoid edema spaces. The capillary density of the superficial plexus was  $0.347 \pm 0.077$  in MT type 1 eyes, significantly lower than in corresponding fellow eyes ( $0.513 \pm 0.080$ ,  $P = .0041$ ) and control eyes ( $0.560 \pm 0.065$ ,  $P = .0005$ ). No difference was observed between MT type 1 fellow eyes and control eyes ( $P = .22$ ). Similarly, the capillary density of the deep plexus

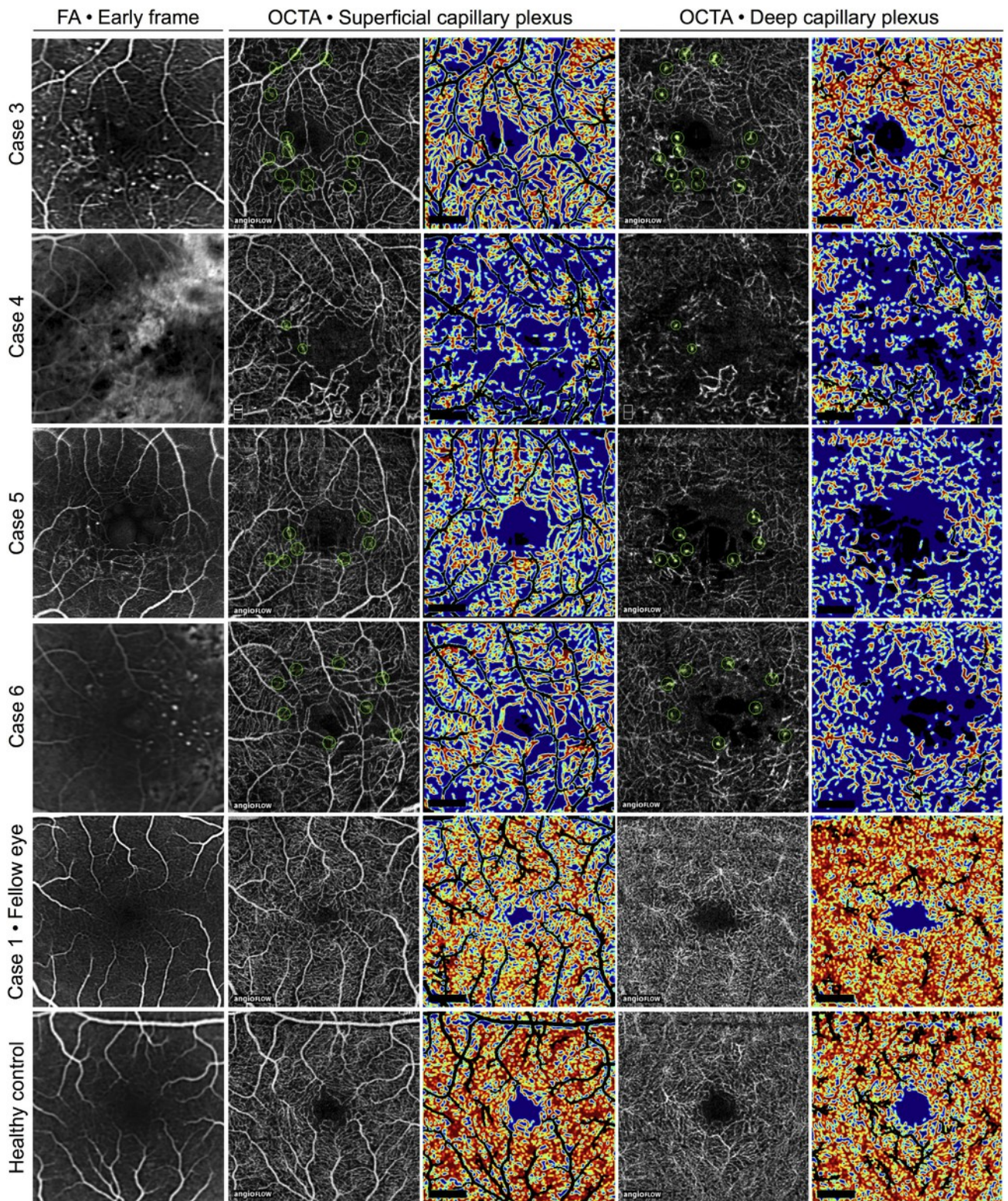


FIGURE 5. Fluorescein angiography and optical coherence tomography angiography with corresponding capillary density maps in 4 eyes with macular telangiectasia type 1 (Cases 3–6), 1 fellow eye of a macular telangiectasia type 1 patient (Case 1), and 1 healthy control eye (Control 10). Each line displays the following images: (Left) early-frame fluorescein angiography; (Middle left) optical coherence tomography angiography of the superficial capillary plexus, with green circles indicating the locations of microvascular lesions identified as telangiectasias in the deep plexus; (Middle) capillary density map of the superficial capillary plexus after subtraction of areas corresponding to larger vessels and cystoid spaces; (Middle right) optical coherence tomography angiography of the deep capillary plexus, with green circles surrounding these microvascular lesions identified as telangiectasias; (Right) capillary density map of

## DISCUSSION

was  $0.357 \pm 0.145$  in MT type 1 eyes, significantly lower than in MT type 1 fellow eyes ( $0.682 \pm 0.054$ ,  $P = .016$ ) and control eyes ( $0.672 \pm 0.064$ ,  $P = .0005$ ). No difference was observed between MT type 1 fellow eyes and control eyes ( $P = .83$ ). Capillary density maps from 4 eyes with MT type 1, 1 MT type 1 fellow eye, and 1 normal eye are represented in [Figure 5](#). Case-by-case capillary densities are graphically reported in [Figure 6](#); values from MT type 1 subjects are detailed in [Table 1](#) and values from control subjects are reported in [Supplemental Table 2](#) (Supplemental Material available at [AJO.com](#)).

• **LOCAL CAPILLARY VESSEL DENSITY AROUND MICROVASCULAR ABNORMALITIES:** Owing to the exclusive localization of abnormalities in the deep plexus, their locations served as reference to assess the perilesional capillary density in both the deep and superficial plexuses ([Figures 3–5](#)). Among MT type 1 eyes, the mean perilesional capillary vessel density inside 100- $\mu\text{m}$ -radius circles centered by the microvascular abnormalities ([Figures 3–5](#), green circles) was  $0.302 \pm 0.076$  in the superficial plexus and  $0.280 \pm 0.170$  in the deep plexus. In order to compare these measures against the capillary density in each plexus, a random distribution of similar, nonoverlapping circular areas was generated over OCTA images, resulting in a mean of 124 areas per image (range, 104–196). Capillary density values were significantly lower in perilesional areas than in areas randomly distributed within the OCTA images, and this finding was observed in both superficial and deep plexuses ( $P = .021$  and  $P = .042$ , respectively) ([Table 1](#)).

• **CORRELATION OF MULTIMODAL IMAGING PARAMETERS AND VISUAL ACUITY:** Among the 7 MT type 1 eyes, morphologic parameters from OCTA, OCT, FA, and visual acuity were evaluated for possible correlations. Exhaustive results are reported in [Table 2](#). Regarding the microvascular density, there was an inverse correlation ( $r = -0.94$ ) between the mean perifoveal intercapillary area on FA and the superficial capillary plexus capillary density on OCTA ( $P = .017$ ), but not with the deep plexus ( $P = .42$ ). There was a positive correlation ( $r = 0.86$ ) in the number of identified telangiectasias between OCTA and FA ( $P = .24$ ). LogMAR best-corrected visual acuity showed an inverse correlation with the capillary density of both superficial ( $r = -0.88$ ) and deep plexuses ( $r = -0.79$ ) on OCTA ( $P = .012$  and  $P = .048$ , respectively), and did not correlate with any other imaging parameter.

WITH OCTA, TELANGIECTASIC MICROANEURYSMS TYPICAL of MT type 1 were identified as focal dilations of the microvasculature. Although OCTA detected fewer lesions than FA in each affected eye, OCTA showed that telangiectasias were exclusively located in the deep capillary plexus. Moreover, in MT type 1 eyes the density of the macular capillary network was reduced in both superficial and deep plexuses, as compared to fellow and healthy control eyes, and the capillary network density of both plexuses was the unique morphologic parameter correlated to the visual acuity of MT type 1 eyes. Finally, a focal decrease in capillary density was observed adjacent to telangiectasia in both plexuses as compared to other vascularized regions of the macula.

In fellow eyes of MT type 1 subjects, OCTA imaging showed no microvascular abnormalities, confirming the observation made by Gass and Blodi and by Yannuzzi and associates, who reported unilateral disease in 90%–95% of cases.<sup>1,4</sup> Although stereoscopic and digital FA initially described telangiectasias as emerging from both the deep and superficial networks,<sup>1,4</sup> OCTA data presented here tend to localize them preferentially in the deep plexus. Abnormal capillary loops, detected in the superficial plexus by OCTA and visible on early-frame FA, may produce dye leakage from incompetent vessels without the typical aspect of aneurysmal lesions, which could explain this discrepancy. Interestingly, early-frame confocal ICGA clearly captured the macular telangiectasias, but, in contrast to FA and OCTA, it failed to provide relevant information on the surrounding microvasculature in MT type 1 ([Figures 3 and 4](#)) or healthy eyes ([Supplemental Figure 2](#), available at [AJO.com](#)).

On OCTA, rarefaction of the capillary bed was systematically observed in eyes affected by MT type 1 but not in fellow or control eyes. Similarly, on FA Gass and Blodi identified “minimal evidence of capillary occlusion or loss” in “most eyes,” whereas Yannuzzi and associates observed “minimal, patchy nonperfusion or capillary ischemia” in “some patients,” clearly pointing to the presence of focal ischemic areas in the macula. These alterations of the macular microvasculature visualized on OCTA and FA may range from mild (Case 2, [Figure 4](#)) to severe (Case 1, [Figure 3](#)). OCTA images and capillary density maps in [Figure 5](#) illustrate quantitatively the presence of patchy capillary loss in the perifoveal

---

the deep capillary plexus after subtraction of areas corresponding to larger vessels and cystoid spaces. Telangiectasias were more numerous on fluorescein angiography than on optical coherence tomography angiography, and were systematically located in the deep capillary plexus. Both techniques showed a diffuse and focal capillary depletion with excessive capillary tortuosity, but optical coherence tomography angiography also identified a relative decrease in capillary density inside the microenvironment of telangiectasias (green circles), in both superficial and deep plexuses. There were no microvascular alterations in the fellow eye of Case 1 and in the control healthy eye, and their capillary densities in both plexuses were higher than in affected eyes.

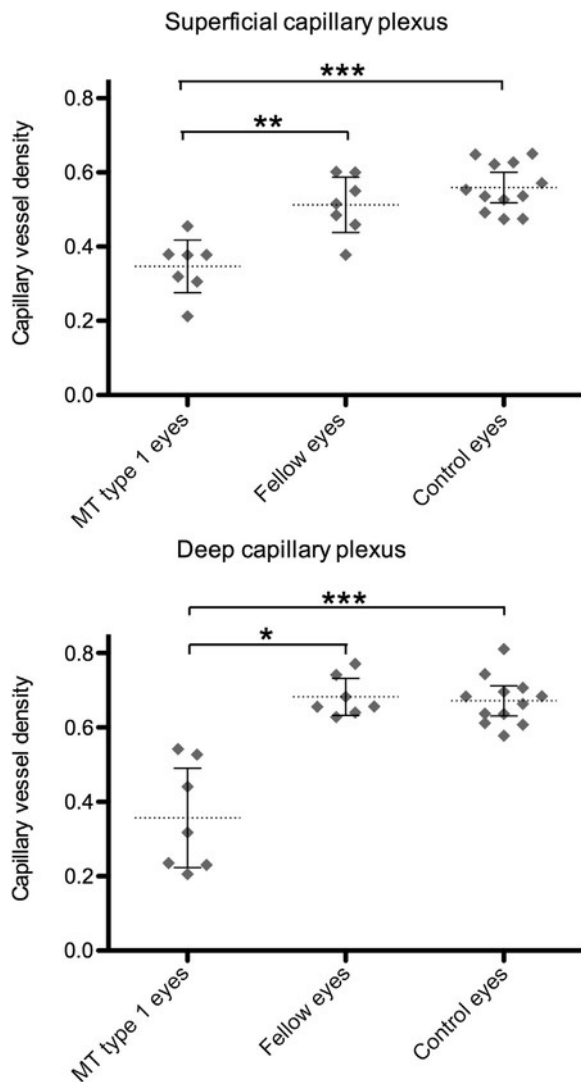


**FIGURE 6.** Capillary vessel density in the superficial and deep capillary plexus among macular telangiectasia type 1 subjects, their fellow eyes, and control eyes from healthy subjects. (Top) In the superficial capillary plexus, the mean capillary density was significantly lower in eyes affected by macular telangiectasia type 1 than in their fellow eyes or control eyes. (Bottom) In the deep capillary plexus, the mean capillary density was also significantly lower in eyes affected by macular telangiectasia type 1 than in their fellow eyes or control eyes. In both plexuses there was no difference in capillary density between fellow eyes and control eyes. MT = macular telangiectasia. \* $P < .05$ ; \*\* $P < .01$ ; \*\*\* $P < .001$ .

microvasculature, involving both plexuses. In addition, the inverse correlation between superficial capillary plexus density on OCTA and mean perifoveal intercapillary area on FA (Table 2) is consistent with the dominant contribution of the superficial plexus to the FA signal.<sup>11</sup> However, the deep plexus participates to the diffuse fluorescent backdrop on FA images classically attributed to choroidal flow,<sup>11</sup> and becomes more visible when occupied

by vascular abnormalities like telangiectasias. Finally, visual acuity was exclusively correlated, among all anatomic parameters, with the capillary density of both plexuses on OCTA, highlighting the relevance of OCTA for the clinical evaluation of macular disorders.

Different investigators have previously suggested an overlap between MT type 1 with extramacular extension and adult-onset Coats disease.<sup>2,4,28</sup> In a report by Smithen and associates, 12 of 13 patients with adult-onset Coats disease had also perimacular telangiectasias with macular edema, and 11 of these patients presented areas of capillary nonperfusion often adjacent to areas of vascular abnormality and described as “a filigree-like network of capillaries.”<sup>28</sup> The similarity of this description with features of MT type 1 observed on OCTA strengthens the hypothesis that retinal telangiectasias localize preferentially in microenvironments where the capillary density is reduced, as observed in the present study.

Telangiectasias could develop as a result of this focal capillary loss, via an excess of proangiogenic factors, such as vascular endothelial growth factor, secreted by surrounding hypoxic retinal cells. A similar mechanism of unbalanced capillary growth from the deep capillary plexus owing to the lack of regulation by depleted Müller cells in a hypoxic environment has been advanced recently by Spaide and associates to explain the deep localization of vascular telangiectasias observed by OCTA in MacTel2.<sup>21</sup> Likewise, the repeated observation of an extra capillary vessel across the foveal avascular zone points to an imbalance in pro- or antiangiogenic factors in these MT type 1 patients. On the other hand, the decrease in capillary density may also occur secondarily to a local elevation in oxygen tension owing to its excessive diffusion from focally dilated capillaries. This is supported by the classical concepts that excessive oxygen tension is a potent inhibitor of retinal vessel growth, as long demonstrated in developmental disorders such as retinopathy of prematurity.<sup>29,30</sup> The effect of higher oxygen tension is also visible along the walls of retinal arterioles, which are surrounded by a local decrease in capillary density.<sup>31</sup> Noticeably, this phenomenon has been recently described on OCTA images of normal eyes,<sup>10</sup> and is exacerbated in MT type 1 eyes, as reported in the present study. Although the absolute vascular flow in a given vascular structure cannot yet be accurately measured by current commercial OCTA devices, it is indirectly reflected by the gray pixel value and size of this structure on OCTA images, the SSADA algorithm output being a nonlinear function of several parameters, including flow speed.<sup>32</sup> Therefore, the elevated brightness and caliber of microvascular lesions identified as telangiectasias on OCTA likely suggest a focal elevation in blood flow velocity. On the other hand, several telangiectasias that appeared on FA and ICGA were not visible on OCTA (as in Case 1, Figure 3). Similarly, Spaide has reported the variable detection of microaneurysms in diabetic retinopathy by OCTA and attributed this artifact to

**TABLE 2.** Correlation Between Fluorescein Angiography, Optical Coherence Tomography Angiography, and Optical Coherence Tomography Findings and Visual Acuity in Patients With Macular Telangiectasia Type 1

P Value ( <i>r</i> <sup>a</sup> )	Abnormal Microvascular Lesions (OCTA), n	Superficial Plexus Capillary Density (OCTA)	Deep Plexus Capillary Density (OCTA)	Abnormal Microvascular Lesions (FA), n	Mean Perifoveal Intercapillary Area (FA), 10 <sup>-3</sup> mm <sup>2</sup>	Abnormal Microvascular Lesions (ICGA), n	Central Macular Thickness, μm
Superficial plexus capillary density (OCTA)	.84						
Deep plexus capillary density (OCTA)	.24	.14					
Abnormal microvascular lesions (FA), n	.024 ( <i>r</i> = 0.86)	.56	.07				
Mean perifoveal intercapillary area (FA), 10 <sup>-3</sup> mm <sup>2</sup>	.36	.017 ( <i>r</i> = -0.94)	.42	.66			
Abnormal microvascular lesions (ICGA), n	.23	.95	.68	.13	.42		
Central macular thickness, μm	.91	.78	.96	.66	.66	.68	
Best-corrected visual acuity, logMAR	.40	.012 ( <i>r</i> = -0.88)	.048 ( <i>r</i> = -0.79)	.24	.06	.68	.40

FA = fluorescein angiography; ICGA = indocyanine green angiography; LogMAR = logarithm of the minimal angle of resolution; OCTA = optical coherence tomography angiography.

<sup>a</sup>Spearman rank correlation.

a slower flow than the OCTA device detection threshold within some of the lesions.<sup>24</sup> Here the number of lesions detected by OCTA was in all cases inferior to those observed by FA, but these counts were positively correlated. Unless OCTA segmentation failed to include all lesions, the most likely explanation is that all eyes harbor a subgroup of poorly perfused telangiectasias.

Several imaging technologies have been employed to evaluate in vivo the density of capillary vessels in the macula of healthy eyes, since fluorescein injection is not ethically permitted in healthy subjects. Using a prototype swept-source OCTA device, Kuehlewein and associates reported a mean vessel density of 0.74 in the superficial plexus and 0.72 in the deep plexus.<sup>33</sup> These values are close to or within the range of our observations in normal eyes (0.47–0.65 and 0.57–0.81, respectively). This limited disparity may be explained by the fact that their measure was performed over a 500-μm annulus outside the foveal avascular zone, whereas we have included this area to take into account its variability and have averaged the capillary density over the whole 3 × 3-mm field of OCTA images.<sup>14,25</sup> Using high-resolution, confocal adaptive optics-based FA, Pinhas and associates have determined that the relative vascular density of the superficial plexus in a 800-μm circle around the fovea was 0.51 (converted to arbitrary units), within the range of our observations.<sup>34</sup> Other investigators have also shown that capillary densities obtained on a prototype speckle variance OCTA device did not differ significantly from those

observed on histology of human donor eyes,<sup>35,36</sup> but similar comparisons need to be repeated using the commercial OCTA system employed in the present study.

Furthermore, there is to date no standard quantitative method to assess the vascular density on OCTA. Most existing methods of vessel detection are based on pixel intensity level after a binary transform. Native OCTA images may also be first skeletonized, as proposed by Agemy and associates,<sup>37</sup> but every additional step comes at the price of losing information. Complex indices based on vessel caliber, number of intersections, or intercapillary distances have also been proposed,<sup>35,36</sup> but they require extra computational effort that will not fit easily into high-workflow clinical settings. Regarding the region of interest over which the density is assessed, several patterns have been advanced, such as using the fields of an ETDRS grid. In the present study we opted for a global density encompassing the whole 3 × 3-mm images after subtracting areas of cystoid edema and larger vessels, in order to obtain comparable values among subjects, and limit the influence of macular edema on capillary density. Also, the foveal avascular zone was not excluded from the region of interest because its variations were part of the capillary density changes observed in MT type 1 eyes. The concentration of values among normal subjects illustrated by the low standard deviation confirmed the relevance of this approach (Figure 6 and Supplemental Table 2). It is also supported by the correlation between the superficial capillary plexus density in MT type 1 eyes with an estimate of

the capillary density extracted from early FA images (Table 2). Future software embedded in OCTA devices should provide quantitative tools that reproductively extract vascular densities and other relevant information, and provide refined measures after removal of confounding areas such as intraretinal edema.<sup>38</sup>

Limitations of this study include the small number of subjects related to the low prevalence of MT type 1, and the absence of longitudinal follow-up of the vascular abnormalities detected on OCTA. Images have been interpreted by multiple observers to maximize the discrimination of true flow from artifacts, but this could not prevent smaller or lower-flow telangiectasias from being missed by the OCTA acquisition, as discussed above and elsewhere.<sup>24</sup> To overcome this limitation owing to the variability in low-flow structure detection, several acquisitions should be performed on each eye and screened for these lesions. Finally, early-frame FA/ICGA images were not available, either for fellow eyes of MT type 1 subjects, because early acquisitions were focused on the diseased eye (except for

Case 1, Figure 5), or for control subjects, because it was unethical to inject them with dye (except for Control 10, Figure 5, who presented a contralateral atypical choroidal nevus requiring retinal imaging). We are unaware of previous reports quantitatively assessing the capillary density changes of MT type 1 patients on OCTA, and could find no reference to it in a computerized search on PubMed.

To summarize, OCTA noninvasively identified focal capillary network abnormalities in better detail than FA and showed a global reduction of capillary network density in both superficial and deep plexuses of MT type 1 eyes, which was correlated to visual acuity levels. Telangiectasias were observed on OCTA exclusively in the deep capillary plexus and were localized in a microenvironment where the superficial and deep capillary densities were lower than in other vascularized regions of the macula. Whether this finding is a cause or consequence of the telangiectasia formation and whether it is present in other vascular disorders with macular telangiectasias remain to be explored.

---

**FUNDING/SUPPORT:** THIS STUDY WAS SUPPORTED BY A GRANT FROM THE LOWY MEDICAL RESEARCH INSTITUTE LTD (La Jolla, CA, USA). Financial disclosures: Alexandre Matet: travel expenses (Laboratoires Alcon S.A.S., Rueil-Malmaison, France; Laboratoires Thea, Clermont-Ferrand, France). The following authors have no financial disclosures: Alejandra Daruich, Ali Dirani, Aude Ambresin, and Francine Behar-Cohen. All authors attest that they meet the current ICMJE criteria for authorship.

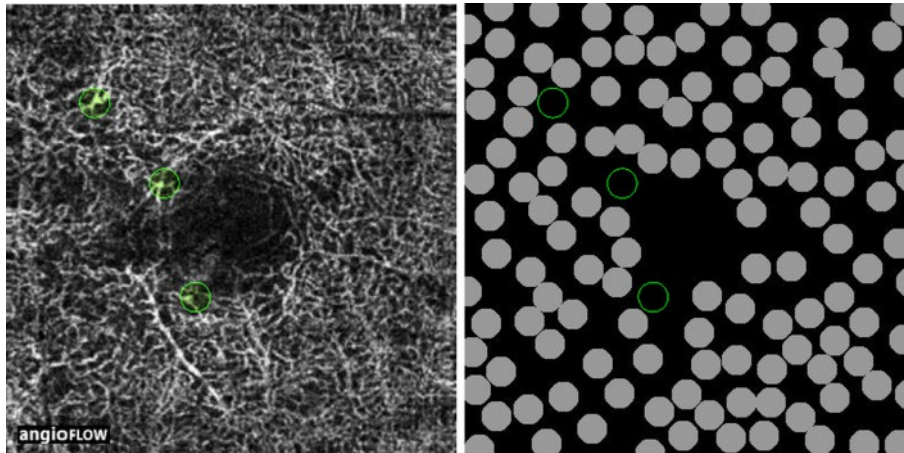
The authors thank Martine Elalouf, MD (Jules-Gonin Eye Hospital, Lausanne, Switzerland), Parnis Parvin, MD (Jules-Gonin Eye Hospital, Lausanne, Switzerland), Sarah Ferreira, optometrist (Jules-Gonin Eye Hospital, Lausanne, Switzerland), Luca Marchionno, optometrist (Jules-Gonin Eye Hospital, Lausanne, Switzerland), and Jean-Dominique de Azevedo, optometrist (Jules-Gonin Eye Hospital, Lausanne, Switzerland), for assistance in image acquisition.

---

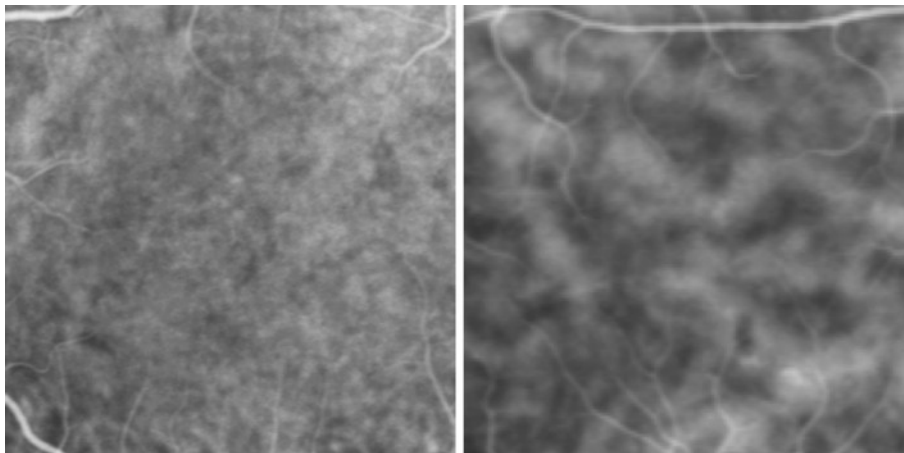
## REFERENCES

1. Gass JD, Blodi BA. Idiopathic juxtafoveolar retinal telangiectasis. Update of classification and follow-up study. *Ophthalmology* 1993;100(10):1536–1546.
2. Cahill M, O’Keefe M, Acheson R, Mulvihill A, Wallace D, Mooney D. Classification of the spectrum of Coats’ disease as subtypes of idiopathic retinal telangiectasis with exudation. *Acta Ophthalmol Scand* 2001;79(6):596–602.
3. Leber PT. Über eine durch Vorkommen multipler Miliaraneurysmen charakterisierte Form von Retinaldegeneration. *Albrecht Von Graefes Arch Für Ophthalmol* 1912; 81(1):1–14.
4. Yannuzzi LA, Bardal AMC, Freund KB, Chen K-J, Eandi CM, Blodi B. Idiopathic macular telangiectasia. *Arch Ophthalmol* 2006;124(4):450–460.
5. Engelbert M, Chew EY, Yannuzzi LA. Macular telangiectasia. In: Ryan SJ, Schachat AP, Wilkinson CP, Hinton DR, Sadda SR, Wiedemann PW, eds. *Retina*. 5th ed. Amsterdam: Elsevier; 2013:1050–1057.
6. Powner MB, Gillies MC, Tretiach M, et al. Perifoveal müller cell depletion in a case of macular telangiectasia type 2. *Ophthalmology* 2010;117(12):2407–2416.
7. Powner MB, Gillies MC, Zhu M, Vevis K, Hunyor AP, Fruttiger M. Loss of Müller’s cells and photoreceptors in macular telangiectasia type 2. *Ophthalmology* 2013;120(11): 2344–2352.
8. Nagiel A, Sadda SR, Sarraf D. A promising future for optical coherence tomography angiography. *JAMA Ophthalmol* 2015; 133(6):629–630.
9. Jia Y, Bailey ST, Hwang TS, et al. Quantitative optical coherence tomography angiography of vascular abnormalities in the living human eye. *Proc Natl Acad Sci U S A* 2015; 112(18):E2395–2402.
10. Bonnín S, Mané V, Couturier A, et al. New insight into the macular deep vascular plexus imaged by optical coherence tomography angiography. *Retina* 2015;35(11):2347–2352.
11. Spaide RF, Klancnik JM, Cooney MJ. Retinal vascular layers imaged by fluorescein angiography and optical coherence tomography angiography. *JAMA Ophthalmol* 2015;133(1): 45–50.
12. Savastano MC, Lumbroso B, Rispoli M. In vivo characterization of retinal vascularization morphology using optical coherence tomography angiography. *Retina* 2015;35(11): 2196–2203.
13. Puliafito CA, Hee MR, Lin CP, et al. Imaging of macular diseases with optical coherence tomography. *Ophthalmology* 1995;102(2):217–229.
14. Shahlaee A, Pefkianaki M, Hsu J, Ho AC. Measurement of foveal avascular zone dimensions and its reliability in healthy eyes using optical coherence tomography angiography. *Am J Ophthalmol* 2016;161:50–55.e1.
15. Coscas F, Glacet-Bernard A, Miere A, et al. Optical coherence tomography angiography in retinal vein occlusion:

- evaluation of superficial and deep capillary plexa. *Am J Ophthalmol* 2016;161:160–171.e1-2.
16. Rispoli M, Savastano MC, Lumbroso B. Capillary network anomalies in branch retinal vein occlusion on optical coherence tomography angiography. *Retina* 2015;35(11):2332–2338.
  17. Suzuki N, Hirano Y, Yoshida M, et al. Microvascular abnormalities on optical coherence tomography angiography in macular edema associated with branch retinal vein occlusion. *Am J Ophthalmol* 2016;161:126–132.e1.
  18. Couturier A, Mané V, Bonnin S, et al. Capillary plexus anomalies in diabetic retinopathy on optical coherence tomography angiography. *Retina* 2015;35(11):2384–2391.
  19. Ishibazawa A, Nagaoka T, Takahashi A, et al. Optical coherence tomography angiography in diabetic retinopathy: a prospective pilot study. *Am J Ophthalmol* 2015;160(1):35–44.e1.
  20. Hwang TS, Jia Y, Gao SS, et al. Optical coherence tomography angiography features of diabetic retinopathy. *Retina* 2015;35(11):2371–2376.
  21. Spaide RF, Klancnik JM, Cooney MJ, et al. Volume-rendering optical coherence tomography angiography of macular telangiectasia type 2. *Ophthalmology* 2015;122(11):2261–2269.
  22. Gaudric A, Krivosic V, Tadayoni R. Outer retina capillary invasion and ellipsoid zone loss in macular telangiectasia type 2 imaged by optical coherence tomography angiography. *Retina* 2015;35(11):2300–2306.
  23. Jia Y, Bailey ST, Wilson DJ, et al. Quantitative optical coherence tomography angiography of choroidal neovascularization in age-related macular degeneration. *Ophthalmology* 2014;121(7):1435–1444.
  24. Spaide RF, Fujimoto JG, Waheed NK. Image artifacts in optical coherence tomography angiography. *Retina* 2015;35(11):2163–2180.
  25. Carpineto P, Mastropasqua R, Marchini G, Toto L, Di Nicola M, Di Antonio L. Reproducibility and repeatability of foveal avascular zone measurements in healthy subjects by optical coherence tomography angiography. *Br J Ophthalmol* 2016;100:671–676.
  26. Arend O, Wolf S, Jung F, et al. Retinal microcirculation in patients with diabetes mellitus: dynamic and morphological analysis of perifoveal capillary network. *Br J Ophthalmol* 1991;75(9):514–518.
  27. Remky A, Arend O, Hendricks S. Short-wavelength automated perimetry and capillary density in early diabetic maculopathy. *Invest Ophthalmol Vis Sci* 2000;41(1):274–281.
  28. Smithen LM, Brown GC, Brucker AJ, Yannuzzi LA, Klais CM, Spaide RF. Coats' disease diagnosed in adulthood. *Ophthalmology* 2005;112(6):1072–1078.
  29. Ashton N, Ward B, Serpell G. Effect of oxygen on developing retinal vessels with particular reference to the problem of retrolental fibroplasia. *Br J Ophthalmol* 1954;38(7):397–432.
  30. Michaelson IC. The mode of development of the vasculature system of the retina, with some observations on its significance for certain retinal diseases. *Trans Ophthalmol Soc UK* 1948;68:137–180.
  31. Michaelson IC, Campbell ACP. The anatomy of the finer retinal vessels, and some observations on their significance in certain retinal diseases. *Trans Ophthalmol Soc UK* 1940;60:71–112.
  32. Jia Y, Tan O, Tokayer J, et al. Split-spectrum amplitude-decorrelation angiography with optical coherence tomography. *Opt Express* 2012;20(4):4710–4725.
  33. Kuehlewein L, Tepelus TC, An L, Durbin MK, Srinivas S, Sadda SR. Noninvasive Visualization and Analysis of the Human Parafoveal Capillary Network Using Swept Source OCT Optical Microangiography. *Invest Ophthalmol Vis Sci*. 2015;56(6):3984–3988.
  34. Pinhas A, Razeen M, Dubow M, et al. Assessment of perfused foveal microvascular density and identification of nonperfused capillaries in healthy and vasculopathic eyes. *Invest Ophthalmol Vis Sci*. 2014;55(12):8056–8066.
  35. Chan G, Balaratnasingam C, Xu J, et al. In vivo optical imaging of human retinal capillary networks using speckle variance optical coherence tomography with quantitative clinico-histological correlation. *Microvasc Res* 2015;100:32–39.
  36. Tan PE, Balaratnasingam C, Xu J, et al. Quantitative comparison of retinal capillary images derived by speckle variance optical coherence tomography with histology. *Invest Ophthalmol Vis Sci* 2015;56(6):3989–3996.
  37. Agemy SA, Scripsema NK, Shah CM, et al. Retinal vascular perfusion density mapping using optical coherence tomography angiography in normals and diabetic retinopathy patients. *Retina* 2015;35(11):2353–2363.
  38. Liu L, Gao SS, Bailey ST, Huang D, Li D, Jia Y. Automated choroidal neovascularization detection algorithm for optical coherence tomography angiography. *Biomed Opt Express* 2015;6(9):3564–3576.



SUPPLEMENTAL FIGURE 1. Method of random distribution of circular areas to compare the capillary density between perilesional areas and the whole 3×3-mm optical coherence tomography angiography image. (Left) Optical coherence tomography angiography of the deep capillary plexus (Case 7) with identification of telangiectasias and 100-μm radius circular perilesional areas. (Right) Random distribution of similar 100-μm radius circular areas over the whole image. 1,000 circular areas were randomly generated and only those that did not overlap with the perilesional areas (green), with a central 0.250-mm<sup>2</sup> disc representing the foveal avascular zone and with each other were retained, yielding a total of 121 areas (light gray).



SUPPLEMENTAL FIGURE 2. Early-frame 3×3-mm indocyanine green angiography in (Left) the fellow eye of a 52-year-old man with macular telangiectasia type 1 (Case 1) and (Right) the healthy control eye of a 51-year-old man, visualizing poorly the foveal microvasculature.

SUPPLEMENTAL TABLE 1. Total number of focal microvascular dilations identified by 3 independent observers in the superficial and deep capillary plexuses on optical coherence tomography angiography, fluorescein and indocyanine-green angiography among 7 eyes with macular telangiectasia type 1.

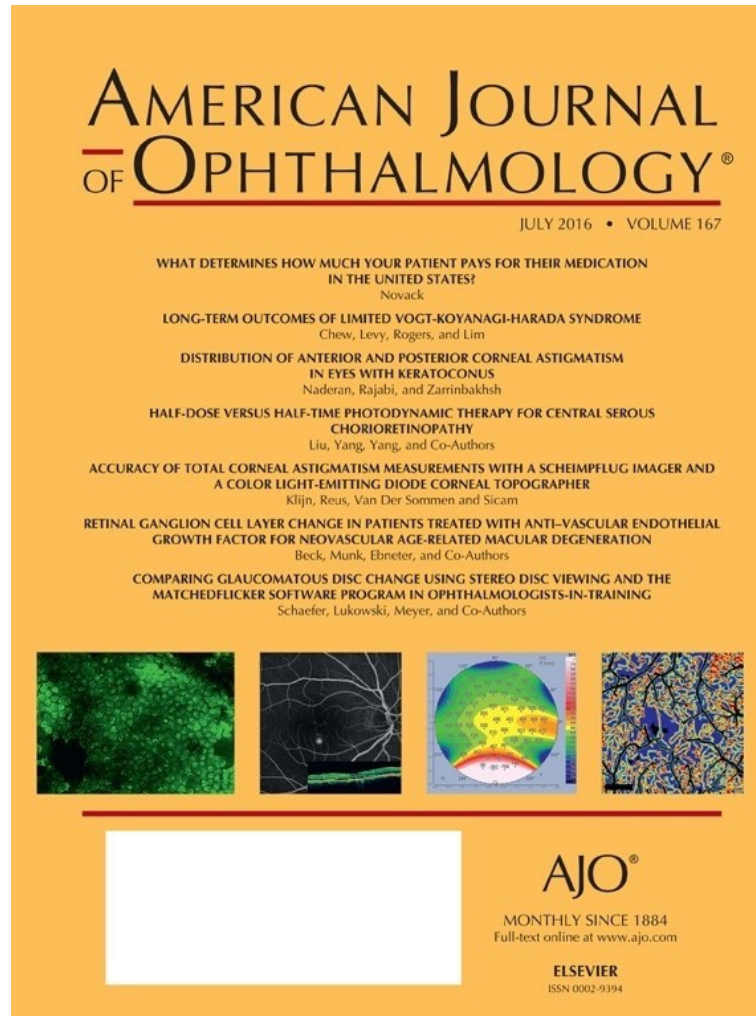
OCTA= optical coherence tomography angiography; FA= fluorescein angiography; ICG: indocyanine green angiography

	Focal microvascular dilations, N.											
	Observer 1				Observer 2				Observer 3			
	OCTA superficial plexus	OCTA deep plexus	FA	ICG	OCTA superficial plexus	OCTA deep plexus	FA	ICG	OCTA superficial plexus	OCTA deep plexus	FA	ICG
Case 1	0	7	56	39	0	7	61	37	0	8	45	38
Case 2	0	5	3	3	0	6	15	3	0	5	4	3
Case 3	0	12	27	NA	0	13	47	NA	0	16	23	NA
Case 4	0	3	2	7	0	3	12	4	0	2	3	3
Case 5	0	7	10	19	0	7	13	18	0	7	13	16
Case 6	0	6	29	NA	0	6	31	NA	0	8	24	NA
Case 7	0	4	15	7	0	2	11	6	0	4	14	6

SUPPLEMENTAL TABLE 2. Total capillary vessel densities in fellow eyes of subjects with macular telangiectasia type 1 and healthy control eyes on optical coherence tomography angiography.

Case, sex (age, years)	Group	Superficial capillary plexus	Deep capillary plexus
1, M (68)	MT type 1 fellow eye	0.602	0.6279
2, M (56)	MT type 1 fellow eye	0.4848	0.6398
3, M (45)	MT type 1 fellow eye	0.5155	0.7414
4, M (51)	MT type 1 fellow eye	0.4591	0.6553
5, M (52)	MT type 1 fellow eye	0.5498	0.6828
6, M (54)	MT type 1 fellow eye	0.3777	0.7713
7, M (74)	MT type 1 fellow eye	0.6003	0.6565
C1, M (66)	Control	0.536	0.8109
C2, M (51)	Control	0.492	0.7068
C3, M (66)	Control	0.6274	0.6836
C4, M (52)	Control	0.5263	0.6118
C5, M (67)	Control	0.4751	0.6375
C6, M (50)	Control	0.6222	0.6831
C7, M (61)	Control	0.5538	0.5775
C8, M (54)	Control	0.6482	0.6962
C9, M (51)	Control	0.5365	0.6636
C10, M (65)	Control	0.6504	0.6367
C11, M (59)	Control	0.5715	0.7434
C12, M (52)	Control	0.4743	0.6072

Cover of the American Journal of Ophthalmology, July 2016 Issue, showing a cover figure (last on the right) selected from the article by Matet et al:  
*Macular telangiectasia type 1: capillary density and microvascular abnormalities assessed by optical coherence tomography angiography*





[3b] Efficacy of intravitreal aflibercept in macular telangiectasia type 1 is linked to the ocular angiogenic profile. *Retina* 2016

Kowalczuk L\*, Matet A\*, Dirani A, Daruich A, Ambresin A, Mantel I, Spaide R, Turck N, Behar-Cohen F<sup>29</sup>

doi: 10.1097/IAE.0000000000001424.

\*= co-first authors

Contribution of the PhD candidate:

- Patient follow-up
- Processing and analysis of OCT and OCT angiography data
- Statistical analyses
- Interpretation of results
- Co-drafting the manuscript



# EFFICACY OF INTRAVITREAL AFLIBERCEPT IN MACULAR TELANGIECTASIA TYPE 1 IS LINKED TO THE OCULAR ANGIOGENIC PROFILE

LAURA KOWALCZUK, PhD,\* ALEXANDRE MATET, MD,\* ALI DIRANI, MD,\*  
ALEJANDRA DARUICH, MD,\* AUDE AMBRESIN, MD,\* IRMELA MANTEL, MD,\*  
RICHARD F. SPAIDE, MD,† NATACHA TURCK, PhD,‡ FRANCINE BEHAR-COHEN, MD, PhD\*

**Purpose:** To evaluate intravitreal aflibercept in macular telangiectasia Type 1 (MacTel 1) patients and measure their ocular angiogenic profile.

**Methods:** Eight subjects with MacTel 1 refractory to bevacizumab, ranibizumab, or laser therapy and switched to aflibercept were included. Best-corrected visual acuity, central macular thickness, and cystic areas quantified on optical coherence tomography B-scans were assessed during 12 months. Perifoveal capillary densities were measured on optical coherence tomography angiography. Aqueous humor was sampled from six patients and eight control subjects undergoing cataract extraction. Growth factors were quantified using a multiarray immunoassay.

**Results:** Over 12 months, patients received  $6.6 \pm 1.4$  (range, 5–8) intravitreal aflibercept injections. Twelve months after switching to aflibercept, best-corrected visual acuity increased by  $\geq 5$  letters in 5 of 8 patients, compared with preaflibercept levels. Mean best-corrected visual acuity improved from 79.6 (~20/50) to 88.0 (~20/35) Early Treatment Diabetic Retinopathy Study letters ( $P = 0.042$ ), and central macular thickness decreased from  $434 \pm 98 \mu\text{m}$  to  $293 \pm 59 \mu\text{m}$  ( $P = 0.014$ ). Compared with control subjects, the profile of angiogenic factors in MacTel 1 eyes revealed no difference in vascular endothelial growth factor-A levels but significantly higher levels of placental growth factor ( $P = 0.029$ ), soluble vascular endothelial growth factor receptor-1 (sFlt-1;  $P = 0.013$ ), vascular endothelial growth factor-D ( $P = 0.050$ ), and Tie-2 ( $P = 0.019$ ). Placental growth factor levels inversely correlated with both superficial and deep capillary plexus densities on optical coherence tomography angiography ( $P = 0.03$ ).

**Conclusion:** The clinical response to aflibercept coupled to the angiogenic profile of MacTel 1 eyes support the implication of the placental growth factor/Flt-1 pathway in MacTel 1.

RETINA 0:1–12, 2016

“Idiopathic juxtafoveal telangiectasia” is a generic term that encompasses different clinical entities first classified by Gass and Oyakawa in 1982,<sup>1</sup> then by Gass and Blodi in 1993.<sup>2</sup> In 2006, Yannuzzi et al<sup>3</sup> proposed a simplified classification under the term “idiopathic macular telangiectasia,” with 2 distinct types: Type 1, “aneurysmal telangiectasia,” and Type 2, “perifoveal telangiectasia,” also known as MacTel. These classifications are based on the clinical features because no specific molecular signature or pathogenic mechanisms have yet been identified.

Idiopathic macular telangiectasia Type 1 (MacTel 1) is usually unilateral and affects mostly men of 40 years

to 50 years of age at presentation.<sup>1</sup> Microvascular ectasia and increased tortuosity of the macular capillary network are visible on fundus examination, may extend to the temporal side of the macula over an area of 2 disk diameter or greater,<sup>1,2</sup> and may be associated to peripheral vascular changes.<sup>3</sup> Telangiectasia frequently causes macular edema with lipid exudates of variable severity and subsequent vision loss. Location, morphologic feature, and degree of leakage of the microvascular ectasia and capillary nonperfusion are best identified on fluorescein angiography.

Whether MacTel 1 is a milder, later, and more central form of Coats disease is debated because both entities

associate vascular telangiectasia with aggressive exudation, unilateral involvement, and male predominance.<sup>3–5</sup> To confirm the diagnosis of MacTel 1, disorders causing secondary telangiectasia must be excluded, which included retinal vein occlusion, diabetic retinopathy, ocular ischemic syndrome, hypertensive retinopathy, and more rarely posterior segment inflammation, radiation maculopathy, sickle-cell maculopathy, or localized retinal capillary hemangioma.

MacTel 1 is a rare disease, and there is no consensus regarding treatment schemes. Laser photocoagulation can be performed on accessible ischemic areas but may also target leaky aneurysms. Intravitreal anti-vascular endothelial growth factor (VEGF) therapy has also been assessed, with inconstant results. Although bevacizumab<sup>6,7</sup> and ranibizumab<sup>8,9</sup> showed some efficacy in reducing macular edema and improving vision, three case series reported that only a minority of patients responded favorably to intravitreal bevacizumab.<sup>10–12</sup> Recently, three groups reported that MacTel 1 patients may be nonresponders or become refractory to bevacizumab<sup>13–15</sup> or ranibizumab,<sup>15</sup> including two case reports describing a favorable response after switching to intravitreal aflibercept.<sup>14,15</sup> Aflibercept is a soluble decoy receptor that associates an immunoglobulin backbone to extracellular sequences of the VEGF receptors, VEGFR-1 (also called Flt-1) and VEGFR-2. In contrast to specific anti-VEGF antibodies such as bevacizumab and ranibizumab, which bind to the VEGF-A isoform only, aflibercept also blocks another ligand of Flt-1, placental growth factor (PlGF). Through its binding to Flt-1, PlGF

is suspected to enhance vascular permeability and to amplify the effects of VEGF on pathologic angiogenesis.<sup>16</sup> Also, PlGF has been implicated in the resistance to anti-VEGF treatments in patients with malignant tumors<sup>17,18</sup> and various retinal diseases, including diabetic macular edema.<sup>19,20</sup> Aflibercept may overcome this hurdle by neutralizing PlGF along with VEGF.<sup>21,22</sup> Interestingly, in an adult rat model, the overexpression of rat PlGF did not induce preretinal neovessels, as observed when VEGF is overexpressed,<sup>23</sup> but produced retinal vessel abnormalization manifested by tortuosity, dilation, and capillary aneurysms,<sup>24</sup> suggesting a potential role of PlGF in the pathogenesis of aneurysmal telangiectasia.

In this context, the aim of this study was to retrospectively evaluate the effect of intravitreal aflibercept therapy in patients with macular edema caused by MacTel 1 and to correlate it to the profile of angiogenic factors in aqueous humor.

## Methods

### Subjects

This retrospective interventional case series involving eight human subjects and eight healthy control subjects adhered to the tenets of the Declaration of Helsinki. The protocol was approved by the local Ethics Committee of the Swiss Department of Health on research involving human subjects (CER-VD N° 95/15 and 340/15) and by an Institutional Review Board from the Western Institutional Review Board (Puyallup, WA). All patients signed an informed consent form before aqueous humor sampling. Six consecutive patients followed from December 2013 to July 2015 at the Jules-Gonin Eye Hospital (Lausanne, Switzerland) and two consecutive patients followed at the Vitreous, Retina, Macula Consultants of New York (New York, NY) were included in this study. Inclusion criteria were as follows: 1) macular edema caused by idiopathic MacTel 1 without medical or ophthalmologic history suggesting secondary macular telangiectasia and 2) persistence of macular edema after a well-conducted treatment by retina specialists with intravitreal bevacizumab (Avastin; Genentech, Inc, South San Francisco, CA), ranibizumab (Lucentis; Novartis Pharma AG, Basel, Switzerland, and Genentech, Inc), and/or laser photocoagulation, justifying a treatment switch to intravitreal aflibercept (Eylea; Bayer, Leverkusen, Germany).

Eight sex-matched and age-matched patients undergoing cataract surgery and having no history of diabetes or retinal disease were included during the same period as control subjects for aqueous humor sampling.

---

From the \*Department of Ophthalmology, University of Lausanne, Jules-Gonin Eye Hospital, Fondation Asile des Aveugles, Lausanne, Switzerland; †Vitreous, Retina, Macula Consultants of New York and LuEsther T. Mertz Retina Research Center, Manhattan Eye, Ear and Throat Hospital, New York, New York; and ‡Department of Human Protein Science, University of Geneva, Geneva, Switzerland.

Supported by a grant from the Lowy Medical Research Institute LTD.

F. Behar-Cohen is a consultant for Bayer, Novartis, Allergan, and Genentech. The remaining authors have no any conflicting interests to disclose.

L. Kowalczyk and A. Matet contributed equally to the work.

Supplemental digital content is available for this article. Direct URL citations appear in the printed text and are provided in the HTML and PDF versions of this article on the journal's Web site ([www.retinajournal.com](http://www.retinajournal.com)).

The study was performed in the Fondation Asile des Aveugles, Jules-Gonin Eye Hospital, which is the Department of Ophthalmology of the University of Lausanne.

This is an open-access article distributed under the terms of the Creative Commons Attribution-Non Commercial-No Derivatives License 4.0 (CCBY-NC-ND), where it is permissible to download and share the work provided it is properly cited. The work cannot be changed in any way or used commercially without permission from the journal.

Reprint requests: Francine Behar-Cohen, MD, PhD, Jules-Gonin Eye Hospital, Avenue de France 15, CP 133, CH-1000, Lausanne 7, Switzerland; e-mail: [francine.behar@gmail.com](mailto:francine.behar@gmail.com)

### *Patient Treatment and Follow-up*

After two initial monthly loading doses, patients received intravitreal aflibercept on a pro re nata (as needed) regimen. Decision for reinjection was made by two retina specialists (R.F.S. or F.B.-C.), and reinjections were performed at an interval of 4 weeks or more. They were indicated in case of persistent or recurrent macular edema manifesting by intraretinal cysts and/or subretinal fluid.

At all visits, best-corrected visual acuity was measured using an Early Treatment Diabetic Retinopathy Study chart, and serial spectral-domain optical coherence tomography (SD-OCT) images on Spectralis (Heidelberg Engineering, Heidelberg, Germany) were obtained. Confocal fluorescein and indocyanine green angiography on Spectralis had been performed in all cases at presentation for the diagnosis of MacTel 1 and were repeated at the discretion of the treating retina specialist. Images of OCT angiography (OCTA) were acquired using the Angiovue RTx 100, based on the AngioVue Imaging System (Optovue, Inc, Fremont, CA).

Clinical charts were retrospectively reviewed, and data were recorded at baseline (corresponding to the last visit before the first intravitreal aflibercept injection), 1 month, and 3, 6, and 12 months after baseline.

### *Spectral-Domain Optical Coherence Tomography Imaging and Quantification of Intraretinal Cysts Area*

At each time point, high-quality, 30° horizontal, single, SD-OCT B-scans and 20° × 20° 97-section horizontal grids were acquired using the follow-up mode on Spectralis. The central macular thickness (CMT) was automatically measured in the central sub-field of an Early Treatment Diabetic Retinopathy Study grid on the built-in software. For graphical purposes, the boundaries of the cystoid edema regions were outlined with a red contour and superimposed over the original SD-OCT images, using a custom semiautomated algorithm on Matlab (Version R2015b; Mathworks, Natick, MA) detailed in the **Supplemental Digital Content 1** (see **Figure**, <http://links.lww.com/IAE/A563>).

### *Optical Coherence Tomography Angiography Imaging and Macular Capillary Density*

The OCTA Angiovue RTx 100 instrument was used to obtain amplitude decorrelation angiography images. This instrument has an A-scan rate of 70,000 scans per second, using a light source centered on 840 nm and a bandwidth of 50 nm. Each OCTA volume contains

304 × 304 A-scans with 2 consecutive B-scans captured at each fixed position before proceeding to the next sampling location. Split-spectrum amplitude-decorrelation angiography was used to extract the OCTA information. Each OCTA volume is acquired in 3 seconds, and 2 orthogonal OCTA volumes are acquired to perform motion correction. Angiography information displayed is the average of the decorrelation values when viewed perpendicularly through the thickness being evaluated.

To obtain comparable 3 × 3-mm OCTA scans between subjects, volumes were automatically segmented by the built-in software to provide images of the superficial plexus (3 μm below the inner limiting membrane to 16 μm below the outer border of the inner plexiform layer) and deep plexus (16–69 μm below the outer border of the inner plexiform layer). The correct segmentation for each patient was controlled before reporting the capillary densities calculated using the AngioVue software.

### *Aqueous Humor Sampling*

At the time of an aflibercept intravitreal injection indicated for macular edema, 50 μL to 150 μL of aqueous humor were sampled by anterior chamber tap before the injection, using a 30-gauge needle and a 1-mL syringe, and immediately frozen at –80°C. Before aqueous humor sampling, a time lapse of at least 7 weeks from the previous anti-VEGF injection (ranibizumab, bevacizumab, or aflibercept) was observed in all patients. Given that pharmacologic observations<sup>25–27</sup> and mathematical models<sup>28</sup> have estimated the vitreous elimination half-life ( $t_{1/2}$ ) of ranibizumab, bevacizumab, and aflibercept to be, respectively,  $t_{1/2} = 3.2$  days to 7.2 days,  $t_{1/2} = 4.9$  days to 5.6 days, and  $t_{1/2} = 4.6$  days to 4.8 days,<sup>25–28</sup> aqueous sampling was performed when no residual anti-VEGF drug remained in the vitreous, after a clearance time of  $\geq 7 \times t_{1/2}$ . In the control group, the anterior chamber tap was performed at the beginning of cataract surgery before any fluid was injected into the anterior chamber.

### *Angiogenic Factor Levels in Aqueous Humors*

Aqueous humor levels of soluble VEGFR-1 (sFlt-1), PlGF, the tyrosine kinase receptor Tie-2 with immunoglobulin-2 and EGF-like domains (Tie-2), VEGF-A<sub>165</sub>, VEGF-C, VEGF-D, and basic fibroblast growth factor were measured, on the same plate, using a multiarray high-sensitive immunoassay (V-PLex Angiogenesis Panel 1 Kit; Meso Scale Discovery, Rockville, MD). This standardized kit was used according to the manufacturer's

instructions. Standard curves for each angiogenic factor were generated with the provided calibration kit, and the samples were assayed in duplicate, without dilution. Data acquisition and analysis were performed with the Meso Scale reader (MSD Quickplex SQ-120; Meso Scale Diagnostics, Rockville, MD) and its dedicated software (Discovery Benchmark Version 4.0.12). Detection thresholds for all angiogenic factors were set between 1 pg/mL and 20 pg/mL, and coefficients of variation were inferior to 10%.

### Statistical Analysis

Results were expressed as mean  $\pm$  standard deviation. Biologic and clinical analyses were carried out on GraphPad Prism 5 (GraphPad Software, Inc, La Jolla, CA). The nonparametric Mann–Whitney *U* test and Wilcoxon paired test were used to compare data, when applicable. Spearman correlation was used to evaluate relationships between angiogenic factors levels and clinical parameters. A 2-tailed *P* value of  $<0.05$  was considered statistically significant.

## Results

### Patient Characteristics

Eight patients with MacTel 1 (7 men and 1 woman) with a mean age of  $63.0 \pm 10.3$  years (range, 45–74 years) were included in this study. Clinical characteristics, previous treatments, and number of intravitreal aflibercept injections are reported in Table 1. All patients had been previously treated with extramacular and/or macular laser photocoagulation, combined with intravitreal anti-VEGF therapy in seven patients. Four patients had

received bevacizumab, two patients had received ranibizumab, and one patient had received sequentially bevacizumab, ranibizumab, and dexamethasone implant. After an optimal treatment regimen with these therapies, the patients had a mean CMT of  $434 \pm 98 \mu\text{m}$ . Over the 12-month study period, they received  $6.6 \pm 1.4$  intravitreal aflibercept injections (range, 5–8 injections).

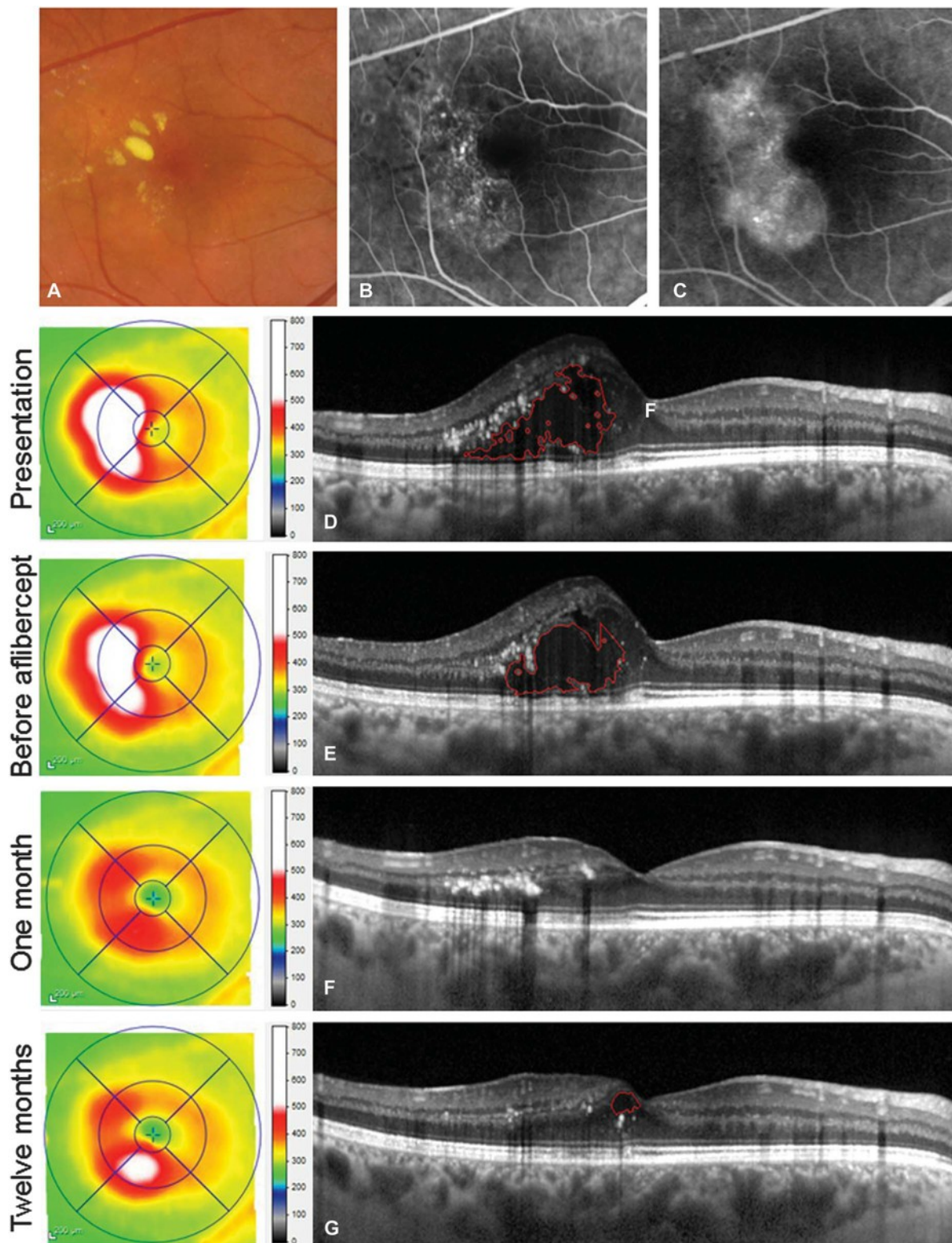
### Effect of Intravitreal Aflibercept Therapy

A clinical illustration of a patient refractory to bevacizumab therapy and responsive to aflibercept therapy is provided in Figure 1 (Case 4). Figure 2 shows the baseline and 12-month SD-OCT B-scans and corresponding thickness maps from the 8 patients included in this study, demonstrating the clinical response to aflibercept treatment.

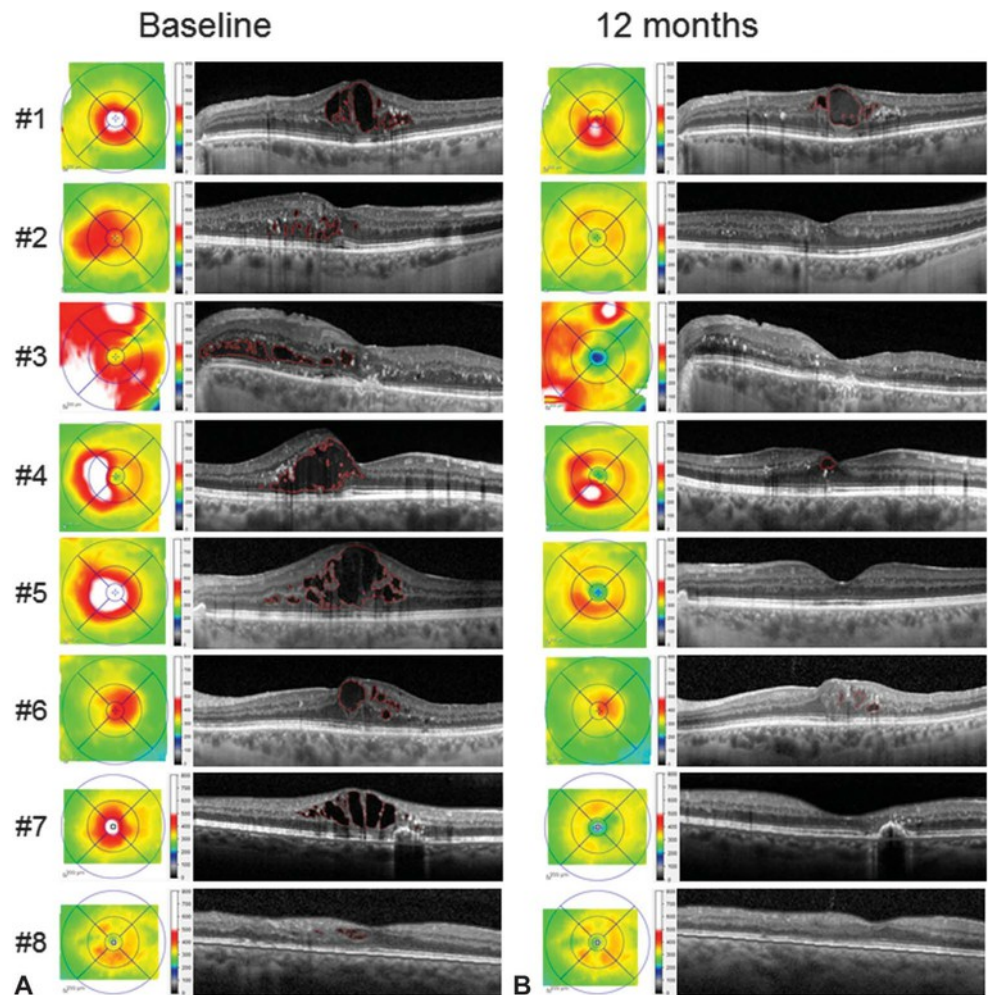
The anatomical and visual outcomes of intravitreal aflibercept therapy by 12 months are summarized in Table 2. The CMT decreased in all patients, with a significant reduction from  $434 \pm 98 \mu\text{m}$  to  $293 \pm 59 \mu\text{m}$  ( $P = 0.014$ ). The best-corrected visual acuity improved in 7 of 8 patients with a mean significant improvement from  $79.6 \pm 16.3$  ( $\sim 20/52$ ) letters to  $88.0 \pm 11.2$  ( $\sim 20/35$ ) Early Treatment Diabetic Retinopathy Study letters ( $P = 0.042$ ). There was an improvement by five or more Early Treatment Diabetic Retinopathy Study letters in five of eight patients. Both anatomical and visual parameters improved progressively over time, as illustrated in Figure 3. After 1 intravitreal aflibercept injection, a reduction in CMT was observed in all patients, with a significant reduction as compared with baseline ( $308.6 \pm 32.9 \mu\text{m}$ ;  $P = 0.016$ ) that was maintained over the 12-month follow-up. By Month 6, visual acuity levels significantly

Table 1. Clinical Characteristics and Treatment History of 8 Patients With MacTel 1, Refractory to Previous Therapies and Treated by Intravitreal Aflibercept During a 12-Month Period

Eye#	Age, Years	Sex	Treatments Received Before Aflibercept		CMT Before Aflibercept Initiation, $\mu\text{m}$	Intravitreal Aflibercept Injections Over 12 Months
			Laser Photocoagulation	Intravitreal Injections (Number)		
1	71	M	Macular + extramacular	Ranibizumab (8)	528	8
2	68	M	Macular + extramacular	Ranibizumab (1)	394	7
3	56	M	Macular + extramacular	Bevacizumab (10)	348	5
4	45	M	Macular	Bevacizumab (6)	396	5
5	54	M	Macular (subthreshold) + extramacular	None	595	7
6	74	M	Macular + extramacular	Bevacizumab (6)	393	8
7	72	F	Macular + photodynamic therapy	Bevacizumab (2) + ranibizumab (2) + dexamethasone (1)	508	8
8	64	M	Macular	Bevacizumab (5)	312	5



**Fig. 1.** Differential effects of bevacizumab and aflibercept on macular edema in a 45-year-old patient with MacTel 1 (Case 4). **A.** Color fundus photograph showing capillary dilations and hard exudates. **B** and **C.** Fluorescein angiography frames at 47 seconds (**B**) and 3.5 minutes (**C**) after dye injection showing leaky microaneurysms. **D–G.** Horizontal optical coherence tomography B-scans of the macula acquired at different time points: At initial presentation (**D**), 1 month after the last of 6 intravitreal bevacizumab injections administered over 7 months (**E**), and 1 month (**F**) and 12 months (**G**) after the first intravitreal aflibercept injection. The patient received 5 intravitreal aflibercept injections over the 12-month follow-up. On each optical coherence tomography image, intraretinal cystoid cavities were outlined by a red line using a semiautomated algorithm.



**Fig. 2.** Clinical effect of aflibercept intravitreal therapy over 12 months in 8 patients with MacTel 1. Optical coherence tomography thickness maps and horizontal B-scans through the fovea at baseline **A** and 12 months after the initiation of intravitreal aflibercept (**B**). Central macular thickness and the area of cystoid spaces on the horizontal B-scans improved in all patients. The regions identified by a semiautomated algorithm as cystoid spaces were outlined by a red contour.

improved ( $88.0 \pm 11.3$  letters [ $\sim 20/35$ ];  $P = 0.02$ ), which was maintained at the 12-month time point.

#### *Angiogenic Factor Levels in Aqueous Humor*

The 8 individuals selected for the control group of aqueous humor analysis were male with a mean age of  $68 \pm 12$  years (range, 50–85 years), not significantly different from the 6 subjects with MacTel 1 from whom aqueous humor was sampled (Cases 1–6: mean age,  $61 \pm 11$  years;  $P = 0.40$ ).

The profiles of angiogenic factors in the aqueous humor of patients with MacTel 1, compared with healthy control subjects, are represented in Figure 4. There was no difference in VEGF-A levels ( $\times 1.3$ ;  $P = 0.95$ ) but significantly higher levels of sFlt-1 ( $\times 4.3$ ;  $P = 0.013$ ), PlGF ( $\times 2.2$ ;  $P = 0.029$ ), and Tie-2 ( $\times 3.7$ ;  $P = 0.019$ ) and VEGF-D ( $\times 6.8$ ;  $P = 0.049$ ). VEGF-C and basic fibroblast growth factor levels were higher without reaching statistical significance. Mean aqueous levels of angiogenic factors in affected and control subjects are reported in the Table 3.

#### *Correlations Between Imaging and Biologic Parameters*

The OCTA scans were analyzed to determine the perifoveal capillary densities in the superficial and deep capillary plexuses. Figure 5 provides an illustration of multimodal imaging in 1 patient (Case 1), with OCTA of the superficial and deep capillary plexuses and the corresponding capillary density maps.

An exhaustive account of the functional and anatomical parameters and aqueous levels of angiogenic factors is given in the **Supplemental Digital Content 2** (see **Table 1**, <http://links.lww.com/IAE/A564>). When exploring possible correlations between these parameters (see **Table 2**, **Supplemental Digital Content 3**, <http://links.lww.com/IAE/A565>), we found a significant inverse correlation between the perifoveal capillary density of both superficial and deep capillary plexuses on OCTA and aqueous levels of PlGF ( $P = 0.03$ ;  $r = -0.89$ ).

Table 2. Functional and Anatomical Outcome of Intravitreal Aflibercept in 8 Patients With MacTel 1

Mean ± SD	Baseline	12 Months	P*
Best-corrected visual acuity, ETDRS letter score (Snellen)	79.6 ± 16.3 (~20/52)	88.0 ± 11.2 (~20/35)	0.042
CMT, μm	434.3 ± 98.0	292.5 ± 58.6	0.014

Baseline values were recorded 1 month after the last administration of the previous intravitreal or laser treatment.

\*Wilcoxon signed rank test.

ETDRS, Early Treatment Diabetic Retinopathy Study; SD, standard deviation.

**Discussion**

In this case series of 8 patients with MacTel 1, treatment with intravitreal aflibercept, that blocks both VEGF-A and PIGF, showed significant anatomical and functional effects on macular edema. Anatomical improvement was observed after one intravitreal injection of aflibercept in all cases, including those incompletely responsive to other anti-VEGF therapies

that do not inhibit the PIGF-mediated Flt1 pathway. These results are supported by measurements of higher levels of PIGF, but not VEGF-A, in the aqueous humor of patients with MacTel 1 compared with healthy control subjects.

To date, there are 2 case reports on the effects of intravitreal aflibercept in MacTel 1. Shibebe et al<sup>14</sup> described the complete resolution of macular edema and visual improvement after 4 aflibercept injections in 1 case of MacTel 1 refractory to 3 monthly bevacizumab injections and to laser photocoagulation. Recently, Kovach et al<sup>15</sup> reported the beneficial effect over 3 years of aflibercept therapy on macular edema secondary to MacTel 1 in 1 patient previously nonresponding to 6 monthly bevacizumab, 7 monthly ranibizumab, and 3 triamcinolone acetonide injections. Before aflibercept became available for retina indication, several investigators had evaluated intravitreal injections of bevacizumab and ranibizumab in Type 1 and Type 2 idiopathic macular telangiectasia, with limited outcomes. Noticeably, the exact role of VEGF in the development of primary telangiectasia is not clear, and intraocular VEGF levels in Type 1 or Type 2 idiopathic macular telangiectasia had not been reported before the present study. Two case reports have suggested a favorable effect of intravitreal bevacizumab on MacTel 1,<sup>6,7</sup> but these observations were not confirmed by 3 small case series. Matsumoto and Yuzawa<sup>10</sup> reported 4 patients with MacTel 1 who received 3 to 4 intravitreal bevacizumab injections over a 6-month period. The microaneurysms regressed in one of the four eyes, but visual acuity did not improve in any of the patients. Takayama et al<sup>11</sup> reported 5 cases with MacTel 1, treated with 2 to 3 intravitreal bevacizumab over 1 year, among which only 1 eye showed a reduction in macular edema and an improvement in visual acuity. Finally, Moon et al<sup>12</sup> also reported 7 patients with MacTel 1 treated with intravitreal bevacizumab during 4 months. Although a significant decrease in CMT was observed on SD-OCT, there was no significant improvement in visual acuity. In idiopathic macular telangiectasia Type 2 (or MacTel), several studies have demonstrated that anti-VEGF

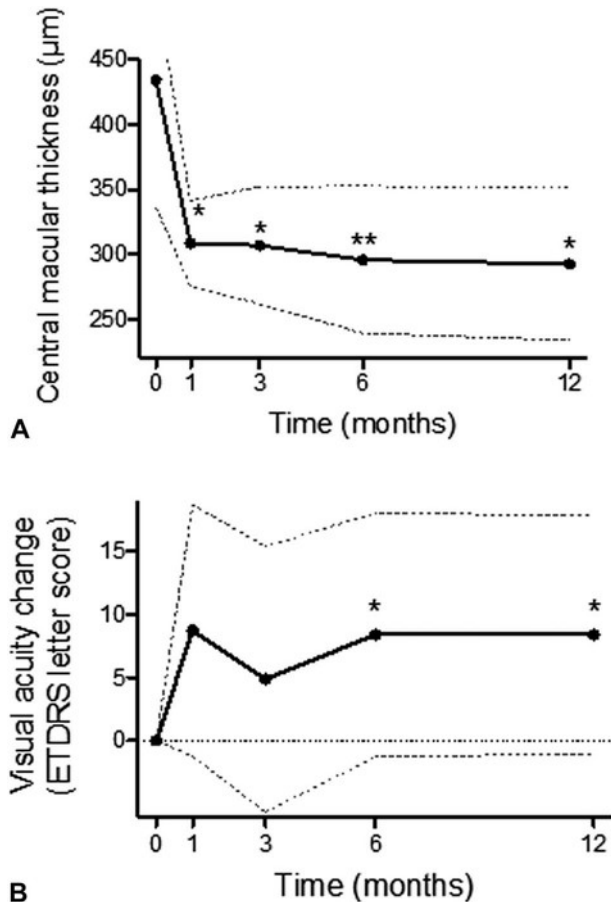


**Fig. 3.** Anatomical and visual effect of intravitreal aflibercept therapy in 8 patients with MacTel 1, over 12 months. **A.** Mean CMT. **B.** Best-corrected visual acuity change (Early Treatment Diabetic Retinopathy Study letter score). All parameters were assessed at baseline, 1 month, 3, 6, and 12 months. The inferior and superior dotted lines indicate the standard deviation. Mean values were compared with baseline using a Wilcoxon paired test (\**P* < 0.05; \*\**P* < 0.01).

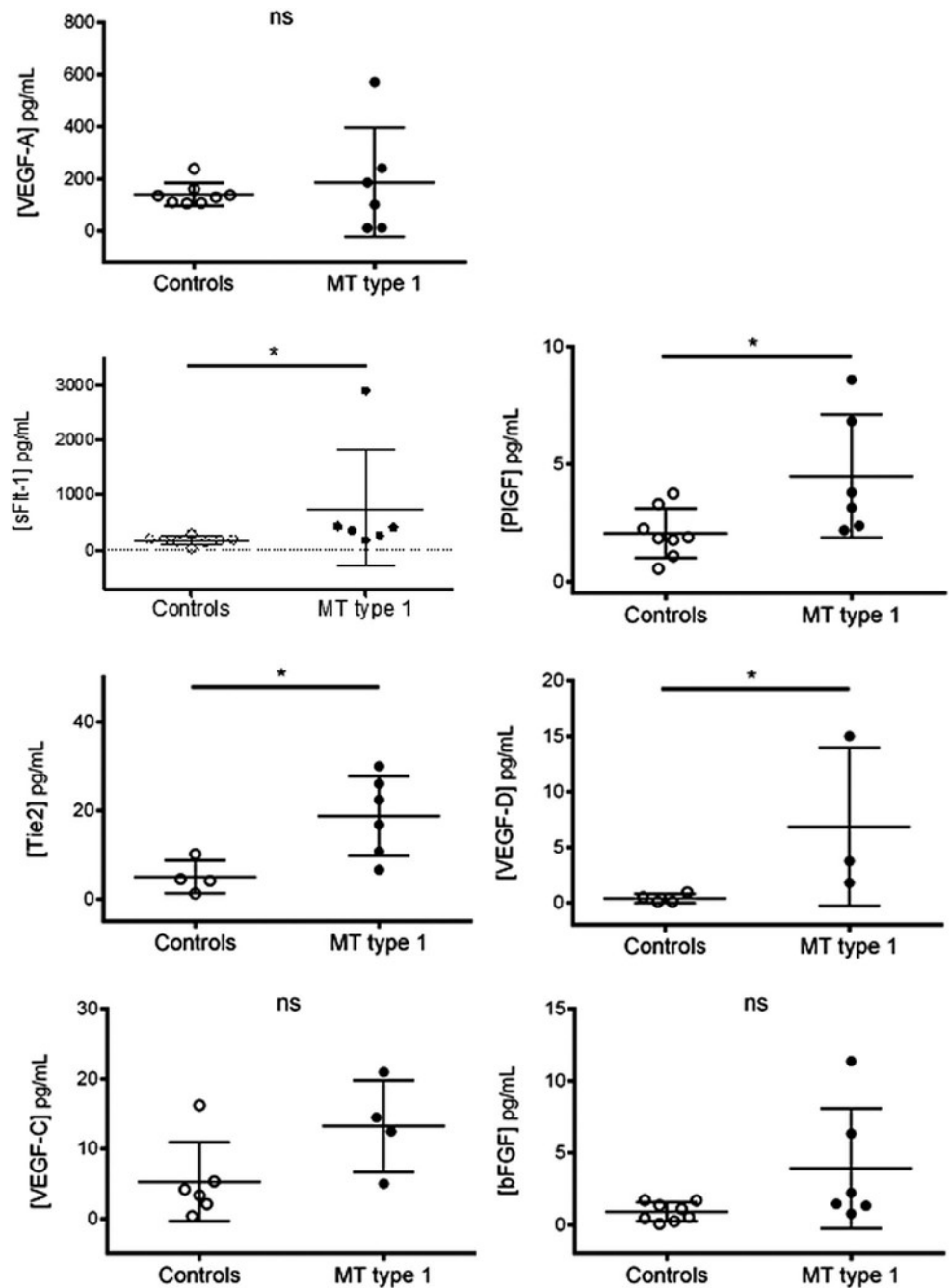


**Fig. 4.** Angiogenic factors profile in the aqueous humor determined by a multiarray high-sensitive immunoassay. VEGF-A, sFlt-1, PlGF, Tie-2, VEGF-D, VEGF-C, and basic fibroblast growth factor (bFGF) levels of male patients with MacTel 1 (n = 6, black dots) were compared with those of healthy age-matched male control subjects undergoing cataract extraction (n = 8, white dots). The levels of Tie-2, VEGF-C, and VEGF-D were below the detection threshold in some aqueous humor samples, explaining the lower number of represented values. Concentrations were compared between affected and control subjects using a Mann–Whitney *U* test. \**P* < 0.05; ns, not significant.

therapy by bevacizumab or ranibizumab did not improve the visual acuity on the long term, although it reduced leakage from telangiectasia in the nonproliferative form of the disease.<sup>29–33</sup>

In Coats disease, which belongs to the same spectrum of microvascular disorders as MacTel 1,<sup>5</sup> anti-VEGF agents have become an effective adjunct therapy in the management of retinal exudation.<sup>34–36</sup> Their clinical efficacy is supported by elevated VEGF levels in the subretinal fluid<sup>37</sup> and aqueous humor<sup>38</sup> of

eyes with Coats disease, as compared with control eyes from age-matched patients with rhegmatogenous retinal detachment or congenital cataract, respectively. Moreover, immune localization of VEGF and VEGF receptors were performed on enucleated eyes with advanced Coats disease<sup>39</sup> and showed that VEGF-A was expressed in vascular endothelial cells and macrophages and that VEGF-R2 (mediating angiogenesis after VEGF-A stimulation) was localized in endothelial cells lining abnormal vessels, but not

Table 3. Angiogenic Factors Levels in Aqueous Humors of Healthy Control Subjects and Patients With MacTel 1, Determined on a Multiarray Immunoassay

Concentrations, Mean $\pm$ SD	Control Subjects, pg/mL	MacTel 1, pg/mL	Fold Change, MacTel 1 vs. Control Subjects	<i>P</i> *
sFlt1	173.9 $\pm$ 71.17	755.9 $\pm$ 1050	$\times 4.3$	0.013
PlGF	2.1 $\pm$ 1.06	4.5 $\pm$ 2.62	$\times 2.2$	0.029
Tie-2	5.0 $\pm$ 3.73	18.7 $\pm$ 9.02	$\times 3.7$	0.019
VEGF-A	140.9 $\pm$ 44.01	187.3 $\pm$ 209.7	$\times 1.3$	0.950
VEGF-C	5.3 $\pm$ 5.63	13.2 $\pm$ 6.55	$\times 2.4$	0.110
VEGF-D	0.4 $\pm$ 0.40	6.8 $\pm$ 7.14	$\times 17.4$	0.049
bFGF	0.9 $\pm$ 0.65	3.9 $\pm$ 4.16	$\times 4.3$	0.060

\*Mann–Whitney test.

bFGF, basic fibroblast growth factor; ETDRS, Early Treatment Diabetic Retinopathy Study; SD, standard deviation; Tie-2, tyrosine kinase with immunoglobulin-2 and EGF-like domains.

VEGF-R1/Flt1 (mediating vascular permeabilization and cell migration and possibly modulating VEGF-R2 activation<sup>16</sup>) or VEGF-R3 (signaling lymphangiogenesis). In contrast to MacTel 1, these data indicate that the VEGF-A–mediated VEGF-R2 pathway is specifically activated in Coats disease, supporting the better response to bevacizumab or ranibizumab in Coats disease than in MacTel 1. Similarly, PlGF was not detected in 18 aqueous humors from patients with wet age-related macular degeneration,<sup>40</sup> supporting the efficacy of bevacizumab in wet age-related macular degeneration.

In contrast, the higher efficacy of aflibercept over specific anti-VEGF antibodies in patients with MacTel 1, previously reported<sup>14,15</sup> and observed in our case

series, suggest that the PlGF-mediated VEGF-R1/Flt1-pathway is involved in the pathophysiology of MacTel 1, leading to vascular abnormalities, such as telangiectasias, microaneurysms, and vascular tortuosity. This assumption is supported by the increased aqueous humor levels of PlGF in MacTel 1 eyes as compared with age-matched healthy control eyes.

In the healthy retina, the level of PlGF expression in endothelial cells is 100-fold higher than the expression of VEGF,<sup>41</sup> and VEGF-R1/Flt-1 is the major VEGF receptor expressed in endothelial cells and in pericytes.<sup>42</sup> In our previous experimental study, long-lasting overexpression of rat PlGF in the rat eye induced vascular tortuosity and aneurysmal dilation of retinal capillaries, without neovascularization.<sup>24</sup>

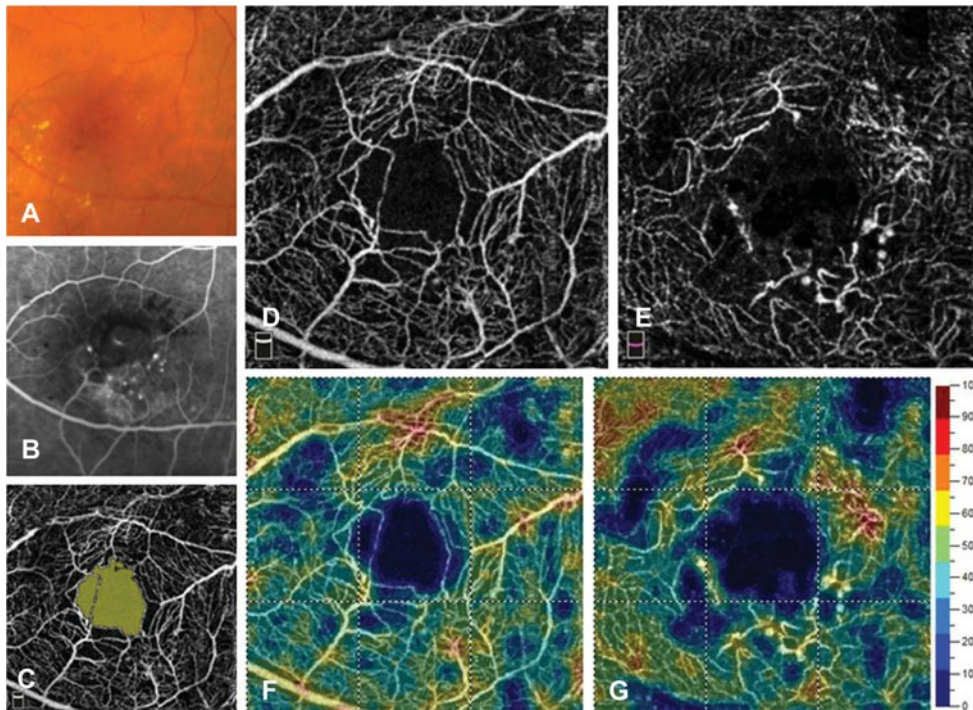


**Fig. 5.** Multimodal imaging in a 71-year-old male patient with MacTel 1 affecting his left eye (Case 1). **A.** Color fundus photograph showing telangiectatic microaneurysms and hard exudates. **B.** Early-frame fluorescein angiogram (1 minute after dye injection) and **(C)** identification of the foveal avascular zone area on a 3  $\times$  3-mm OCTA image. 3  $\times$  3-mm OCTA images of the superficial **(D)** and deep **(E)** capillary plexus used to assess the corresponding capillary densities **(F and G)**. The deep plexus shows pronounced capillary telangiectasis and microaneurysm formation in the inferotemporal macula.

Similarly, overactivation of the PIGF–VEGFR-1/Flt-1 pathway induced a substantial increase in the branching, tortuosity, and leakiness of vessels in different organs of rodent models, including skin,<sup>43</sup> and branches of the aorta.<sup>44</sup> Moreover, in MacTel 1 patients, macular edema results from vascular abnormalization and leakage without true neovascularization,<sup>3</sup> which is consistent with the nonelevated VEGF-A levels measured in their aqueous humor. Along with the telangiectasia, variably extended focal area of decreased perfusion is a classical finding in MacTel 1.<sup>2,3</sup> This observation was recently confirmed using OCTA.<sup>45</sup> Under these minimally ischemic conditions, PIGF could be a major player in the development of abnormal vessels, as shown here by the positive correlation between aqueous PIGF levels and the extension of capillary loss in the superficial and deep capillary plexus on OCTA. In addition, higher levels of the sFlt-1, which binds with a high affinity to both PIGF and VEGF-A,<sup>46</sup> were measured in MacTel 1 eyes, as compared with control eyes, indicating a possible counterregulatory increase in sFlt-1 in response to high PIGF levels. Levels of the soluble form of the angiopoietin receptor Tie-2 were also higher in MacTel 1 eyes. Interestingly, the Flt-1/VEGF signaling,<sup>47</sup> and the Ang-Tie2 signaling are involved in the loss of pericytes,<sup>48</sup> which could contribute to microaneurysm formation.<sup>42</sup>

The role of VEGF-A has also been questioned in other aneurysmal disorders affecting smaller or larger vessels. For instance, in abdominal aortic aneurysm, no significant difference in VEGF-A expression was demonstrated between the aortic wall of pathologic specimens and normal aortas from organ donors, but the expression of VEGF-C and VEGF-D was significantly increased in the abluminal layer of the aorta.<sup>49</sup> Moreover, the difference in angiogenic factor levels could affect the response to treatments, as in colorectal cancer where high circulating levels of VEGF-D are suspected to reduce the efficacy of bevacizumab therapy.<sup>50</sup> Remarkably, VEGF-D levels, but not VEGF-A levels, were significantly increased in the aqueous humor of MacTel 1 patients, suggesting that it may also contribute to abnormal retinal vessel dilation and to resistance to intravitreal bevacizumab.

A similar approach has been recently proposed by Noma et al,<sup>51,52</sup> who investigated the aqueous profile of angiogenic factors in retinal vein occlusions and found increased levels of VEGF-A, PIGF, and sFlt-1 compared with control eyes. Noticeably, microvascular remodeling causing secondary telangiectasia occur in retinal vein occlusions that may be PIGF mediated. In contrast to MacTel 1, macular

edema caused by vein occlusions respond favorably to bevacizumab,<sup>53,54</sup> ranibizumab,<sup>55,56</sup> or aflibercept<sup>57</sup> therapy, which may be linked to the relative elevation of both VEGF-A and PIGF in the ocular media of these patients.

The present study has several limitations, including the small sample size, because of the low prevalence of MacTel 1. The only way to increase the statistical power and significance would be to get more samples from MacTel 1 patients, which requires an inordinate amount of time and would hinder reporting of a worthwhile treatment. In addition, the follow-up duration was limited to 12 months, as a result of the recent availability of aflibercept, and we did not report the follow-up on OCTA for possible microvascular changes with aflibercept therapy, also the result of the recent availability of this imaging technology. Also, other angiogenic or inflammatory factors could have been assessed with the multiarray immunoassay experiment, but we focused on the major angiogenic factors and receptors of the VEGF family presumed to be involved in retinal vascular diseases.

In conclusion, we found that MacTel 1 patients with macular edema have higher aqueous humor levels of PIGF, but not VEGF-A, as compared with sex-matched and age-matched control subjects. Aflibercept, a neutralizer of both VEGF-A and PIGF, exerts beneficial anatomical and functional effects in these patients who did not show a good response to therapy other than aflibercept. To elucidate this effect and the observed angiogenic profile, a hypothesis suggesting PIGF–VEGFR-1/Flt-1 pathway activation in MacTel 1 was generated, which best explained the data. These results should be confirmed by larger prospective studies.

**Key words:** aflibercept, macular telangiectasia, retina.

### Acknowledgments

The authors thank Christina Stathopoulos and Cédric Mayer from Jules-Gonin Eye Hospital for clinical assistance and Catherine Fouda from the Department of Human Protein Science, University of Geneva for technical assistance in the multiarray immune assays.

### References

1. Gass JD, Oyakawa RT. Idiopathic juxtafoveolar retinal telangiectasis. *Arch Ophthalmol* 1982;100:769–780.
2. Gass JD, Blodi BA. Idiopathic juxtafoveolar retinal telangiectasis. Update of classification and follow-up study. *Ophthalmology* 1993;100:1536–1546.

3. Yannuzzi LA, Bardal AM, Freund KB, et al. Idiopathic macular telangiectasia. *Arch Ophthalmol* 2006;124:450–460.
4. Smithen LM, Brown GC, Brucker AJ, et al. Coats' disease diagnosed in adulthood. *Ophthalmology* 2005;112:1072–1078.
5. Cahill M, O'Keefe M, Acheson R, et al. Classification of the spectrum of Coats' disease as subtypes of idiopathic retinal telangiectasis with exudation. *Acta Ophthalmol Scand* 2001;79:596–602.
6. Gamulescu MA, Walter A, Sachs H, Helbig H. Bevacizumab in the treatment of idiopathic macular telangiectasia. *Graefes Arch Clin Exp Ophthalmol* 2008;246:1189–1193.
7. Koay CL, Chew FLM, Visvaraja S. Bevacizumab and type 1 idiopathic macular telangiectasia. *Eye (Lond)* 2011;25:1663–1665. author reply 1665.
8. Ciarnella A, Verrilli S, Fenicia V, et al. Intravitreal ranibizumab and laser photocoagulation in the management of idiopathic juxtafoveolar retinal telangiectasia type 1: a case report. *Case Rep Ophthalmol* 2012;3:298–303.
9. Rouvas A, Malamos P, Douvali M, et al. Twelve months of follow-up after intravitreal injection of ranibizumab for the treatment of idiopathic parafoveal telangiectasia. *Clin Ophthalmol* 2013;7:1357–1362.
10. Matsumoto Y, Yuzawa M. Intravitreal bevacizumab therapy for idiopathic macular telangiectasia. *Jpn J Ophthalmol* 2010;54:320–324.
11. Takayama K, Ooto S, Tamura H, et al. Intravitreal bevacizumab for type 1 idiopathic macular telangiectasia. *Eye (Lond)* 2010;24:1492–1497.
12. Moon BG, Kim YJ, Yoon YH, Lee JY. Use of intravitreal bevacizumab injections to treat type 1 idiopathic macular telangiectasia. *Graefes Arch Clin Exp Ophthalmol* 2012;250:1697–1699.
13. Loutfi M, Papathomas T, Kamal A. Macular oedema related to idiopathic macular telangiectasia type 1 treated with dexamethasone intravitreal implant (ozurdex). *Case Rep Ophthalmol Med* 2014;2014:231913.
14. Shibebe O, Vaze A, Gillies M, Gray T. Macular oedema in idiopathic macular telangiectasia type 1 responsive to aflibercept but not bevacizumab. *Case Rep Ophthalmol Med* 2014;2014:219792. 1.
15. Kovach JL, Hess H, Rosenfeld PJ. Macular telangiectasia type 1 managed with long-term aflibercept therapy. *Ophthalmic Surg Lasers Imaging Retina* 2016;47:593–595.
16. Autiero M, Waltenberger J, Communi D, et al. Role of PIGF in the intra- and intermolecular cross talk between the VEGF receptors Flt1 and Flk1. *Nat Med* 2003;9:936–943.
17. Fischer C, Jonckx B, Mazzone M, et al. Anti-PIGF inhibits growth of VEGF(R)-inhibitor-resistant tumors without affecting healthy vessels. *Cell* 2007;131:463–475.
18. Fan F, Samuel S, Gaur P, et al. Chronic exposure of colorectal cancer cells to bevacizumab promotes compensatory pathways that mediate tumour cell migration. *Br J Cancer* 2011;104:1270–1277.
19. Miyamoto N, de Kozak Y, Jeanny JC, et al. Placental growth factor-1 and epithelial haemato-retinal barrier breakdown: potential implication in the pathogenesis of diabetic retinopathy. *Diabetologia* 2007;50:461–470.
20. Rahimy E, Shahlaee A, Khan MA, et al. Conversion to aflibercept after prior anti-VEGF therapy for persistent diabetic macular edema. *Am J Ophthalmol* 2016;164:118–127.e2.
21. Papadopoulos N, Martin J, Ruan Q, et al. Binding and neutralization of vascular endothelial growth factor (VEGF) and related ligands by VEGF Trap, ranibizumab and bevacizumab. *Angiogenesis* 2012;15:171–185.
22. Fischer C, Mazzone M, Jonckx B, Carmeliet P. FLT1 and its ligands VEGFB and PIGF: drug targets for anti-angiogenic therapy? *Nat Rev Cancer* 2008;8:942–956.
23. Okamoto N, Tobe T, Hackett SF, et al. Transgenic mice with increased expression of vascular endothelial growth factor in the retina: a new model of intraretinal and subretinal neovascularization. *Am J Pathol* 1997;151:281–291.
24. Kowalczyk L, Touchard E, Omri S, et al. Placental growth factor contributes to micro-vascular abnormalization and blood-retinal barrier breakdown in diabetic retinopathy. *PLoS One* 2011;6:e17462.
25. Krohne TU, Liu Z, Holz FG, Meyer CH. Intraocular pharmacokinetics of ranibizumab following a single intravitreal injection in humans. *Am J Ophthalmol* 2012;154:682–686.
26. Moisseiev E, Waisbourd M, Ben-Artzi E, et al. Pharmacokinetics of bevacizumab after topical and intravitreal administration in human eyes. *Graefes Arch Clin Exp Ophthalmol* 2014;252:331–337.
27. Christoforidis JB, Williams MM, Kothandaraman S, et al. Pharmacokinetic properties of intravitreal I-124-aflibercept in a rabbit model using PET/CT. *Curr Eye Res* 2012;37:1171–1174.
28. Stewart MW, Rosenfeld PJ, Penha FM, et al. Pharmacokinetic rationale for dosing every 2 weeks versus 4 weeks with intravitreal ranibizumab, bevacizumab, and aflibercept (vascular endothelial growth factor Trap-eye). *Retina* 2012;32:434–457.
29. Charbel Issa P, Scholl HP, Holz FG. Short-term effects of intravitreal bevacizumab in type II idiopathic macular telangiectasia. *Retin Cases Brief Rep* 2007;1:189–191.
30. Charbel Issa P, Finger RP, Kruse K, et al. Monthly ranibizumab for nonproliferative macular telangiectasia type 2: a 12-month prospective study. *Am J Ophthalmol* 2011;151:876–886.
31. Do DV, Bressler SB, Cassard SD, et al. Ranibizumab for macular telangiectasia type 2 in the absence of subretinal neovascularization. *Retina* 2014;34:2063–2071.
32. Kupitz EH, Heeren TFC, Holz FG, Charbel Issa P. Poor long-term outcome of anti-vascular endothelial growth factor therapy in nonproliferative macular telangiectasia type 2. *Retina* 2015;35:2619–2626.
33. Roller AB, Folk JC, Patel NM, et al. Intravitreal bevacizumab for treatment of proliferative and nonproliferative type 2 idiopathic macular telangiectasia. *Retina* 2011;31:1848–1855.
34. Sigler EJ, Randolph JC, Calzada JJ, et al. Current management of Coats disease. *Surv Ophthalmol* 2014;59:30–46.
35. Gaillard MC, Mataftsi A, Balmer A, et al. Ranibizumab in the management of advanced Coats disease stages 3B and 4: long-term outcomes. *Retina* 2014;34:2275–2281.
36. Daruich A, Matet A, Tran HV, et al. Extramacular fibrosis in Coats' disease. *Retina* 2016;36:2022–2028.
37. Zhang H, Liu ZL. Increased nitric oxide and vascular endothelial growth factor levels in the aqueous humor of patients with Coats' disease. *Ocul Pharmacol Ther* 2012;28:397–401.
38. He YG, Wang H, Zhao B, et al. Elevated vascular endothelial growth factor level in Coats' disease and possible therapeutic role of bevacizumab. *Graefes Arch Clin Exp Ophthalmol* 2010;248:1519–1522.
39. Kase S, Rao NA, Yoshikawa H, et al. Expression of vascular endothelial growth factor in eyes with Coats' disease. *Invest Ophthalmol Vis Sci* 2013;54:57–62.
40. Muether PS, Neuhann I, Buhl C, et al. Intraocular growth factors and cytokines in patients with dry and neovascular age-related macular degeneration. *Retina* 2013;33:1809–1814.

41. Yonekura H, Sakurai S, Liu X, et al. Placenta growth factor and vascular endothelial growth factor B and C expression in microvascular endothelial cells and pericytes. Implication in autocrine and paracrine regulation of angiogenesis. *J Biol Chem* 1999;274:35172–35178.
42. Witmer AN, Vrensen GF, Van Noorden CJ, Schlingemann RO. Vascular endothelial growth factors and angiogenesis in eye disease. *Prog Retin Eye Res* 2003;22:1–29. Review.
43. Odorisio T, Schietroma C, Zaccaria ML, et al. Mice over-expressing placenta growth factor exhibit increased vascularization and vessel permeability. *J Cell Sci* 2002;115:2559–2567.
44. Kearney JB, Kappas NC, Ellerstrom C, et al. The VEGF receptor flt-1 (VEGFR-1) is a positive modulator of vascular sprout formation and branching morphogenesis. *Blood* 2004;103:4527–4535.
45. Matet A, Daruich A, Dirani A, et al. Macular telangiectasia type 1: capillary density and microvascular abnormalities assessed by optical coherence tomography angiography. *Am J Ophthalmol* 2016;167:18–30.
46. Shibuya M. Vascular endothelial growth factor receptor-1 (VEGFR-1/Flt-1): a dual regulator for angiogenesis. *Angiogenesis* 2006;9:225–230. discussion 231.
47. Cao R, Xue Y, Hedlund EM, et al. VEGFR1-mediated pericyte ablation links VEGF and PLGF to cancer-associated retinopathy. *Proc Natl Acad Sci U S A* 2010;107:856–861.
48. Cai J, Ruan Q, Chen ZJ, Han S. Connection of pericyte-angiopoietin-Tie-2 system in diabetic retinopathy: friend or foe? *Future Med Chem* 2012;4:2163–2176.
49. Wolanska M, Bankowska-Guszczyn E, Sobolewski K, Kowalewski R. Expression of VEGFs and its receptors in abdominal aortic aneurysm. *Int Angiol* 2015;34:520–528.
50. Weickhardt AJ, Williams DS, Lee CK, et al. Vascular endothelial growth factor D expression is a potential biomarker of bevacizumab benefit in colorectal cancer. *Br J Cancer* 2015;113:37–45.
51. Noma H, Mimura T, Yasuda K, Shimura M. Role of soluble vascular endothelial growth factor receptors-1 and -2, their ligands, and other factors in branch retinal vein occlusion with macular edema. *Invest Ophthalmol Vis Sci* 2014;55:3878–3885.
52. Noma H, Mimura T, Yasuda K, Shimura M. Role of soluble vascular endothelial growth factor receptor signaling and other factors or cytokines in central retinal vein occlusion with macular edema. *Invest Ophthalmol Vis Sci* 2015;56:1122–1128.
53. Ferrara DC, Koizumi H, Spaide RF. Early bevacizumab treatment of central retinal vein occlusion. *Am J Ophthalmol* 2007;144:864–871.
54. Priglinger SG, Wolf AH, Kreutzer TC, et al. Intravitreal bevacizumab injections for treatment of central retinal vein occlusion: six-month results of a prospective trial. *Retina* 2007;27:1004–1012.
55. Brown DM, Campochiaro PA, Singh RP, et al. Ranibizumab for macular edema following central retinal vein occlusion: six-month primary end point results of a phase III study. *Ophthalmology* 2010;117:1124–1133.e1.
56. Kinge B, Stordahl PB, Forsaa V, et al. Efficacy of ranibizumab in patients with macular edema secondary to central retinal vein occlusion: results from the sham-controlled ROCC study. *Am J Ophthalmol* 2010;150:310–314.
57. Heier JS, Clark WL, Boyer DS, et al. Intravitreal aflibercept injection for macular edema due to central retinal vein occlusion: two-year results from the COPERNICUS study. *Ophthalmology* 2014;121:1414–1420.e1.

**Supplementary Table 1.** Case-by-case values of angiogenic factor levels in aqueous humor, spectral-domain optical coherence tomography and optical coherence tomography angiography parameters, and visual acuity levels in six patients with macular telangiectasia type 1 who underwent aqueous humor tap.

Eye	Angiogenic factors levels in aqueous humor (pg/mL)							SD-OCT			OCT angiography			Baseline BCVA, ETDRS letter score
	sFlt-1	PlGF	Tie-2	VEGF-A	VEGF-C	VEGF-D	bFGF	Baseline central macular thickness, $\mu\text{m}$	Baseline area of hyporeflective cavities, $\times 10^{-3} \text{mm}^2$	Perifoveal density of superficial capillary plexus	Perifoveal density of deep capillary plexus	Foveal avascular zone area, $\text{mm}^2$		
1	418.05	3.79	22.41	12.16	5.03	U.D.	1.34	528	385.7	45.12	42.32	0.557	68	
2	432.49	6.83	16.78	571.91	U.D.	3.74	11.37	394	96.2	43.4	45.94	0.42	95	
3	353.38	8.60	25.98	100.86	20.95	1.79	2.23	348	277.4	38.61	39.04	1.098	48	
4	179.16	2.19	10.75	241.11	14.46	U.D.	0.79	396	535.9	52.83	57.97	0.199	99	
5	2890.88	2.39	29.94	11.47	12.49	15.01	6.33	595	761.4	50.6	48.49	0.603	83	
6	261.27	3.16	6.60	186.33	U.D.	U.D.	1.46	393	192.6	50.93	52.42	0.205	84	

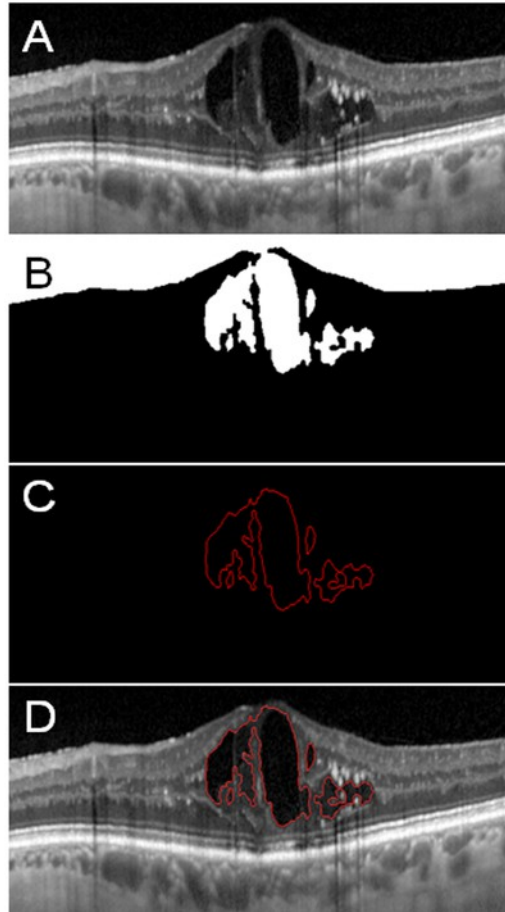
BCVA, Best-Corrected Visual Acuity; bFGF, basic Fibroblast Growth Factor; OCT, Optical Coherence Tomography; PlGF, Placental Growth Factor; SD-OCT, Spectral Domain OCT; sFlt1, soluble VEGF receptor 1; Tie-2, Tyrosine kinase with immunoglobulin-2 and EGF-like domains; U.D., Undetectable; VEGF, Vascular Endothelial Growth Factor

**Supplementary Table 2. Correlation between anatomical, functional and biological parameters in six patients with macular telangiectasia type 1.**

P-values ( <i>r</i> ) <sup>a</sup>	SD-OCT		OCT angiography			Baseline BCVA, ETDRS letters
	Baseline central macular thickness, $\mu\text{m}$	Baseline area of hyporeflective cavities, $\times 10^{-3} \text{ mm}^2$	Perifoveal density of superficial capillary plexus	Perifoveal density of deep capillary plexus	Foveal avascular zone area, $\text{mm}^2$	
sFlt-1, pg/ml	0.4	0.9	0.4	0.4	0.2	0.6
PlGF, pg/ml	0.2	0.2	0.03 ( $r = -0.89$ )	0.03 ( $r = -0.89$ )	0.2	0.2
Tie-2, pg/ml	0.5	0.4	0.2	0.2	0.03 ( $r = 0.89$ )	0.2
VEGF-A, pg/ml	0.4	0.2	0.6	0.6	0.2	0.14
VEGF-C, pg/ml	0.3	0.8	0.9	0.9	0.8	0.9
VEGF-D, pg/ml	0.3	1.0	0.3	0.3	1.0	1.0
bFGF, pg/ml	0.9	0.5	0.5	0.5	0.4	0.8
Baseline BCVA, ETDRS letters	0.8	0.9	0.06	0.06	0.03 ( $r = -0.89$ )	-

<sup>a</sup> Spearman rank correlation. The correlation coefficient *r* is indicated when *P*-values  $\leq 0.05$ .

OCT= optical coherence tomography; SD-OCT= spectral domain OCT; VEGF= vascular endothelial growth factor; sFlt1= soluble VEGF receptor 1; PlGF=placental growth factor; Tie-2= tyrosine kinase with immunoglobulin-2 and EGF-like domains; bFGF= basic fibroblast growth factor; BCVA= best-corrected visual acuity



**Supplemental Figure. Semi-automated method to detect intraretinal cysts on optical coherence tomography.** (Top) original horizontal B-scan spectral-domain optical coherence tomography through the fovea; (Middle top) detection of hyporeflective spaces by binary transformation; (Middle bottom) identification of boundaries of hyporeflective spaces, outlined in red; (Bottom) final image with cyst boundaries outlined in red, superimposed over the original B-scan.



[3c] Radiation maculopathy after proton beam therapy for uveal melanoma: optical coherence tomography angiography alterations influencing visual acuity. *Investigative Ophthalmology and Vision Science* 2017

Matet A, Daruich A, Zografos L<sup>31</sup>

doi: 10.1167/iovs.17-22324.

Contribution of PhD candidate:

- Processing and analysis of OCT and OCT angiography data
- Statistical analyses
- Interpretation of results
- Drafting the manuscript



# Radiation Maculopathy After Proton Beam Therapy for Uveal Melanoma: Optical Coherence Tomography Angiography Alterations Influencing Visual Acuity

Alexandre Matet, Alejandra Daruich, and Leonidas Zografos

Department of Ophthalmology, University of Lausanne, Jules-Gonin Eye Hospital, Fondation Asile des Aveugles, Lausanne, Switzerland

Correspondence: Alexandre Matet, Hôpital Ophtalmique Jules-Gonin, Fondation Asile des Aveugles, Avenue de France 15, CP 5143, 1002 Lausanne, Switzerland; alexmatet@gmail.com.

Submitted: May 31, 2017  
Accepted: July 4, 2017

Citation: Matet A, Daruich A, Zografos L. Radiation maculopathy after proton beam therapy for uveal melanoma: optical coherence tomography angiography alterations influencing visual acuity. *Invest Ophthalmol Vis Sci*. 2017;58:3851-3861. DOI:10.1167/iov.17-22324

**PURPOSE.** To analyze microvascular and structural changes in radiation maculopathy and their influence on visual acuity (VA), using optical coherence tomography (OCT) and OCT angiography (OCTA).

**METHODS.** This was a retrospective analysis of consecutive patients with radiation maculopathy, 12 months or more after proton-beam irradiation for uveal melanoma, imaged with fluorescein angiography, OCT, and OCTA. Clinical parameters potentially affecting VA were recorded, including OCTA-derived metrics: foveal avascular zone (FAZ) area, vascular density, and local fractal dimension of the superficial (SCP) and deep capillary plexuses (DCP). Nonirradiated fellow eyes served as controls.

**RESULTS.** Ninety-three patients were included. FAZ was larger, while SCP/DCP capillary density and local fractal dimension were lower in the 35 irradiated than in the 35 fellow eyes ( $P < 0.0001$ ). Microvascular alterations graded on fluorescein angiography (minimally damaged/disrupted/disorganized) were correlated to FAZ area and SCP/DCP density on OCTA ( $P < 0.01$ ). By univariate analysis, worse VA was associated to macular detachment at presentation ( $P = 0.024$ ), total macular irradiation ( $P = 0.0008$ ), higher central macular thickness (CMT) ( $P = 0.019$ ), higher absolute CMT variation ( $P < 0.0001$ ), cystoid edema ( $P = 0.030$ ), ellipsoid zone disruption ( $P = 0.002$ ), larger FAZ ( $P < 0.0001$ ), lower SCP ( $P = 0.001$ ) and DCP capillary density ( $P < 0.0001$ ), and lower SCP ( $P = 0.009$ ) and DCP local fractal dimension ( $P < 0.0001$ ). Two multivariate models with either capillary density or fractal dimension as covariate showed that younger age ( $P = 0.014/0.017$ ), ellipsoid zone disruption ( $P = 0.034/0.019$ ), larger FAZ ( $P = 0.0006/0.002$ ), and lower DCP density ( $P = 0.008$ ) or DCP fractal dimension ( $P = 0.012$ ), respectively, were associated with worse VA.

**CONCLUSIONS.** VA of eyes with radiation maculopathy is influenced by structural and microvascular factors identified with OCTA, including FAZ area and DCP integrity.

**Keywords:** melanoma, optical coherence tomography, radiation damage, image analysis, microcirculation

Radiation maculopathy is a devastating cause of visual impairment in eyes irradiated for intraocular tumors,<sup>1</sup> the most frequent indication being uveal melanoma. Currently, proton-beam therapy allows local tumor control and eye preservation in most cases. Yet, for tumors close to or involving the macula, visual acuity may be jeopardized by the irradiation of the macular microvasculature, leading to the development of radiation maculopathy. This delayed complication presents clinically with lipid exudates and hemorrhages on fundus examination, cystoid macular edema or macular thinning in end-stage disease on optical coherence tomography (OCT), and exudative telangiectasia with disrupted vascular network and nonperfusion areas on fluorescein angiography (FA).<sup>2</sup>

OCT angiography (OCTA) is a recent noninvasive technique visualizing the macular microvasculature via flow detection. Its advantages over FA are its higher resolution and reproducibility,<sup>3,4</sup> and its ability to segment capillary plexuses forming the macular microvasculature and their alterations. Since macular

capillaries are the primary site of injury in radiation maculopathy, OCTA is a powerful tool to investigate these pathologic changes. Moreover, the recent adjunction of quantitative tools to OCTA provides access to retinal microcirculatory metrics, such as foveal avascular zone (FAZ) dimensions,<sup>5,6</sup> capillary density,<sup>7,8</sup> and capillary network fractal dimension,<sup>9</sup> at the level of both plexuses. Fractal dimension is a promising endpoint to measure vascular network disorganization in OCTA images, which has been used successfully in diabetic retinopathy<sup>10-12</sup> and posterior uveitis.<sup>13</sup>

Ocular irradiation by I-125 plaque brachytherapy induces microvascular changes detected by OCTA.<sup>14,15</sup> However, the consequences of proton-beam therapy, a major treatment modality for uveal melanoma, have not been assessed by OCTA. In this study, we investigated the spectrum of structural and microvascular alterations in radiation maculopathy after proton-beam therapy for uveal melanoma, and their respective influence on visual acuity, using OCT and OCTA.



## METHODS

### Study Subjects

This observational case series adhered to the tenets of the Declaration of Helsinki and was approved by the local Ethics Committee (CER-VD No. 2016-01861). Medical records, OCT, OCTA, and FA images from consecutive subjects treated by proton-beam irradiation for uveal melanoma, and presenting with radiation maculopathy from August 2015 to July 2016, were retrospectively analyzed. Clinical records included systemic (sex, age, presence of hypertension or diabetes), tumor-related (largest diameter, height, localization, and presence of macular detachment at presentation), and treatment-related data (degree of macular irradiation, time since proton-beam therapy, and intravitreal anti-vascular endothelial growth factor [VEGF] treatment). At our institution, plaque brachytherapy is performed for anteriorly located choroidal tumors (located  $\geq 4$  mm from the macula) of limited thickness ( $\leq 5$  mm). In these cases, macular irradiation is very limited, and radiation maculopathy rarely develops. Therefore, only proton-beam-irradiated patients were included, to analyze the consequences of unavoidable macular irradiation. Proton-beam therapy was administered according to an individualized protocol established on the EyePlan software<sup>16</sup> (v3.06c), after implantation of tantalum clips.

Eyes with history of other retinal disease, those that had received proton therapy less than 12 months earlier, with low-quality OCTA acquisitions (signal strength index  $< 40$ ) or with severe motion artifacts, were excluded. When available, multimodal imaging acquired in the fellow nonirradiated eye, including OCTA, served as control.

### Multimodal Imaging

B-mode, en face OCT and OCTA images were acquired on Angiovue RTx 100 (Optovue, Inc., Fremont, CA, USA). The correct automatic segmentation providing OCTA images of the superficial and deep plexuses was visually controlled. Central macular thickness (CMT) was measured on OCT volumes in the central subfield of an adapted Early Treatment of Diabetic Retinopathy Study (ETDRS) grid centered on the fovea.

FA was performed on Spectralis (Heidelberg Engineering, Heidelberg, Germany). Early frames (20–30 seconds after dye injection) were acquired with a 30° lens. A 20 × 20° 97-section B-mode OCT raster scan was acquired on Spectralis.

### Capillary Network Density and Foveal Avascular Zone

The mean vascular density of 3 × 3-mm OCTA images centered on the fovea was obtained by using the built-in AngioAnalytics software of the RTx 100 device (v2016.1.0.26), at the level of the superficial and deep capillary plexuses.

The area of the FAZ was measured manually by two independent observers on masked OCTA images of the superficial capillary plexus, using ImageJ (v1.50c4, Wayne Rasband; <http://imagej.nih.gov/ij/>); provided in the public domain by the National Institutes of Health, Bethesda, MD, USA). Capillary vessels surrounding the FAZ were outlined by using the free contour function, to obtain the FAZ area in square millimeter (pixel-to-millimeter scale, 304:3). The mean from the two observers was retained.

### Local Fractal Dimension

The local fractal dimension, based on the box-counting method, was used to assess the degree of superficial and deep

plexus disorganization on 3 × 3-mm OCTA. This method relies on the self-similarity of a vascular network at different scales. It calculates the fractal dimension,  $D_f$ , such that the number  $N$  of boxes of increasing pixel size  $R$  needed to cover a fractal object in the image follows a power-law:  $D_f = \log(N)/\log(R)$ . For a two-dimensional image,  $D_f$  is between 1 and 2. If the object is fractal over a limited range of box size  $R$ , this property is reflected by the local fractal dimension,  $D_{f_{local}} = -d(\log(N))/d(\log(R))$ , corresponding to the local slope of the  $D_f$  function for a given box size range. If the  $D_{f_{local}}$  function is constant over a range of box sizes, then the image has a fractal behavior over these  $R$  values.

The local fractal dimension was estimated from the skeletonized 304 × 304-pixel .bmp image files exported by the OCTA software, by using a custom algorithm adapted from the “boxcount” program<sup>17</sup> on Matlab (R2015b; MathWorks, Inc., Natick, MA, USA). From preliminary assessments showing that capillary networks on OCTA images presented a quasi-fractal behavior for box sizes ranging from 2<sup>3</sup> to 2<sup>5</sup> (8 × 8 to 32 × 32 pixels), the local fractal dimension was calculated as the mean value of the  $D_{f_{local}}$  function over 2<sup>3</sup>-to-2<sup>5</sup>-pixel boxes in each OCTA image. Illustrations of the pixel grids used to calculate the local fractal dimension of skeletonized OCTA images are provided in Figures 1 and 2.

### Grading of Abnormal Features

Early-frame 30° fluorescein angiograms and OCTA images of the superficial and deep capillary plexuses were classified into three categories after qualitative evaluation of the macular microvasculature: minimally damaged (absent or minimal alterations), disrupted (focal interruptions of the perifoveal capillary ring), and disorganized (diffuse or multifocal capillary depletion).

OCT raster scans acquired on Spectralis were used to assess the presence of intraretinal cysts and ellipsoid zone disruption.

All OCT, FA, and OCTA gradings were performed by two independent observers (AM, AD). In case of discrepancy, images were adjudicated by the senior investigator (LZ).

### Statistical Analyses

Analyses were performed on Prism (version 5.0f; GraphPad Software, La Jolla, CA, USA), using the Wilcoxon test for paired comparisons, Pearson coefficients for correlations,  $\chi^2$ , or Fisher's test for contingency analysis, where appropriate. Interobserver agreement was estimated with the weighted Cohen's  $\kappa$  for FA, OCT, and OCTA gradings, and the intraclass correlation coefficient (ICC) for FAZ measurements, using the “irr” package<sup>18</sup> on R (v3.3.0 [2016]; R Foundation for Statistical Computing, Vienna, Austria). Clinical factors potentially influencing best-corrected visual acuity (BCVA) were investigated by using uni- and multivariate linear regression followed by stepwise forward regression, using the “MASS” package<sup>19</sup> on R. Variables with significance level  $\leq .2$  in the univariate analysis, without strong correlation with each other (Pearson  $r < 0.5$ ), were computed into the multivariate model. The logarithm of the minimal angle of resolution (logMAR) was used for BCVA calculations. For descriptive purposes, BCVA was categorized into discrete levels ( $\leq 20/200$ , 20/125–20/50, and  $\geq 20/40$ ).  $P$  values  $< 0.05$  were considered significant.

## RESULTS

Of 117 patients diagnosed with radiation maculopathy after receiving proton-beam irradiation for uveal melanoma, 14 were excluded owing to low OCTA image quality. The 93 included

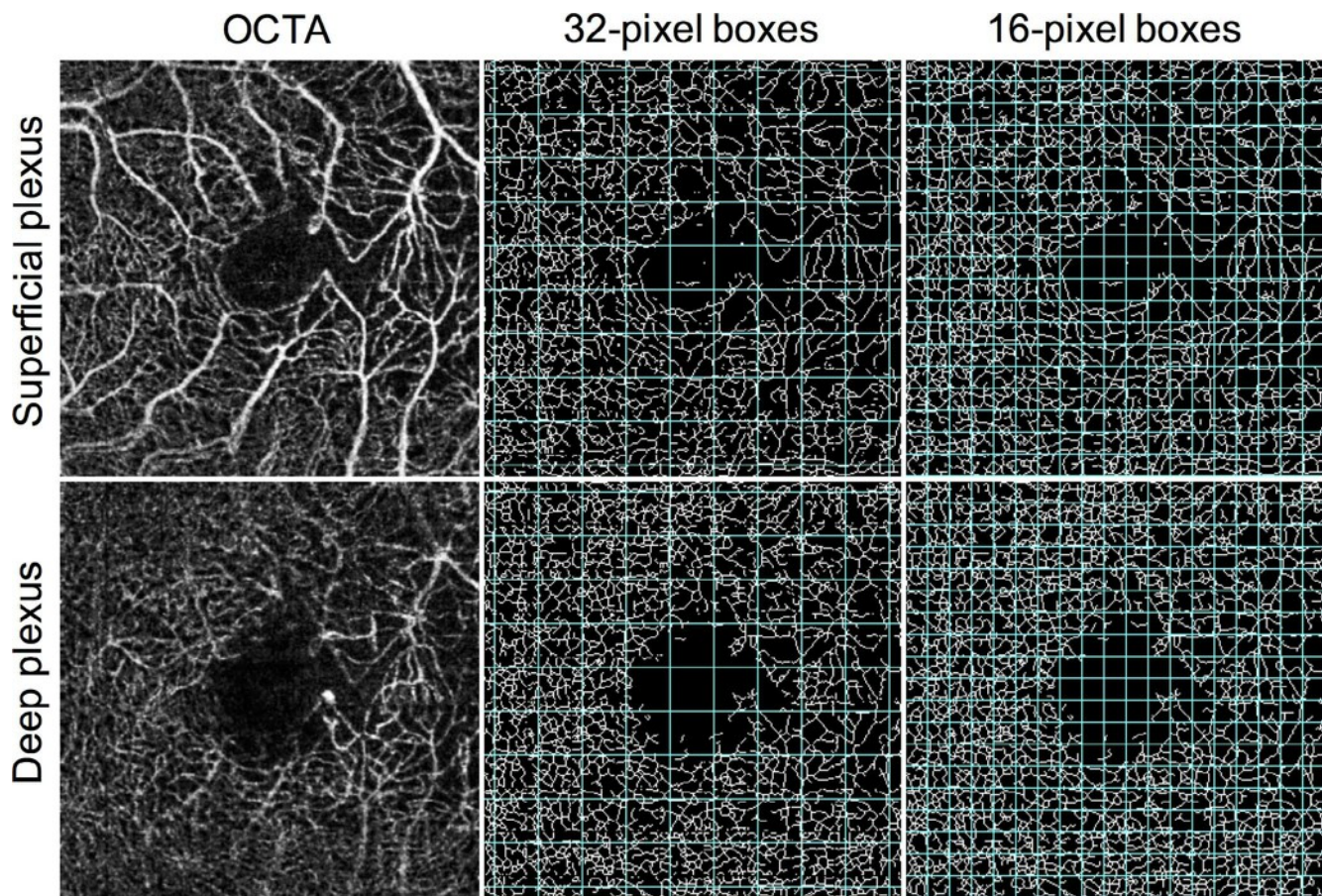


**FIGURE 1.** Determination of the local fractal dimension in optical coherence tomography images of a 49-year-old woman with moderately severe radiation maculopathy following proton-beam therapy for uveal melanoma. Best-corrected visual acuity was 20/30. The box-counting method was applied to the superficial (*top*) and deep (*bottom*) capillary plexuses. *Top* and *bottom left*, Original optical coherence tomography angiography images were skeletonized and superimposed with boxes of decreasing size: 32 pixels (*top* and *bottom middle*) and 16 pixels (*top* and *bottom right*), and 8 pixels (not shown). The number  $N$  of 32-, 16-, and 8-pixel boxes required to cover the vascular network was counted, and the local fractal dimension was estimated as the mean value of  $-d(\log(N))/d(\log(R))$ , where  $R$  is the box size in pixels. In this case, the local fractal dimension was 1.879 and 1.880 in the superficial and deep plexus, respectively.

patients (50 women, 43 men; mean age:  $61.4 \pm 12$  years [33–84 years]) presented a broad dispersion of BCVA levels in their irradiated eye, from hand motion to 20/20. BCVA was  $\leq 20/200$  in 33 eyes (36%), between 20/125 and 20/50 in 41 eyes (44%), and  $\geq 20/40$  in 19 eyes (20%). Mean duration since proton-beam treatment was  $3.8 \pm 2.7$  years (range, 1–15 years). According to treatment plans, all eyes received a collateral macular irradiation  $\geq 20$  Gy, and 43 eyes (46%) with posteriorly located melanomas received a full-dose macular irradiation. Clinical characteristics according to BCVA levels and overall descriptive characteristics are reported in Table 1 and Supplementary Table 1, respectively.

OCTA examination of the fellow eye was available in 35 subjects. OCTA-derived indicators of the macular microvasculature integrity in irradiated and nonirradiated fellow eyes are reported in Table 2. The FAZ was larger in irradiated than in fellow eyes ( $P < 0.0001$ ). Similarly, capillary density and capillary network local fractal dimension of the superficial and deep plexuses were lower in irradiated than in nonirradiated eyes ( $P < 0.0001$ ).

There was substantial agreement between raters for the qualitative grading of microvascular abnormalities on FA ( $\kappa = 0.63$ ) and OCTA ( $\kappa = 0.66$  and  $0.65$  for the superficial and deep plexus, respectively). There was an excellent agreement for the FAZ area (ICC = 0.99), and for the detection of intraretinal

cysts ( $\kappa = 0.94$ ) and ellipsoid zone disruption on OCT ( $\kappa = 0.86$ ).

Figure 3 illustrates the spectrum of structural and microvascular alterations observed in eyes with radiation maculopathy when using OCT, FA, and OCTA. The SCP and DCP imaged by OCTA were graded as minimally damaged in 35 and 16 eyes, disrupted in 42 and 47 eyes, and disorganized in 16 and 30 eyes, respectively. According to these categories, alterations were more severe in the deep than the superficial plexus ( $P = 0.003$ ). In 34 eyes (37%), alterations in the deep plexus were more severely graded than in the superficial plexus, while the inverse occurred in only five cases (5%) ( $P < 0.0001$ ).

OCT and OCTA findings according to BCVA levels are reported in Table 3. Since CMT may be abnormally increased or decreased in eyes with radiation maculopathy, depending on the presence of macular edema or thinning, the absolute change in CMT from the mean value observed in the 35 nonirradiated fellow eyes (261  $\mu\text{m}$ ) was considered as a clinical variable in the analysis.

A correlation analysis between OCTA-derived parameters revealed that qualitative grading (minimally damaged, disrupted, disorganized), vascular density, and local fractal dimension were positively correlated with each other in the SCP and DCP, and between both plexuses ( $P < 0.009$ ). The correlation was strongest between vascular density and local fractal dimension

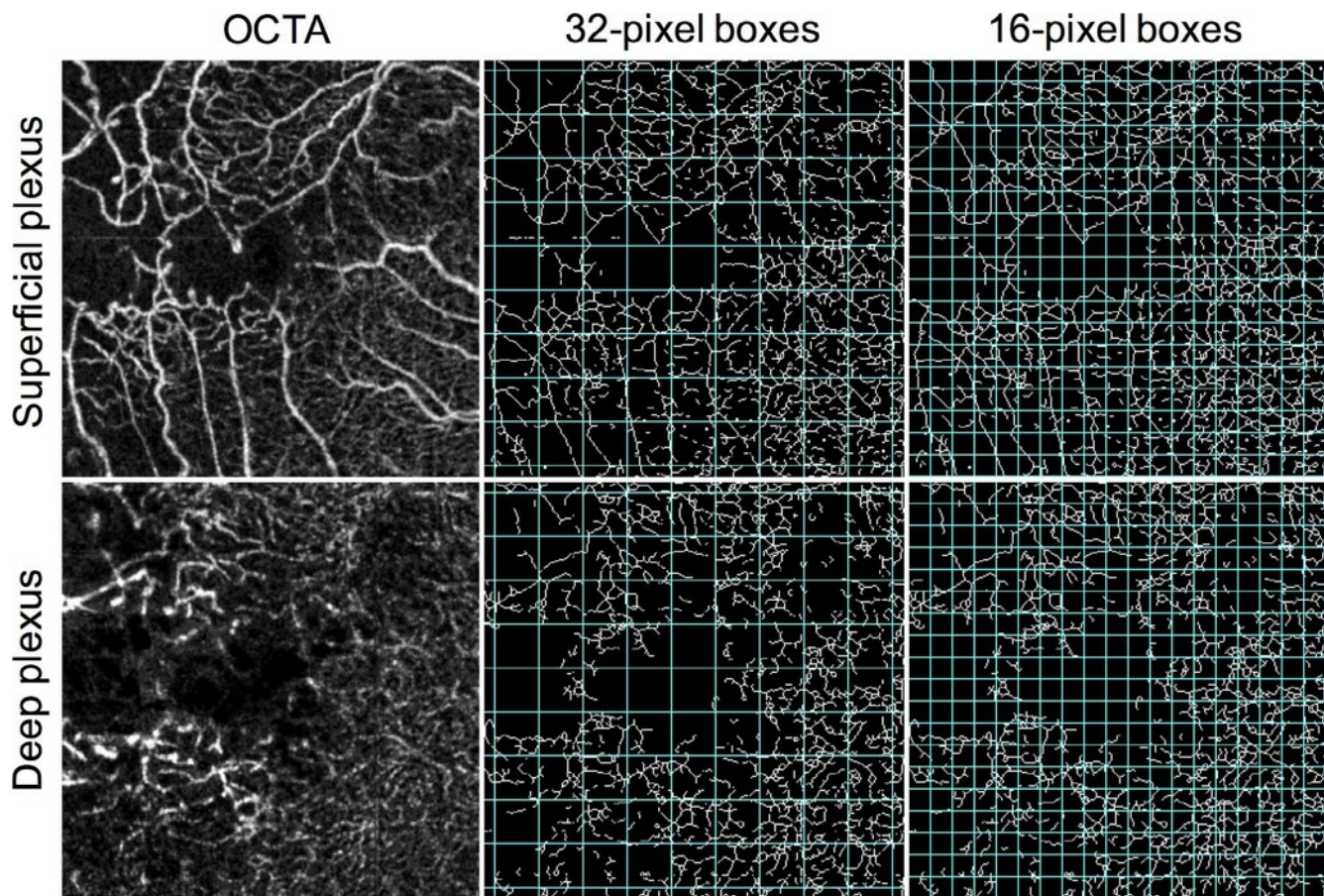


**FIGURE 2.** Determination of the local fractal dimension of optical coherence tomography images of a 70-year old man with severe radiation maculopathy following proton-beam therapy for uveal melanoma. Best-corrected visual acuity was 20/100. The box-counting method was applied to the superficial (*top*) and deep (*bottom*) capillary plexuses. *Top* and *bottom left*, Original optical coherence tomography angiography images were skeletonized and superimposed with boxes of decreasing size: 32 pixels (*top* and *bottom middle*), 16 pixels (*top* and *bottom right*), and 8 pixels (not shown). The number  $N$  of 32-, 16-, and 8-pixel boxes required to cover the vascular network was counted, and the local fractal dimension was estimated as the mean value of  $-\text{d}(\log(N))/\text{d}(\log(R))$ , where  $R$  is the box size in pixels. In this case, the local fractal dimension was 1.862 and 1.862 in the superficial and the deep plexus, respectively, lower than in the less severe case shown in Figure 1.

within each capillary plexus (Pearson  $r = 0.79$  and  $0.74$  in the superficial and deep plexuses, respectively). CMT and CMT absolute change on OCT were correlated to vascular density ( $P < 0.022$ ) and local fractal dimension ( $P < 0.0001$ ) in the deep plexus, but not the superficial plexus. The FAZ area was correlated with all OCT- and OCTA-derived metrics ( $P < 0.015$  and  $P < 0.009$ , respectively). Finally, the qualitative grading of

microvascular alteration on FA was correlated with CMT absolute change ( $P < 0.0001$ ) and all OCTA-derived metrics ( $P < 0.01$ ), except local fractal dimension. The detailed correlation matrix is reported in Table 4.

A series of uni- and multivariate analyses were conducted to investigate the influence of clinical and imaging parameters on BCVA. Results are reported in Table 5. Among clinical factors,

**TABLE 1.** Clinical and Multimodal Imaging Characteristics According to the Final Visual Acuity in 93 Patients Who Underwent Proton-Beam Therapy for Uveal Melanoma

Final BCVA, Snellen	$\leq 20/200$ ( $n = 33$ )	20/125–20/50 ( $n = 41$ )	$\geq 20/40$ ( $n = 19$ )
Sex, male/female, No.	18/15	19/22	6/13
Age, y	$55.7 \pm 11.4$	$65.4 \pm 10.3$	$62.5 \pm 13.1$
Tumor height, mm	$4.9 \pm 2.0$	$4.6 \pm 1.8$	$4.0 \pm 1.3$
Tumor distance to the fovea, disc diameter	$1.0 \pm 1.1$	$1.7 \pm 1.1$	$1.8 \pm 1.0$
Macular detachment at presentation, No. (%)	26 (79)	25 (61)	7 (37)
Total macular irradiation, No. (%)	23 (70)	17 (41)	3 (16)
Time since irradiation, y	$3.8 \pm 2.7$	$4.0 \pm 3.2$	$3.2 \pm 1.2$
Treatment by intravitreal anti-VEGF, No. (%)	9 (27)	18 (44)	7 (37)
Hypertension	13 (39%)	17 (41%)	6 (32%)
Diabetes	2 (6%)	4 (10%)	2 (11%)

Continuous quantitative values are reported as mean  $\pm$  standard deviation.

**TABLE 2.** Comparison of Optical Coherence Tomography Angiography-Derived Metrics of the Parafoveal Microvasculature Between 35 Eyes Treated With Proton-Beam Therapy for Uveal Melanoma, and Their Nonirradiated Fellow Eyes

OCTA Parameter	Irradiated Eyes ( <i>n</i> = 35)	Nonirradiated Fellow Eyes ( <i>n</i> = 35)	<i>P</i> Value†
Foveal avascular zone area,* × 10 <sup>-3</sup> mm <sup>2</sup>	1.373 ± 1.84 (0.139-7.125)	0.266 ± 0.113 (0.022-0.522)	<0.0001
Capillary density			
Superficial plexus	39.56 ± 5.23 (29.89-51.17)	52.67 ± 2.42 (48.87-58.19)	<0.0001
Deep plexus	45.19 ± 6.69 (23.43-58.41)	58.69 ± 2.23 (52.83-62.75)	<0.0001
Local fractal dimension			
Superficial plexus	1.828 ± 0.046 (1.715-1.896)	1.908 ± .007 (1.893-1.921)	<0.0001
Deep plexus	1.819 ± 0.099 (1.353-1.900)	1.902 ± .008 (1.885-1.924)	<0.0001

Values are provided as mean ± standard deviation (range).

\* Measured at the level of the superficial capillary plexus.

† Wilcoxon paired signed-rank test.

the univariate analysis identified macular detachment at presentation ( $P = 0.024$ ), tumor distance to the fovea ( $P = 0.001$ ), and total macular irradiation ( $P = 0.0008$ ) as associated with worse BCVA levels, while older age was near significantly associated with better BCVA levels ( $P = 0.068$ ). Among imaging factors, higher CMT ( $P = 0.019$ ), higher absolute CMT change ( $P < 0.0001$ ), presence of intraretinal cystoid edema ( $P = 0.030$ ) or ellipsoid zone disruption ( $P = 0.002$ ), larger FAZ area ( $P < 0.0001$ ), lower superficial ( $P = 0.001$ ) and deep capillary density ( $P < 0.0001$ ), and lower superficial ( $P = 0.009$ ) and deep local fractal dimension ( $P < 0.0001$ ) were all associated with worse BCVA levels. Since vascular density and local fractal dimension were strongly correlated in the superficial and deep plexuses (Pearson  $r = 0.79$  and  $0.74$ , respectively; Table 4), and therefore could not be entered simultaneously in a multivariate model, two separate models were computed with either vascular density or local fractal dimension as covariate. In the first model, younger age ( $P = 0.014$ ), presence of ellipsoid zone disruption ( $P = 0.034$ ), larger FAZ area ( $P = 0.0006$ ), and lower deep plexus vascular density ( $P = 0.008$ ) were associated with worse BCVA levels (adjusted  $R^2 = 0.44$ ). The second model yielded similar results, with younger age ( $P = 0.017$ ), presence of ellipsoid zone disruption ( $P = 0.019$ ), larger FAZ area ( $P = 0.002$ ), and lower deep plexus local fractal dimension ( $P = 0.012$ ) associated with worse BCVA levels (adjusted  $R^2 = 0.43$ ). In both models, neither tumor distance to the fovea nor total macular irradiation had a significant influence on BCVA.

## DISCUSSION

These results illustrate the variable alterations affecting the macula and its vasculature after proton-beam therapy for uveal melanoma, and how they influence visual function. All investigated OCTA-derived metrics were altered in irradiated eyes, as compared to fellow eyes. Visual acuity was independently influenced by larger FAZ area, lower deep plexus vascular density, and lower deep plexus local fractal dimension. Younger age and presence of ellipsoid zone disruption were also independently associated with worse vision. Moreover, tumor proximity to the fovea and total macular irradiation had a negative influence on visual acuity in the univariate, but not in the multivariate analysis, showing the unpredictable course of radiation maculopathy with respect to tumor- and treatment-related characteristics. Accordingly, Patel et al.<sup>20</sup> have reported that a proportion of eyes with uveal melanoma involving the fovea maintain good vision despite macular irradiation.

Signs of radiation maculopathy on fundus examination are detected in up to 89% of eyes with uveal melanoma within 3 years of proton-beam treatment.<sup>21</sup> Macular irradiation and

diabetes<sup>21</sup> are recognized as risk factors for radiation maculopathy. In uveal melanoma involving the fovea, smaller tumors and better baseline BCVA are identified as independent factors of better visual outcome.<sup>20</sup>

OCTA is particularly suitable to image microvascular changes such as capillary nonperfusion, telangiectasia, and FAZ alterations, hallmarks of radiation maculopathy.<sup>21-24</sup> However, no study has yet evaluated OCTA changes after proton-beam therapy, and their relationship with visual function. After plaque brachytherapy, Veverka et al.<sup>15</sup> describe gradual alterations of the macular microvasculature on OCTA. Shields et al.<sup>14</sup> have reported a decreased capillary density in both plexuses, as well as FAZ enlargement. Finally, Say et al.<sup>25</sup> have reported decreased capillary density in irradiated eyes without clinically patent maculopathy.

In the present study, we identified a relationship between radiation-induced microvascular changes on OCTA and visual function, using three different endpoints: FAZ area, automated built-in vascular density, and custom local fractal dimension of the vascular network. These endpoints reflect macular capillary network disorganization and consistently showed some degree of correlation with each other. The multivariate analysis confirmed that FAZ, deep plexus capillary density, and deep plexus local fractal dimension were associated with visual acuity. Noticeably, an observer-dependent grading of capillary network integrity was correlated to these morphologic parameters, illustrating the relevance of a clinical grading system based on OCTA in radiation maculopathy, as previously proposed.<sup>15</sup>

Although no study has yet compared vascular changes on OCTA following brachytherapy and proton-beam irradiation, a qualitative comparison of our findings with the detailed characteristics reported by Shields et al.<sup>14</sup> shows a comparable FAZ enlargement (1.12 vs. 1.25 mm<sup>2</sup>), after similar mean duration since irradiation (45.1 vs. 46 months). Authors have also reported vascular densities based on a custom method before it became standardized in OCTA devices, which prevents reliable comparison. Therefore, additional studies evaluating both modalities with standardized OCTA metrics are needed to compare their impact on retinal plexuses, and potentially identify predictive biomarkers of treatment outcome.

Interestingly, comparable results have been reported in other disorders presenting perifoveal capillary dropout. FAZ enlargement is related to worse vision in diabetic retinopathy and retinal vein occlusions.<sup>26,27</sup> Capillary density of both plexuses is correlated to visual loss in diabetic retinopathy,<sup>28</sup> branch retinal vein occlusion,<sup>29,30</sup> and idiopathic macular telangiectasia type 1 (MacTel1).<sup>31</sup> In addition, several investigators have shown that decreased perfusion is more frequent

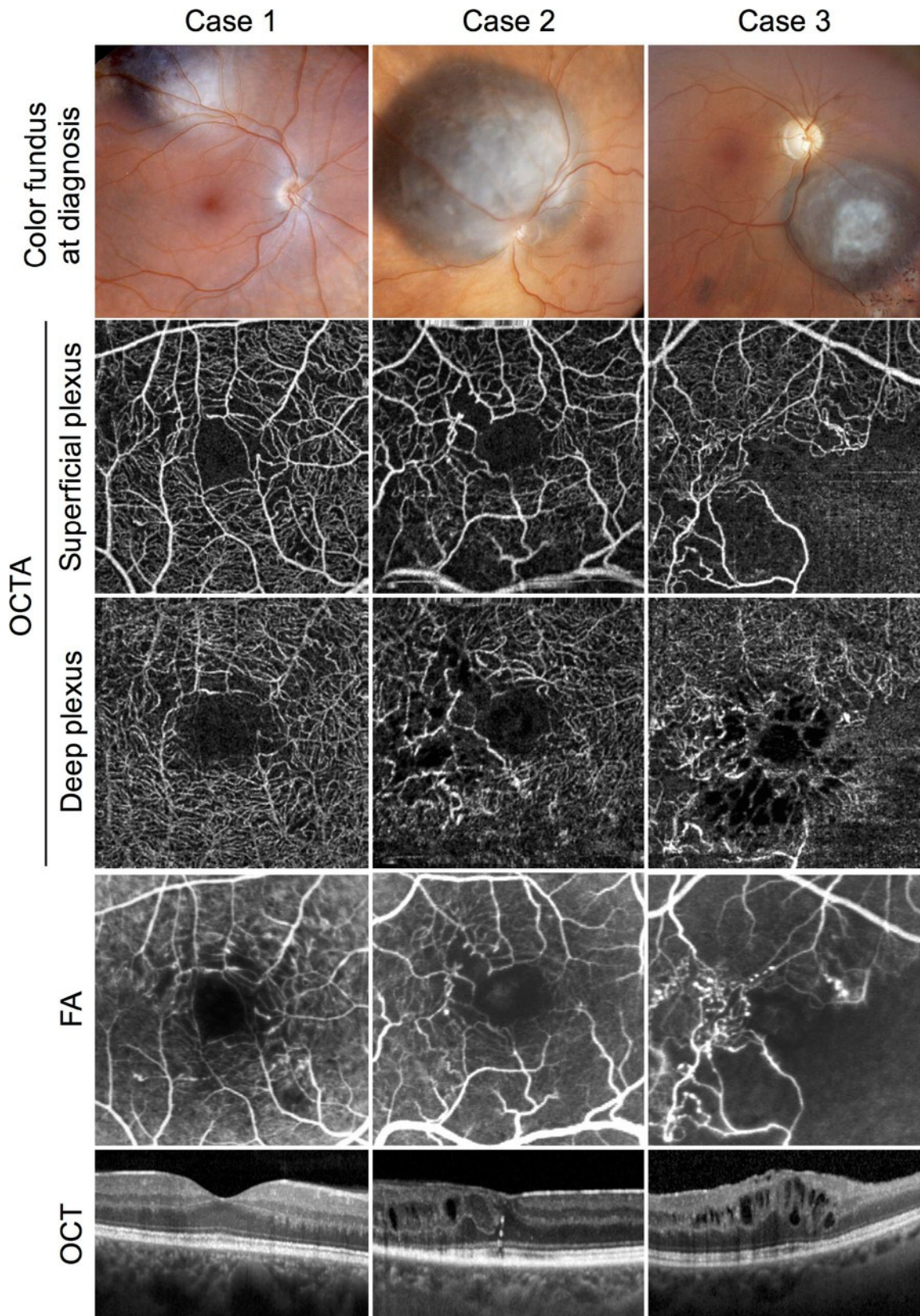


**FIGURE 3.** Spectrum of microvascular alterations in radiation maculopathy following proton-beam therapy for uveal melanoma visualized by multimodal imaging. Color fundus photograph at tumor diagnosis showing its localization with respect to the macula (*upper line*). Optical coherence tomography angiography of the superficial (*second line*) and deep (*third line*) capillary plexuses. Fluorescein angiogram 30 to 50 seconds after dye injection (*fourth line*) and horizontal foveal optical coherence tomography scan (*lower line*). Radiation maculopathy of variable severity was diagnosed in three subjects: a 47-year old man with minimally damaged superficial and deep plexuses (*left column*, case 1), a 67-year old man with disrupted superficial and deep plexuses (*middle column*, case 2), and a 63-year old woman with disorganized superficial and deep plexuses (*right column*, case 3).

**TABLE 3.** Optical Coherence Tomography and Optical Coherence Tomography Angiography Characteristics According to the Final Visual Acuity in 93 Patients Who Underwent Proton-Beam Therapy for Uveal Melanoma

Final BCVA, Snellen	≤20/200 (n = 33)	20/125–20/50 (n = 41)	≥20/40 (n = 19)
Central macular thickness, μm	323 ± 186	309 ± 104	286 ± 63
Central macular thickness absolute change,* μm	137 ± 140	81 ± 80	46 ± 49
Intraretinal cysts, No. (%)	19 (58)	20 (49)	6 (32)
Ellipsoid zone disruption, No. (%)	27 (82)	26 (63)	7 (37)
Foveal avascular zone area,† mm <sup>2</sup>	2.038 ± 1.953	0.697 ± 0.730	0.470 ± 0.505
SCP qualitative grading, No. (%)			
Minimally damaged	6 (18)	16 (39)	13 (68)
Disrupted	13 (39)	23 (56)	6 (32)
Disorganized	14 (43)	2 (5)	0 (0)
DCP qualitative grading, No. (%)			
Minimally damaged	2 (6)	3 (7)	11 (58)
Disrupted	7 (21)	32 (78)	8 (42)
Disorganized	24 (72)	6 (15)	0 (0)
SCP capillary density	37.0 ± 3.8	39.0 ± 4.8	42.8 ± 6.0
DCP capillary density	42.6 ± 6.7	44.8 ± 5.5	49.8 ± 4.9
SCP local fractal dimension	1.804 ± 0.047	1.817 ± 0.050	1.851 ± 0.048
DCP local fractal dimension	1.790 ± 0.106	1.827 ± 0.055	1.856 ± 0.042

Continuous quantitative values are reported as mean ± standard deviation.

\* Compared to a reference thickness of 261 μm, observed in 35 nonirradiated fellow eyes.

† Measured at the level of the superficial capillary plexus.

in the deep than superficial plexus, in central or branch vein occlusion,<sup>32–34</sup> diabetic retinopathy,<sup>35</sup> and MacTel1.<sup>36</sup> In resolved branch retinal vein occlusion, deep plexus nonperfusion has recently been identified as a more critical determinant of BCVA than superficial plexus nonperfusion.<sup>30</sup> Noticeably, vascular and structural alterations of radiation maculopathy present similarities with diabetic retinopathy, retinal vein occlusion, or MacTel1, including macular edema, microaneurysms, and capillary nonperfusion.

In the present study, OCTA revealed that the deep plexus of irradiated eyes was more severely altered than the superficial plexus. Consistently, Spaide<sup>36</sup> has reported one case of radiation maculopathy, using volume-rendering display, that showed alterations of both plexuses in the irradiated area, and adjacent areas of deep plexus nonperfusion colocalizing with macular edema. A similar pattern is visible in Figure 3, case 3. Whether deep plexus disruption is a cause or consequence of macular edema is not elucidated. Deep plexus alterations may impede the intake of interstitial fluid flow from the superficial to the deep plexus, leading to intraretinal fluid accumulation.<sup>36</sup> Deep plexus disruption could also result from tissue displacement by cystoid edema cavities, but the possibility of small interconnected capillaries forming this plexus to be stretched by edema is unlikely.<sup>35,36</sup> Finally, it could also result from shadowing or edema-related signal artifacts.<sup>33,36,37</sup> Here, the causal relationship between edema formation and deep plexus alteration was possibly indicated by the stronger correlation of CMT (and CMT change) with deep plexus changes, assessed by grading, vascular density, and local fractal dimension, than with superficial plexus changes (see Table 4). Importantly, this effect was controlled after statistical adjustment in the multivariate analysis, indicating that deep plexus abnormalities influence visual acuity independently from the presence of edema.

Several hypotheses could explain the greater radiosensitivity of deep plexus than superficial plexus capillaries. Microvascular radiation injury generates endothelial cell loss by impairing cell division, leading to progressive capillary closure and delayed-onset microangiopathy. This cytotoxic effect

results from “direct” DNA damage by radiation, which impairs cell division, and “indirect” free radical generation, which in turn induces DNA alterations.<sup>38</sup> Although endothelial cell turnover is slow,<sup>39</sup> an increasing fraction of endothelial cell population enters mitosis over the months following irradiation, triggering foci of endothelial damage and leading to microangiopathy.<sup>40</sup> Radiation-induced injury to retinal capillaries may also depend on other mechanisms than cell cycle disruption. The smaller-caliber deep plexus capillaries are more vulnerable to obturation by endothelial cell swelling, than larger superficial capillaries. Consistently, smaller capillaries are more radiosensitive than larger ones.<sup>41</sup> Another possibility would be the different nature of endothelial cells in the deep plexus, where capillaries form an interconnected, short-segment meshwork drained by small vortices.<sup>42</sup> In addition, the deep plexus is mainly composed of capillaries, unlike the superficial plexus formed by gradually smaller arterioles, capillaries, and progressively larger venules. Finally, deep plexus flow derives exclusively from the superficial plexus, so that deep plexus endothelial cells may receive a greater amount of downstream inflammatory or apoptotic signaling molecules from the upstream part of the superficial plexus after irradiation.

This study also identified younger age as an independent factor of worse visual outcomes in radiation maculopathy. Younger age has already been recognized as an independent risk factor for radiation maculopathy after plaque brachytherapy,<sup>43</sup> although this finding remains controversial.<sup>44</sup> As detailed above, radio-induced endothelial damage mostly results from apoptosis during cell division. Yet, endothelial cells become less proliferative with older age, undergoing fewer cellular divisions over time and ultimately not proliferating, a state called replicative senescence.<sup>45,46</sup> This effect of aging may explain the greater radiosensitivity of the macular microvasculature in younger subjects.

Ellipsoid zone disruption, indicating photoreceptor damage, was associated with worse visual outcomes after irradiation. Consistently, photoreceptor damage may result from long-standing macular edema, as observed here. Several factors not

TABLE 4. Correlation Between Multimodal Imaging Methods Assessing the Parafoveal Microvasculature in 93 Eyes Treated by Proton-Beam Therapy for Uveal Melanoma

P Value (Pearson <i>r</i> )	OCTA							
	Central Macular Thickness Change‡	Foveal Avascular Zone Area§	SCP Grading	DCP Grading	SCP Vascular Density	DCP Vascular Density	SCP Local Fractal Dimension	DCP Local Fractal Dimension
FA								
Degree of microvascular damage†	0.39	0.007 ( <i>r</i> = 0.42)	<0.0001 ( <i>r</i> = 0.54)	0.010 ( <i>r</i> = 0.27)	0.004 ( <i>r</i> = -0.28)	0.001 ( <i>r</i> = -0.30)	0.67	0.39
OCT								
Central macular thickness	<0.0001 ( <i>r</i> = 0.83)	0.015 ( <i>r</i> = 0.25)	0.24	0.005 ( <i>r</i> = 0.29)	0.53	0.022 ( <i>r</i> = -0.24)	0.56	<0.0001 ( <i>r</i> = -0.49)
Central macular thickness change‡		<0.0001 ( <i>r</i> = 0.09)	0.003 ( <i>r</i> = 0.30)	0.0002 ( <i>r</i> = 0.38)	0.66	0.001 ( <i>r</i> = -0.33)	0.14	<0.0001 ( <i>r</i> = -0.56)
OCTA								
Foveal avascular zone area§			<0.0001 ( <i>r</i> = 0.54)	<0.0001 ( <i>r</i> = 0.40)	0.008 ( <i>r</i> = -0.27)	0.009 ( <i>r</i> = -0.27)	0.005 ( <i>r</i> = -0.29)	0.001 ( <i>r</i> = -0.34)
SCP grading				<0.0001 ( <i>r</i> = 0.57)	0.002 ( <i>r</i> = -0.32)	<0.0001 ( <i>r</i> = -0.40)	0.003 ( <i>r</i> = -0.30)	0.0003 ( <i>r</i> = -0.37)
DCP grading				0.002 ( <i>r</i> = -0.31)	0.0004 ( <i>r</i> = -0.36)	0.0004 ( <i>r</i> = -0.36)	0.003 ( <i>r</i> = -0.31)	0.001 ( <i>r</i> = -0.34)
SCP vascular density					<0.0001 ( <i>r</i> = 0.62)	<0.0001 ( <i>r</i> = 0.79)	<0.0001 ( <i>r</i> = 0.79)	0.001 ( <i>r</i> = 0.33)
DCP vascular density							<0.0001 ( <i>r</i> = 0.56)	<0.0001 ( <i>r</i> = 0.74)
SCP local fractal dimension								<0.0001 ( <i>r</i> = 0.50)

\* Pearson *r* values are reported if *P* < 0.05.

† Graded as minimal, moderate, or severe.

‡ Compared to a reference thickness of 261 μm, observed in 35 nonirradiated fellow eyes.

§ Measured on optical coherence tomography images of the superficial capillary plexus.

|| Graded as minimally damaged, disrupted, or disorganized.

**TABLE 5.** Factors Influencing Best-Corrected Visual Acuity in 93 Patients Who Underwent Proton-Beam Therapy for Uveal Melanoma, Assessed by Univariate Analysis

	Multivariate					
	Univariate		Model 1 With Capillary Density		Model 2 With Local Fractal Dimension	
	Coefficient (Standard Error)	P Value‡	Coefficient (Standard Error)	P Value§	Coefficient (Standard Error)	P Value§
Clinical parameters						
Male sex	0.18 (0.12)	0.14	-	-	-	-
Age, by 10-y intervals	-0.09 (0.05)	0.068	-0.11 (0.04)	0.014	-0.11 (0.04)	0.017
Hypertension	0.06 (0.13)	0.63	-	-	-	-
Diabetes	-0.19 (0.22)	0.40	-	-	-	-
Tumor height > 5 mm	0.17 (0.13)	0.18	-	-	-	-
Tumor distance to fovea, DD	-0.18 (0.05)	0.001	-	-	-	-
Macular detachment at presentation	0.29 (0.13)	0.024	-	-	-	-
Total macular irradiation	0.47 (0.13)	0.0008	-	-	-	-
Time since irradiation, by 1-y intervals	0.02 (0.02)	0.38	-	-	-	-
OCT and OCTA parameters						
Central macular thickness, by 50 $\mu$ m	0.05 (0.02)	0.019	-	-	-	-
Central macular thickness absolute change,* by 10- $\mu$ m intervals	0.03 (0.01)	<0.0001	-	-	-	-
Intraretinal cysts	0.27 (0.12)	0.030	-	-	-	-
Ellipsoid zone disruption	0.40 (0.12)	0.002	0.26 (0.12)	0.034	0.30 (0.12)	0.019
Foveal avascular zone area†	0.22 (0.04)	<0.0001	0.13 (0.04)	0.0006	0.13 (0.04)	0.002
Capillary density, SCP	-0.04 (0.01)	0.001	-	-	x	x
Capillary density, DCP	-0.04 (-0.01)	<0.0001	-0.03 (0.01)	0.008	x	x
Local fractal dimension, SCP	-3.18 (1.19)	0.009	x	x	-	-
Local fractal dimension, DCP	-3.19 (0.72)	<0.0001	x	x	-1.81 (0.71)	0.012

Visual outcome was represented by visual acuity converted to the logarithm of minimal angle of resolution. DD, disc diameter.

\* Compared to a reference thickness of 261  $\mu$ m, observed in 35 nonirradiated fellow eyes.

† Measured at the level of the superficial capillary plexus.

‡ Univariate linear regression, with best-corrected visual acuity as outcome (logarithm of the minimum angle of resolution).

§ Multivariate generalized linear model, with best-corrected visual acuity as outcome (logarithm of the minimum angle of resolution). Capillary density and local fractal dimension of both plexuses were computed in two separate models owing to their strong correlation. Adjusted  $R^2 = 0.44$  (model 1) and 0.43 (model 2).

influencing the visual outcome were also identified. Treatment by anti-VEGF did not modify the visual outcome because at the time of OCTA examination it had been administered mostly as prophylaxis to reduce the risk of secondary neovascularization, as previously reported.<sup>47</sup> The few number of eyes that received anti-VEGF because of macular edema had lower BCVA, inducing a selection bias. Recent data suggest that prophylactic bimonthly anti-VEGF therapy may contribute to vision retention after proton-beam therapy for tumors close to the macula.<sup>48</sup> Further studies are needed to address the exact effect of anti-VEGF agents on radio-induced OCTA features.

In this report, local fractal dimension was used to assess superficial and deep plexus disorganization in OCTA images. Fractal dimension has previously been used to investigate the retinal microvasculature in fundus<sup>49-52</sup> or OCTA<sup>10,12,13</sup> images. By evaluating pattern repetition at different scales,<sup>53</sup> fractal dimension is particularly adapted to assess the integrity of arborized vascular networks. However, the retinal vasculature does not follow a perfect fractal behavior at all scales. Therefore, the "local" fractal dimension, limiting the fractal analysis to a given scale range, as illustrated in Figures 1 and 2, may provide a reliable indicator of fractal behavior of the macular capillary network on OCTA.

This study had limitations, including its retrospective design and the use of the recent OCTA technology that lacks consensual terminology<sup>54</sup> and processing tools. Moreover, artifacts in OCTA acquisition and interpretation may alter the results, although low-quality images were discarded. Say et al.<sup>55</sup>

have provided a comprehensive list of potential artifacts in OCTA imaging of irradiated eyes and shown that they were more frequent in eyes with worse visual function.

Overall, these results identified structural and microvascular factors contributing to the visual outcome of eyes with radiation maculopathy. Although FA remains the gold standard for the diagnosis and prognosis of radiation maculopathy, OCTA-derived quantitative metrics may offer promising tools. Future studies should evaluate the role of OCTA in predicting treatment response in radiation maculopathy.

### Acknowledgments

The authors thank Marc Curchod and Laureen Vallat, MSc (Jules-Gonin Eye Hospital, Fondation Asile des Aveugles, Lausanne, Switzerland) for technical assistance; Alessia Pica, MD (Paul-Scherer Institute, Villigen, Switzerland) and Francine Behar-Cohen, MD, PhD (INSERM and Université Paris Descartes, Paris, France, and University of Lausanne, Switzerland) for fruitful discussions.

Supported by the Faculty of Biology and Medicine Research Commission Fund, University of Lausanne, Switzerland (AM).

Disclosure: **A. Matet**, None; **A. Daruich**, None; **L. Zografos**, None

### References

- Giuliari GP, Sadaka A, Hinkle DM, Simpson ER. Current treatments for radiation retinopathy. *Acta Oncol.* 2011;50:6-13.

2. Reichstein D. Current treatments and preventive strategies for radiation retinopathy. *Curr Opin Ophthalmol*. 2015;26:157-166.
3. Nagiel A, Sadda SR, Sarraf D. A promising future for optical coherence tomography angiography. *JAMA Ophthalmol*. 2015;133:629-630.
4. Jia Y, Bailey ST, Hwang TS, et al. Quantitative optical coherence tomography angiography of vascular abnormalities in the living human eye. *Proc Natl Acad Sci U S A*. 2015;112:E2395-E2402.
5. Hwang TS, Jia Y, Gao SS, et al. Optical coherence tomography angiography features of diabetic retinopathy. *Retina*. 2015;35:2371-2376.
6. Freiberg FJ, Pfau M, Wons J, Wirth MA, Becker MD, Michels S. Optical coherence tomography angiography of the foveal avascular zone in diabetic retinopathy. *Graefes Arch Clin Exp Ophthalmol*. 2016;254:1051-1058.
7. Agemy SA, Scripsema NK, Shah CM, et al. Retinal vascular perfusion density mapping using optical coherence tomography angiography in normals and diabetic retinopathy patients. *Retina*. 2015;35:2353-2363.
8. Shahlaee A, Samara WA, Hsu J, et al. In vivo assessment of macular vascular density in healthy human eyes using optical coherence tomography angiography. *Am J Ophthalmol*. 2016;165:39-46.
9. Gadde SGK, Anegondi N, Bhanushali D, et al. Quantification of vessel density in retinal optical coherence tomography angiography images using local fractal dimension. *Invest Ophthalmol Vis Sci*. 2016;57:246-252.
10. Zahid S, Dolz-Marco R, Freund KB, et al. Fractal dimensional analysis of optical coherence tomography angiography in eyes with diabetic retinopathy. *Invest Ophthalmol Vis Sci*. 2016;57:4940-4947.
11. Bhanushali D, Anegondi N, Gadde SGK, et al. Linking retinal microvasculature features with severity of diabetic retinopathy using optical coherence tomography angiography. *Invest Ophthalmol Vis Sci*. 2016;57:519-525.
12. Kim AY, Chu Z, Shahidzadeh A, Wang RK, Puliafito CA, Kashani AH. Quantifying microvascular density and morphology in diabetic retinopathy using spectral-domain optical coherence tomography angiography. *Invest Ophthalmol Vis Sci*. 2016;57:OCT362-OCT370.
13. Kim AY, Rodger DC, Shahidzadeh A, et al. Quantifying retinal microvascular changes in uveitis using spectral-domain optical coherence tomography angiography. *Am J Ophthalmol*. 2016;171:101-112.
14. Shields CL, Say EAT, Samara WA, Khoo CTL, Mashayekhi A, Shields JA. Optical coherence tomography angiography of the macula after plaque radiotherapy of choroidal melanoma: comparison of irradiated versus nonirradiated eyes in 65 patients. *Retina*. 2016;36:1493-1505.
15. Veverka KK, Abouchehade JE, Iezzi R, Pulido JS. Noninvasive grading of radiation retinopathy the use of optical coherence tomography angiography. *Retina*. 2015;35:2400-2410.
16. Goitein M, Miller T. Planning proton therapy of the eye. *Med Phys*. 1983;10:275-283.
17. Moisy F. Boxcount: fractal dimension using the "box-counting" method for 1D, 2D and 3D sets. Available at: <https://ch.mathworks.com/matlabcentral/fileexchange/13063-boxcount/content/boxcount/html/demo.html>. Published 2008. Accessed March 18, 2017.
18. Cohen J. A coefficient of agreement for nominal scales. *Educ Psychol Meas*. 1960;20:37-46.
19. Venables WN, Ripley BD. *Modern Applied Statistics With S*. 4th ed. New York: Springer; 2002.
20. Patel AV, Lane AM, Morrison MA, et al. Visual outcomes after proton beam irradiation for choroidal melanomas involving the fovea. *Ophthalmology*. 2016;123:369-377.
21. Guyer DR, Mukai S, Egan KM, Seddon JM, Walsh SM, Gragoudas ES. Radiation maculopathy after proton beam irradiation for choroidal melanoma. *Ophthalmology*. 1992;99:1278-1285.
22. Gass JD. A fluorescein angiographic study of macular dysfunction secondary to retinal vascular disease, VI: X-ray irradiation, carotid artery occlusion, collagen vascular disease, and vitritis. *Arch Ophthalmol*. 1968;80:606-617.
23. Hayreh SS. Post-radiation retinopathy: a fluorescence fundus angiographic study. *Br J Ophthalmol*. 1970;54:705-714.
24. Brown GC, Shields JA, Sanborn G, Augsburger JJ, Savino PJ, Schatz NJ. Radiation retinopathy. *Ophthalmology*. 1982;89:1494-1501.
25. Say EAT, Samara WA, Khoo CTL, et al. Parafoveal capillary density after plaque radiotherapy for choroidal melanoma: analysis of eyes without radiation maculopathy. *Retina*. 2016;36:1670-1678.
26. Balaratnasingam C, Inoue M, Ahn S, et al. Visual acuity is correlated with the area of the foveal avascular zone in diabetic retinopathy and retinal vein occlusion. *Ophthalmology*. 2016;123:2352-2367.
27. Casselholmde Salles M, Kvanta A, Amrén U, Epstein D. Optical coherence tomography angiography in central retinal vein occlusion: correlation between the foveal avascular zone and visual acuity. *Invest Ophthalmol Vis Sci*. 2016;57:OCT242-OCT246.
28. Samara WA, Shahlaee A, Adam MK, et al. Quantification of diabetic macular ischemia using optical coherence tomography angiography and its relationship with visual acuity. *Ophthalmology*. 2016;124:235-244.
29. Samara WA, Shahlaee A, Sridhar J, Khan MA, Ho AC, Hsu J. Quantitative optical coherence tomography angiography features and visual function in eyes with branch retinal vein occlusion. *Am J Ophthalmol*. 2016;166:76-83.
30. Wakabayashi T, Sato T, Hara-Ueno C, et al. Retinal microvasculature and visual acuity in eyes with branch retinal vein occlusion: imaging analysis by optical coherence tomography angiography. *Invest Ophthalmol Vis Sci*. 2017;58:2087-2094.
31. Matet A, Daruich A, Dirani A, Ambresin A, Behar-Cohen F. Macular telangiectasia type 1: capillary density and microvascular abnormalities assessed by optical coherence tomography angiography. *Am J Ophthalmol*. 2016;167:18-30.
32. Adhi M, Filho MAB, Louzada RN, et al. Retinal capillary network and foveal avascular zone in eyes with vein occlusion and fellow eyes analyzed with optical coherence tomography angiography. *Invest Ophthalmol Vis Sci*. 2016;57:OCT486-OCT494.
33. Coscas F, Glacet-Bernard A, Miere A, et al. Optical coherence tomography angiography in retinal vein occlusion: evaluation of superficial and deep capillary plexa. *Am J Ophthalmol*. 2016;161:160-171.e2.
34. Rispoli M, Savastano MC, Lumbroso B. Capillary network anomalies in branch retinal vein occlusion on optical coherence tomography angiography. *Retina*. 2015;35:2332-2338.
35. Mané V, Dupas B, Gaudric A, et al. Correlation between cystoid spaces in chronic diabetic macular edema and capillary nonperfusion detected by optical coherence tomography angiography. *Retina*. 2016;36:S102-S110.
36. Spaide RE. Retinal vascular cystoid macular edema: review and new theory. *Retina*. 2016;36:1823-1842.
37. Couturier A, Mané V, Bonnini S, et al. Capillary plexus anomalies in diabetic retinopathy on optical coherence tomography. *Retina*. 2015;35:2384-2391.
38. Horgan N, Shields CL, Mashayekhi A, Shields JA. Classification and treatment of radiation maculopathy. *Curr Opin Ophthalmol*. 2010;21:233-238.
39. Engerman RL, Pfaffenbach D, Davis MD. Cell turnover of capillaries. *Lab Invest*. 1967;17:738-743.

40. Archer DB, Gardiner TA. Ionizing radiation and the retina. *Curr Opin Ophthalmol*. 1994;5:59-65.
41. Dimitrievich GS, Fischer-Dzoga K, Griem ML. Radiosensitivity of vascular tissue, I: differential radiosensitivity of capillaries: a quantitative in vivo study. *Radiat Res*. 1984;99:511-535.
42. Bonnin S, Mané V, Couturier A, et al. New insight into the macular deep vascular plexus imaged by optical coherence tomography. *Retina*. 2015;35:2347-2352.
43. Krema H, Xu W, Payne D, Maria Vasquez L, Pavlin CJ, Simpson R. Factors predictive of radiation retinopathy post 125Iodine brachytherapy for uveal melanoma. *Can J Ophthalmol*. 2011;46:158-163.
44. Aziz HA, Singh N, Bena J, Wilkinson A, Singh AD. Vision loss following episcleral brachytherapy for uveal melanoma: development of a vision prognostication tool. *JAMA Ophthalmol*. 2016;134:615-620.
45. Vasa M, Breitschopf K, Zeiher AM, Dimmeler S. Nitric oxide activates telomerase and delays endothelial cell senescence. *Circ Res*. 2000;87:540-542.
46. Minamino T, Miyauchi H, Yoshida T, Ishida Y, Yoshida H, Komuro I. Endothelial cell senescence in human atherosclerosis. *Circulation*. 2002;105:1541-1544.
47. Mantel I, Schalenbourg A, Bergin C, Petrovic A, Weber DC, Zografos L. Prophylactic use of bevacizumab to avoid anterior segment neovascularization following proton therapy for uveal melanoma. *Am J Ophthalmol*. 2014;158:693-701.e2.
48. Kim IK, Lane AM, Jain P, Awh C, Gragoudas ES. Ranibizumab for the prevention of radiation complications in patients treated with proton beam irradiation for choroidal melanoma. *Trans Am Ophthalmol Soc*. 2016;114:T2.
49. Daxer A. Characterisation of the neovascularisation process in diabetic retinopathy by means of fractal geometry: diagnostic implications. *Graefes Arch Clin Exp Ophthalmol*. 1993;681-686.
50. Thomas GN, Ong SY, Tham YC, et al. Measurement of macular fractal dimension using a computer-assisted program. *Invest Ophthalmol Vis Sci*. 2014;55:2237-2243.
51. Cheung N, Donaghue KC, Liew G, et al. Quantitative assessment of early diabetic retinopathy using fractal analysis. *Diabetes Care*. 2009;32:106-110.
52. Williams MA, McGowan AJ, Cardwell CR, et al. Retinal microvascular network attenuation in Alzheimer's disease. *Alzheimers Dement (Amst)*. 2015;1:229-235.
53. Mandelbrot B. How long is the coast of Britain: statistical self-similarity and fractional dimension. *Science*. 1967;156:636-638.
54. Fawzi AA. Consensus on optical coherence tomographic angiography nomenclature. *JAMA Ophthalmol*. 2017;135:377-378.
55. Say EAT, Ferenczy S, Magrath GN, Samara WA, Khoo CTL, Shields CL. Image quality and artifacts on optical coherence tomography angiography: comparison of pathologic and paired fellow eyes in 65 patients with unilateral choroidal melanoma treated with plaque radiotherapy [published online ahead of print November 23, 2016]. *Retina*. doi:10.1097/IAE.0000000000001414.

SUPPLEMENTARY TABLE 1. Descriptive clinical and multimodal imaging characteristics in 93 patients who underwent proton-beam therapy for uveal melanoma.

Sex (male/female), N.	43/50
Age, year	61.4±12.0 [33-85]
Tumor height, mm	4.6±1.8 [1.7-10.2]
Largest tumor diameter, mm	14.1±3.6 [6-23]
Tumor distance to the fovea, disc diameter	1.5±1.1 [0-4.7]
Extramacular localization, N. (%)	49 (53%)
Temporal, N. (%)	20 (22%)
Nasal, N. (%)	8 (9%)
Superior, N. (%)	16 (17%)
Inferior, N. (%)	4 (4%)
Macular localization, N. (%)	44 (47%)
Involving the fovea, N. (%)	17 (18%)
Extrafoveal, N. (%)	28 (30%)
Macular detachment at presentation, N. (%)	58 (62%)
Total macular irradiation, N. (%)	43 (46%)
Time since irradiation, year	3.8±2.7 [1-15]
Treatment by intravitreal anti-VEGF, N. (%)	34 (37%)
Hypertension	36 (39%)
Diabetes	8 (9%)

BCVA= best-corrected visual acuity; VEGF= vascular endothelial growth factor;

Continuous quantitative values are reported as mean ± standard deviation [range].

## APPENDICES

### Appendix 1: MatLab code for perifoveal intercapillary areas on OCT angiography

```
function intercapillary_area_iteration

file_list=dir('*.bmp');

%Prepare csv file for mean IA collection
cd('./-RESULTS')
f_IA_RESULTS=fopen('RESULTS_IA_MEAN.csv','w');
fprintf(f_IA_RESULTS,'%s; %s; %s; %s; %s\n','Name','Mean IA','SD IA','Min IA','Max IA');

%Return to working directory and process images
cd('../')

for i=1:length(file_list)
    FileName=file_list(i).name;

    %remove '_skel.bmp' at the end of FileName
    PatientName=FileName(1:end-9);

    %open image
    [~,X]=fileparts(file_list(i).name);
    A=imread(sprintf('%s.bmp',X));

    %function intercapillary_area running on each OCTA image
    B=im2bw(A);

    %filtering: 3 for SCP and 5 for DCP
    B2=bwareafilt(B,[3,inf]);
    B2a=bwmorph(B2,'dilate');
    B2b=bwmorph(B2a,'bridge');

    B3=1-B2b;
    B4=bwareaopen(B3,4);

    % IA=intercapillary areas / threshold for bwconncomp= 8
    CC=bwconncomp(B4,8);
    scale=size(B3,1)/3;
    IA=regionprops(CC,'area');

    %result in 10^3 mm2
    IA2=struct2array(IA)/scale^2*1000;
    IA2=sort(IA2,'descend');
    IA_mean=mean(IA2);
    IA_SD=std(IA2);
    IA_min=min(IA2);
    IA_max=max(IA2);

    %graphical representation of interpapillary areas
    numPixels = cellfun(@numel,CC.PixelIdxList);
    for i=1:size(numPixels,2)
        [~,idx] = max(numPixels);
        CC.PixelIdxList2{i}=CC.PixelIdxList{idx};
        numPixels(1,idx)=0;
    end

    CC.PixelIdxList=CC.PixelIdxList2;
    CC.NumObjects=size(numPixels,2);
    CC=rmfield(CC,'PixelIdxList2');

    B4_a=bwareafilt(B4,[2000 100000]);
    B4_b=bwareafilt(B4,[1000 1999]);
```

```

B4_c=bwareafilt(B4,[400 999]);
B4_d=bwareafilt(B4,[150 399]);
B4_e=bwareafilt(B4,[0 149]);

%necessary for color matrices
B_zeros=zeros(size(B4));

%create color map in blue and orange shades / FAZ and large defects in dark
%blue (like vessels)
B4_e_color=cat(3,B_zeros,.3*B4_e,.7*B4_e);
B4_d_color=cat(3,.2*B4_d,.6*B4_d,B4_d);
B4_c_color=cat(3,B4_c,B4_c,.6*B4_c);
B4_b_color=cat(3,B4_b,.8*B4_b,.6*B4_b);
B4_a_color=cat(3,B4_a,.8*B4_a,B4_a);

B4_color_final=B4_a_color+B4_b_color+B4_c_color+B4_d_color+B4_e_color;

%add image of vessels - dark blue
B_add=imadd(B4_color_final,double(cat(3,B_zeros,B_zeros,.5*(1-B4))));

    %save image
    cd('./-RESULTS/IMAGES/')
    imwrite(B_add,sprintf('%s_IA.png',PatientName),'png');

    %save value of all IAs from the processed OCTA image in csv
    cd('../Intercapillary_areas')
    f_IA=fopen(sprintf('%s_IA.csv',PatientName),'w');
    for i=1:length(IA2)
        fprintf(f_IA,'%4f\n',IA2(i));
    end
    fclose(f_IA);

    %save IA mean and descriptive values
    cd('../')
    fprintf(f_IA_RESULTS,'%s; %4f; %4f; %4f; %4f\n',PatientName, IA_mean,
IA_SD, IA_min, IA_max);

    %return to working directory for next iteration
    cd('../')
end
fclose(f_IA_RESULTS);
end

```

## Appendix 2: MatLab code for file moving and renaming

```
function MoveRename

%%CAUTION: removes file from source folder!!!

folder_list=dir();

    %PROCESS ALL FILES in folder except initial destination files and
    %HIDDEN FILES

    %SUP
for i=3:length(folder_list)
    patientName=folder_list(i).name;
    movefile(sprintf('%s/Layer_0/0(1)-Enface.bmp',patientName),sprintf('-
SUP/%s_sup.bmp',patientName));
end

    %SUP_bin
for i=11:length(folder_list)
    patientName=folder_list(i).name;
    movefile(sprintf('%s/Layer_0/3-Extracted_Vessel.bmp',patientName),sprintf('-
SUP_bin/%s_sup_bin.bmp',patientName));
end

    %SUP_skel
for i=11:length(folder_list)
    patientName=folder_list(i).name;
    movefile(sprintf('%s/Layer_0/1-Skeleton.bmp',patientName),sprintf('-
SUP_skel/%s_sup_skel.bmp',patientName));
end

    %DEEP
for i=11:length(folder_list)
    patientName=folder_list(i).name;
    movefile(sprintf('%s/Layer_1/0(1)-Enface.bmp',patientName),sprintf('-
DEEP/%s_deep.bmp',patientName));
end

    %DEEP_bin
for i=11:length(folder_list)
    patientName=folder_list(i).name;
    movefile(sprintf('%s/Layer_1/3-Extracted_Vessel.bmp',patientName),sprintf('-
DEEP_bin/%s_deep_bin.bmp',patientName));
end

    %DEEP_skel
for i=11:length(folder_list)
    patientName=folder_list(i).name;
    movefile(sprintf('%s/Layer_1/1-Skeleton.bmp',patientName),sprintf('-
DEEP_skel/%s_deep_skel.bmp',patientName));
end

    %SECTOR DEFINITION
for i=11:length(folder_list)
    patientName=folder_list(i).name;
    movefile(sprintf('%s/Layer_0/0(2)-SectorDefinition.bmp',patientName),sprintf('-
-SECTOR/%s_sector.bmp',patientName));
end

end
```

### Appendix 3: MatLab code for extracting OCT angiography images from Angiovue screen captures

```
function crop_octa
file_list=dir('*.*JPG');

for i=1:length(file_list)
[~,X]=fileparts(file_list(i).name);
A=imread(sprintf('%s.*JPG',X));

B=imcrop(A,[422 130 598 598]);

imwrite(B,sprintf('%s_crop.jpg',X),'jpg');
end
end
```

## Appendix 4: MatLab code for extracting OCT layer thickness quantitative values in injected and non-injected areas from Spectralis

```
function layer_png
%note: sprintf to include variable inside a string

%*****
%VERTICAL SCANS
%*****

%VERTICAL SCANS: select first M3, then J0, J15, M1.

h=msgbox({'Select VERTICAL scans: M3 then J0, J15, M1' ' ' 'In M3, select 3 points
and 2 vertical lines:' ' left inferior curve corner' ' 100µm scale' ' right
superior curve corner' ' fovea line' ' bleb limit line' ' ' 'In J0, J15, M1,
select 3 vertical lines:' ' left limit of curve' ' right limit of curve'
' fovea'});

%VERTICAL M3
%manual designation of the file to be processed - extension can be modified
[file,folder]=uigetfile('.png');
[Z,X]=fileparts(file);
M3 = imread(sprintf('%s.png',X));
imshow(M3)

%zero of y axis and left inferior corner
[xa,ya]=ginput(1);
%scale : 100 µm above ya
[xb,yb]=ginput(1);
%upper right corner
[xc,yc]=ginput(1);
%fovea line
[xfovea_M3,yfovea_M3]=ginput(1);
%bleb line
[xbleb_M3,ybleb_M3]=ginput(1);

L=abs(ya-yb);

%VERTICAL J0
J0 = imread(uigetfile('.png'));
imshow(J0)

%left vertical limit of curve
[xa_J0,z]=ginput(1);
%right vertical limit of curve
[xc_J0,zz]=ginput(1);
%fovea line
[xfovea_J0,zzz]=ginput(1);

%VERTICAL J15
J15 = imread(uigetfile('.png'));
imshow(J15)

%left vertical limit of curve
[xa_J15,z]=ginput(1);
%right vertical limit of curve
[xc_J15,zz]=ginput(1);
%fovea line
[xfovea_J15,zzz]=ginput(1);

%VERTICAL M1
M1 = imread(uigetfile('.png'));
imshow(M1)

%left vertical limit of curve
[xa_M1,z]=ginput(1);
%right vertical limit of curve
```

```

[xc_M1,zz]=ginput(1);
%fovea line
[xfovea_M1,zzz]=ginput(1);

%defines the minimal left and right limits common to the 4 curves
Xleft=min([xfovea_J0-xa_J0 xfovea_J15-xa_J15 xfovea_M1-xa_M1 xfovea_M3-xa]);
Xright=min([xc_J0-xfovea_J0 xc_J15-xfovea_J15 xc_M1-xfovea_M1 xc-xfovea_M3]);

J0_crop=imcrop(J0,[xfovea_J0-Xleft,yc,Xleft+Xright,abs(yc-ya-1)]);
J15_crop=imcrop(J15,[xfovea_J15-Xleft,yc,Xleft+Xright,abs(yc-ya-1)]);
M1_crop=imcrop(M1,[xfovea_M1-Xleft,yc,Xleft+Xright,abs(yc-ya-1)]);
M3_crop=imcrop(M3,[xfovea_M3-Xleft,yc,Xleft+Xright,abs(yc-ya-1)]);

%detection of logical curves
%detection of J0 curve
R_J0 = J0_crop(:,:,1) < 100;
G_J0 = J0_crop(:,:,2) < 100;
B_J0 = J0_crop(:,:,3) < 100;

logical_J0 = R_J0 & G_J0 & B_J0;

%detection of J15 curve
R_J15 = J15_crop(:,:,1) < 100;
G_J15 = J15_crop(:,:,2) < 100;
B_J15 = J15_crop(:,:,3) < 100;

logical_J15 = R_J15 & G_J15 & B_J15;

%detection of M1 curve
R_M1 = M1_crop(:,:,1) < 100;
G_M1 = M1_crop(:,:,2) < 100;
B_M1 = M1_crop(:,:,3) < 100;

logical_M1 = R_M1 & G_M1 & B_M1;

%detection of M3 curve
R_M3 = M3_crop(:,:,1) < 100;
G_M3 = M3_crop(:,:,2) < 100;
B_M3 = M3_crop(:,:,3) < 100;

logical_M3 = R_M3 & G_M3 & B_M3;

%save logical curves
imwrite(logical_J0, sprintf('%s_logical_J0 v.png',X),'png');
imwrite(logical_J15, sprintf('%s_logical_J15 v.png',X),'png');
imwrite(logical_M1, sprintf('%s_logical_M1 v.png',X),'png');
imwrite(logical_M3, sprintf('%s_logical_M3 v.png',X),'png');

A_vertical=[];
for x=1:(Xleft+Xright)-1
y_J0=100/L*abs(abs(ya-yc)-find(logical_J0(:,x),1,'first'));
y_J15=100/L*abs(abs(ya-yc)-find(logical_J15(:,x),1,'first'));
y_M1=100/L*abs(abs(ya-yc)-find(logical_M1(:,x),1,'first'));
y_M3=100/L*abs(abs(ya-yc)-find(logical_M3(:,x),1,'first'));
a=[x,y_J0,y_J15,y_M1,y_M3];
%vertical concatenation with the growing (x rows, 2 column)-matrix
A_vertical=[A_vertical;a];
end
A_vertical;

%define variables for x distances to shorten the formulae
X_v=Xleft+Xright;
X_bleb_v=Xleft+xbleb_M3-xfovea_M3;

A_total_vertical=horzcat([1-X_bleb_v:X_v-X_bleb_v-1],[1-Xleft:Xright-1],A_vertical);
B_total_vertical=num2cell(A_total_vertical);

% fprintf function to create .csv file (csvwrite does not handle cell arrays
% combining text and numbers). %f for decimal figures (numbers), %s for

```

```

% string (text) and %c for single letters. Modified from guidelines
% to produce a .csv file with ";" (semicolon) as separator (readable by
% Excel)
f_total=fopen(sprintf('%s_total_v.csv',X),'w');
for n=1:round(Xleft+Xright)-2
fprintf(f_total, '%.2f; %.2f; %.2f; %.2f; %.2f; %.2f;
%.2f\n',B_total_vertical{n,:});
end
fclose(f_total);

%*****
%HORIZONTAL SCANS
%*****

%HORIZONTAL SCANS: select first M3, then J0, J15, M1.
%SIDE: LEFT or RIGHT EYE?

prompt = {'Right or left eye? Answer r or l'};
dlg_title = 'Side';
side = inputdlg(prompt);

h=msgbox({'Select HORIZONTAL scans: M3 then J0, J15, M1' ' ' 'In M3, select 4
vertical lines:' ' left curve limit' ' (100µm scale already defined)' ' right
curve limit' ' fovea line' ' bleb limit line' ' ' 'In J0, J15, M1, select 3
vertical lines:' ' left limit of curve' ' right limit of curve' ' fovea'});

%HORIZONTAL M3
M3_h = imread(uigetfile('.png'));
imshow(M3_h)

%zero of y axis and left inferior corner
[xa,z]=ginput(1);
%100µm scale: already defined
%upper right corner
[xc,zz]=ginput(1);
%fovea line
[xfovea_M3_h,yfovea_M3_h]=ginput(1);
%bleb line
[xbleb_M3_h,ybleb_M3_h]=ginput(1);

%HORIZONTAL J0
J0_h = imread(uigetfile('.png'));
imshow(J0_h)

%left vertical limit of curve
[xa_J0,z]=ginput(1);
%right vertical limit of curve
[xc_J0,zz]=ginput(1);
%fovea line
[xfovea_J0,zzz]=ginput(1);

%HORIZONTAL J15
J15_h = imread(uigetfile('.png'));
imshow(J15_h)

%left vertical limit of curve
[xa_J15,z]=ginput(1);
%right vertical limit of curve
[xc_J15,zz]=ginput(1);
%fovea line
[xfovea_J15,zzz]=ginput(1);

%HORIZONTAL M1
M1_h = imread(uigetfile('.png'));
imshow(M1_h)

%left vertical limit of curve
[xa_M1,z]=ginput(1);
%right vertical limit of curve
[xc_M1,zz]=ginput(1);

```

```

%fovea line
[xfovea_M1,zzz]=ginput(1);

%defines the minimal left and right limits common to the 4 curves
Xleft_h=min([xfovea_J0-xa_J0 xfovea_J15-xa_J15 xfovea_M1-xa_M1 xfovea_M3_h-xa]);
Xright_h=min([xc_J0-xfovea_J0 xc_J15-xfovea_J15 xc_M1-xfovea_M1 xc-xfovea_M3_h]);

J0_h_crop=imcrop(J0_h,[xfovea_J0-Xleft_h,yc,Xleft_h+Xright_h,abs(yc-ya-1)]);
J15_h_crop=imcrop(J15_h,[xfovea_J15-Xleft_h,yc,Xleft_h+Xright_h,abs(yc-ya-1)]);
M1_h_crop=imcrop(M1_h,[xfovea_M1-Xleft_h,yc,Xleft_h+Xright_h,abs(yc-ya-1)]);
M3_h_crop=imcrop(M3_h,[xfovea_M3_h-Xleft_h,yc,Xleft_h+Xright_h,abs(yc-ya-1)]);

%detection of logical curves
%detection of J0 curve
R_J0_h = J0_h_crop(:,:,1) < 100;
G_J0_h = J0_h_crop(:,:,2) < 100;
B_J0_h = J0_h_crop(:,:,3) < 100;

logical_J0_h = R_J0_h & G_J0_h & B_J0_h;

%detection of J15 curve
R_J15_h = J15_h_crop(:,:,1) < 100;
G_J15_h = J15_h_crop(:,:,2) < 100;
B_J15_h = J15_h_crop(:,:,3) < 100;

logical_J15_h = R_J15_h & G_J15_h & B_J15_h;

%detection of M1 curve
R_M1_h = M1_h_crop(:,:,1) < 100;
G_M1_h = M1_h_crop(:,:,2) < 100;
B_M1_h = M1_h_crop(:,:,3) < 100;

logical_M1_h = R_M1_h & G_M1_h & B_M1_h;

%detection of M3 curve
R_M3_h = M3_h_crop(:,:,1) < 100;
G_M3_h = M3_h_crop(:,:,2) < 100;
B_M3_h = M3_h_crop(:,:,3) < 100;

logical_M3_h = R_M3_h & G_M3_h & B_M3_h;

%save logical curves
imwrite(logical_J0_h, sprintf('%s_logical_J0 h.png',X),'png');
imwrite(logical_J15_h, sprintf('%s_logical_J15 h.png',X),'png');
imwrite(logical_M1_h, sprintf('%s_logical_M1 h.png',X),'png');
imwrite(logical_M3_h, sprintf('%s_logical_M3 h.png',X),'png');

A_horizontal=[];
for x=1:(Xleft_h+Xright_h)-1
y_J0_h=100/L*abs(abs(ya-yc)-find(logical_J0_h(:,x),1,'first'));
y_J15_h=100/L*abs(abs(ya-yc)-find(logical_J15_h(:,x),1,'first'));
y_M1_h=100/L*abs(abs(ya-yc)-find(logical_M1_h(:,x),1,'first'));
y_M3_h=100/L*abs(abs(ya-yc)-find(logical_M3_h(:,x),1,'first'));
a_h=[x,y_J0_h,y_J15_h,y_M1_h,y_M3_h];
%vertical concatenation with the growing (x rows, 2 column)-matrix
A_horizontal=[A_horizontal;a_h];
end
A_horizontal;

%define variables for x distances to shorten the formulae
X_h=Xleft_h+Xright_h;

X_bleb_h=Xleft_h+xbleb_M3_h-xfovea_M3_h;

A_total_horizontal=horzcat([1-X_bleb_h:X_h-X_bleb_h-1],[1-Xleft_h:Xright_h-1],A_horizontal);
B_total_horizontal=num2cell(A_total_horizontal);

% fprintf function to create .csv file (csvwrite does not handle cell arrays
% combining text and numbers). %f for decimal figures (numbers), %s for

```

```

% string (text) and %c for single letters. Modified from guidelines
% to produce a .csv file with ";" (semicolon) as separator (readable by
% Excel)
f_total_h=fopen(sprintf('%s_total_h.csv',X),'w');
for n=1:round(Xleft_h+Xright_h)-2
fprintf(f_total_h,'%2f; %2f; %2f; %2f; %2f; %2f;
%2f\n',B_total_horizontal{n,:});
end
fclose(f_total_h);

%*****
%FINAL STEP: CREATE TABLE WITH MEANS
%*****

%FOR LEFT EYES
if side{1}=='l'
weight_in_v=(X_v-X_bleb_v)/(X_v-X_bleb_v+X_h-X_bleb_h);
weight_in_h=(X_h-X_bleb_h)/(X_v-X_bleb_v+X_h-X_bleb_h);

weight_out_v=X_bleb_v/(X_bleb_v+X_bleb_h);
weight_out_h=X_bleb_h/(X_bleb_v+X_bleb_h);

mean_out_v_J0 = mean(A_vertical(1:round(X_bleb_v)-1,2));
mean_out_v_J15= mean(A_vertical(1:round(X_bleb_v)-1,3));
mean_out_v_M1 = mean(A_vertical(1:round(X_bleb_v)-1,4));
mean_out_v_M3 = mean(A_vertical(1:round(X_bleb_v)-1,5));

mean_in_v_J0 = mean(A_vertical(round(X_bleb_v):round(X_v)-2,2));
mean_in_v_J15= mean(A_vertical(round(X_bleb_v):round(X_v)-2,3));
mean_in_v_M1 = mean(A_vertical(round(X_bleb_v):round(X_v)-2,4));
mean_in_v_M3 = mean(A_vertical(round(X_bleb_v):round(X_v)-2,5));

mean_out_h_J0 = mean(A_horizontal(1:round(X_bleb_h)-1,2));
mean_out_h_J15= mean(A_horizontal(1:round(X_bleb_h)-1,3));
mean_out_h_M1 = mean(A_horizontal(1:round(X_bleb_h)-1,4));
mean_out_h_M3 = mean(A_horizontal(1:round(X_bleb_h)-1,5));

mean_in_h_J0 = mean(A_horizontal(round(X_bleb_h):round(X_h)-2,2));
mean_in_h_J15= mean(A_horizontal(round(X_bleb_h):round(X_h)-2,3));
mean_in_h_M1 = mean(A_horizontal(round(X_bleb_h):round(X_h)-2,4));
mean_in_h_M3 = mean(A_horizontal(round(X_bleb_h):round(X_h)-2,5));

A_mean_v_h={sprintf('%s',X) 'outside_bleb_vertical' 'inside_bleb_vertical'
'outside_bleb_horizontal' 'inside_bleb_horizontal' 'outside_bleb_weighted_mean'
'inside_bleb_weighted_mean';'J0' mean_out_v_J0 mean_in_v_J0 mean_out_h_J0
mean_in_h_J0 weight_out_v*mean_out_v_J0+weight_out_h*mean_out_h_J0
weight_in_v*mean_in_v_J0+weight_in_h*mean_in_h_J0; 'J15' mean_out_v_J15
mean_in_v_J15 mean_out_h_J15 mean_in_h_J15
weight_out_v*mean_out_v_J15+weight_out_h*mean_out_h_J15
weight_in_v*mean_in_v_J15+weight_in_h*mean_in_h_J15;'M1' mean_out_v_M1 mean_in_v_M1
mean_out_h_M1 mean_in_h_M1 weight_out_v*mean_out_v_M1+weight_out_h*mean_out_h_M1
weight_in_v*mean_in_v_M1+weight_in_h*mean_in_h_M1; 'M3' mean_out_v_M3 mean_in_v_M3
mean_out_h_M3 mean_in_h_M3 weight_out_v*mean_out_v_M3+weight_out_h*mean_out_h_M3
weight_in_v*mean_in_v_M3+weight_in_h*mean_in_h_M3};

%FOR RIGHT EYES
elseif side{1}=='r'
weight_in_v=(X_v-X_bleb_v)/(X_v-X_bleb_v+X_bleb_h);
weight_in_h=X_bleb_h/(X_v-X_bleb_v+X_bleb_h);

weight_out_v=X_bleb_v/(X_bleb_v+X_h-X_bleb_h);
weight_out_h=(X_h-X_bleb_h)/(X_bleb_v+X_h-X_bleb_h);

mean_out_v_J0 = mean(A_vertical(1:round(X_bleb_v)-1,2));
mean_out_v_J15= mean(A_vertical(1:round(X_bleb_v)-1,3));
mean_out_v_M1 = mean(A_vertical(1:round(X_bleb_v)-1,4));
mean_out_v_M3 = mean(A_vertical(1:round(X_bleb_v)-1,5));

mean_in_v_J0 = mean(A_vertical(round(X_bleb_v):round(X_v)-2,2));
mean_in_v_J15= mean(A_vertical(round(X_bleb_v):round(X_v)-2,3));

```

```

mean_in_v_M1 = mean(A_vertical(round(X_bleb_v):round(X_v)-2,4));
mean_in_v_M3 = mean(A_vertical(round(X_bleb_v):round(X_v)-2,5));

mean_out_h_J0 = mean(A_horizontal(round(X_bleb_h):round(X_h)-2,2));
mean_out_h_J15= mean(A_horizontal(round(X_bleb_h):round(X_h)-2,3));
mean_out_h_M1 = mean(A_horizontal(round(X_bleb_h):round(X_h)-2,4));
mean_out_h_M3 = mean(A_horizontal(round(X_bleb_h):round(X_h)-2,5));

mean_in_h_J0 = mean(A_horizontal(1:round(X_bleb_h)-1,2));
mean_in_h_J15= mean(A_horizontal(1:round(X_bleb_h)-1,3));
mean_in_h_M1 = mean(A_horizontal(1:round(X_bleb_h)-1,4));
mean_in_h_M3 = mean(A_horizontal(1:round(X_bleb_h)-1,5));

A_mean_v_h={sprintf('%s',X) 'outside_bleb_vertical' 'inside_bleb_vertical'
'outside_bleb_horizontal' 'inside_bleb_horizontal' 'outside_bleb_weighted_mean'
'inside_bleb_weighted_mean';'J0' mean_out_v_J0 mean_in_v_J0 mean_out_h_J0
mean_in_h_J0 weight_out_v*mean_out_v_J0+weight_out_h*mean_out_h_J0
weight_in_v*mean_in_v_J0+weight_in_h*mean_in_h_J0; 'J15' mean_out_v_J15
mean_in_v_J15 mean_out_h_J15 mean_in_h_J15
weight_out_v*mean_out_v_J15+weight_out_h*mean_out_h_J15
weight_in_v*mean_in_v_J15+weight_in_h*mean_in_h_J15;'M1' mean_out_v_M1 mean_in_v_M1
mean_out_h_M1 mean_in_h_M1 weight_out_v*mean_out_v_M1+weight_out_h*mean_out_h_M1
weight_in_v*mean_in_v_M1+weight_in_h*mean_in_h_M1; 'M3' mean_out_v_M3 mean_in_v_M3
mean_out_h_M3 mean_in_h_M3 weight_out_v*mean_out_v_M3+weight_out_h*mean_out_h_M3
weight_in_v*mean_in_v_M3+weight_in_h*mean_in_h_M3};
end

%print final .csv file with mean values

f_mean=fopen(sprintf('%s_mean_v_h.csv',X),'w');
fprintf(f_mean,'%s; %s; %s; %s; %s; %s; %s\n',A_mean_v_h{1,:});
fprintf(f_mean,'%s; %.2f; %.2f; %.2f; %.2f; %.2f; %.2f\n',A_mean_v_h{2,:});
fprintf(f_mean,'%s; %.2f; %.2f; %.2f; %.2f; %.2f; %.2f\n',A_mean_v_h{3,:});
fprintf(f_mean,'%s; %.2f; %.2f; %.2f; %.2f; %.2f; %.2f\n',A_mean_v_h{4,:});
fprintf(f_mean,'%s; %.2f; %.2f; %.2f; %.2f; %.2f; %.2f\n',A_mean_v_h{5,:});
fclose(f_mean);

end

```

## Appendix 5: MatLab code for computing fluorescein expansion ratios on fluorescein angiography

```
function leak_area

[file, folder]=uigetfile('.tif');
[Z,W]=fileparts(file);
A=imread(sprintf('%s.tif',W));

%conversion to gray
B=rgb2gray(A);

%identification of the central point in leakage zone
imshow(B)
[x0,y0]=ginput(1);

%threshold determination
intensity0=impixel(B,x0,y0);
thresh=mean(intensity0/255*0.75);

C=im2bw(B,thresh);
imshow(C)

mask=roipoly(C);
leak_area=C.*mask;

area_pixel=bwarea(leak_area)
area_mm2=area_pixel*(200/9)^2/1000

%extract contour
area_contour= bwmorph(leak_area,'remove');

%green color for contour
R=0.6; G=1; Blue=0.6;
area_contour_green=cat(3,area_contour*R,area_contour*G,area_contour*Blue);

%combine FA image and green contour and save tif
B=im2double(B);
B2=immultiply(B,area_contour);
B3=imsubtract(B,B2);
B4=cat(3,B3,B3,B3);
h=imadd(B4,area_contour_green);
imshow(h)
imwrite(h,sprintf('%s_contour.tif',W),'tif');

%save data in .csv file
f_angio=fopen(sprintf('%s_leak.csv',W),'w');
fprintf(f_angio,'%s; %s; %s\n','pixel^2 area leakage', '10^-3 mm^2 area leakage','intensity threshold');
fprintf(f_angio,'%4f; %4f; %4f\n',area_pixel,area_mm2,thresh);
fclose(f_angio);
end
```

## Appendix 6: MatLab code for segmenting subretinal fluid volume in OCT stacks

```

function srf_segment
%%ADJUSTABLE PARAMETERS:
%% - threshold ratio hyper/hyporeflective pixels (around 1.3)
%% - r cursor for record of radius (around r+8)
%% - coefficient defining oct_crop3

%ask index number of initial file
prompt = {'Index number of initial OCT file?'};
dlg_title = 'OCT number';
n_oct1 = inputdlg(prompt);
n_oct1 = str2double(n_oct1);

file_list=dir('*.png');

%identify reference point in a reference image (chosen close to the
%beginning of the image list where SRD is small)
oct_ref=imread(file_list(round(length(file_list)/6)).name);

    oct_gray=rgb2gray(oct_ref);
    oct_gray=oct_gray(:,:,1);
    oct_crop=imcrop(oct_gray,[510,30,485,400]);
    oct_crop2=im2double(oct_crop);
    oct_crop3=oct_crop2-0.1;

    %Ldiag, L1, L2, dimpad1 and dimpad2 will serve for all files - they have
    identical size
    Ldiag=sqrt(size(oct_crop2,1)^2+size(oct_crop2,2)^2);

    %for later crop and numerical integration
    L1=size(oct_crop2,1)-1;
    L2=size(oct_crop2,2)-1;

    %preparer matrix for numerical integration
    C=zeros(0,L2+1);

    %create pad of '1s' around image to prevent border effect
    dimpad1=round(Ldiag/4);
    dimpad2=round(Ldiag/4);
    oct_pad=padarray(oct_crop2,[dimpad1 dimpad2],1,'both');
    imshow(oct_pad)

    [y0,x0_local]=ginput(1);

    %ADJUSTABLE PARAMETERS
    threshold_reflectivity=1.1;
    angles=[0 3 5 10 15 20 25 30 40 50 60 80 90 100 120 130 135 140 145 150 160 165
167 170 173 175 177 180 183 185 187 190 195 200 205 210 215 220 225 230 240 250 260
265 270 275 280 285 290 300 310 320 340 345 350 355 357 360 3];

    %PROCESS ALL FILES
for i=1:length(file_list)
    [~,X]=fileparts(file_list(i).name);
    oct=imread(sprintf('%s.png',X));

    %crop oct scan and remove possible borders due to rotation for follow-up
alignment
    oct_gray=rgb2gray(oct);
    oct_gray=oct_gray(:,:,1);
    oct_crop=imcrop(oct_gray,[510,30,485,400]);
    oct_crop2=im2double(oct_crop);

    %empirical correction factor for high intensity images - to homogenize images
(low mean image
    %intensity mean to 20/255 = 0.08
    oct_crop3=(0.08/mean2(oct_crop2))*oct_crop2;

```

```

%subtraction to reduce noise
oct_crop3=oct_crop2-0.2;
oct_crop3(oct_crop3<0.05)=0;

%create pad
oct_pad=padarray(oct_crop3,[dimpad1 dimpad2],1,'both');

%create convolution image for denoising and averaging
oct_conv20=1.5*conv2(oct_pad,ones(20)/400,'same');
oct_conv20(oct_conv20<0.05)=0;
oct_conv20(oct_conv20>1)=1;

%code for reference point relocation deleted

%segment SRF (angular iterations)
A=zeros(0,2);

for theta=angles
    B=zeros(0,1);

    for r=3:round(min(x0_local,y0)-1);

        roi0=imcrop(oct_conv20,[round(y0+r*sin(theta*2*pi/360)-
3),round(x0_local+r*cos(theta*2*pi/360)-3),4,4]);
        roi13=imcrop(oct_conv20,[round(y0+(r+4)*sin(theta*2*pi/360)-
3),round(x0_local+(r+4)*cos(theta*2*pi/360)-3),4,4]);

        b=mean2(roi13)/mean2(roi0);
        B= vertcat(B,b);
    end

    if isempty(find(B>threshold_reflectivity))==1
        B_min=A(find(angles==theta)-1,2);

    else B_min=min(find(B>threshold_reflectivity));
    end

    a=[theta,B_min+3];
    A=vertcat(A,a);
end

%create mask
SRF_1=round(y0+A(:,2).*sin(A(:,1)*2*pi/360));
SRF_2=round(x0_local+A(:,2).*cos(A(:,1)*2*pi/360));
SRF_mask=horzcat(SRF_1,SRF_2);

oct_mask=poly2mask(SRF_1,SRF_2,size(oct_pad,1),size(oct_pad,2));
se = strel('disk',8);
oct_close = imclose(oct_mask,se);
oct_close=bwmorph(oct_close,'dilate');
imshow(oct_mask)
imshow(oct_close)

%add red contour to oct image
oct_remove=bwmorph(oct_close,'remove');
oct_remove=bwmorph(oct_remove,'dilate');
R=1; G=0; B=0;
oct_remove_red=cat(3,R*oct_remove,G*oct_remove,B*oct_remove);
%combine OCT image and red contour
g=cat(3,oct_pad,oct_pad,oct_pad);
h=imadd(g,oct_remove_red);
h_crop=imcrop(h,[dimpad1+1 dimpad2+1 L2 L1]);

%crop file for volume calculation
oct_close_nopad=imcrop(oct_close,[dimpad1+1 dimpad2+1 L2 L1]);

%matrix for numerical integration // vertical oct scale: 51 pix=0.2mm
c=0.2/51*sum(oct_close_nopad,1);
C=vertcat(C,c);

```

```

    %save images
    imwrite(oct_crop2,sprintf('oct_crop_%s.png',X),'png');
    imwrite(oct_pad,sprintf('oct_pad_%s.png',X),'png');
    imwrite(oct_mask,sprintf('oct_mask_%s.png',X),'png');
    imwrite(oct_close,sprintf('oct_close_%s.png',X),'png');
    imwrite(h_crop,sprintf('oct_contour_%s.png',X),'png');

end

%numerical integration
n_oct_sup=n_oct1-1;
n_oct_inf=97-(n_oct1-1)-length(file_list);

C_sup=zeros(n_oct_sup,L2+1);
C_inf=zeros(n_oct_inf,L2+1);

C_final=vertcat(C_sup,C,C_inf);

%VOLUME INTEGRATION
volume_srf=0.0111*trapz(0.0625*trapz(C_final));

%register value
f_quantif=fopen('-volume_srf.csv','w');
fprintf(f_quantif,'%s; %s; %s\n','SRF VOLUME','Threshold reflectivity','Number of
sections');
fprintf(f_quantif,'%4f; %4f;
%4f\n',volume_srf,threshold_reflectivity,length(file_list));
fclose(f_quantif);

%heat map
I2=mat2gray(C_final);
I2=imresize(I2, [L2 L2]);

N = 256;
I2_N = round(N * (I2-min(I2(:)))/(max(I2(:))-min(I2(:))));
cmap = jet(N); % see also hot, etc.
C_heatmap = ind2rgb(I2_N,cmap);
imwrite(C_heatmap,'-heatmap.png');

%heat map with sliding mean (convolution)
I3=conv2(I2,ones(5)/25,'same');

I3_N = round(N * (I3-min(I3(:)))/(max(I3(:))-min(I3(:))));
cmap = jet(N); % see also hot, etc.
C_heatmap_conv = ind2rgb(I3_N,cmap);
imwrite(C_heatmap_conv,'-heatmap_conv.png');

%save integration matrix and image
dlmwrite('-integration_matrix.txt',C_final);
imwrite(I2,'-integration_image.png');
end

```

## Appendix 7: MatLab code for segmenting choriocapillaris flow voids on OCT angiography

```
function octa_voids_analysis

%create mask to remove label in lower left corner
mask=zeros(60);
mask=padarray(mask, [548 0],1, 'pre');
mask=padarray(mask, [0 548],1, 'post');

%create .csv file to write results
f_total=fopen('TOTAL_AREAS.csv','w');
fprintf(f_total,'%s; %s; %s\n','Image','Total_area','Number_voids');

file_list=dir('*.JPG');

for i=1:length(file_list)

%open image
[~,X]=fileparts(file_list(i).name);
octa=imread(sprintf('%s.JPG',X));

octa=octa(:,:,1);
octa=imresize(octa, [608 608]);
T=adaptthresh(octa,'Statistic','median','ForegroundPolarity','dark');

octa_bin=imbinarize(octa,T);
octa_bin_bridge=bwmorph(octa_bin,'bridge');
octa_bin_closed=bwmorph(octa_bin_bridge,'close');
octa_voids=1-octa_bin_closed;

octa_voids_mask=octa_voids.*mask;

%for illustration purposes:
octa_bin_closed_mask=octa_bin_closed.*mask;
octa_bin_mask=octa_bin.*mask;
octa_neg_mask=(1-octa_bin).*mask;

%for area calculations
%filtering of voids>10'000 μm2 according to Spaide AJO 2016
octa_voids_mask_filt=bwareafilt(im2bw(octa_voids_mask),[300 400000]);
CC=bwconncomp(octa_voids_mask_filt);
area_voids=regionprops(CC,'Area');
total_area=bwarea(octa_voids_mask_filt);

%save images
imwrite(octa_bin_mask,sprintf('%s_bin.png',X),'png');
imwrite(octa_neg_mask,sprintf('%s_neg.png',X),'png');
imwrite(octa_bin_closed_mask,sprintf('%s_bin_closed.png',X),'png');
imwrite(octa_voids_mask,sprintf('%s_voids.png',X),'png');
imwrite(octa_voids_mask_filt,sprintf('%s_voids_filt.png',X),'png');

%add total area value and number of filtered voids to the global .csv file
fprintf(f_total,'%s; %.1f; %.1f\n',X,total_area,size(area_voids,1));

%save detailed areas in an image-specific .csv file
area_voids_table=struct2table(area_voids);
writetable(area_voids_table,sprintf('%s_areas.csv',X));
end
fclose(f_total);
end
```

## Appendix 8: MatLab code for global capillary density after subtraction of large vessels and cystoid spaces on OCT angiography

```
function vesseldensity_square

%files opening:
%%superficial plexus
[file, folder]= uigetfile('.jpg');
[Z,X]=fileparts(file);
S = imread(sprintf('%s.jpg',X));

%define mean of avascular area (FAZ)
mask=roipoly(S);
threshold=mean(S(mask))+2*std2(S(mask));

S2=rgb2gray(S);
S3=logical(S2>threshold);
S3=bwpropfilt(S3,'Area',[20 Inf]);
S4=im2double(S3);
colormap('jet');

%adjust the size of the sliding matrix
slidingmean=conv2(S4,ones(5)/25,'same');

%code for heat map without using imagesc (pb with export)
I=slidingmean;
N = 256;
I_N = round(N * (I-min(I(:)))/(max(I(:))-min(I(:))));
cmap = jet(N); % see also hot, etc.
densitymap = ind2rgb(I_N,cmap);

%save densitymap
imwrite(densitymap,sprintf('%s_densitymap.tif',X),'tif');

%remove areas of cystic edema
%%ADJUST 0.01 for controls (no detection of cysts) and 0.04 for patients
%%%%%%%%%%%%%%%%%%%%%%%%%%%%%%%%%%%%%%%%%%%%%%%%%%%%%%%%%%%%%%%%%%%%%%%%
J=im2bw(S,0.04);
%%%%%%%%%%%%%%%%%%%%%%%%%%%%%%%%%%%%%%%%%%%%%%%%%%%%%%%%%%%%%%%%%%%%%%%%
J2=bwmorph(J,'majority');
J2=bwmorph(J2,'majority');
J2=bwmorph(J2,'majority');
J2=bwmorph(J2,'majority');
J2=bwmorph(J2,'majority');
J2=bwmorph(J2,'majority');
J2=bwmorph(J2,'majority');
J3=bwareaopen(1-J2,70);

%enlarge notext mask and remove text
notext_mask2=ones(size(J));
notext_mask2(350:393,2:120)=0;
J4=immultiply(J3,notext_mask2);

imwrite(J4,sprintf('%s_cysts.tif',X),'tif');

%identification of large vessels
%%%%%%%%%%%%%%%%%%%%%%%%%%%%%%%%%%%%%%%%%%%%%%%%%%%%%%%%%%%%%%%%%%%%%%%%
E=im2bw(S,0.5);
%%%%%%%%%%%%%%%%%%%%%%%%%%%%%%%%%%%%%%%%%%%%%%%%%%%%%%%%%%%%%%%%%%%%%%%%
F=bwareaopen(E,100);
Fclose=bwmorph(F,'close');
Fclose2=bwmorph(Fclose,'thicken');
imwrite(Fclose2,sprintf('%s_large_vessels.tif',X),'tif');

%new figure without large vessels
```

```

S7=imsubtract(S3,Fclose2);
slidingmean2=conv2(S7,ones(5)/25,'same');

%code for heat map without using imagesc (pb with export)
I2=slidingmean;
N = 256;
I2_N = round(N * (I2-min(I2(:)))/(max(I2(:))-min(I2(:))));
cmap = jet(N); % see also hot, etc.
densitymap2 = ind2rgb(I2_N,cmap);

%save densitymap2
imwrite(densitymap2,sprintf('%s_densitymap2.tif',X),'tif');

%measure of capillary density
%remove edema cysts
S8=immultiply(S7,1-J4);

%small notext mask and remove text
notext_mask=ones(size(S8));
notext_mask(369:384,12:89)=0;
S9=immultiply(S8,notext_mask);

%remove cysts
S10=immultiply(S9,1-J4);

%remove large vessels
S11=immultiply(S10,1-Fclose2);

%total area for density calculations
total_area=immultiply(1-Fclose2,immultiply(1-J4,notext_mask));

%save images used for density calculation
imwrite(total_area,sprintf('%s_total_area.tif',X),'tif');
imwrite(S11,sprintf('%s_vessel_density.tif',X),'tif');

%remove large vessels and cysts from density maps
densitymap_novessels=densitymap.*repmat(1-Fclose2,[1,1,3]);
densitymap_novessels_cysts=densitymap_novessels.*repmat(1-J4,[1,1,3]);

%small notext mask and remove text
notext_mask=ones(size(densitymap_novessels_cysts));
notext_mask(369:384,12:89,:)=0;
densitymap_novessels_cysts_notext=densitymap_novessels_cysts.*notext_mask;
imshow(densitymap_novessels_cysts_notext)

imwrite(densitymap_novessels,sprintf('%s_densitymap_novessels.tif',X),'tif');
imwrite(densitymap_novessels_cysts,sprintf('%s_densitymap_novessels_cysts.tif',X),'tif');
imwrite(densitymap_novessels_cysts_notext,sprintf('%s_densitymap_novessels_cysts_no
text.tif',X),'tif');

%mean intensity over ROI
mean_density=sum(sum(S11))/sum(sum(total_area))

%save results
f_quantif2=fopen(sprintf('density_%s.csv',X),'w');
fprintf(f_quantif2,'%s; %s; %s\n','vessel_density','Total_vessels','Total_area');
fprintf(f_quantif2,'%4f; %4f;
%4f\n',mean_density,sum(sum(S11)),sum(sum(total_area)));
fclose(f_quantif2);

end

```

## Appendix 9: MatLab code for local capillary density on OCT angiography

```
function local_density

%files opening:
%%deep plexus
[file, folder]= uigetfile('.jpg');
[Z, name_deep]=fileparts(file);
D = imread(sprintf('%s.jpg', name_deep));

%%sup plexus: binary image
[file, folder]= uigetfile('.tif');
[Z, name_sup]=fileparts(file);
S = imread(sprintf('%s.tif', name_sup));

%%sup plexus: total area without cysts nor large vessels
[file, folder]= uigetfile('.tif');
[Z, name_totalarea]=fileparts(file);
V = imread(sprintf('%s.tif', name_totalarea));

min1=min([size(D,1), size(S,1), size(V,1)]);
min2=min([size(D,2), size(S,2), size(V,2)]);
min3=min([min1, min2]);
D_crop=imcrop(D, [0 0 min3 min3]);
S_crop=imcrop(S, [0 0 min3 min3]);
V_crop=imcrop(V, [0 0 min3 min3]);

imshow(D_crop)
%ask n
prompt = 'What is the number of abnormal microvascular lesions? '
n = input(prompt);

local_density=[];
circles=zeros(min3,min3);
circles=im2bw(circles);

for i=1:n
[a,b]=ginput(1);

%definition of circular ROI: radius = 13.4 pixels = 100 microns
X=[];
Y=[];
for j=0:360
    xj=round(a+10*cosd(j));
    yj=round(b+10*sind(j));
X=[X,xj];
Y=[Y,yj];
end
circ_ROI=poly2mask(X,Y,min3,min3);

V_crop_bin=im2bw(V_crop);
circ_ROI_novessels=immultiply(circ_ROI,V_crop_bin);
S_crop_bin=im2bw(S_crop);
C=immultiply(S_crop_bin,circ_ROI_novessels);
sum_capillaries=sum(sum(C));
sum_ROI=sum(sum(circ_ROI_novessels));
density=sum_capillaries/sum_ROI;
local_density=[local_density,density];
circles=imadd(circles,circ_ROI);
circles=im2bw(circles);
end
local_density

%save results
f_quantif2=fopen(sprintf('density_%s.csv', name_deep), 'w');
fprintf(f_quantif2, '%s\n', 'local_density');
for i=1:n
```

```
fprintf(f_quantif2, '%.4f\n', local_density(i));  
end  
fclose(f_quantif2);  
  
imwrite(circles, sprintf('%s_circles.tif', name_deep), 'tif');  
  
end
```

## Appendix 10: MatLab code for generation of randomly distributed circles over OCT angiography images

```
function random_local_density2

%files opening:
%%deep plexus
[file, folder]= uigetfile('.jpg');
[Z, name_deep]=fileparts(file);
D = imread(sprintf('%s.jpg', name_deep));

%%deep plexus: circles identified around telangiectasias
[file, folder]= uigetfile('.tif');
[Z, name_regions]=fileparts(file);
R = imread(sprintf('%s.tif', name_regions));

%%sup plexus: binary image
[file, folder]= uigetfile('.tif');
[Z, name_sup]=fileparts(file);
S = imread(sprintf('%s.tif', name_sup));

%%sup plexus: total area without cysts nor large vessels
[file, folder]= uigetfile('.tif');
[Z, name_totalarea]=fileparts(file);
V = imread(sprintf('%s.tif', name_totalarea));

min1=min([size(D,1),size(S,1),size(V,1)]);
min2=min([size(D,2),size(S,2),size(V,2)]);
min3=min([min1,min2]);
D_crop=imcrop(D, [0 0 min3 min3]);
S_crop=imcrop(S, [0 0 min3 min3]);
V_crop=imcrop(V, [0 0 min3 min3]);
R_crop=imcrop(R, [0 0 min3 min3]);

local_density=[];
circles=zeros(min3,min3);
circles=im2bw(circles);

r=round(rand(1000,2)*min3);

%definition of FAZ (area=0.252 mm2) to exclude this localisation.
%Circle of radius = 282 microns = 37.83 pixels
X=[];
Y=[];
for j=0:360
    xj=round(min3/2+37.83*cosd(j));
    yj=round(min3/2+37.83*sind(j));
X=[X,xj];
Y=[Y,yj];
end

FAZ=poly2mask(X,Y,min3,min3);
R_crop_FAZ=imadd(R_crop,FAZ);
R_crop_FAZ=im2bw(R_crop_FAZ);

for i=1:1000
%definition of circular ROI: radius = 13.4 pixels = 100 microns
X=[];
Y=[];
for j=0:360
    xj=round(r(i,1)+13.4*cosd(j));
    yj=round(r(i,2)+13.4*sind(j));
X=[X,xj];
Y=[Y,yj];
end
circ_ROI=poly2mask(X,Y,min3,min3);
```

```

V_crop_bin=im2bw(V_crop);
circ_ROI_novessels=immultiply(circ_ROI,V_crop_bin);
S_crop_bin=im2bw(S_crop);
C=immultiply(S_crop_bin,circ_ROI_novessels);
sum_capillaries=sum(sum(C));
sum_ROI=sum(sum(circ_ROI_novessels));
density=sum_capillaries/sum_ROI;

R_crop_FAZ_circles=imadd(R_crop_FAZ,circles);
if sum(sum(immultiply(circ_ROI,R_crop_FAZ_circles)))==0
local_density=[local_density,density];
circles=imadd(circles,circ_ROI);
circles=im2bw(circles);
end

end

n=size(local_density,2);

%save results
f_quantif2=fopen(sprintf('random_density_noregions_%s.csv',name_deep),'w');
fprintf(f_quantif2,'%s\n','local_density');
for i=1:n
fprintf(f_quantif2,'% .4f\n',local_density(i));
end
fclose(f_quantif2);

imwrite(circles,sprintf('%s_random_circles_noregions.tif',name_deep),'tif');

end

```

## Appendix 11: MatLab code for perifoveal intercapillary areas on fluorescein angiography

```
function PIA_angiofluo_square

%FA 3x3mmm
[file, folder]= uigetfile('.tif');
[Z, title]=fileparts(file);
A=imread(sprintf('%s.tif', title));
A=imresize(A, [1000 1000]);
A2=rgb2gray(A);
imshow(A2)
%define FAZ edges
h=imfreehand();
mask=createMask(h);

%ex: polygon ROI: mask=roipoly(A2);

B=im2bw(A2, 0.23);
B1=bwmorph(B, 'thin');
B2=bwmorph(B1, 'skel');
B3=bwmorph(B2, 'skel');
B4=bwmorph(B3, 'close');
B4=bwmorph(B4, 'bridge');
B5=bwmorph(B4, 'skel');
B5=bwmorph(B5, 'skel');
B5=bwmorph(B5, 'skel');

B6=1-B5;
B7=bwmorph(B6, 'erode');
B7noFAZ=B7.*(1-mask);

% PIA=perifoveal intercapillary areas:
CC=bwconncomp(B7noFAZ, 8);
scale=size(B7, 1)/3000;
PIA=regionprops(CC, 'area');

%write csv PIA
PIA2=struct2array(PIA);

f_quantif=fopen(sprintf('%s_PIA.csv', title), 'w');
for n=1:length(PIA2)
fprintf(f_quantif, '%.4f\n', PIA2(n)/scale^2);
end
fclose(f_quantif);

%overlay images
R=.4; G=.4; B=.25;
OVR=cat(3, R*B7noFAZ, G*B7noFAZ, B*B7noFAZ);

A3=im2double(A);
A_OVR=imadd(A3, OVR);

%save images:
imwrite(mask, sprintf('%s_FAZ.tif', title), 'tif');

imwrite(B5, sprintf('%s_bin.tif', title), 'tif');
imwrite(B7noFAZ, sprintf('%s_PIA.tif', title), 'tif');
imwrite(A2_OVR, sprintf('%s_PIA_OVR.tif', title), 'tif');

end
```

## Appendix 12: MatLab code for cystoid cavities area and outlining

```
function edema

%chose OCT: initial, pre aflibercept 1, post aflibercept 1 or final
[file, folder]= uigetfile('.tif');
[Z,X]=fileparts(file);
oct = imread(sprintf('%s.tif',X));
imshow(oct)

%scale: identify center, then upper right corner of scale (vertical and
%horizontal)
%scale: pixel/ $\mu\text{m}$ 
[x0,y0]=ginput(1);
[xh,yv]=ginput(1);

scale_v=abs(yv-y0)/200;
scale_h=abs(xh-x0)/200;

oct_crop=imcrop;
imshow(oct_crop)

%%%%%%%%ADUST%%%%%%%%
oct_BW=1-im2bw(oct_crop,0.24);
%%%%%%%%%%%%%%%%
oct_BW2=medfilt2(medfilt2(oct_BW));
oct_BW3=bwmorph(oct_BW2,'close');
oct_BW4=bwareaopen(oct_BW3,40);
imshow(oct_BW4)
mask=roipoly(oct_BW4);
oct_cysts=oct_BW4.*mask;

area_pixels=bwarea(oct_cysts);
area_oct=bwarea(oct_cysts)/(scale_v*scale_h);

%extract contour of cysts
oct_remove= bwmorph(oct_cysts,'remove');

%red color for contour
R=1; B=0; G=0;
oct_remove_red=cat(3,R*oct_remove,B*oct_remove,G*oct_remove);

%combine OCT image and red contour and save tif
g=im2double(oct_crop);
h=imadd(g,oct_remove_red);
imshow(h)
imwrite(h,sprintf('OCT_cysts_%s.tif',X),'tif');

%save data in .csv file
f_oct=fopen(sprintf('%s_area.csv',X),'w');
fprintf(f_oct,'%s; %s; %s; %s\n','area_μm','area_pixels','scale_v','scale_h');
fprintf(f_oct,'%0.2f; %0.2f; %0.4f; %0.4f\n',area_oct,area_pixels,scale_v,scale_h);
fclose(f_oct);

area_oct
end
```



```

%INF
A_parafovea_inf_crop=imcrop(A_parafovea_sup_inf,[1 (upper_edge+120) 304 304-
(upper_edge+120)]);
black_sup=zeros(304-size(A_parafovea_inf_crop,1),304);
A_parafovea_inf=vertcat(black_sup,A_parafovea_inf_crop);
A_parafovea_inf=im2bw(A_parafovea_inf);

%temp & nasal:
A_parafovea_temp_nas=im2bw(bwpropfilt(A_parafovea,'Orientation',[60 120]) +
bwpropfilt(A_parafovea,'Orientation',[-120 -60]));

%determine location of LEFT region on IMAGE (as appears on screen)
%(then attribution to temp or nasal)
left_edge=find(sum(A_parafovea_temp_nas,1),1);
A_parafovea_left_crop=imcrop(A_parafovea_temp_nas,[1 1 (left_edge+120) 304]);
%add black cropped right part:
black_right=zeros(304,304-size(A_parafovea_left_crop,2));
A_parafovea_left=horzcat(A_parafovea_left_crop,black_right);
A_parafovea_left=im2bw(A_parafovea_left);

%RIGHT region of IMAGE (as appears on screen)
A_parafovea_right_crop=imcrop(A_parafovea_temp_nas,[(left_edge+120) 1 304-
(left_edge+120) 304]);
black_left=zeros(304,304-size(A_parafovea_right_crop,2));
A_parafovea_right=horzcat(black_left,A_parafovea_right_crop);
A_parafovea_right=im2bw(A_parafovea_right);

%distinguish OD & OS
LATERALITY_OS=strfind('PatientName','_OS');
%OD
if isempty(LATERALITY_OS)
A_parafovea_temp=A_parafovea_left;
A_parafovea_nas=A_parafovea_right;

else
%OS
A_parafovea_temp=A_parafovea_right;
A_parafovea_nas=A_parafovea_left;

end

%save extracted sector images

%create folder and make it writeable
mkdir('..--RESULTS',sprintf('%s/',PatientName));
fileattrib(sprintf('..--RESULTS/%s',PatientName),'+w');

cd(sprintf('..--RESULTS/%s',PatientName))

imwrite(A_grid,sprintf('%s_sector_grid.png',PatientName),'png');
imwrite(A_frame,sprintf('%s_sector_frame.png',PatientName),'png');
imwrite(A_parafovea,sprintf('%s_sector_parafovea.png',PatientName),'png');
imwrite(A_center,sprintf('%s_sector_center.png',PatientName),'png');
imwrite(A_parafovea_sup,sprintf('%s_sector_paraf_sup.png',PatientName),'png');
imwrite(A_parafovea_inf,sprintf('%s_sector_paraf_inf.png',PatientName),'png');
imwrite(A_parafovea_temp,sprintf('%s_sector_paraf_temp.png',PatientName),'png')
;
imwrite(A_parafovea_nas,sprintf('%s_sector_paraf_nas.png',PatientName),'png');

%PROCESS OCTA IMAGES:
cd('.../..--SUP_skel')
sup_skel=imread(sprintf('%s_sup_skel.bmp',PatientName));

cd('..--DEEP_skel')
deep_skel=imread(sprintf('%s_deep_skel.bmp',PatientName));
%Return to RESULTS/PatientName folder
cd(sprintf('..--RESULTS/%s',PatientName))

%SCP: make binary & remove connected regions of ?2 pixels

```

```

sup_skel=im2bw(sup_skel);
sup_skel_filt=bwareafilt(sup_skel,[3,inf]);

%DCP: make binary & remove connected regions of ?4 pixels (more noise)
deep_skel=im2bw(deep_skel);
deep_skel_filt=bwareafilt(deep_skel,[5,inf]);

%sector regions in SCP & DCP
%SCP
sup_skel_grid=immultiply(sup_skel_filt,A_grid);
sup_skel_frame=immultiply(sup_skel_filt,A_frame);
sup_skel_parafovea=immultiply(sup_skel_filt,A_parafovea);
sup_skel_center=immultiply(sup_skel_filt,A_center);
sup_skel_inf=immultiply(sup_skel_filt,A_parafovea_inf);
sup_skel_sup=immultiply(sup_skel_filt,A_parafovea_sup);
sup_skel_temp=immultiply(sup_skel_filt,A_parafovea_temp);
sup_skel_nas=immultiply(sup_skel_filt,A_parafovea_nas);
%DCP
deep_skel_grid=immultiply(deep_skel_filt,A_grid);
deep_skel_frame=immultiply(deep_skel_filt,A_frame);
deep_skel_parafovea=immultiply(deep_skel_filt,A_parafovea);
deep_skel_center=immultiply(deep_skel_filt,A_center);
deep_skel_inf=immultiply(deep_skel_filt,A_parafovea_inf);
deep_skel_sup=immultiply(deep_skel_filt,A_parafovea_sup);
deep_skel_temp=immultiply(deep_skel_filt,A_parafovea_temp);
deep_skel_nas=immultiply(deep_skel_filt,A_parafovea_nas);

%LOCAL FRACTAL DIMENSION lDf
%SCP
%3x3mm image
[n,r] = boxcount(sup_skel_filt,'slope');
df = -diff(log(n))./diff(log(r));
lDf_scp_total=mean(df(4:5));
print(sprintf('%s_scp_plot_total',PatientName),'-dpng');

%grid
[n,r] = boxcount(sup_skel_grid,'slope');
df = -diff(log(n))./diff(log(r));
lDf_scp_grid=mean(df(4:5));
print(sprintf('%s_scp_plot_grid',PatientName),'-dpng');

%frame
[n,r] = boxcount(sup_skel_frame,'slope');
df = -diff(log(n))./diff(log(r));
lDf_scp_frame=mean(df(4:5));
print(sprintf('%s_scp_plot_frame',PatientName),'-dpng');

%center
[n,r] = boxcount(sup_skel_center,'slope');
df = -diff(log(n))./diff(log(r));
lDf_scp_center=mean(df(4:5));
print(sprintf('%s_scp_plot_center',PatientName),'-dpng');

%parafovea
[n,r] = boxcount(sup_skel_parafovea,'slope');
df = -diff(log(n))./diff(log(r));
lDf_scp_parafovea=mean(df(4:5));
print(sprintf('%s_scp_plot_parafovea',PatientName),'-dpng');

%sup
[n,r] = boxcount(sup_skel_sup,'slope');
df = -diff(log(n))./diff(log(r));
lDf_scp_sup=mean(df(4:5));
print(sprintf('%s_scp_plot_sup',PatientName),'-dpng');

%inf
[n,r] = boxcount(sup_skel_inf,'slope');
df = -diff(log(n))./diff(log(r));
lDf_scp_inf=mean(df(4:5));

```

```

print(sprintf('%s_scp_plot_inf',PatientName),'-dpng');

%temp
[n,r] = boxcount(sup_skel_temp,'slope');
df = -diff(log(n))./diff(log(r));
lDf_scp_temp=mean(df(4:5));
print(sprintf('%s_scp_plot_temp',PatientName),'-dpng');

%nasal
[n,r] = boxcount(sup_skel_nas,'slope');
df = -diff(log(n))./diff(log(r));
lDf_scp_nas=mean(df(4:5));
print(sprintf('%s_scp_plot_nas',PatientName),'-dpng');

%%%DCP%%%
%3x3mm image
[n,r] = boxcount(deep_skel_filt,'slope');
df = -diff(log(n))./diff(log(r));
lDf_dcp_total=mean(df(4:5));
print(sprintf('%s_dcp_plot_total',PatientName),'-dpng');

%grid
[n,r] = boxcount(deep_skel_grid,'slope');
df = -diff(log(n))./diff(log(r));
lDf_dcp_grid=mean(df(4:5));
print(sprintf('%s_dcp_plot_grid',PatientName),'-dpng');

%frame
[n,r] = boxcount(deep_skel_frame,'slope');
df = -diff(log(n))./diff(log(r));
lDf_dcp_frame=mean(df(4:5));
print(sprintf('%s_dcp_plot_frame',PatientName),'-dpng');

%center
[n,r] = boxcount(deep_skel_center,'slope');
df = -diff(log(n))./diff(log(r));
lDf_dcp_center=mean(df(4:5));
print(sprintf('%s_dcp_plot_center',PatientName),'-dpng');

%parafovea
[n,r] = boxcount(deep_skel_parafovea,'slope');
df = -diff(log(n))./diff(log(r));
lDf_dcp_parafovea=mean(df(4:5));
print(sprintf('%s_dcp_plot_parafovea',PatientName),'-dpng');

%sup
[n,r] = boxcount(deep_skel_sup,'slope');
df = -diff(log(n))./diff(log(r));
lDf_dcp_sup=mean(df(4:5));
print(sprintf('%s_dcp_plot_sup',PatientName),'-dpng');

%inf
[n,r] = boxcount(deep_skel_inf,'slope');
df = -diff(log(n))./diff(log(r));
lDf_dcp_inf=mean(df(4:5));
print(sprintf('%s_dcp_plot_inf',PatientName),'-dpng');

%temp
[n,r] = boxcount(deep_skel_temp,'slope');
df = -diff(log(n))./diff(log(r));
lDf_dcp_temp=mean(df(4:5));
print(sprintf('%s_dcp_plot_temp',PatientName),'-dpng');

%nasal
[n,r] = boxcount(deep_skel_nas,'slope');
df = -diff(log(n))./diff(log(r));
lDf_dcp_nas=mean(df(4:5));
print(sprintf('%s_dcp_plot_nas',PatientName),'-dpng');

```

```

%%%SAVE IMAGES%%%
imwrite(sup_skel_grid,sprintf('%s_scp_grid.png',PatientName),'png');
imwrite(sup_skel_frame,sprintf('%s_scp_frame.png',PatientName),'png');
imwrite(sup_skel_parafovea,sprintf('%s_scp_parafovea.png',PatientName),'png');
imwrite(sup_skel_center,sprintf('%s_scp_center.png',PatientName),'png');
imwrite(sup_skel_inf,sprintf('%s_scp_inf.png',PatientName),'png');
imwrite(sup_skel_sup,sprintf('%s_scp_sup.png',PatientName),'png');
imwrite(sup_skel_temp,sprintf('%s_scp_temp.png',PatientName),'png');
imwrite(sup_skel_nas,sprintf('%s_scp_nas.png',PatientName),'png');

imwrite(deep_skel_grid,sprintf('%s_dcp_grid.png',PatientName),'png');
imwrite(deep_skel_frame,sprintf('%s_dcp_frame.png',PatientName),'png');
imwrite(deep_skel_parafovea,sprintf('%s_dcp_parafovea.png',PatientName),'png');
imwrite(deep_skel_center,sprintf('%s_dcp_center.png',PatientName),'png');
imwrite(deep_skel_inf,sprintf('%s_dcp_inf.png',PatientName),'png');
imwrite(deep_skel_sup,sprintf('%s_dcp_sup.png',PatientName),'png');
imwrite(deep_skel_temp,sprintf('%s_dcp_temp.png',PatientName),'png');
imwrite(deep_skel_nas,sprintf('%s_dcp_nas.png',PatientName),'png');

cd('../../--SECTOR');

%%%SAVE VALUES in csv%%%
fprintf(f_fractal,'%s; %.4f; %.4f; %.4f; %.4f; %.4f; %.4f; %.4f; %.4f; %.4f;
%.4f; %.4f; %.4f; %.4f; %.4f; %.4f; %.4f; %.4f; %.4f\n',PatientName, lDf_scp_total,
lDf_scp_grid, lDf_scp_frame, lDf_scp_center, lDf_scp_parafovea, lDf_scp_sup,
lDf_scp_inf, lDf_scp_temp, lDf_scp_nas, lDf_dcp_total, lDf_dcp_grid, lDf_dcp_frame,
lDf_dcp_center, lDf_dcp_parafovea, lDf_dcp_sup, lDf_dcp_inf, lDf_dcp_temp,
lDf_dcp_nas);

end

fclose(f_fractal);

end

```